CHEMO-MECHANICS OF IRON PHOSPHATE CATHODE

IN ALKALI METAL-ION BATTERIES

By

BERTAN OZDOGRU

Bachelor of Science in Chemical Engineering
Izmir Institute of Technology
Izmir, Turkey
2015

Master of Science in Chemical Engineering
Izmir Institute of Technology
Izmir, Turkey
2018

Submitted to the Faculty of the
Graduate College of the
Oklahoma State University
in partial fulfillment of
the requirements for
the Degree of
DOCTOR OF PHILOSOPHY
December, 2022

CHEMO-MECHANICS OF IRON PHOSPHATE CATHODE

IN ALKALI METAL-ION BATTERIES

Dissertation Approved:

Dr. Omer Ozgur Capraz

Dissertation Adviser

Dr. Mari Andiappan

Dr. Jindal Shah

Dr. Sandip Harimkar

Dr. Behrad Koohbor

ACKNOWLEDGEMENTS

If someone asks me what the Ph.D. study is, I can describe it as the journey of understanding what you are made of. As all journeys, it contains both success and failure, learning and teaching, and most importantly, personal sacrifices. I believe that the harder the challenge, you will receive a better reward. I am glad that I have made the journey and see its end. However, I didn't walk alone during this outstanding journey. It is a humbling and proud experience to acknowledge these people who have helped me along my journey.

First, I would like to express my gratitude to my advisor, Dr. Ömer Özgür Çapraz, for believing in me in the first place and accepting me as his first student. His tolerance, guidance and support was invaluable during my academic research. His vision, love of science and approach to science shaped my approach to science and inspired me.

I had a great opportunity to collaborate with several experts from battery community. I would like to thank Dr. Vijayakumar Murugesan, Dr. Min-Kyu Song and Dr. Vilas G Pol kindly for their support and collaboration. I would also like to thank Younghwan Cha and Zheng Li for their fruitful discussions.

Moreover, I would like to thank my committee members Dr. Mari Andiappan, Dr. Jindal Shah, Dr. Sandip Harimkar and Dr. Behrad Koohbor for their valuable support during my research. Their intriguing approach to my research question shaped the way I conducted my research while their critiques helped me understand the areas I needed to study.

I would like to thank my lab-mates Hannah Dykes, Darrell Gregory for their support and help during and after leaving Oklahoma State University. I would also like to thank my current lab-mate, Batuhan Bal, for his constant support and suggestion throughout my time in the AMEE Lab.

I am indebted to four very special colleagues; Anil Ronte, Atiya Banerjee, Ravi Teja Addanki Tirumala and Harshal Kaushik. Anil's companionship during my time with him as roommates helped me adopt living in a new country. Whenever I needed support in my research, I turned to Ravi Teja for his constant support and wisdom. Discussions with Atiya and Harshal let me broaden my vision not only in science but areas such as literature and music, while they let me participate in their road trips and helped me see the all-around United States. They have become my best friends and family at Oklahoma State University.

I wish to express my appreciation to my mother, Mihriban, and my late father, Mehmet, for their moral support and encouragement throughout my life. They have fed my appetite for science and have sacrificed a lot to support my passion. I have also received unconditional support from my dear sister, Benay, and my niece, Lara. No words can express my deepest gratitude to my family members.

Name: BERTAN OZDOGRU

Date of Degree: DECEMBER, 2022

Title of Study: CHEMO-MECHANICS OF IRON PHOSPHATE CATHODE IN ALKALI METAL-ION BATTERIES

Major Field: CHEMICAL ENGINEERING

Abstract: Utilization of renewable energy sources requires the use of grid-scale stationary energy storage that requires low-cost, safe, and nontoxic systems. For these applications, "beyond" lithium-ion battery chemistries, such as sodium and potassium-ion batteries, are possible alternatives due to their abundance and lower cost. However, their larger ionic radius and chemical reactivity can cause performance degradation in the long-term because of chemo-mechanical instabilities. The main goal of the work is to elucidate the relationship between chemo-mechanics of different alkali-metal ion intercalation and chemo-physical response of electrode materials. Investigation of this phenomena carried out by utilizing in-situ strain measurement coupled with in-situ XRD, HR-TEM, and mathematical model. First stage of the investigation focused on the effect of different alkali metals on the same host structure. Initial findings indicated that iron phosphate host structure experienced larger-than-expected expansion during first lithium and sodium intercalation, which became more reversible in subsequent cycles. During potassium intercalation, in-situ XRD and HR-TEM results showed the amorphization of iron phosphate structure. By employing DIC technique, reversible deformations in the amorphous phase was tracked during electrochemical redox reaction. Comparing the effect of these alkali metal on redox chemistry and mechanical deformation showed that strain rate, instead of absolute value of the strain, is critical factor in the amorphization of crystal structure. Second stage of the research focused on the effect of cycling rate on the mechanical deformation of electrode materials. In-situ strain measurements, coupled with GITT analysis and transport-mechanics model indicated that, lower diffusivity of sodium in the cathode results in the steep concentration gradient and misfit strain generation at faster scan rates. In the case of lithium intercalation, in situ strain measurements during pulsed current charge/discharge experiments indicated that at faster scan rates, phase transformation was delayed. In the last stage, DIC system was employed to investigate mechanical deformation of LAGP solid electrolyte for all-solid-state battery applications. During this study, increase strains at the metal/solid electrolyte interphase coincided with increase in the overpotential. This result experimentally showed the relationship between overpotential generation and strain evolution between metal/solid electrolyte interphase. These findings indicate that 1) strain rate is critical to the amorphization of crystal structure and 2) chemical reactivity of different alkali metals cause difference in mechanical response of electrode materials when batteries cycled at different scan rates. Understanding the similarities and differences between alkali metals on mechanical deformation will provide new insights into the selection of battery materials for beyond lithium-ion battery applications.

TABLE OF CONTENTS

LIST OF TABLES

LIST OF FIGURES

Figure   Page

CHAPTER I

INTRODUCTION

1.1 Battery Technologies and Definitions

Roots for commercial energy storage technology can be traced back to the Volta battery in 1800[1]. Since then, batteries evolved into technologies such as lead-acid, nickel-metal hydrates (Ni-MH), or nickel-cadmium (Ni-Cd) batteries. These batteries, while affordable to produce and readily available, they had very low volumetric and gravimetric energy capacity for portable applications[2]. With the afford of recent Nobel winners Dr. Goodenough, Dr. Whittingham, and Dr. Yoshino, materials such as graphite and $LiCoO_2$ for Li-Ion batteries were discovered. Using these discoveries, Sony Corporation announced the first commercially successful Li-ion batteries we know today in 1991 and started the era of lithium-ion batteries[3]. Li-ion batteries have since then affected everyday life by mobile devices, electrical vehicles, and aviation technologies.

Typical battery components are shown in **Figure 1**. In a typical setup, a battery consists of four main components[4].

- o **Electrode**: Electrochemical oxidation/reduction reaction takes place at the surface of the electrode and ions are stored in their structure. For electrochemical systems, an anode is an electrode that has low electrochemical potential whereas a cathode is an electrode with high electrochemical potential.

- **Electrolyte:** It facilities the ion transfer between the electrodes while preventing any electron transfer. It can be ionic liquids, solid-state ceramic, polymeric, salts dissolved in aqueous solutions, or organic solutions.

- **Separator.** Separators are essential in battery applications to prevent short circuits (Direct transfer of electrons between two electrodes) due to the proximity of two electrodes. They can be considered ionically conducting-electronically insulating materials.

- **External Circuit:** It is the place where the electrons are transferred between two electrodes. They do not participate in the electrochemical reaction.

In commercial lithium-ion batteries, anode and cathode materials are prepared by mixing conductive additives (to increase the conductivity) and polymeric binders (to keep everything together). This mixture is made into a slurry and cast onto current collectors to prepare the composite electrode. Then, a separator is placed between the anode and cathode. Finally, liquid electrolyte fills the pores of electrodes and separator to create a continuous transport pathway between two electrodes. With the assembly completed, the battery is ready for electrochemical reactions.

Before going into details about battery operation, the difference between electrochemical and chemical reactions should be discussed. The main differences between chemical and electrochemical reactions can be listed as follow[5].

- **Separation of oxidation and reduction reactions**: Since the electrons involved in the reactions are transferred through the external circuit, oxidation and reduction take place on *the anode and cathode electrodes* simultaneously during electrochemical reactions. In chemical reactions, both oxidation and reduction reactions happen on *the same* surface.

o **Heterogeneity of the reaction**: Electrochemical reactions *always occur heterogeneously*, which means they occur at the interface between the electrolyte and electrode surface. Chemical reactions can occur both homogeneously and heterogeneously.
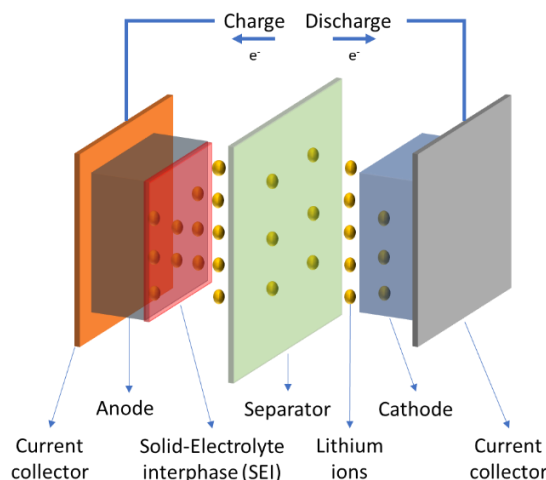
Figure 1. Schematic of a common Li-ion battery with the main components. During the charging, Li ions are removed from the cathode structure and inserted into the anode by diffusing through electrolyte and separator. Electrons generated during the removal of Li ions also transferred to the anode through the external circuit. During the discharge, the opposite of charging observed, where lithium ions and electrons transferred to the cathode via electrolyte and external circuit, respectively. SEI layer shown in the figure is composed of decomposition products of electrolyte salt, solvent, and composite electrode structure.

o **Electrons as work source:** Generally, when the external circuit is completed, electrons spontaneously flows from anode to cathode until equilibrium is achieved. The reason for this spontaneity is the energy of the electrons in the anode is higher than the cathode side. If the circuit is connected to an external device; such as a portable device, electron energy can be converted into work. Discharge of the battery can be a good example of this application.

o **Control of direction and rate of reaction:** For electrochemical systems, the electric potential is a measure of the electron energy. By adjusting the potential or applied current, one can alter the rate of reaction or change the direction of the reaction altogether.

During the charging of the battery, ions are removed from the cathode material (oxidation) and inserted into the anode material (reduction) by transporting through the electrolyte. Electrons

generated at the cathode side are transferred to the anode side via the external circuit. During the discharging, opposite to charging, ions and electrons moved from anode side (oxidation) to cathode side (reduction). During battery operation, some of the organic electrolyte and electrolyte salt might decompose on the surface of the electrode to form solid-electrolyte interphase (SEI) due to side reactions. The good SEI layer protects the electrode and prevents further electrolyte decomposition. However, the undesirable SEI layer can diminish the surface reactions and cause the rapid capacity fade in the battery.

1.2 "Beyond" Li-ion Batteries

With the help of studies done on lithium-ion batteries for the last 30 years, researchers achieved higher and lighter energy storage solutions for mobile applications. Advancements in portable technologies significantly increased electrical energy usage in the world. Due to the depletion of non-renewable energy sources, the utilization of renewable energy has also increased. Data from the US Energy Information Administration in **Figure 2** shows that electricity consumption in the world will increase by 30% in the year 2050[6]. In this period, renewable energy production will be doubled while the contribution of coal will be halved. Currently, the State of Oklahoma alone generates 17% of its electricity from wind power, which correlates to 9% of all wind power generated in USA[7]. While this contribution will lead to a reduction in fossil fuel use, it comes with
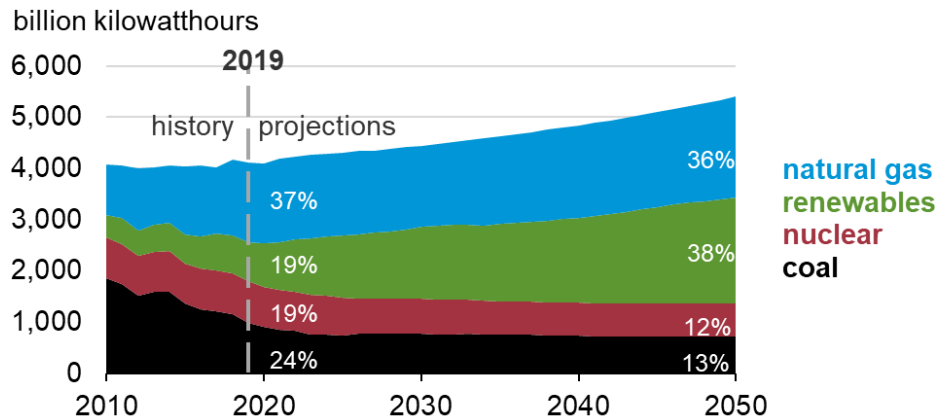
Figure 2. World energy consumption estimation up to the year 2050. The figure is taken from[6]

its own set of problems. Oscillation observed in **Figure 3** caused by environmental effects such as day and night cycles, seasonal changes, etc. Thus, the energy produced from renewable energy should be stored to mitigate this oscillation. With these reasons in mind, researchers started working on stationary energy storage solutions for renewable energy sources.
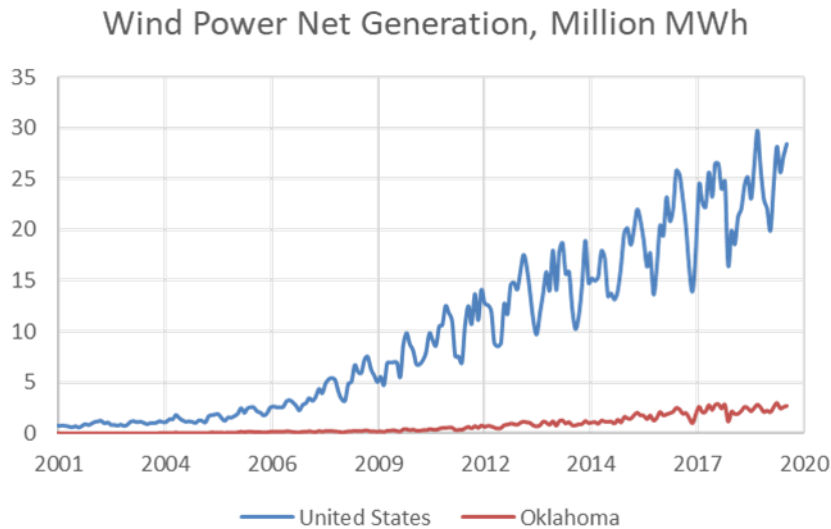
Figure 3. Wind energy production in Oklahoma, and the USA between 2001 to 2019. The figure is reproduced from[7]

The main parameters for large scale stationary energy storage are the cost and lifetime of the battery. Therefore, the scarcity and price of the lithium, shown in **Table 1**, makes it unsuitable for this application. For this reason, researchers have been investigated other battery chemistries to develop more affordable batteries. Sodium and potassium chemistry, which belong to alkali metals in the 1A group, have been taken serious attention by the researchers for the last ten years[8]. **Table 1** compares the physical, chemical, and economical differences among Li-ion, Na-ion, and K-ion batteries. Both sodium and potassium materials are much affordable compared to lithium. These alkali metals are expected to undergo similar electrochemical reactions due to their monovalent structure. Because of this similarity, these metals can replace lithium. This, in turn, will significantly reduce the prices, which is the primary concern for large scale energy storage solutions.

While first studies on sodium-ion batteries started at the same time as lithium-ion batteries[9], however, higher energy density potential of lithium-ion batteries shifted the research in this direction. Studies on cathode materials were conducted throughout the 1970s and 1980s, but a suitable anode material wasn't available for sodium batteries[10–12]. Discovery of hard carbon as sodium insertion anode significantly increased the number of studies for sodium-ion battery applications[13]. Afterward, sodium-ion battery research started to pick up. Currently, Faradion Limited based in the United Kingdom produces commercial sodium-ion batteries for renewable energy power storage applications with a capacity of 150-160 mAh/g.

Table 1. Physical and economic characteristics of lithium, sodium, and potassium. Prices for carbonates and metals are from 2017. The table is reproduced from[8]

	Lithium	Sodium	Potassium
Atomic Number	3	11	19
Atomic Mass (u)	6.941	22.99	39.0983
Atomic Radius (pm)	145	180	220
Covalent Radius (pm)	128	166	203
Melting Point (ºC)	180.54	97.72	63.38
Crust Abundance (mass %)	0.0017	2.3	1.5
Crust Abundance (molar %)	0.005	2.1	0.78
Voltage vs S.H.E. (V)	-3.04	-2.71	-2.93
Cost of carbonate (US$ ton^{-1})	23000	200	1000
Cost of industrial-grade metal (US$ ton^{-1})	100,000	3,000	13,000

Potassium has its unique advantages compared to sodium for beyond lithium-ion batteries. While it is less abundant compared to sodium, it offers lower reduction potential compared to sodium[14].In electrochemistry, the lower reduction potential means that electrons have higher energy[4]. This means that potassium batteries can offer higher operating potentials and energy densities compared to sodium. Potassium also possesses lower Lewis acidity, resulting in faster transport rates through the electrolyte-electrode interface. However, in comparison with Li and Na ions, K ions diffuse much slower in the electrode structure due to their larger atomic radius[8]. After the discovery of potassium intercalation into graphite structure in 2015, potassium ion battery research increased its

importance in the research community[15]. This larger atomic radius significantly alters the requirements of cathode materials where the larger interlayer distance required from the cathode side also. Polyanionic materials like $KFeSO_4F$, $KVPO_4F$, $K_3V_2(PO_4)_2F_3$, Prussian blue analogs, and other organic compounds are widely studied as cathode material for potassium-ion batteries[16]. While beyond lithium-ion batteries offer a more abundant and affordable option for energy storage, lithium-ion battery research is still the dominant research area among researchers. The primary reason is the insufficient performance of the Na-ion and K-ion batteries due to the rapid capacity fade associated with the mechanical and chemical instabilities.

1.3 Chemo-mechanical Degradation Mechanisms in Batteries

Lifetime and capacity of batteries are affected by many factors. During the electrochemical reactions, a composite electrode interacts with electrolyte and ions transferred between two electrodes. During these interactions, both electrode and electrolyte undergo irreversible changes. The performance of electrode worsens by cycling due to the dissolution of active material[17] and particle failure[18] and SEI formation[19]. A combination of these factors is considered as the chemo-mechanical degradation mechanism in batteries.

As mentioned in the previous part, a composite electrode consists of three main ingredients: active material, binder, and conductive additive. During battery operation, the active ion is inserted or removed from the active material, while the binder and conductive additive stay inert. During the ion transport, electrode material undergoes chemical and physical changes due to the electrochemical reaction. Since electrochemical reaction occurs in the interface between electrolyte and electrode, this results in the formation of ion rich and ion deficient areas in the electrode particle. Resulting concentration difference causes volume inhomogeneity inside the electrode particle itself. Also, free expansion of ion rich areas restricted by the current collector and limited space in battery packing. The buildup of pressure within and between the active material particles

results in the stress generation. Under the stress, the active material is prone to be fractured which causes loss connection between the current collector and creates an inactive electrode in the composite. This is considered as mechanical degradation.

Due to the irreversible interaction between electrode and electrolyte, the SEI layer forms on the electrode surface. This layer is beneficial because it passivates the electrode surface and prevents the further degradation of electrolyte. During the ion transport to the active material particle, its volume change might be up to 300%, depending on the electrode[20]. If the SEI layer formed during the cycling is stiff and expansion is large enough, this layer will crack. To passivate the freshly formed surface, the electrolyte will decompose at that point to create a fresh SEI layer. Repeated expansion and contraction of active material will cause further electrolyte decomposition and thickening of the said layer. This is considered as surface instability. Because both mechanical and surface instabilities are coupled, it can be simply called chemo-mechanical degradation of the electrode. All these chemo-mechanical degradation pathways can be seen in **Figure 4**[21]. Due to their bigger ionic radius, insertion and removal of sodium and potassium from the host structure will induce much higher strain and stress generation within the electrode structure. Understanding the relationship between electrochemically induced mechanical changes on the electrode with different active ions and battery performance is crucial for bridging the gap between lithium-ion and beyond lithium-ion battery research. This work will focus on the characterization of the mechanical response of similar host structures (for cathodes) with different active ions, specifically lithium, sodium, and potassium.

Mathematical models developed for lithium-ion batteries show that insertion or removal of lithium might cause a concentration gradient within the electrode particle. Depending on the type of electrode material, this change can be caused by the insertion/removal of lithium ions into/from the lattice structure of the electrode (graphite[22], lithium cobalt oxide[23], lithium nickel cobalt manganese oxide[24], etc.) or the alloying/dealloying of lithium ions with the host structure (tin/antimony[25],
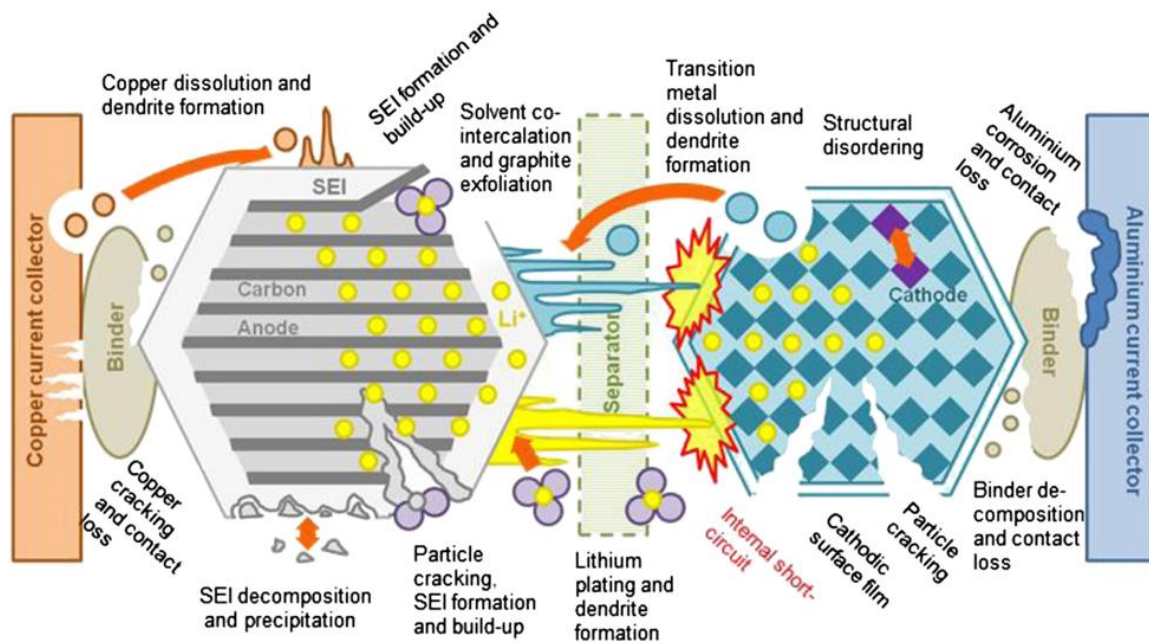
Figure 4. Visual representation of chemo-mechanical degradation pathways for a battery. Figure is taken from[61].

silicon[26], etc.). Depending on the material properties and cycling rate, the concentration gradient results in misfit strain generation between lithiated and lithium deficient zones, as well as stress generation due to expansion and contact between active materials[21]. Models suggest that during these changes if the material is too brittle or gradient is too sharp, electrode material starts to degrade under the intense mechanical loads[22,27,28].

To understand how the intercalation chemistry and associated strains influence the mechanical stability of the electrode particles, researchers have employed different experimental methods to investigate. Ex-situ analysis of electrode particles employing various experimental procedures gives us valuable information on how this phenomenon occurs and affects the electrodes. However, understanding the dynamic changes during the electrochemical reaction is crucial. Therefore, in-situ experimental procedures coupled with the electrochemical response of the electrode give us a better picture to design next-generation electrodes. Some of the in-situ analyses can be listed but not limited to SEM[29], TEM[26], AFM[30], XRD[23,24,31,32], XAS[31], curvature measurements[33–35], and digital image correlations[36–38]. Methods such as XRD, XAS, AFM, SEM or TEM gives very

detailed information on particle level at very high resolutions, they require specialist equipment and can lack the quantitative analysis tools to understand electrode particle.

The digital image correlation (DIC) method is an optical method at which, displacements are calculated by tracking the speckle pattern of initial and final images. The computer tracks the deformation by following the random speckle pattern; natural or artificial, on the surface of interest. DIC method successfully utilized to track the mechanical changes on alloys[39], metal structures[40], and biological materials[41,42]. The DIC method for electrochemical systems provides a simple experimental procedure with a powerful quantitative analysis tool. In this research, we will use the DIC method to quantify the strain generated in a similar host with different alkali metal insertion and removal and compare them.

1.4 Proposed Research

We hypothesize that, due to the larger ionic radius of sodium and potassium, insertion and removal of these alkali ions will induce larger chemo-mechanical degradation in the electrode material. The effect of different alkali ion insertion and removal can be tracked with the DIC method. Combination of the strain evolution with electrochemical response can give us insight into how different alkali ions affect similar electrode structures. In this research, we are proposing to utilize the digital image correlation method to track the changes in the same composite electrode structure with different alkali ion intercalation. The novel part of this study is the quantitative comparison of different active ions on the same host structure, for example, lithium iron phosphate or polyanionic compounds. Parameters such as electrode composition, polymer binder type, electrolyte composition, and effect of cycling rate will also be investigated. These studies will also provide crucial insights into how these parameters affect the strain generation with different alkali metal ions. Our objective is to understand the physical response of the cathodes upon intercalation of alkali-metal ions

Chapter 2 describes some of the electrochemical characterization techniques that will be utilized during the proposed research. Chapter 3 shows the in-situ strain measurement experimental setup and explains the DIC method. Chapter 4 shows the preliminary study done for the in-situ strain evolution of perovskite iron phosphate structure during the intercalation of lithium and sodium ions. In this study, we have investigated how lithium and sodium affect the same composite iron phosphate structure. Chapter 5 incorporates in-situ XRD and in-situ strain measurements to investigate the effect of potassium intercalation into iron phosphate structure. By using in-situ XRD, we showed that during potassium intercalation, crystalline iron phosphate structure amorphized. Utilization of in-situ strain system, we were able to show the expansion and shrinkage of composite electrode during electrochemical redox reactions. In Chapter 6, we compared the effect of lithium, sodium, and potassium intercalation into iron phosphate host structure. At similar state of discharge, sodium and potassium intercalation showed similar expansion in the electrode. Interestingly, while the absolute strain at the end of discharge was higher in sodium intercalation, strain rates were higher in potassium intercalation. This result indicates that, strain rate, not the absolute strain, is crucial factor for the amorphization of iron phosphate structure. Chapter 7 shows the effect of cycling rate on the strain evolution during the sodium intercalation into iron phosphate structure. At higher scan rates, we observed lower capacity in the composite electrode, while as slower scan rates, electrode undergoes lower strain generation for the same state of charge/discharge. We have developed a mathematical model to compute the concentration profile and mismatch strain generation during electrochemical cycling. In Chapter 8, we investigated the effect of cycling rate on the iron phosphate host structure during lithium intercalation. In Chapter 9, we have established a new experimental protocol for our in-situ strain measurement system to investigate the strain evolution in all-solid-state ceramic electrolyte batteries using symmetric cells. In this study, we showed the relationship between overpotential generation and strain evolution at the interphases, where higher strains resulted with higher overpotential during electrochemical

cycling. Large shear strains were detected at the middle of ceramic electrolyte, where fractures were detected using ex-situ micro-X-ray computed tomography.

CHAPTER II

ELECTROCHEMICAL CHARACTERIZATION TECHNIQUES

In its core, electrochemistry investigates how the electrons and ions are moved through the reaction media. It is crucial for researchers to understand the transport and kinetic parameters, as well as evaluate the performance of an electrochemical system. These parameters can be used to determine the suitability of the electrode and electrolytes under operating conditions. To investigate these, researchers set up experimental procedures, such as Cyclic Voltammetry (CV), galvanostatic cycling, Electrochemical Impedance Spectroscopy (EIS) and Galvanostatic Intermittent Titration Technique (GITT) for the analysis of electrode and electrolytes. This section will briefly explain these methods and theories behind them.

2.1 Cyclic Voltammetry

In a cyclic voltammetry experiment, the potential of the working electrode is changed at a constant sweep rate (V/s) until a certain switching potential. At the switching potential, the direction of the sweep is changed. If the sweep is in a positive direction, meaning the potential difference between two electrodes increases, it is named anodic scan. If the sweep is in negative direction, it is called cathodic scan. During both anodic and cathodic scan, current evolution is monitored. Representation of voltage change during cyclic voltammetry can be seen in **Figure 5**.
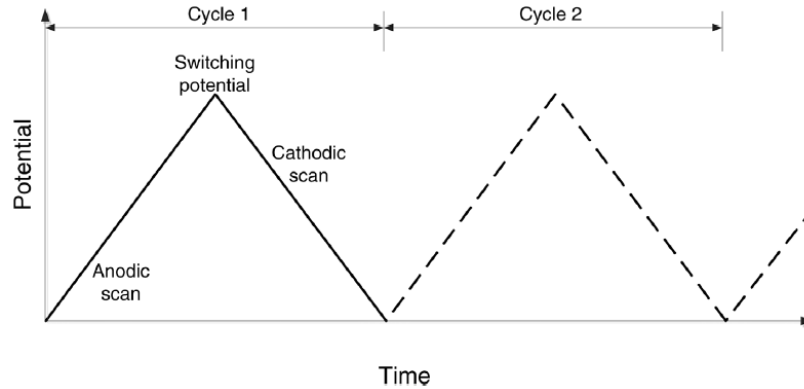
Figure 5. Voltage evolution during cyclic voltammetry versus time. The figure is taken from[5].

In the battery systems, during the anodic scan, positive electrode (cathode) loses an electron (oxidation) and releases the active ion to the electrolyte responsible for electrochemical reaction. This electron travels through the external circuit and reaches the negative electrode (anode). To complete the electrochemical redox reaction, active ions transported through the electrolyte react with an electron on the anode surface (reduction). During this process, energy is supplied to the battery cell. During this step, the battery is charged, and active ions transferred from cathode to anode. The current response of the anodic scan is represented as positive values.

Opposite to this, during the cathodic scan, anode oxidizes and releases the active ion to the electrolyte. The electron travels through the external circuit and reaches the cathode. There, active ion transported through the electrolyte reduces at the cathode surface. This reaction occurs spontaneously when the external circuit is completed. Thus, this step is called discharge step where the active ions transported from anode to cathode. The current response of the cathodic scan is represented as negative values.

As mentioned before, during cyclic voltammetry, the current is monitored during the voltage change. Then, current vs voltage is plotted. **Figure 6** shows a typical CV curve. Peak points observed on the CV plot can represent different electrochemical reactions, including phase changes in an electrode material. The correlation between peak positions and phase changes will be explained in the later chapters. We can also plot the current or current density values vs time, as

14

shown in **Figure 7**. The area under the curves for anodic and cathodic scans will give the charge and discharge capacity of the battery. The simple equation given below can be used to calculate these values.
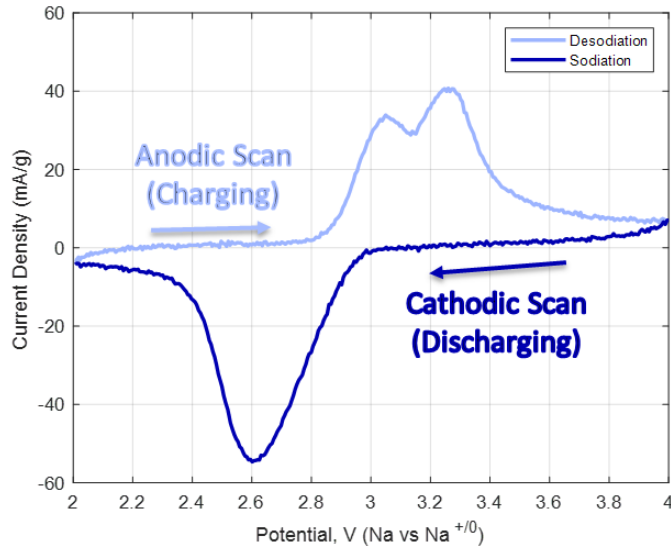
Figure 6. Representative CV curve

$$Q(t) = \left| \frac{1}{m} \int_0^t I(t)dt \right| \tag{1}$$

- o   Q(t) = Specific Capacity, Ah/g

- o   m = Mass of active material, g

- o   t = Time, s

- o   I(t) = Current at time t, A

The CV method is a powerful tool to understand the response of a battery during operation and it allows to control the surface potential of the electrode. It allows to investigate the chemical behavior of the electrode during battery cycling such as phase transformations and irreversible reactions. However, due to constant changes in the applied potential, the surface reaction rate changes. The galvanostatic cycle applies constant current on the electrode surface and monitors the potential of the battery cell. Also, capacity calculation with CV can be problematic due to nonzero current

15

response at the switching potential. In these situations, galvanostatic cycling should also be carried out.
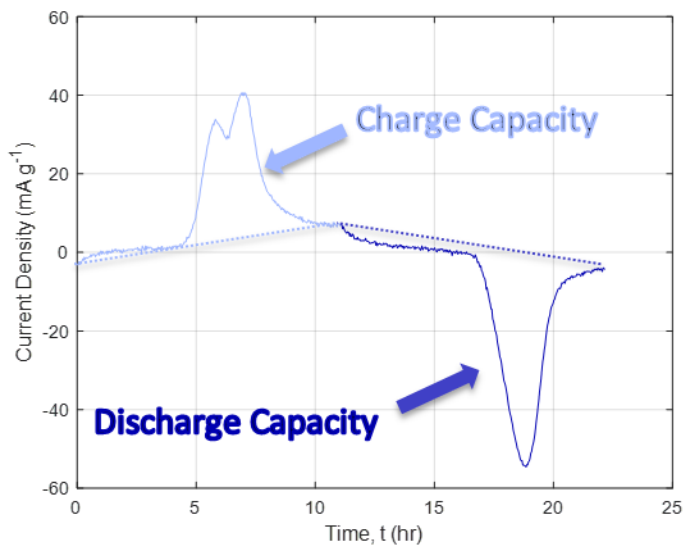
Figure 7. Current density versus time plot for capacity calculation

2.2 Galvanostatic Cycling

During the galvanostatic cycling, applied current to the battery is kept constant and the evolution of voltage is monitored. Similar to CV convention, during the anodic scan, the current is kept at a positive value (charging) and active ions are transported from cathode to anode. During the cathodic scan, the current is kept at a negative value and active ions are transported from anode to cathode (discharging). The current and voltage response of typical galvanostatic cycling is given in **Figure 8**.

Since the current is kept constant during anodic and cathodic scan, Equation 1 can be further simplified to Equation 2. For galvanostatic cycling, charge and discharge current generally represented as C-rate, which is calculated from the theoretical capacity of the battery. The theoretical capacity of a battery is calculated by Faraday's Law, shown in Equation 3. Generally, it will have a unit of mAh/g. C-rate is a measure of the rate where the anodic and cathodic scans carried out relative to the maximum capacity. For example, 0.1C means that it will take ten hours

16

to completely charge or discharge the battery with the current applied to the battery. Higher C-rate

means that the battery will be charged or discharged at a much faster rate.
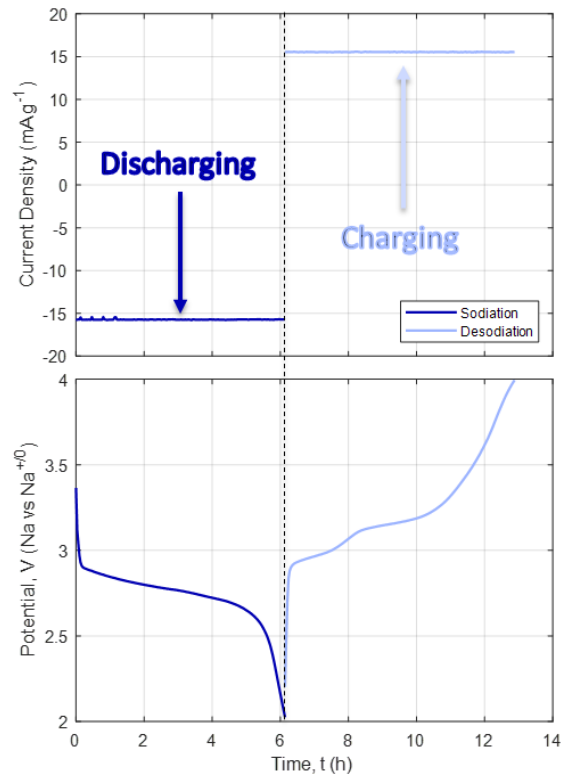
Figure 8. (top) Current and (bottom) voltage evolution of a battery system during galvanostatic cycling

$$Q(t) = \left| \frac{1}{m} I t_{charge \; or \; discharge} \right| \qquad (2)$$

$$Q_{theoretical} = \frac{nF}{M_w} \qquad (3)$$

- o n = Number of charge carrier (1 for alkali metals)

- o F = Faraday number, 26,801 mAh/mol

- o M_w = Molecular weight of active material, g/mol

2.3 Galvanostatic Intermittent Titration Technique (GITT)

Techniques previously described in this chapter can be used to show us how the current and voltage

is changed during the battery. One of the factors that affect this behavior is the diffusion of active

ions through the electrode. Since the transport of the active ion involves the mass transfer, knowing the chemical diffusion rate of active ion is important. It dictates how fast or slow active ions can be transported to the reactive sides of the electrodes. Galvanostatic intermittent titration technique (GITT) is a powerful tool for us to understand this kinetic parameter.

GITT procedure consists of a series of current pulses, followed by a relaxation period where no current passes through the battery. During the anodic scan, cell potential rapidly increases proportional to iR drop. iR drop is caused by the internal resistance of the battery and it is the combination of uncompensated resistance of the battery R_{un} and charge transfer resistance R_{ct}. After the rapid increase, due to iR drop, potential slowly increases due to the current pulse. During the current pulse, an active ion concentration gradient occurs between the surface and the bulk of the electrode. During the relaxation period, active ion concentration inside the electrode becomes more homogeneous due to the diffusion. The potential of the electrode rapidly decreases proportional to the iR drop at the beginning of the relaxation period. Then, potential slowly decreases until quasi-equilibrium achieved (dE/dt ~ 0, E = Potential). This procedure is repeated until the battery is fully charged.

During the cathodic scan, cell potential rapidly decreases proportional to iR drop. After the rapid decrease, potential slowly decreases due to the current pulse. During the relaxation period, the potential of the electrode rapidly increases proportional to the iR drop. Then, potential slowly increases until quasi-equilibrium achieved (dE/dt ~ 0). This procedure is repeated until the battery is fully discharged.

Using the GITT, chemical diffusion coefficient can be calculated using Equation 4.

$$D = \frac{4}{\pi}\left(\frac{IV_m}{nFS}\right)^2\left[\frac{dE}{d\delta}\bigg/\frac{dE}{d\sqrt{t}}\right]^2 \tag{4}$$

18

- D = Chemical diffusion rate, cm^2/s

- I = Current, C/s (A)

- V_m = Molar volume of electrode, cm^3/mol

- n = Charge number (1 for alkali metals)

- F = Faraday Constant, 96485 C/mol

- S = Area of electrode-electrolyte interface, cm^2

- $dE/d\delta$ = Slope of the coulometric titration curve

- $dE/d\sqrt{t}$ = Slope of linearized potential E (V) versus $d\sqrt{t}$

In situations where sufficiently small current is applied for short time intervals, both $dE/d\delta$ and $dE/d\sqrt{t}$ can be considered linear. Thus, Equation 4 can be further simplified and takes the form shown in Equation 5.

$$D = \frac{4}{\pi\tau}\left(\frac{mV_m}{M_wS}\right)^2\left[\frac{\Delta E_s}{\Delta E_t}\right]^2 \tag{4}$$

- τ = Current pulse duration, s

- m = Electrode mass, g

- M_w = Molecular weight of active material, g/mol

- ΔE_s = Change in voltage during the current pulse

- ΔE_t = Total change in the voltage after neglecting the iR drop

The plot of voltage evolution versus time gives us information about ΔE_s and ΔE_t values. These values can be seen in **Figure 9**.
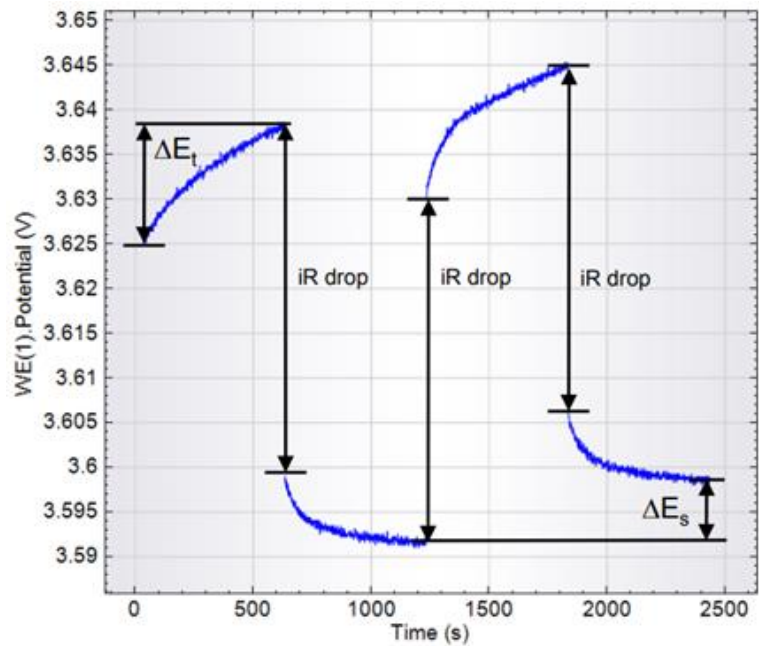
Figure 9. Visual representation of ΔE_s and ΔE_t. The figure is taken from[43]

CHAPTER III

IN-SITU STRAIN MEASUREMENT AND DIGITAL IMAGE CORRELATION

To investigate the strain evolution in an unconstraint electrode, we have constructed a custom in situ strain measurement setup. In this chapter details of the experimental setup and custom cell and Digital Image Correlation (DIC) method will be discussed.

3.1 Experimental Setup

Figure 10 shows the setup for the in-situ strain measurements. This system is previously utilized to investigate the in-situ strain generation on electrode materials such as graphite, lithium manganese oxide, and lithium iron phosphate[33,36–38,44]. Since the DIC method is an image-based method, images were captured with Grasshopper3 5.0 MP camera (Sony IMX250, resolution, 2448 (w)*2048(h) pixel). To increase the zoom, the camera is connected to a 12.0X adjustable zoom lens (NAVITAR). This setup is fixed on a lab jack to adjust the height of the camera setup. For the illumination of the subject area, a single constant high intensity LED light source was used (BiNFU). The custom cell is fixed on an XY translator. XY translator, coupled with the camera lab jack, enables the adjustment in all three axes. The white light source is used for the unconstrained electrodes that possess a natural speckle pattern for DIC measurement. If the electrode does not possess a natural speckle pattern or changes color during the electrochemical cycling, a laser system is also available. This system consists of a 532 nm green laser, a shutter, and an Arduino controller. Prior to the assembly of the custom cell, the surface of the electrode is decorated with a fluorescent

dye. The laser is then excited the fluorescent dye on the surface and the filter is used to capture fluorescence emission coming from the dye. To prevent the degradation of dye due to long exposure to the laser light, the shutter is kept closed and only opened before image capture. Both image capture and shutter control are done with a lab made LabView program.
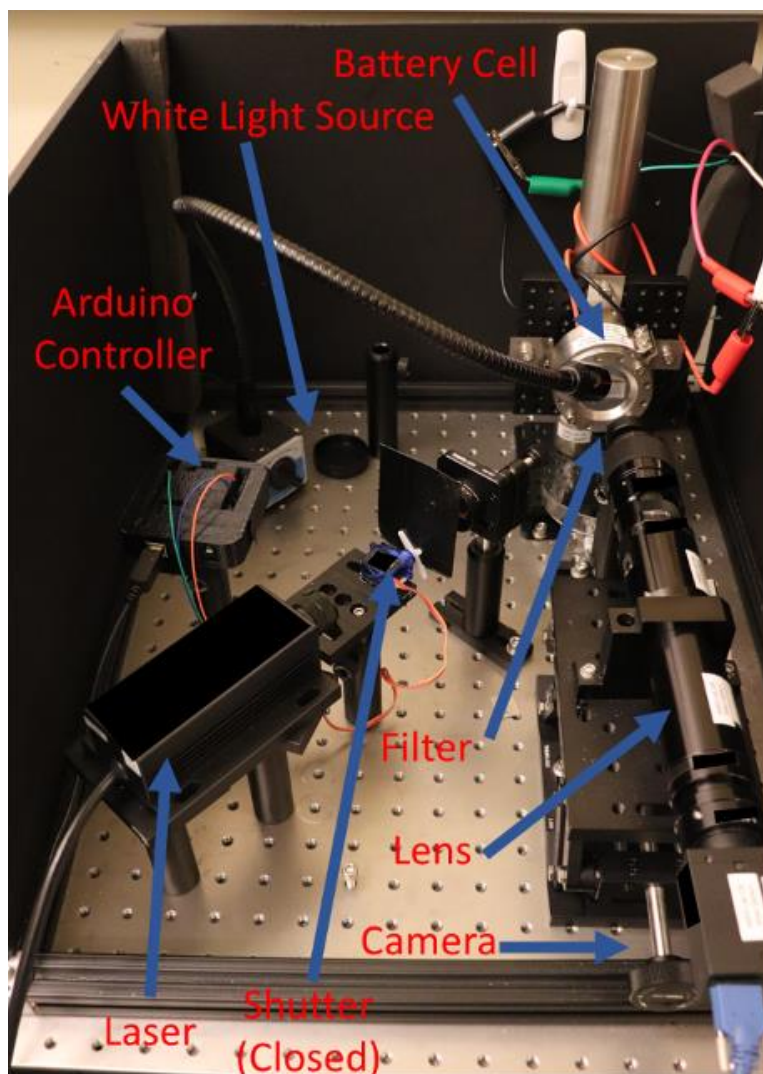
Figure 10. In situ strain measurement setup and its components

Captured images during the electrochemical cycling analyzed by Vic-2D 6 program. Vic-2D 6 tracks the changes in speckle pattern positions relative to a reference image, like in **Figure 11**, to calculate the strain generation. A subset size of 111 x 111 pixels and a step size of 15 is used during the image correlation. Strain calculations are synchronized with the electrochemical response of the electrode (current and voltage) using a lab-made MATLAB program.
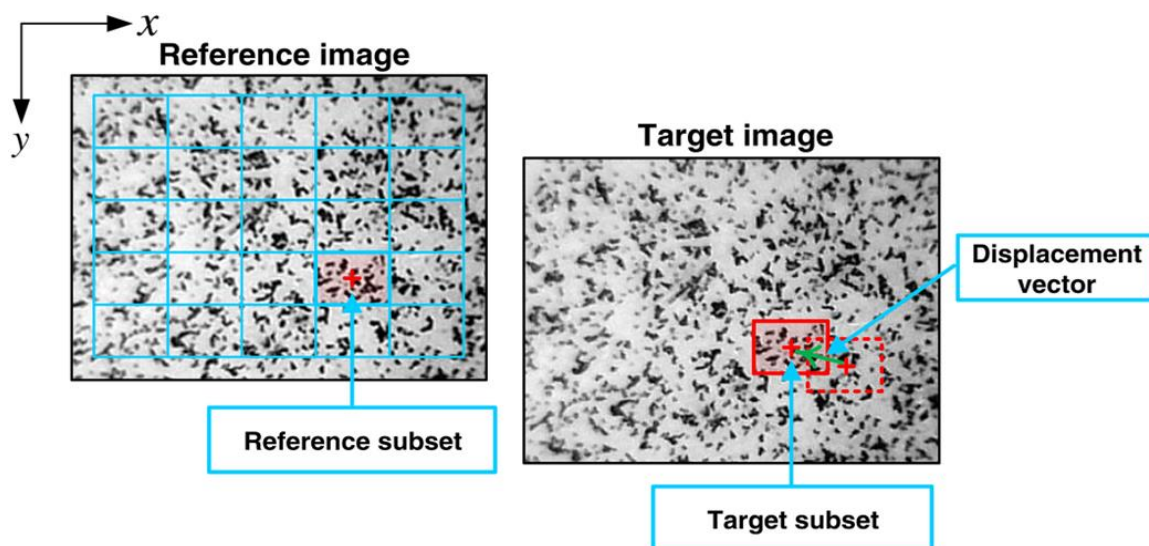
Figure 11. Undeformed (reference) image and (right) deformed image for DIC technique. Picture is taken from[243]

To run the strain experiments, a custom cell, shown in **Figure 12** is utilized. The custom cell consists of two electrode holders for working and counter electrode, a quartz window (99.995 % SiO_2, 1/16 in thick, 2 in diameter, GM Quartz) for optical access to the working electrode, main body made from polychlorotrifluoroethylene (PCTFE, Plastics International) and a metal flange to secure the glass window in place. To seal the custom cell, Viton O-rings used at the electrical connections, electrolyte fill port and between glass window and main body. Free-standing working electrode is placed on the working electrode holder and spot-welded to the holder using a 100 µm thick SS316 foil (Grainger), as shown in **Figure 13**. To limit the deflection of unconstrained electrode during electrochemical cycling, a polymer support arm is placed on top of the free-standing electrode without touching the electrode to minimize the z-axis deflection towards the camera.

During the drying period of the electrode, removal of solvent from the casted composite electrode causes the free-standing electrode to shrink. Since the uptake of electrolyte into the composite electrode structure can affect the results obtained during the electrochemical cycling, after the assembly of the custom cell, a 24-hour resting period was carried out. During this period, a positive strain of approximately 0.16% was developed on normal directions, ε_{xx} and ε_{yy} while shear strain

23

$\mathcal{E}_{xy}$ was zero, shown in **Figure 14**a. This shows us that volume of the electrode expanded during the resting period. Since both normal directions showed similar strain evolution, strain evolution in the $\mathcal{E}_{xx}$ direction will be reported.
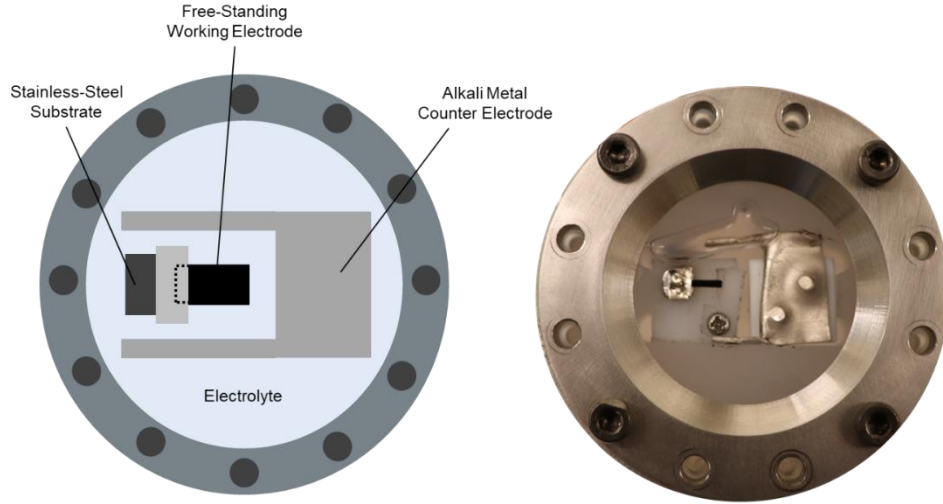
Figure 12. (left) Schematic and (right) actual top view for the custom cell for strain experiments

While the whole experimental setup is located on a passively isolated optical table to isolate it from floor vibrations, factors such as time varying drift, spatial distortions and electrolyte uptake can cause strain evolution factors, can result in erroneous strain calculation[45]. In order to calculate the error in our measurements, we tracked the strain evolution in $\mathcal{E}_{xx}$ direction for five different experiments during the 12-hour resting period. As it can be seen in **Figure 14**b, all electrodes
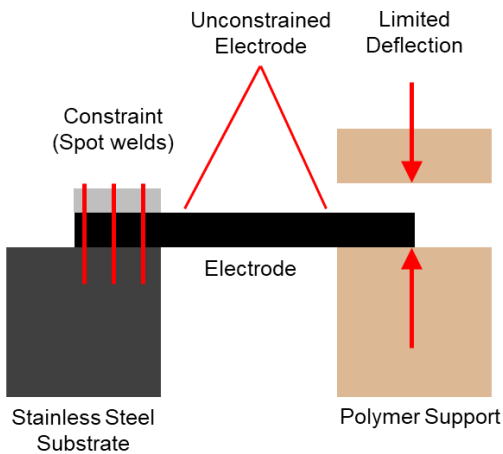
Figure 13. Side view of the free-standing working electrode holder

experienced expansion during the 12-hour resting period, between 0.0011% to 0.0478%. This indicates that, the error in our strain measurements is 0.0245% ± 0.0178%/12 h.
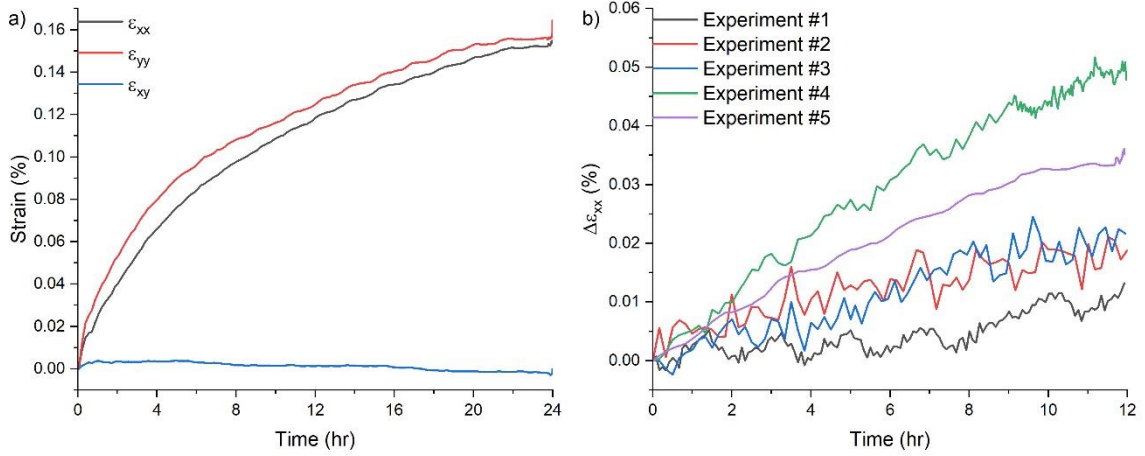
Figure 14. (a) Strain evolution of lithium iron phosphate composite electrode during the 24-hour rest period for normal strains ε_{xx}, ε_{yy}, and shear strain ε_{xy}. (b) Variation of strain during 12-hour resting period for Evolution of strain for 12-hour rest period for five different experiments. Deviation of strain during 12-hour rest period is 0.0245% ± 0.0178% /12 h.

CHAPTER IV

ELECTROCHEMICAL STRAIN EVOLUTION IN IRON PHOSPHATE COMPOSITE

CATHODES DURING LITHIUM AND SODIUM ION INTERCALATION

Bertan Özdogru[1], Hannah Dykes[1], Shubhankar Padwal[2], Sandip Harimkar[2], Ö. Özgür Çapraz[1]

1) The School of Chemical Engineering, Oklahoma State University, Stillwater, OK 74078

2) The School of Mechanical Engineering, Oklahoma State University, Stillwater, OK 74078

ABSTRACT

Sodiation-induced electrochemical strain generation in composite iron phosphate ($FePO_4$) host material is compared with lithiation-induced strain evolution. $FePO_4$ composite materials are prepared by an electrochemical displacement technique using pristine composite $LiFePO_4$ as the starting material. The composite $FePO_4$ electrodes have identical composition, binder, conductive additives, and particle morphology for both Na^+ and Li^+ ion intercalation. We employ digital image correlation to investigate potential-dependent mechanical changes in $FePO_4$ host material during alkali-metal ion intercalation via cyclic voltammetry and galvanostatic cycling. The $FePO_4$ electrode experience much larger strains during the first sodiation (~2.40 %) compared to the first lithiation (~0.60%). Strains in the subsequent cycles slowly decreased to more reversible strains upon both Na^+ and Li^+ ion intercalation. Analysis of strain derivatives during lithiation, delithiation and sodiation exhibit a single peak that coincide with associated phase transformation. The relative expansion in the composite electrode during Na^+ ion intercalation with respect to Li^+ ion intercalation is much greater than the relative expansions in electrode cell volume reported by the previous diffraction studies. We hypothesize that amorphization and slower Na^+ diffusion in the electrode can lead to additional strain development compared to Li intercalation. Our results provide new insights into the mechanics of alkali metal-ion intercalation in cathodes.
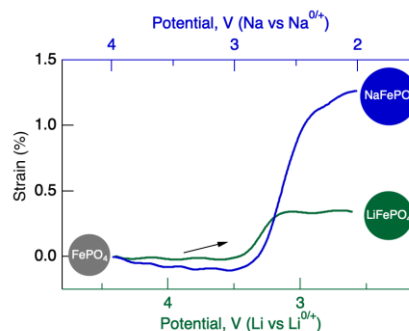
Keywords: Na-ion battery, Li-ion battery, strain, digital image correlation, iron phosphate

4.1 Introduction

The increasing demand for stationary grid-scale energy storage to utilize renewable energies requires low-cost, safe and nontoxic systems. Na-ion batteries are a potential alternative to Li-ion batteries in search of lower-cost, abundant resources, and comparable energy density. Over the past decade, there has been a tremendous effort to develop cathode materials for Na-ion batteries[14,46,47]. Comparative studies of intercalation mechanisms of Li-ion and Na-ion battery electrodes are critical to identifying their operational similarities and differences. Many studies mostly focused on electrochemical characterization and investigation of the crystal structures of the electrode materials[48–52]. However, understanding the impact of alkali metal ions on the chemo-mechanical stability of the electrodes is necessary to order to enhance the lifetime and performance of electrode materials for Na-ion batteries.

During alkali metal-ion intercalation, considerable volumetric changes, and the formation of the cathode-electrolyte interface (CEI) on the electrode cause chemo-mechanical changes in the electrodes[33,34]. Larger alkali metal-ions causes greater volumetric changes and lattice distortions in the cathode structure[53,54]. Even small changes in volume upon alkali metal-ion intercalation can cause particle fracturing in the brittle cathode materials[55–57]. Particle fracture results in isolation of nonreactive electrode particles in the composite network and causes new surfaces to be exposed to the electrolyte, which increases the decomposition of the electrolytes. The repeated formation of more CEI layers and the generation of more isolated electrode particles cause a further decrease in electrode capacity[58–61]. These chemo-mechanical changes are the decisive element behind the capacity fade and ultimately lead to battery failure. An improved understanding of chemo-mechanical deformations is important to design robust Na-ion battery cathodes with longer cycle life.

Various *in-situ* experimental techniques have been employed to investigate the coupling between electrochemistry and the mechanics of Li-ion batteries. These techniques include transmission electron microscopy[20,62], scanning electron microscopy[29], X-ray diffraction[32,54,63–65], X-ray absorption spectroscopy[31,66], atomic force microscopy[30], curvature measurements[33–35,44] and digital image correlations[36–38]. Surprisingly, in situ TEM only detected particle fracturing during lithiation of the FeS_2 electrode, although the electrode undergoes larger volumetric expansion upon sodium and potassium intercalation compared to lithium[62]. XRD study revealed the impact of alkali metal ions on crystal structure changes and phase transformations in battery electrodes[31]. Synchrotron radiation powder X-ray diffraction (PXD) and pair distribution function (PDF) analysis demonstrated the formation of amorphous phases in iron phosphate electrodes during Na intercalation[20]. Previously, we performed *in situ* stress and strain measurements in composite lithium manganese oxide and lithium iron phosphate electrodes[33,37,38,44]. These studies revealed stress and strain generation in the electrode associated with dynamic changes in the electrode/electrolyte interface and the electrode structure.

In this study, we chose an iron phosphate framework to study the role of Na and Li ions on the chemo-mechanical response of the electrode. Lithium iron phosphate ($LiFePO_4$, LFP) is an inexpensive and environmentally benign cathode material widely used in commercial Li-ion batteries. Olivine-type sodium iron phosphate ($NaFePO_4$, NFP) is structurally analogous to $LiFePO_4$ and has attracted much attention as a potential cathode material for Na-ion batteries. $LiFePO_4$ and $NaFePO_4$ have 3.5 V vs Li/Li^+ and 2.8 V vs Na/Na^+, respectively and comparable theoretical capacities of 170 and 154 mAh g^{-1}, respectively. Both sodium and lithium are alkali metals located in the s-block of the periodic table and have a single charge in their cation form. However, intercalation chemistry and electrochemistry of Na^+ and Li^+ ions in the $FePO_4$ framework is quite different. Compared to lithiation of the $FePO_4$ host structure, slower solid-state diffusion occurs and larger activation energy is required during Na^+ ion intercalation[67,68]. Intercalation of Li^+

ion into the host $FePO_4$ framework to form $LiFePO_4$ results in a ~6.9% expansion in the unit cell volume. Delithiation and lithiation of LFP also occur via a two-phase mechanism between lithium-rich ($Li_{1-\alpha}FePO_4$) and lithium poor ($Li_\beta FePO_4$) phases in lithium iron phosphate. Unlike the delithiation of $LiFePO_4$, the charge curve of $NaFePO_4$ exhibits two voltage plateaus separated by the formation of an intermediate $Na_{x\approx2/3}FePO_4$ phase. The unit cell volume of $NaFePO_4$ reduces 13.5% and 17.6% during the formation of intermediate phase $Na_{x\approx2/3}FePO_4$, and final $FePO_4$ phase during desodiation, respectively[32]. Phase transformations during Na intercalation cause larger misfit strain at the interface between the growing and the consumed phases, in comparison, to phase transformation during Li^+ ion intercalation[20,64].

We investigated electrochemical strain generation in composite $FePO_4$ cathode during Li^+ and Na^+ ion intercalation via cyclic voltammetry at 50 µV/s or galvanostatic cycle at C/10 rate. Strains are monitored using *in situ*, optical, full-field digital image correlation (DIC) technique. A host $FePO_4$ framework is initially formed by the electrochemical delithiation of the $LiFePO_4$ composite electrode. Our results show that the $FePO_4$ electrode undergoes unprecedented expansion during the first lithium and sodium intercalation. Reversible strains are observed in the subsequent cycles during both lithium and sodium intercalation. Significantly large volumetric expansion is detected upon Na^+ ion intercalation into $FePO_4$ compared to Li^+ ion intercalation.

4.2 Experimental

4.2.1 Sample Preparation

Composite electrodes were prepared by mixing active material with a binder and conductive carbon in 8:1:1 mass ratio. Initially, sodium carboxymethyl cellulose (binder, CMC, average MW ~700,000, Aldrich) was dissolved in ultra-pure water with a 1:40 mass ratio. Then, the calculated amount of pristine lithium iron phosphate (active material, LFP, Hanwha Chemical) and Super P

(conductive additive, carbon black, >99%, metal basis, Alfa Aesar) was added to the binder solution. The average particle size of LFP particles was measured by scanning electron microscopy and it is 250 nm. The slurry was mixed for 30 minutes with Thinky centrifugal mixer at 2000 RPM mixing speed. Composite electrodes were cast onto the copper foil (9 µm thick, >99.99%, MTI) with a doctor blade to control the slurry thickness. The slurry was then dried under ambient conditions for 16 h. Dried electrodes were carefully peeled off to create the freestanding electrode for strain measurements.

The electrolyte solution was prepared by mixing ethylene carbonate (EC, anhydrous, 99%, Acros Organics) and dimethyl carbonate (DMC, anhydrous, >99%, Aldrich) in 1:1 volume ratio inside the glove box under an argon atmosphere. Oxygen and water content inside the glove box kept below 1 ppm all the time. Either 1 M lithium perchlorate (LiClO4, battery grade, dry, 99.99%< Aldrich) or 1 M sodium perchlorate (NaClO4, ACS grade, >98%, Aldrich) was added to the EC/DMC solution.

Li foils (99.9% metal basis, Alfa Aesar) were used as purchased without proceeding any further treatment and were kept inside the argon-filled glove box. For Na-ion batteries, sodium cubes immersed in mineral oil (Na, 99.9%, metal basis, Sigma Aldrich) were cleaned with hexane inside the glovebox. Cleaned Na cubes were stored in EC:DMC solution in a 1:1 volume ratio for future use. Before custom cell assembly, Na cubes were removed from the solvent solution, dried with a filter paper, and cut into pieces with a stainless-steel scalpel. The cut piece was placed inside a polyethylene bag and rolled into the shape of a foil using a rolling pin. Flattened Na foil was then placed into the battery cell as a counter electrode.

4.2.2 Battery Cycling

Iron phosphate (FP) composite electrode was formed by electrochemical displacement technique using pristine LFP composite electrode[67,68]. The pristine LFP electrode was electrochemically

31

delithiated by sweeping the voltage from open circuit potential to 4.4 V (vs Li counter electrode) or to 4.0 V (vs Na counter electrode).). In some cases, the pristine electrode was also electrochemically delithiated via galvanostatic cycling against either Li or Na counter electrode at a rate of C/10. For lithium intercalation, FP composite electrodes were cycled against Li counter electrode in 1 M $LiClO_4$ in 1:1 (v:v) EC:DMC electrolyte between 2.6-4.4 V voltages using Arbin potentiostat/galvanostat (MSTAT21044). For sodium intercalation, FP composite electrodes were cycled against Na counter electrode in 1 M $NaClO_4$ in 1:1 (v:v) EC:DMC electrolyte between 2/0-4.0 V. The electrodes were cycled at either via cyclic voltammetry a scan rate of 50 µV/s or galvanostatic cycling at C/10 rate.

4.2.3 Strain Measurements

A detailed description of the custom battery cell was described in our previous publication[36,37]. The main body of the custom battery cell and the electrode holders were made from polychlorotrifluoroethylene (PCTFE, Plastics International). For optical access, a quartz window (99.995 % SiO_2, 1/16 in thick, 2 in diameter, McMaster-Carr) was placed on the top of the custom cell and sealed with Viton O-rings (Grainger). Analysis of the strain generation was carried out by taking images of the freestanding electrode throughout the electrochemical cycling periods. Images were captured with Grasshopper3 5.0 MP camera (Sony IMX250, resolution, 2448 (w)*2048(h) pixel) with 2.0X fixed and 12.0X adjustable zoom lens (NAVITAR) for an effective resolution of 0.45 µm/pixel. For illumination, a single constant high intensity LED light source was used (Amazon). Images were captured every 2 minutes during cyclic voltammetry at a scan rate of 50 µV/s or galvanostatic cycling at C/10. The natural speckle pattern of the LFP composite electrode was used to calculate the strain generation on the electrode using Digital Image Correlation. Full-field strain measurements were performed on an area of interest of 750 µm(w) x 500 µm(h). Strains were synchronized with the electrochemical response of the electrodes (current and voltage) using a lab-made MATLAB program.

4.3 Results and Discussion

4.3.1 Formation of Iron Phosphate

Pristine lithium iron phosphate (LFP) composite electrodes were electrochemically delithiated against either Li or Na counter metal electrodes to form iron phosphate electrodes. **Figure 15**a shows the current response in the pristine LFP electrode during linear sweep voltammetry at 50 μV/s between open circuit potential to 4.4 V vs Li counter metal electrode in 1 M $LiPF_6$ in EC/DMC electrolyte. The open-circuit potential prior to linear sweep was 3.29 V vs $Li/Li^{0/+}$. The open-circuit potential of the electrodes was very similar to our previous measurements (3.29 V vs $Li^{0/+}$)[44]. A single current peak was observed at 3.64 V vs $Li/Li^{0/+}$ during the first charge cycle during the removal of Li ions. The distinct current peak is associated with a two-phase reaction mechanism between lithium-rich and lithium poor-phase in lithium iron phosphate[52]. The current dramatically decreased to almost zero around 3.80 V vs $Li/Li^{0/+}$ when lithium iron phosphate was converted into the iron phosphate structure. The delithiation capacity is calculated to be 157 mAh g^{-1}, which is close to the theoretical capacity of LFP (170 mAh g^{-1}). The corresponding strain generation during electrochemical delithiation of the electrode is shown in **Figure 15**b. The volume of the composite electrode started to shrink at the onset of the current rise. The strain continuously decreased during the removal of Li ions from the electrode until the current became almost zero at higher potentials. The magnitude of the strain at 4.4 V was -0.32 %.

Figure 15c shows the current response of the pristine LFP electrode while voltage was increased at a constant rate of 50 μV/s from open circuit potential to 4.0 V against Na metal counter electrode. The open-circuit potential of the electrode prior to cycling was 2.97 V vs $Na/Na^{0/+}$, which corresponds to 3.30 V vs $Li/Li^{0/+}$. A single current peak was observed at 3.60 V vs $Na/Na^{0/+}$ during the anodic scan. Current dramatically decreased to almost zero around 3.651 V. A single current peak at similar potential is also reported for electrochemical delithiation of carbon-coated lithium

iron phosphate against Na metal[68]. The depletion of current at higher potentials during charge corresponds to the removal of electrochemically accessible Li ions from the host LFP structures. Delithiation capacity is calculated to be 161 mAh g^{-1}, which is very similar to when pristine lithium iron phosphate electrode is delithiated against Li counter metal (**Figure 15**a). Michaelis et al. previously demonstrated similar electrochemical behavior of carbon-coated lithium iron phosphate electrodes during electrochemical delithiation against Na counter metal[68]. Therefore, the chemical composition of the composite electrode became iron phosphate (FP) as a result of delithiation. The corresponding strain generation in the composite electrode is shown in **Figure 15**d. Strain reduced to -0.33% at the end of the anodic scan at 4.0V vs Na/Na$^{0/+}$. Similar strain reduction is also observed when the pristine LFP electrode was electrochemically delithiated against the Li counter electrode (**Figure 15**b).
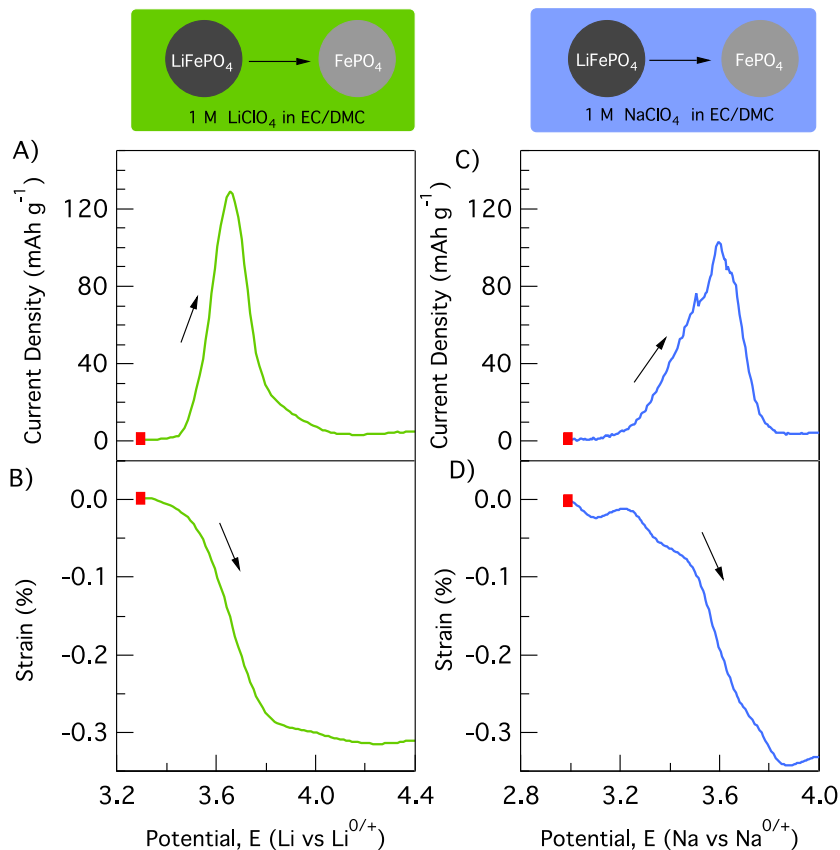
Figure 15. Formation of iron phosphate (FePO$_4$) electrode by electrochemical delithiation of pristine lithium iron phosphate (LiFePO$_4$) at 50 µV/s against (A, B) Li and (C, D) Na metal counter electrode. Red square demonstrated the initial point of the experiments.

The iron phosphate electrodes were also formed by electrochemical delithiation of the pristine LFP composite electrodes via galvanostatic charging at C/10 rate (**Figure A1.** Formation of iron phosphate, $FePO_4$ electrode by electrochemical delithiation of pristine lithium iron phosphate, $LiFePO_4$ at C/10 against A,C) Li metal counter electrode in 1 M $LiClO_4$ in EC/DMC or B,D) Na metal counter electrode in 1 M Na $NaClO_4$ in EC/DMC.). The pristine LFP electrode showed very flat potential plateaus around 3.47 (vs $Li/Li^{0/+}$) and 3.27 V (vs $Li/Li^{0/+}$) during electrochemical delithiation against Li and Na counter electrodes, respectively. Delithiation capacity is calculated as 154 and 152 mAh g^{-1} when the electrode is cycled against Li and Na electrodes, respectively. The corresponding strain generation in the composite electrode was -0.26 and -0.30 % during electrochemical delithiation against Li and Na counter electrodes, respectively. Overall, similar capacity and strain evolution are observed during electrochemical displacement of Li ions from the pristine LFP electrode when the pristine electrode is charged either via linear sweep voltammetry at 50 µV/s or galvanostatic cycling at C/10 rate.

The main goal of the formation of the iron phosphate electrode is to enable a baseline to study the deformation mechanics of Li and Na intercalation into the identical electrodes in terms of active material loading in composite electrode, particle size, binder, and porosity of the composite electrode. Strain measurements in the composite electrodes exhibit a strong dependence on morphology and structure of the active material, and composition of the composite electrode[36,69]. Similar capacity and strain evolution in pristine LFP electrodes during electrochemical delithiation against both Li and Na counter electrodes indicate that the formed FP electrodes have similar morphology, structure and composition In the following section, the role of alkali-ion intercalation on the mechanical deformations of the composite iron phosphate electrodes were investigated in detail.

4.3.2 Li⁺ and Na⁺ ion Intercalation via Cyclic Voltammetry

Figure 16a shows the current response of the FP composite electrode during lithiation and delithiation for 4 cycles. Cyclic voltammetry began immediately after the electrochemical delithiation of the pristine LFP electrode by linear sweep voltammetry. Each cycle starts with the insertion of Li^+ ions during the cathodic scan and follows with the removal of the Li^+ ions during the anodic scan. A distinct peak in current density was observed at 3.58 and 3.29 V during each lithiation and delithiation cycles, respectively. Previous X-ray diffraction studies demonstrated that electrochemical lithiation and delithiation of LFP electrodes is a two-phase mechanism for electrode particles larger than 100 nm (in this work, the particles are around 250 nm in diameter)[70–75]. The bulk phase transformation results in a single peak in the current response. The interval between the oxidation and reduction potentials is 0.29 V, consistent with prior reports[44,76,77]. The magnitude and shape of the current evolution were reversible through subsequent cycles, demonstrating a similar discharge and charge capacities in the electrode.

The corresponding strain generation in the FP composite electrode during lithium intercalation is shown in **Figure 16**b. Strain values were set to zero at the beginning of the first cathodic scan. The strain was slowly generated to around 0.1% until the onset of current reduction at 3.5 V. The volume of the electrode rapidly expanded from 0.1% to 0.64% between 3.5 and 3.1 V as a result of lithium intercalation. The strain was almost constant below 3.1 V, resulting in a 0.68% expansion at the end of the first lithiation cycle. During the first delithiation cycle, strain value did not change significantly between 2.8 and 3.4 V. A sharp contraction in the electrode volume was observed at the onset of the current rise. Strain decreased from 0.64% to 0.36% between 3.4 and 3.8 V. The strain value was almost constant at higher potentials. At the end of the first cycle, the electrode did not return to its original size, resulting in 0.33% irreversible strain. Strain decreased as Li^+ ions are removed from the electrode and it increased as a result of intercalation of Li^+ ions back to the electrode during subsequent delithiation and lithiation cycles, respectively.

Figure 16c shows the current evolution in the FP composite electrode during Na^+ intercalation. During first sodiation (cathodic) scan, the current was almost zero until the potential reached 2.90 V. The current reached its minimum value (-57 mAh/g) at around 2.50 V and then increased back to -7.5 mAh/g at 2.0 V. The current slightly becomes positive at the beginning of the first desodiation (anodic) scan. Then, it increased rapidly at around 2.80 V and two-distinct current peaks emerged at 3.05 and 3.26 V. The current slowly reduced to 7 mAh/g at the end of the first desodiation cycle. In the subsequent cycles, a single current peak at around 2.59 V was observed during sodiation and two-distinct current peaks at around 3.05 and 3.26 V were observed during the desodiation of the electrode. A similar current response during Na^+ intercalation of iron phosphate electrodes was reported in the literature[67,68]. The shape of the current evolution during cyclic voltammetry is similar with each cycle, which demonstrates the reversible electrochemical sodiation and desodiation of sodium iron phosphate (NFP) composite electrode. The removal of Na^+ ions from NFP involves the formation of an intermediate phase, $Na_{0.7}FePO_4$ during desodiation[78]. In the first step, $NaFePO_4$ transforms into an intermediate phase, $Na_{0.7}FePO_4$ at 3.05 V. In the second step, previously formed $Na_{0.7}FePO_4$ transforms into $FePO_4$ at 3.26 V[32,48,54,64,79]. Previously, Heubner et al. studied the structure of the lithium iron phosphate electrode cycled

against Na counter electrode using the x-ray diffraction technique. They reported the successful formation of olivine type sodium iron phosphate (NaFePO$_4$, NFP) phase after the first discharge cycle[68]. Similar to their report, two distinct current peaks during charging and a single current peak at lower potentials during discharging observed in **Figure 16**c also demonstrate a reversible phase transformation between FePO$_4$ and NaFePO$_4$.

The corresponding strain generation in the electrode is shown in **Figure 16**d. During the early stages of the first sodiation (cathodic) cycle at potential until about 3.0 V, strain change was negligible. The composite electrode experienced 2.43% expansion during the generation of negative current between 2.90 and 2.00 V. During the first desodiation (anodic) scan, strain slightly increased to 2.61% until the onset of the current rise at 2.80 V. The volume of the electrode contracted upon the removal of Na$^+$ ions from the electrode. At the end of the first cycle (4.0 V), the electrode did not return to its original size, resulting in a 1.27% irreversible strain. The
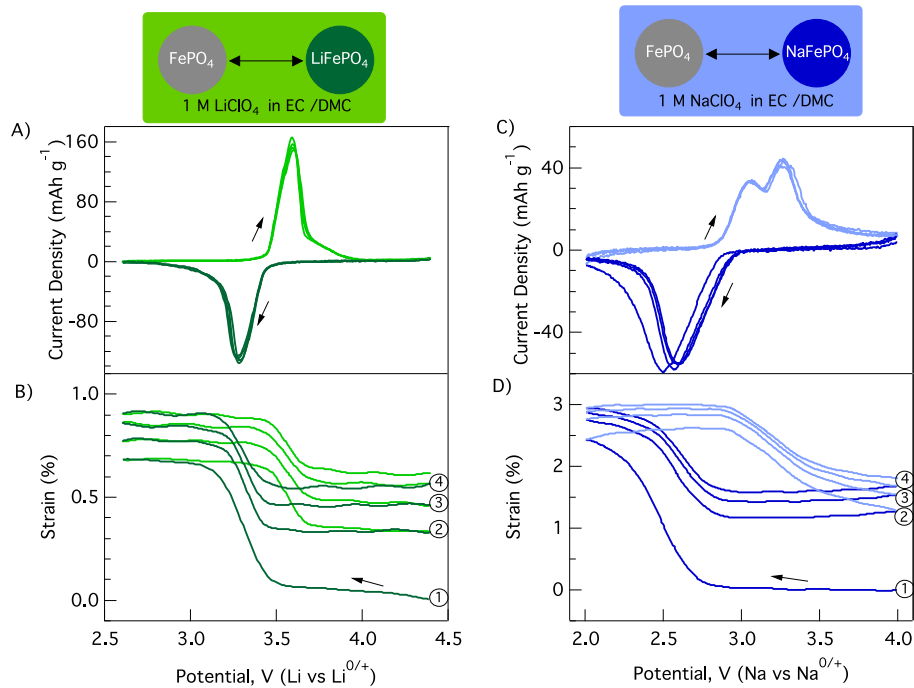
Figure 16. Current and strain evolution in iron phosphate composite electrodes during (A, B) lithium intercalation and (C, D) Na intercalation 50 µV/s. The electrodes are first electrochemically delithiated against Li metal or Na metal counter electrode. Strain set to zero at the beginning of first lithiation and sodiation.

cumulative irreversible strain increased with additional cycles to 1.54%, 1.67%, and 1.79% by the end of 2nd, 3rd and 4th cycles, respectively. Overall, the shape and magnitude of the strain generation in the subsequent cycles are similar, demonstrating the reversible sodiation and desodiation of the composite electrode.

4.3.3 Li$^+$ and Na$^+$ ion Intercalation via Galvanostatic Cycling

The iron phosphate electrodes were also galvanostatic cycled at C/10 rate against Na or Li working electrode. Unlike the cyclic voltammetry, galvanostatic cycling applies constant flux of ions into and out of the electrode. **Figure 17**a shows the potential evolution during Li$^+$ ion intercalation with respect to time for four cycles. A two-phase reaction between LiFePO$_4$ and FePO$_4$ results in a single potential plateau in the galvanostatic cycling. The LFP electrode showed very flat potential plateaus around 3.41 and 3.44 V during lithiation and delithiation cycles, respectively. The potential hysteresis between lithiated and delithiated electrode was around 30 mV for the four cycles (**Figure A2.** Potential and strain evolution with respect to capacity in LiFePO$_4$ composite electrode during Li intercalation in 1 M LiClO$_4$ in EC/DMC at C/10 rate. Dark and light green lines demonstrate lithiation and delithiation cycles, respectively. The top right figure highlights the potential evolution 3.35 – 3.5 V during sodiation and desodiation at different cycle numbers. The figure is generated from data in **Figure 16**.). The lithiation and delithiation capacities were 142 and 152 mAh g^{-1} during the first cycle, which is close to the theoretical capacity of LFP, 170 mAh/g. The capacities did not change significantly with the cycle numbers (**Table A4**). **Figure 17**b shows the corresponding strain generation in the electrode. The composite electrode expanded by 0.58% because of Li intercalation into the FePO$_4$ electrode during the first lithiation. The volume of the electrode shrank during the first delithiation due to the Li extraction. The electrode did not return to its original volume, resulting in a generation of 0.23 % strain at the end of the first cycle. As expected, the expansion and contraction in the electrode volume were observed during the

subsequent lithiation and delithiation cycles. However, cumulative irreversible strains increased slowly with cycle number and became 0.40% by the end of the fourth cycle.

Potential and strain evolution in iron phosphate electrode during Na^+ ion intercalation at C/10 rate with respect to time are shown in **Figure 17**c and **Figure 17**d. During the first sodiation, a unique potential plateau was observed around 2.70 V. The slope of the potential plateau during the first sodiation was slightly shallower than the subsequent sodiation cycles (**Figure A3.** Potential and strain evolution with respect to capacity in $NaFePO_4$ composite electrode during Li intercalation in 1 M $NaClO_4$ in EC/DMC at C/10 rate. Dark and light blue lines demonstrate sodiation and desodiation cycles, respectively. The top right figure highlights the potential evolution between 2.6 – 2.9 V during sodiation at different cycle numbers. The figure is generated from data in **Figure 17**.). Two distinct plateaus were observed at around 2.95 and 3.17 V during the first desodiation. The shape of the potential plateaus was very similar in the subsequent desodiation cycles. Two potential plateaus during desodiation are corresponding to the appearance of intermediate $Na_{0.7}FePO_4$ during the transition of $NaFePO_4$ phase to $FePO_4$ phase [68]. The initial sodiation and desodiation capacities of the electrode were 130 and 115 mAh/g, respectively. The capacities decreased to 103 and 108 mAh/g during the second sodiation and desodiation cycles. At the fourth cycle, sodiation and desodiation capacities became 96 and 104 mAh/g, respectively. The corresponding strain generation in the composite electrode during sodium intercalation is shown in **Figure 17**d. The strains linearly increased with respect to the sodiation capacity, resulting in a 2.30% expansion in the electrode at the end of the first sodiation (**Figure A5.** Strain derivatives in $NaFePO_4$ composite electrode during Na intercalation in 1 M $NaClO_4$ in EC/DMC for (A) 1st, (B) 2nd, and (C) 3rd cycles at 50 μV/s.). The extraction of Na^+ ions during desodiation causes a reduction in electrode volume. The irreversible strain at the end of the first cycle was 1.0%. The cumulative

irreversible strain slowly increased with additional cycles to 1.26%, 1.45%, and 1.55% by the end of 2nd, 3rd, and 4th cycles, respectively.
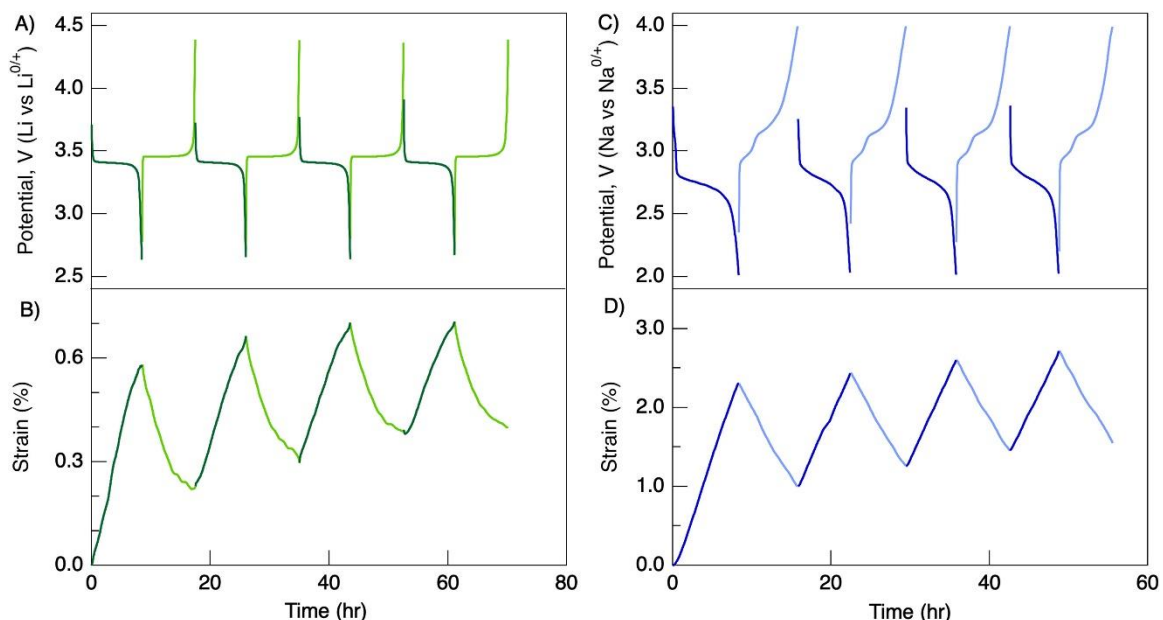
Figure 17. Current density (A,C) and strain derivatives (B,D) in LiFePO$_4$ (A,C) and NaFePO$_4$ (B, D) composite electrodes cycled at 50 μV/s in 1 M LiClO$_4$ in EC/DMC and 1 M NaClO$_4$ in EC/DMC electrolytes, respectively at 4th cycle.

4.3.4 Strain Derivatives

Strain derivatives are calculated to investigate localized changes in the FePO$_4$ structure upon Li and Na intercalation. The phase transformation behavior of lithium iron phosphate particles in the electrode has been a subject of debate[80]. The proposed phase-transformation models such as the isotropic shrinkage core[81] and domino cascade[82] models are based on steady-state results. The particle size and cycling rate influence the complex Li intercalation mechanism in the LiFePO$_4$ electrode[83]. However, the consensus exists for LFP particles with a diameter larger than ca. 100 nm, the electrode undergoes phase reactions between LiFePO$_4$ and FePO$_4$ phases with an abrupt interface between the growing and shrinking domains during electrochemical lithiation and delithiation[71,72,84–86]. The particle size of lithium iron phosphate in this study is approximately 250 nm. The phase change in the electrode is manifested as a single potential plateau during both lithiation/delithiation process[85]. Unlike the delithiation mechanism, the desodiation of olivine-type

NaFePO$_4$ occurs in two voltage plateaus separated by a voltage drop that corresponds to the formation of an intermediate Na$_{x\approx0.7}$FePO$_4$ phase[32,48,64,79]. Similar to lithiation, the sodiation mechanism of the FePO$_4$ electrode is also manifested by a single potential plateau during galvanostatic cycling[78].
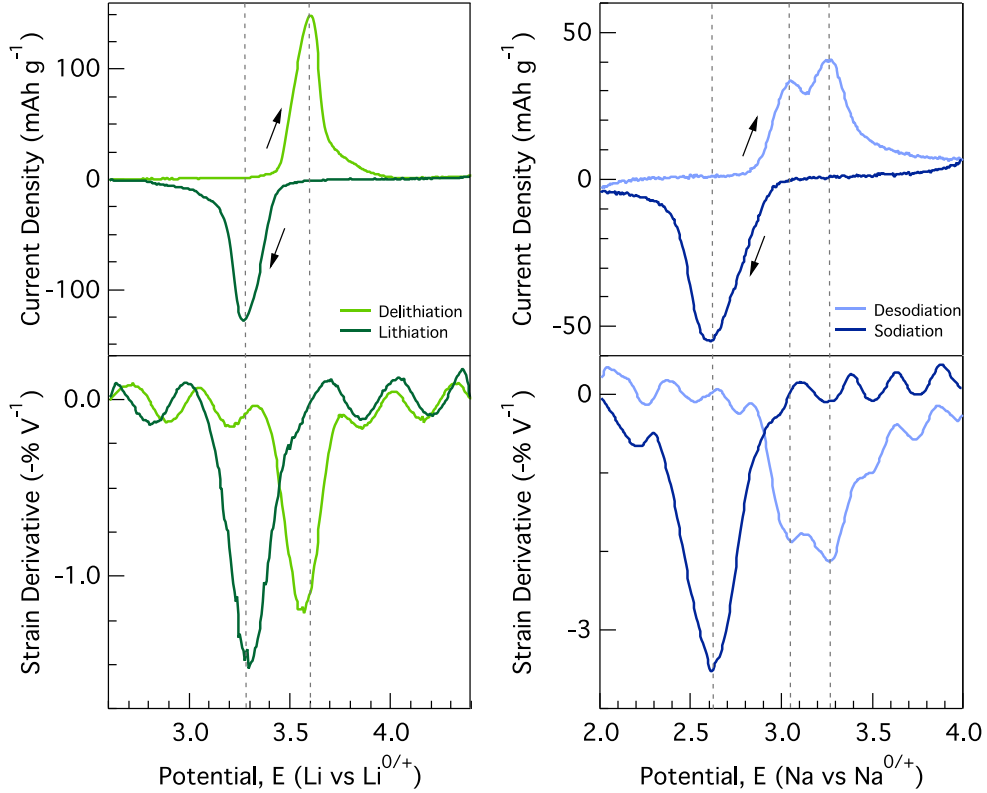
Figure 18. Strain derivatives in FePO$_4$ composite electrode during (left) Li intercalation and (right) Na intercalation in the 4th cycle at 50 µV/s.

The evolution of strain derivatives during potentiostatic and galvanostatic cycles of Li$^+$ and Na$^+$ ions is presented in **Figure 18** and **Figure 19**, respectively. We previously reported that the digital image correlation technique was able to detect phase transformation induced. nano-scale changes in the composite electrodes including graphite, lithium iron phosphate, and lithium manganese oxide during battery cycling[33,37,38,44]. Strain derivatives were calculated by taking the derivative of strain with respect to the electrochemical potential. During the delithiation, a single strain derivative was observed on the onset of the maximum current located at 3.55 V vs Li/Li$^{0/+}$. During the lithiation, the single strain derivative peak aligned well with the current peak within a 0.025 V

margin. Similarly, strain derivatives were also calculated for lithium intercalation during galvanostatic cycling and plotted alongside the capacity derivatives in **Figure A6.** Capacity and strain derivatives in LiFePO$_4$ composite electrode cycled at C/10 rate 1 M LiClO$_4$ in EC/DMC.. Due to very flat potential profiles during both lithiation and delithiation, sharp peaks were observed on both strain and capacity derivatives. The location of these derivatives takes place at similar
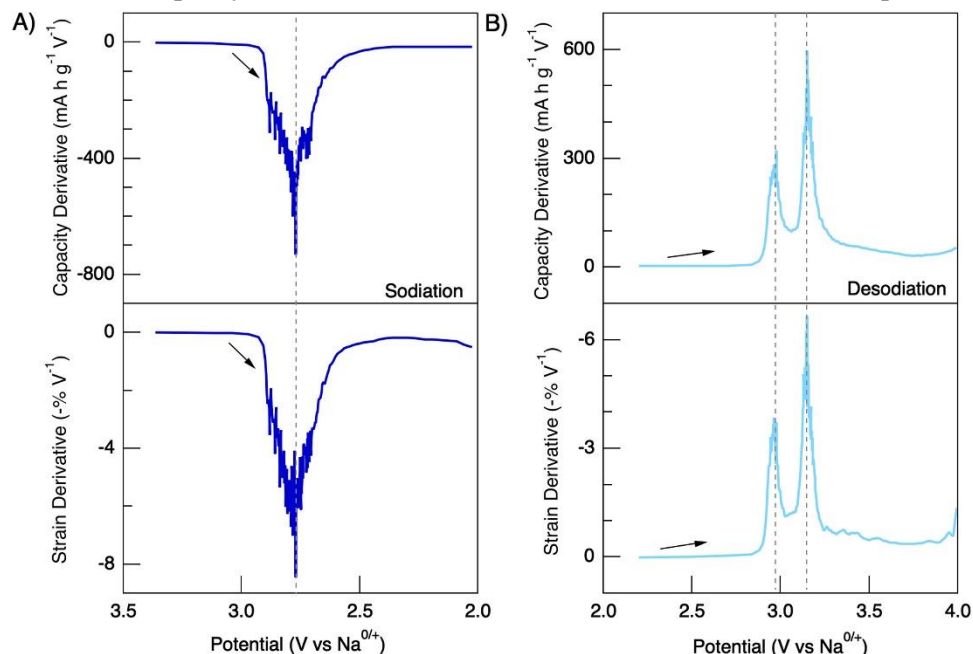
Figure 19. Current density (A,B) and strain derivatives (C,D) in NaFePO$_4$ composite electrode cycled at C/10 rate in 1 M NaClO$_4$ in EC/DMC electrolyte at 4th cycle

potentials.

In the case of Na intercalation via cyclic voltammetry, two distinct strain derivative peaks were observed at potentials 3.03 and 3.26 V, which correspond to current peaks. These current peaks are correlated with the structural changes in the electrode associated with phase transformations[32]. During Na insertion into the electrode, a single strain derivative was observed at the potential where the current reached its maximum. The magnitude of the strain derivative during the phase transition of FePO$_4$ to NaFePO$_4$ is much larger than the strain derivative observed during the phase transition from FePO$_4$ to LiFePO$_4$. Strain and capacity derivatives during the fourth cycle are shown in **Figure 19**. Similar to cyclic voltammetry, single strain derivatives were observed during sodiation whereas

43

there are two strain derivatives peaks during the desodiation cycle. These strain derivative peaks were observed at the potentials where the capacity derivatives reach its maxima or minima. Interestingly, the magnitude and shape of strain and capacity derivatives almost have a linear relationship.

The location of the strain derivative peaks corresponded well to the location of current peaks for both Li and Na intercalation mechanisms. These derivative peaks were repeatedly observed at a similar potential where the current or capacity derivatives reached their maxima or minima in the previous cycles too (**Figure A4.** Strain derivatives in $LiFePO_4$ composite electrode during Li intercalation in 1 M $LiClO_4$ in EC/DMC for (A) 1st, (B) 2nd, and (C) 3rd cycles at 50 µV/s.-**Figure A7**). This correspondence indicated that reversible strains developed in the macroscale iron phosphate composite electrode are directly related to the nano-scale changes in the lattice structure associated with lithiated or sodiated iron phosphate structures.

4.3.5 Comparison of Strains during Na and Li Intercalation

Large irreversible strain generation during the first cathodic scan in the iron phosphate electrode during the intercalation of Li^+ and Na^+ ions is observed in **Figure 16**. Strains are categorized as "anodic", "cathodic" and "irreversible strain" to compare the strain evolution in the iron phosphate electrode during Li^+ and Na^+ intercalation. Strain values are shifted to start from zero at the beginning of each cycle to calculate strain generation in each cycle. The strain change during the extraction of alkali-ions from the electrode is labeled as "anodic strain". It is calculated by subtracting the strain value at the end of the anodic cycle (4.4 V for Li^+ and 4.0 V for Na^+) from the strain value at the beginning of the cycle (2.6 V for Li^+ and 2.0 V for Na^+). The strain change during the insertion of alkali ions into the $FePO_4$ electrode is labeled as "cathodic strain". It is calculated by subtracting the strain value at the end of the cathodic cycle (2.6 V for Li^+ and 2.0 V for Na^+) from the strain value at the beginning of the cycle (4.4 V for Li^+ and 4.0 V for Na^+),

respectively. Strain value at the of each cycle is labeled as "irreversible strain" and it is calculated by subtracting the strain value at the end of the cycle from the initial strain value at the beginning of the cycle.

Figure 20 demonstrates the anodic, cathodic, and irreversible strains in FP composite electrodes during Li^+ and Na^+ intercalation via potentiostatic and galvanostatic cycling. Average anodic, cathodic, and irreversible strains are calculated from the individual experiments listed in **Table A1**-**Table A4**. In the cyclic voltammetry, cathodic strain reduced rapidly from 0.57% at the first lithiation to 0.44% at the second lithiation. In the subsequent cycles, the cathodic strain reduced slowly with cycle number to 0.38% and 0.35% in the 3rd and 4th cycles, respectively. In the galvanostatic cycling, the cathodic strain decreased from 0.62 in the first cycle to 0.48 at the second lithiation. The strain continued to decrease slowly to 0.43 and 0.36 in the 3rd and 4th galvanostatic cycles, respectively. A similar fade in intercalation-induced strains is also observed in a composite $LiMn_2O_4$ by digital image correlation and curvature measurements[35,37]. The anodic strain during the delithiation cycles slowly decreased from -0.34% to 0.29% and from -0.40 to -0.34 during the initial four potentiostatic and galvanostatic cycles, respectively. As a result of anodic and cathodic strains, the irreversible strain generation at each cycle reduced from 0.23% to 0.06% and from 0.23% to 0.03% between the first and fourth potentiostatic and galvanostatic cycles, respectively.

Similar trends in anodic and cathodic strain generation with cycle numbers are observed upon Na^+ intercalation in the $NaFePO_4$ composite electrode. However, as expected, the magnitude of strain generation during Na^+ intercalation is greater than that of the Li^+ intercalation. When the electrode is cycled at 50 μV/s, the magnitude of the cathodic strain dropped sharply from 2.63% at the first sodiation to 1.56% at the 2nd sodiation. Then, cathodic strain slowly decreases to 1.41% and 1.33% at 3rd and 4th sodiation cycles, respectively. Similarly, a large sodiation strain, 2.34%, was recorded during the first galvanostatic cycling at C/10 rate. The sodiation strain became 1.46% at the second galvanostatic cycle and reduced to 1.26% at the 4th galvanostatic cycle. The value of anodic strain

during the extraction of Na$^+$ slowly decreased from -1.33% to -1.22% and from -1.28% to -1.16%

during the potentiostatic and galvanostatic cycles, respectively. Irreversible strain in the electrode
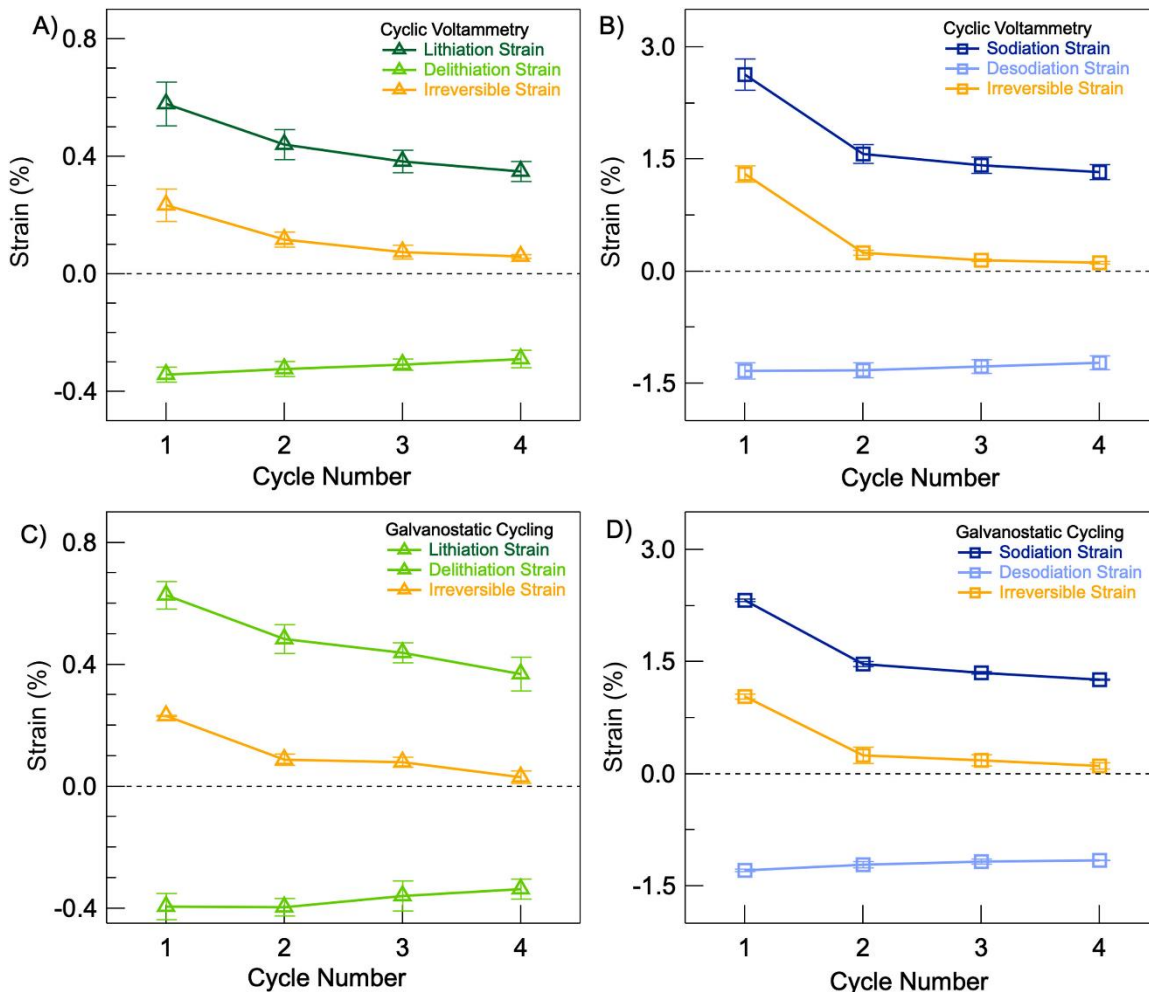
Figure 20. The role of Alkali metal-ion on Strains: Iron Phosphate composite electrodes were cycled during A, C) lithium and B, D) sodium intercalation via A, B) cyclic voltammetry at 50 µV/s and C, D) galvanostatic cycling at C/10 rate. Dark green and light green with triangle shape represents lithiation and delithiation strain in each cycle with error bars. Dark blue and light blue with square shape represents anodic and cathodic strains during each desodiation and sodiation, respectively. The orange triangle and square shape represent irreversible strains at the end of each Li and Na intercalation cycle, respectively. Original data is in **Table A1**-**Table A4**.

decreased from 1.30 to 0.10% and from 1.03% to 0.10% during the first four potentiostatic and

galvanostatic cycles, respectively.

Intercalation of alkali metal-ions induces phase transformation in the host FePO$_4$ structure.

However, differences in the reaction chemistry between lithium and sodium cause different

electrochemical response and phase stabilities[32]. The ionic radius of Na^+ (1.02 Å) is larger than the ionic radius of Li^+ (0.76 Å)[14]. As a result, the intercalation of Na^+ into the host structure induces larger changes in the lattice compared to Li^+ intercalation. Previous XRD studies investigated the unit cell parameter changes on the $FePO_4$ and A_xFePO_4, where A represents Li or Na while x represents the amount of alkali metal in the electrode structure (**Table A5**). The unit cell volume of the fully lithiated phase, $LiFePO_4$ is 6.9% larger than the $FePO_4$ phase. Sodiation of the electrode induced a 17.6% increase in the unit volume when $FePO_4$ transformed into the $NaFePO_4$ phase[32]. Relative change in the unit cell volume is almost 2.55 times greater when the electrode is fully sodiated compared to a fully lithiated one. However, our results demonstrate much larger volumetric changes during Na^+ ion intercalation in the composite electrode than Li^+ ion intercalation.

The number of alkali metal-ion ions removed from or inserted into the electrode defines the electrode capacity and directly influences strain evolution in the electrodes. The state of charge and discharge of the electrode is calculated by dividing the experimental capacity by the theoretical capacity. The experimental capacities are calculated by the integration of current with time and the electrode was cycled at C/10 rate. Capacity and strain evolutions in individual experiments during the charging/discharging cycles for Li-ion and Na-ion chemistries are listed in **Table A3** and **Table A4**. Strains were divided by state of charge/discharge in order to calculate the strain per unit state of charge/discharge in the composite electrode. **Figure 21** shows the expansion and contraction in the volume of electrode per unit charge/discharge upon Na^+ and Li^+ ion intercalation at C/10 rate. The corresponding ratio of the strain per unit state-of-discharge upon Na^+ ion intercalation is approximately 4.75 times greater than the corresponding ratio for Li^+ ion intercalation at the fourth cycle.

We also calculate the relative strain per unit discharge when the electrode is cycled via cyclic voltammetry at 50 µV/s. Values in Li_aFePO_4 and Na_aFePO_4 composite electrodes are calculated as

47

0.84 and 0.67 in the fourth cycle from **Figure 16**. During the fourth cycle, the expansions in the electrode upon Li^+ and Na^+ intercalation are 0.33% and 1.26%, respectively. If we divide strain evolution upon alkali metal-ion insertion by state of discharge, we found that the electrode
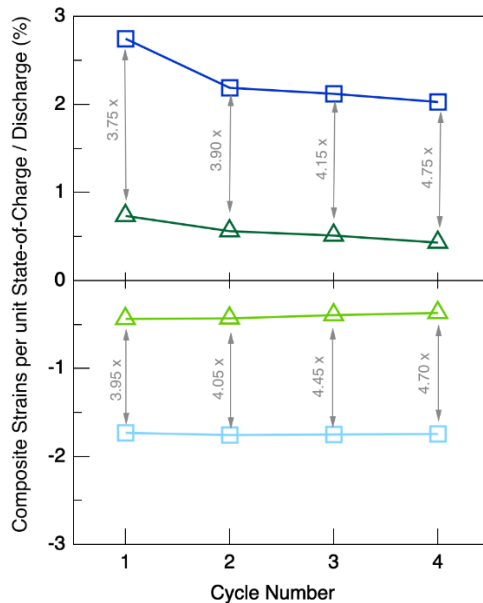
Figure 21. The strain per unit state-of-charge / discharge in iron phosphate composite upon lithium (triangle) and sodium intercalation (square). The electrodes were galvanostatically cycled at C/10 rate. Original data is in the **Table A3** and **Table A4**.

experienced 0.39 and 1.88 relative expansion with respect to each alkali metal-ion insertion. Again, the strain per state-of-discharge is approximately 4.75 times greater upon Na^+ ion intercalation compared to the Li^+ ion insertion.

Our results show a striking difference in relative volumetric expansion in composite iron phosphate cathode upon Na^+ vs Li^+ intercalation when cycled either galvanostatic at C/10 rate or cyclic voltammetry at 50 µV/s. The ratio of the volumetric changes upon Na^+ ion intercalation in the composite electrode with respect to Li^+ ion intercalation is unprecedently larger than the ratio of the volumetric changes in the crystal structure measured by previous X-ray diffractometry studies. The differences between composite strains in this study versus particle strains in XRD studies may be originated from the misfit strains in the composite electrode and / or the formation of amorphous phases in the $FePO_4$ electrode.

The Na^+ intercalation-induced expansions during the first cathodic cycle is significantly different than those during the subsequent cycles (**Figure 21**). It suggests that larger cathodic strain in the first cycle might be associated with the structural deformations in the $FePO_4$ composite electrode during Na^+ intercalation. Also, shallower potential slope with respect to capacity is observed during the first sodiation compared to the subsequent cycles in **Figure A3.** Potential and strain evolution with respect to capacity in $NaFePO_4$ composite electrode during Li intercalation in 1 M $NaClO_4$ in EC/DMC at C/10 rate. Dark and light blue lines demonstrate sodiation and desodiation cycles, respectively. The top right figure highlights the potential evolution between 2.6 – 2.9 V during sodiation at different cycle numbers. The figure is generated from data in **Figure 17**.. Yet-Ming Chiang et al. investigated the crystalline structure of $FePO_4$ during sodium intercalation using synchrotron radiation powder X-ray diffraction[20]. Surprisingly, almost negligible change in the cell volume was recorded during the first sodiation of $FePO_4$. However, they observed an almost 20% decline in the total crystalline phase percentage compared to the starting iron phosphate. The loss of the crystalline phase during the early cycles in LFP is also detected using operando characterization[87–89]. The x-ray diffraction studies support the observation of a large ratio of Na^+ / Li^+ ion-induced strains during the first cathodic scan.

Suo et al. developed a continuum model to study mismatch between two phases in the electrode particles[22]. The continuum model calculated larger misfit strains due to localized lithium distribution near the surface at higher scan rates. In this study, $FePO_4$ composite electrode with the same particle size is cycled against Li and Na counter metals at the same scan rate. Therefore, inhomogeneity is inversely related to the diffusivity of the alkali metal-ion in the solid electrode matrix. Impedance spectroscopy study measured the diffusion coefficients for lithiation and sodiation of $FePO_4$ as 1.3×10^{-14} and 2.2×10^{-15} cm^2/s, respectively[68]. The solid-state diffusion of Li in $FePO_4$ is much faster than Na diffusion. Monte Carlo simulations predicted the interruptions in Na^+ diffusion in $FePO_4$ due to Na^+/Fe^{2+} defect formation[53]. Molecular dynamic

calculations discussed the impact of lattice strains on the alkali metal-ion transport in the host structure[90]. The slower diffusion of Na ions in the solid matrix can lead to the generation of misfit strains in the composite electrode, in addition to the lattice strains. Additional efforts are required to understand the origin of the large strains during first Li^+ and Na^+ ion intercalation such as scan rate studies, the combination of x-ray diffraction and X-ray absorption spectroscopy-based experimental studies; and continuum model and DFT-based computational studies.

4.4 Conclusion

Understanding the fundamental differences and similarities between the intercalation mechanisms of Li and Na ions into electrodes is crucial for further developments in Na-ion batteries. In this work, digital image correlation was used to measure in situ strains in composite iron phosphate electrode during Li^+ and Na^+ intercalation. Composite iron phosphate electrodes were prepared by electrochemical delithiation of the pristine lithium iron phosphate. Similar discharge capacity and strain evolution were observed when the pristine lithium iron phosphate was electrochemical delithiated against Na and Li counter metals. Unprecedented large strains were observed during both first Li^+ and Na^+ insertion into the iron phosphate electrode. The strain becomes reversible in the later cycles during both Li^+ and Na^+ intercalation. As expected, larger volumetric expansions are observed in the iron phosphate electrode upon Na^+ intercalation compared to Li^+ intercalation at 50 µV/s. However, the relative volumetric changes upon Na^+ vs Li^+ in the composite electrode was astonishing compared to reported values by previous x-ray diffraction studies. Our results show that digital image correlation can be used to measure strain evolution in the composite electrodes during different alkali-ion intercalation. The remarkably large relative volumetric changes upon Na^+ vs Li^+ intercalation in the composite electrode have significant implications for developing battery electrodes for commercialization of Na-ion and K-ion batteries. Commercial

electrodes are constrained by current collectors and battery packaging, therefore large volumetric expansions in free-standing model electrodes will be translated into stress generation in constrained electrodes. These stresses will directly reduce battery performance and lifetime, which are crucial for stationary applications such as grid storage.

CHAPTER V

IN SITU PROBING POTASSIUM-ION INTERCALATION-INDUCED AMORPHIZATION IN

CRYSTALLINE IRON PHOSPHATE CATHODE MATERIALS

Bertan Özdogru[1], Younghwan Cha[2], Bharat Gwalani[3], Vijayakumar Murugesan[3], Min-Kyu Song[2]
and Ömer Özgür Çapraz[1]

1) The School of Chemical Engineering, Oklahoma State University, Stillwater, OK 74078

2) School of Mechanical and Materials Engineering, Washington State University, Pullman, WA
99164

3) Joint Center for Energy Storage Research, Pacific Northwest National Laboratory, 902 Battelle
Blvd, Richland, WA 99354

ABSTRACT

Na-ion and K-ion batteries are promising alternatives for large-scale energy storage due to their abundance and low cost. Intercalation of these large ions could cause irreversible structural deformation and partial to complete amorphization in the crystalline electrodes. Lack of understanding of dynamic changes in the amorphous nanostructure during battery operation is the bottleneck for further developments. Here, we report the utilization of in-operando digital image correlation and XRD techniques to probe dynamic changes in the amorphous phase of iron phosphate during potassium ion intercalation. In-operando XRD demonstrates amorphization in the electrode's nanostructure during the first charge and discharge cycle. Additionally, ex-situ HR-TEM further confirms the amorphization after potassium ion intercalation. In situ strain analysis detects reversible deformations associated with redox reactions in the amorphous phases. Our approach offers new insights on the mechanism of ion intercalation in the amorphous nanostructure which are highly potent for development next generation batteries.

5.1 Introduction

Rechargeable Li-ion batteries have been used to power consumer electronics and electric vehicles. The increasing demand on Li-ion batteries has created concern due to their limited and unevenly distributed resources. Rechargeable alkali metal-ion batteries with earth-abundant elements as charge carriers (Na and K) are promising alternatives for large-scale energy devices and stationary storage[91]. Na-ion (NIBs) and K-ion (KIBs) batteries are expected to share similar electrochemical properties with Li-ion batteries because they are monovalent[92,93]. However, many challenges remain to commercialize NIBs and KIBs including new electrode chemistries and mitigating chemo-mechanical degradations. Traditional electrode materials designed for Li-ion batteries may not be ideal to allow reversible charge storage of Na and K-ions due to their different size, mass and reactivity. Intensive efforts have been focused to develop new electrode nanostructures for these battery systems[94].

During insertion / removal of charge carriers, the electrode structures often undergo phase transformation, associated with the volume mismatch between the new phase and existing phase in the electrode particle. Depending on the phase transformation pathway and volume mismatch, insertion of alkali-ion into the host structure can cause plastic deformation, mechanical fracturing and even amorphization in the electrode[20,95–98]. Insertion of Li-ions into silicon can cause up to 300% volumetric expansion and the extraordinary high transformation strain causes amorphization, which provides a desirable platform for hosting Li ions in the electrode[99]. The high transformation strains during Na intercalation into $FePO_4$ (17% volume expansion) also cause the formation of amorphous phases between the primary phases, which is beneficial to alleviate the misfit strain energy[20].

The traditional crystalline electrodes may not be able to accommodate the insertion of Na or K-ions due to their size and reactivity with the host structure. For example, graphite structures allow

reversible intercalation with Li ions, but are unable to host Na ions[13,100,101]. Layered metal oxides can only host a fraction of K-ions, although they allow reversible cycling with Li and Na ions[14,102,103]. Unlike crystalline structures, the amorphous electrodes have short-range orders with long-range disordered structures. Due to the unique arrangement of atomic clusters in amorphous materials, they can store larger ions and provide flexibility to lattice distortions[91]. The amorphous materials can be identified by transmission electron microscopy (TEM) while the chemical composition can be analyzed with energy dispersive X-ray spectroscopy (EDS) techniques. The material chemistry of the amorphous materials also has been studied by utilizing Fourier-transform infrared spectroscopy, Raman spectroscopy and X-ray absorption spectroscopy. Although these techniques provide vital information about the chemistry of the amorphous materials, there is lack of understanding of the physical and dynamic behavior of amorphous materials during battery cycling. The chemo-mechanical analysis of dynamic changes in the amorphous materials as well as amorphization of crystalline structures during battery operation is very challenging due to the disordered nature of the amorphous phases.

Motivated by this, here, we propose a new experimental approach to monitor dynamic physical and structural changes in the amorphous phase of the electrodes by combining in situ strain measurements via digital image correlation (DIC) and in-operando XRD technique. Intercalation of K-ions into crystalline iron phosphate, $FePO_4$ host structure is chosen as a model system. Previous ex-situ XRD study demonstrated the amorphization of the crystalline $FePO_4$ upon K intercalation[96]. XRD technique can detect crystallographic evolutions in crystalline structures such as lattice parameters, interplanar spacing and phase identification. DIC technique has been used to characterize in situ electrochemical strain evolution in the composite electrodes associated with reversible (e.g., phase transformations) and irreversible (e.g., solid-electrolyte interface) deformations[33,34,36,104–106]. Previous DIC study investigated the relative strain evolutions upon Na and Li intercalation into $FePO_4$ electrode and these relative strains were found to be much greater

than relative expansions in crystal unit cell volume reported by the previous diffraction studies[107]. The discrepancy in volumetric changes in the electrode between XRD and DIC studies was associated with the formation of amorphous phase in the electrode upon Na-ion intercalation, which cannot be quantified by diffraction alone.

In this study, crystalline $FePO_4$ electrode is first formed by utilizing electrochemical ion displacement method. Then, K-ions were intercalated into the $FePO_4$ electrode during in situ monitoring of electrochemical strain generation and structural changes by performing DIC and XRD techniques. The details of in situ strain measurements by digital image correlation and experimental setup is provided in the Supporting Information. The electrode lost its crystallinity during the first cycle and Bragg peaks did not show any significant changes in the subsequent cycles. On the other hand, the electrode showed reversible expansions and shrinkage in its volume upon discharge and charge cycles, respectively. The strain derivatives demonstrated a characteristic peak at specific potentials during K intercalation, which suggests reversible redox chemistry in the amorphous phase of the electrode.

5.2 Results and Discussion

The crystalline $FePO_4$ host structure is generated by employing electrochemical displacement method[107]. The average particle size is about 238 ± 56 nm and the particle size range from 100 nm to 400 nm (**Figure B1** and **Figure B2**). **Figure 22**A and **Figure 22**B show the voltage and strain evolution in the electrode during the removal of Li ions. The single potential plateau around 3.67V vs $K/K^{+/0}$ indicates the formation of Li-deficient $FePO_4$ from Li-rich $FePO_4$, via a two-phase reaction mechanism[14,52]. Delithiation capacity was calculated as 187 mAh/g and it is close to the theoretical capacity of lithium iron phosphate, $LiFePO_4$, which is 170 mAh/g. Removal of Li ions from $LiFePO_4$ structure results in 0.18% contractions in the composite electrode (**Figure 22**B).

Figure 22C-G show the evolution of crystalline structure of composite electrode during electrochemical displacement to remove Li from pristine LiFePO$_4$ electrode. At the onset of the charge (3.6 V vs K/K$^+$), the pristine electrode demonstrates well-defined XRD peaks around 29.5°, 32°, 35.5° and 37.8°, which are associated with the crystalline structure of the LiFePO$_4$ electrode[14]. During the process, the intensity of these peaks gradually decreases with the increase in voltage and eventually disappears at around 4.3V, which indicates the removal of Li ions from LiFePO$_4$ structure. At the same time, new peaks started to appear around 30.5°, 36.5° and 37.2° , which are associated with FePO$_4$ crystalline structure. Intensity of these peaks increases as more Li ions are removed from the crystalline structure, indicating the conversion of LiFePO$_4$ to FePO$_4$. Overall, the XRD patterns show the successful phase transition of the crystalline structure of the pristine LiFePO$_4$ into FePO$_4$ when the electrode was charged against K counter electrode.
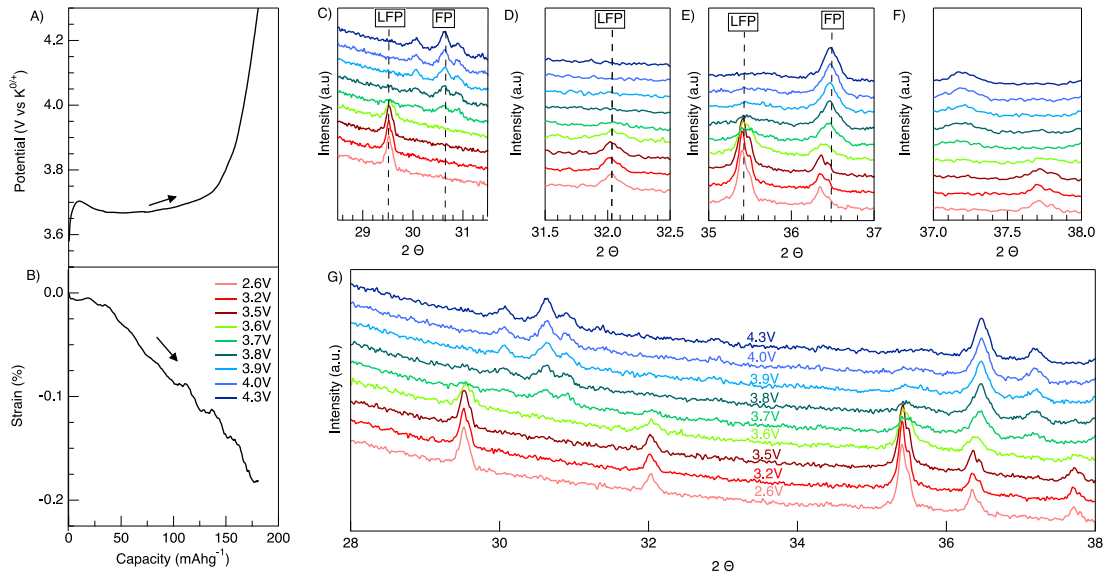
Figure 22. Formation of FePO$_4$ electrode by electrochemical displacement of Li from LiFePO$_4$ electrode. The pristine LiFePO$_4$ electrode was delithiated at C/10 rate against K counter electrode until to 4.3 V vs K/K$^{+/0}$. (A) Voltage and (B) strain evolution during the extraction of Li ions from LiFePO$_4$. The C-rate is calculated based on theoretical capacity of LiFePO$_4$, which is 170 mAh/g. (C-G) Evolution of LiFePO$_4$ composite electrode's crystalline structure measured with in-operando XRD during electrochemical displacement process. Color change from red to blue indicates the increase in voltage as described in the figure.

After the formation of crystalline FePO$_4$ structure with electrochemical displacement, the electrode is continuously discharged / charged with K-ions at C/25 rate (**Figure 23**). During the first

discharge, voltage sharply decreased to 2.3 V and showed a very small plateau around 2.3 V. After the plateau region, voltage continued to decrease until the lower cutoff voltage of 1.5 V. Discharge capacity was 43 mAh/g. Intercalation of K into the $FePO_4$ structure resulted in the electrode expanding about 0.66%. The strains show non-linear increase with the discharge capacity (**Figure B5** and **Figure B6**). Positions of the Bragg peaks in the $FePO_4$ structure before the first discharge were recorded for (211), (020), (311) and (121). The initial structure of the electrode before the first discharge demonstrated typical $FePO_4$ crystalline features[67]. Decrease of the intensity of the XRD peaks at 30.5°, 36.5° and 37.2° indicates the reduction in crystallinity of the electrode due to K-ion insertion. These peaks are also shifted towards lower 2θ, indicating the increase in interplanar spacing with the K-ion intercalation. **Table B1** shows the increase in the interplanar spacing along <311>, <121>, <211> and <020> by more than 0.5 picometer at the end of the discharge cycle. No $LiFePO_4$ peaks appeared during the first discharge.

During the first charge, voltage increased sharply until around 2.3V voltage, and then it had shallower slope until the upper cutoff voltage of 4.3 V. Charge capacity was about 40 mAh/g. While the removal of the K after the first charge caused reduction of electrode volume, the electrode did not return to its original volume, resulting in an irreversible expansion of about 0.21% at the end of the first cycle. Increase in the intensity of the XRD peaks suggests the partial recovery of the electrode's crystallinity. Also, these peaks are shifted towards higher 2θ, indicating the decrease in interplanar spacing due to removal of K-ions.

In the subsequent discharge and charge cycles, intercalation of K into the cathode structure resulted in volumetric expansions and reductions, respectively. The difference in strain evolution between each charge and discharge cycle leads to increase in irreversible strains in the electrode, which becomes 0.41% by the end of the fourth cycle. Although both capacity and strain generation indicate the K-ion intercalation into the electrode, intensity and location of the XRD peaks did not show any significant changes during the subsequent cycles. This indicates that crystallinity and

interplanar spacing in the electrode does not change anymore in the crystalline part of the electrode and suggests that K-ions are intercalated into the amorphized phase of the electrode.
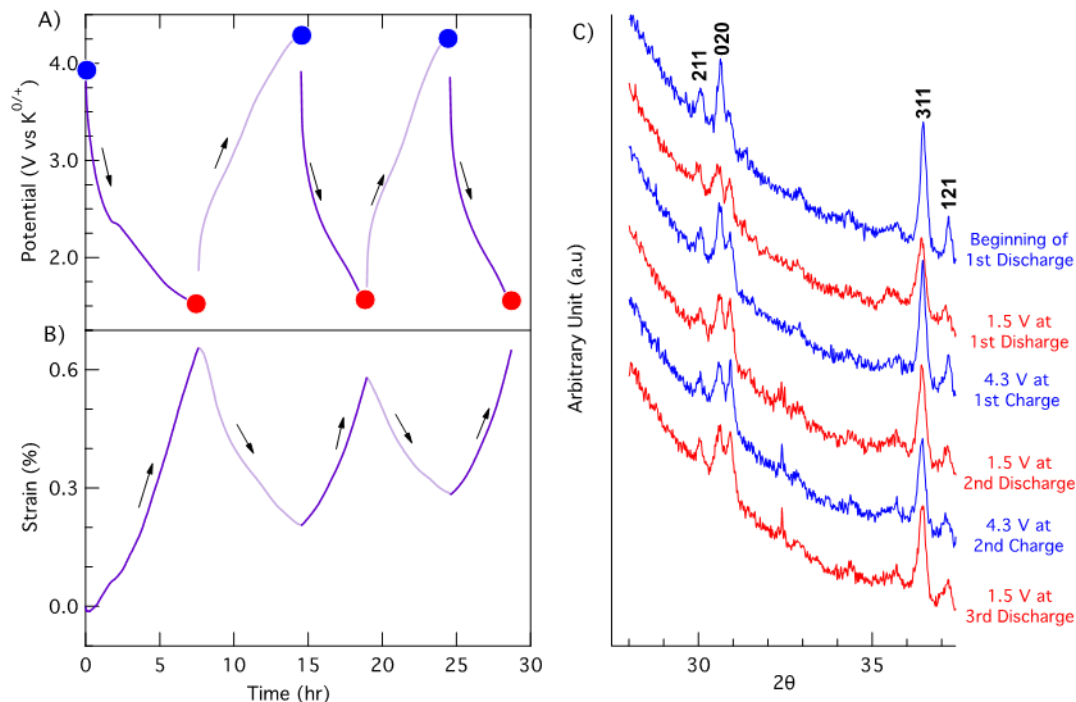
Figure 23. Discharge and charge of FePO4 composite electrode with K-ions: A) Voltage and B) strain evolution in the composite electrode during K intercalation at C/25 rate. C) Corresponding XRD patterns at the beginning and end of charge / discharge cycles. Arrows indicates the direction of the cycles. The C-rate is calculated based on theoretical capacity of potassium iron phosphate, which is 141 mAh/g.

High resolution transmission electron microscopy (HRTEM) was conducted to investigate the amorphization and phase distortions in the electrode structure upon K-ion intercalation. **Figure 24**A-B suggests two major phases in the electrode structure after the third discharge cycle. Particles with diameter ~200 nm are consistently indexed as $FePO_4$ phase and these particles show the formation of amorphous layer on their periphery (**Figure 24**D–E). The ordered lattice fringes and diffraction maxima in **Figure 24**A indicates the $FePO_4$ crystalline structure. The lattice fringe width in Fig 3E are also in a good agreement with literature[72]. HAADF STEM image in **Figure 24**B shows amorphized smaller particles with diameter ~50 nm around the crystalline $FePO_4$. (**Figure 24**A). The existence of smaller particles with amorphous structure in the TEM images indicates

the plastic deformations in the electrode particles upon K-ion insertion. Additionally, nano crystals with 2-5 nm are observed within these amorphized particles (**Figure 24**F). The corresponding lattice fridge width of the nano crystals is about 2.4 to 2.7 Å. Based on the previous potassium iron phosphate study[108], these nano crystals could be $KFe_2(PO_4)_2$. Elemental analysis of the electrode particles was conducted via STEM-EDS (**Figure 24**C). The Fe, P and O elements are homogeneously distributed in the crystalline $FePO_4$ particles. However, K was mostly found on the near surface of these particle and its location coincide with the amorphous layer seen in **Figure 24**D. The TEM analysis indicates the penetration of K-ions ranges from 5 nm to 25 nm. Amorphization in the crystalline $FePO_4$ particles after intercalation with K-ions is confirmed by our HRTEM results.
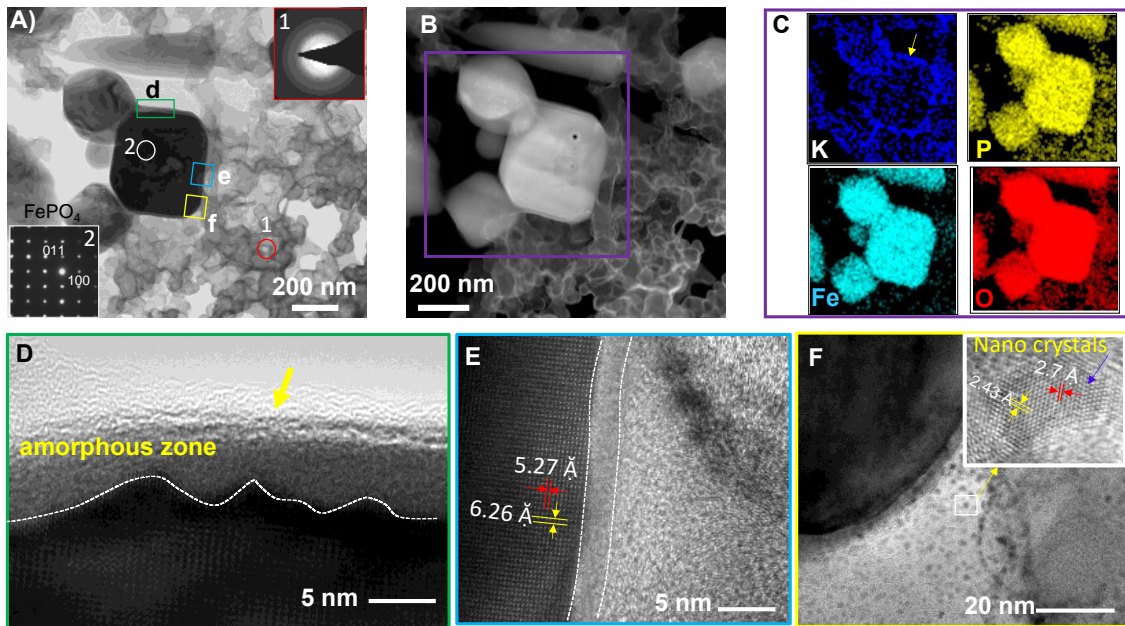
Figure 24. TEM results from the potassium iron phosphate electrode after third discharge cycle. A) bright field TEM (BFTEM) image showing the crystals of unreacted FePO4 and reaction product. The inset sub-figure 1 shows selected area electron diffraction (SAED) ring pattern taken from the circular red area in the Fig A. The inset sub-figure 2 shows the SAED pattern taken from the circular white area in the Fig A. B) HAADF STEM image of the crystalline particles and the amorphous region around them. C) Elemental analysis of Fe, P, K, and O from the purple area described the Fig B. D) HRTEM image taken from the green boxed area marked on the Fig A. E) HRTEM image taken from the blue boxed area marked on the Fig A. The image also shows the corresponding lattice fringe widths on the crystalline part of the electrode. F) High-resolution TEM image taken from the yellow boxed area marked on the Fig A. The inlet figure shows the lattice fringe widths taken.

To better understand nanoscale structural changes in the electrode during charge and discharge cycles, capacity and strain derivatives with respect to voltage were calculated to investigate the charge behavior and physical response of the $FePO_4$ electrode during K intercalation. Previous studies on graphite[34,104], lithium manganese oxide (LMO)[33,37,38], lithium iron phosphate (LFP)[44] and sodium iron phosphate (NFP)[107] electrodes showed that the evolution of the strain derivatives with potential closely matches with the phase transformations in the electrode structure. In the studies, the location of the strain derivative peaks was in good agreement with evolution of the electrochemical response of the materials associated with the nanoscale changes in their structure. Charging / discharging of graphite, LMO, LFP or NFP electrodes leads to changes in the crystalline structure associated with the phase transformations, which are well-reported by XRD studies. On the other hand, a previous ex-situ XRD study showed significant loss of crystallinity in the $FePO_4$ structure after K intercalation, which is associated with the amorphization of the structure upon large K-ion intercalation[96].

Strain and capacity derivatives are calculated by taking a derivative with respect to potential. **Figure 25** shows the detailed picture of the progression in XRD peaks at selected voltages during discharge cycles, alongside the capacity and strain derivatives. During the first potassiation, two distinct strain derivative peaks were observed at around 2.3 V and 1.55 V. The location of these peaks was closely aligned with the location of capacity derivatives within 3 mV. The absolute value of the strain and capacity derivatives at around 1.55V were found to be greater than the ones at around 2.3V. Previous strain study demonstrated that the magnitude of the strain derivatives aligns well with the nanoscale changes in the electrode structure during Li intercalation into LMO cathodes. Therefore, the macroscale strain measurements are highly sensitive to nano-scale changes in the electrode structure[33]. On the other hand, intensity of the XRD peaks reduced slowly when the voltage was decreasing from about 3V to 1.5V during the first discharge cycle. Also, their location was slowly shifted toward higher 2θ while inserting more K-ions into the electrode

structure (**Figure B10**). Previous study based on amorphous FePO$_4$ showed the formation of KFe$_2$(PO$_4$)$_2$ crystalline structure during the first K intercalation in the electrode structure[108].

Strain and capacity derivative peaks around 2.3 V and 1.55 V disappeared in the consecutive potassiation cycles. A single characteristic peak in capacity derivative emerged at around 1.9 V. The rate of strain derivatives also changed at around 1.9V in the subsequent discharge cycle, demonstrated as a shoulder in **Figure 25**B. On the other hand, both location and intensity of the Braggs peaks did not change during the 2nd and 3rd discharge cycles. The combination of XRD and strain derivative analysis suggests the reversible electrochemical reaction and associated structural changes in the amorphous phase of the FePO$_4$ at around 1.9V.
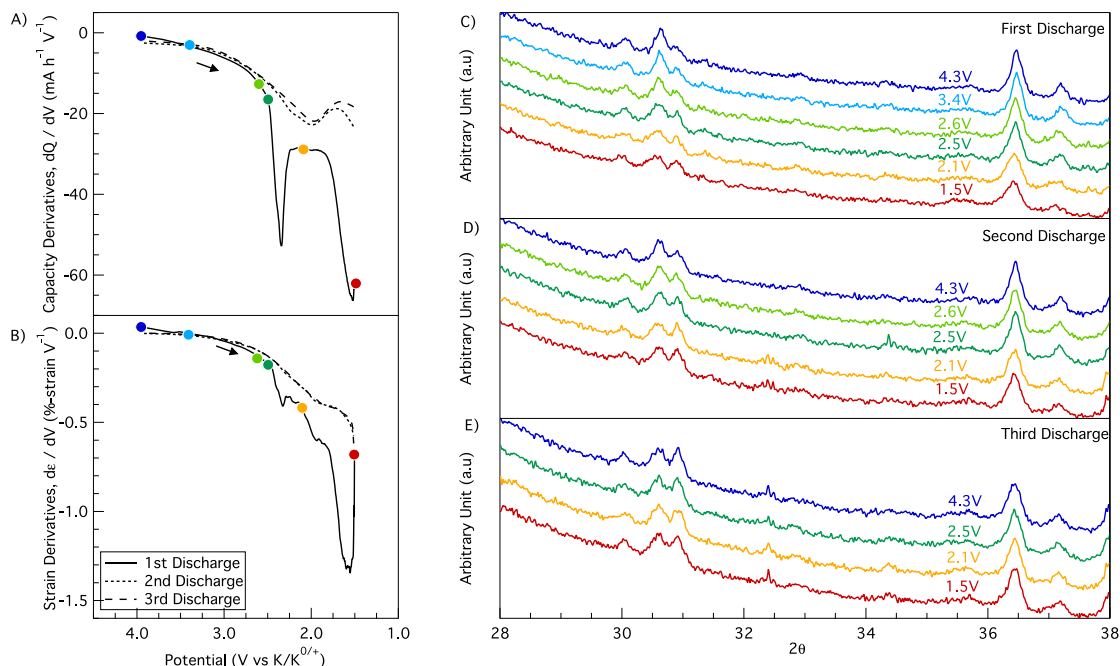
Figure 25. Structural, physical, and electrochemical response of the iron phosphate during first three discharge cycles A) capacity and B) strain derivatives with respect to voltage. C-E) Corresponding XRD patterns at selected potentials colored and potential values are written for each pattern as shown in the figure.

Figure 26 shows the detailed picture of the progression in XRD peaks at selected voltages during charge cycles, alongside the capacity and strain derivatives. During the first depotassiation, there are three minima peaks in capacity derivatives at around 2.8, 3.2 and 3.8 V. The associated peaks

in the strain derivatives are clearly observed at 2.8 and 3.8V. The strain derivative had a shoulder at around 3.2 V, which aligns with the location of the capacity derivative peak in 3.2 V. The magnitude of the strain derivative peak at 2.8V was greater than the other detected strain derivative peaks during the charge cycle. On the other hand, both location and intensity of the Braggs peaks were almost the same until the higher voltages towards the end of the first charge cycle. The increases in the peak intensities were detected above around 4.0V and the peaks were shifted to lower 2θ. In the subsequent charge cycles, derivative peaks in 3.2 and 3.8V disappeared and there was only one characteristic peak observed in both strain and capacity derivatives at around 2.8V. On the other hand, both location and intensity of the Braggs peaks did not change during the 2nd charge cycle. The combination of strain analysis with in-situ XRD data suggests the phase transformation in the amorphous phase of the electrode at around 2.8V during charge cycles.
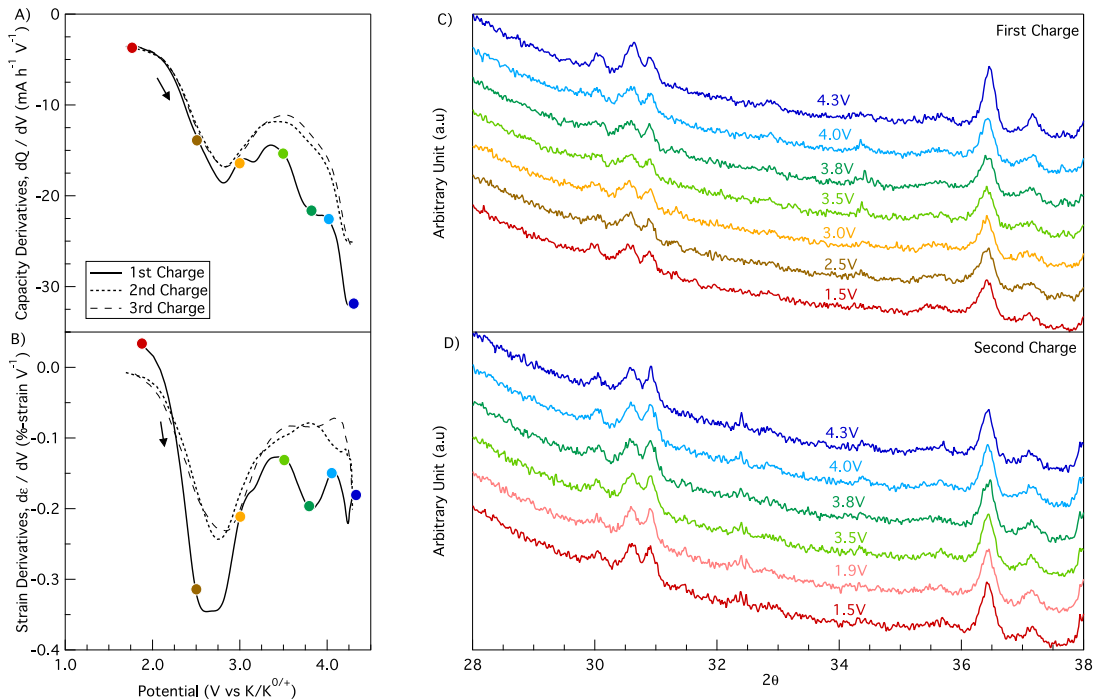
Figure 26. Structural, physical, and electrochemical response of the FePO$_4$ during charge cycles A) capacity and B) strain derivatives with respect to voltage. C-D) Corresponding XRD patterns at selected potentials colored and potential values are written for each pattern as shown in the figure.

To examine the impact of the electrolyte decomposition on the capacity and strain derivatives during K intercalation into $FePO_4$ cathodes, the electrode was also cycled in 0.5 M KPF_6 in PC electrolyte (**Figure B12** and **Figure B14**). The evolution of the strain derivative peak during the first discharge cycle was significantly different than the subsequent discharge cycles. Large irreversible capacity in the first cycle upon K-ion intercalation is also reported in the literature and it was associated with the structural deformation[7]. HR-TEM images (**Figure 24**) is evident for amorphous phase upon K-ion intercalation in our measurements. The irreversible characteristic of the strain and capacity derivatives in the first discharge is associate with the amorphization in the electrode structure. The electrode demonstrated two distinct strain and capacity derivative peaks at around 2.8 and 3.8 V during the first charge cycle. Like the strain behavior of the electrode when cycled in EC: DMC solvent, the peak at around 3.8V disappeared in the subsequent charge cycles. Beyond the first cycle, the electrode experiences reversible strain and capacity derivatives around the similar potentials when the electrode cycled in either EC: DMC or PC solvent, pointing out that the behavior of charge and physical response in the electrode is associated with the changes in the electrode structure. Also, in both cases, the magnitude of the strain derivatives at the end of the first discharge cycle is significantly larger than the ones at the subsequent discharge cycles, regardless of the electrolyte. Overall, strain derivative analysis suggests a significant structural deformation during the first cycle and electrodes demonstrate reversible mechanical and electrochemical responses in the subsequent cycles.

Interestingly, the distinct differences between the first cycle and the subsequent cycles during K intercalation into $FePO_4$ are observed in both strain measurements and XRD analysis. In-operando XRD analysis demonstrated the changes in the electrode structure during the first cycle and in-situ strain analysis showed irreversible strain and capacity derivatives only observed during the first cycle. Beyond the first cycle, the electrode no longer undergoes any detectable changes in its crystallinity in the XRD analysis. Both evolution profile of the strain and capacity derivatives

become highly reversible beyond the first cycle. TEM measurements confirm the amorphization in the crystalline iron phosphate electrode and amorphous phases were found to be rich with K elements in the discharged electrode. Although in-operando XRD analysis was not able to capture any changes in the crystalline structure of the electrode during the subsequent cycles, strain derivatives analysis indicates a reversible physical change in the electrode as a result of redox chemistry in the electrode upon reversible K-ion intercalation. The reversible strain and capacity derivatives suggest the phase transformations in the electrode structure at redox potentials of 1.9V during discharge and 2.8 V during charge cycles, respectively.

5.3 Conclusion

Identifying the redox reactions in the amorphous phase and its associated volumetric changes upon K intercalation into amorphous phase is an important step to understand the dynamic and kinetic changes in the amorphous electrodes. We foresee that a similar approach can be utilized to study chemo-mechanics of amorphous electrodes for many different battery chemistries including Na-ion, K-ion and Zn-ion batteries. In situ probing of dynamic changes in the amorphous materials during battery cycling can provide fundamental knowledge to establish a structure – mechanics-performance relationship for amorphous materials.

CHAPTER VI

THE IMPACT OF ALKALI-ION INTERCALATION ON REDOX CHEMISTRY AND

MECHANICAL DEFORMATIONS: CASE STUDY ON INTERCALATION OF Li, Na, AND

K IONS INTO FePO$_4$ CATHODE

Bertan Özdogru[1], Behrad Koohbor[2] and Ö. Özgür Çapraz[1]

1) The School of Chemical Engineering, Oklahoma State University, Stillwater, OK 74078

2) Department of Mechanical Engineering, Rowan University, Glassboro, NJ 08028

ABSTRACT

Batteries made of charge carriers from Earth-crust abundant materials (e.g., Na, K and Mg) have received extensive attention as an alternative to Li-ion batteries for grid storage. However, a lack of understanding of the behavior of these larger ions in the electrode materials hinders the development of electrode structures suitable for these large ions. In this study, we investigate the impact of alkali ions (Li, Na and K) on the redox chemistry and mechanical deformations of iron phosphate composite cathodes by using electrochemical techniques and *in situ* digital image correlation. Na-ion and Li-ion intercalation demonstrate a nearly linear correlation between electrochemical strains and the state of charge / discharge. The strain development shows non-linear dependance on the state of charge / discharge for K ions. Strain rate calculations show that K ion intercalation results in a progressive increase in the strain rate for all cycles. Li and Na intercalation induce nearly constant strain rates with the exception of the first discharge cycle of Na intercalation. When the same amount of ions are inserted into the electrode, the electrode shows the lowest strain generation upon Li intercalation compared to larger alkali ions. Na and K ions induce similar volumetric changes in the electrode when the state of charge / discharge is around 30%. Although the electrode experiences larger absolute strain generation at the end of the discharge cycles upon Na intercalation, strain rates were found to be greater for K ions. Potential-dependent behaviors also demonstrate more sluggish redox reactions during K intercalation, compared to Li and Na. Our quantitative analysis suggests that the strain rate, rather than the absolute value of strain, is the critical factor in amorphization of the crystalline electrode .

Keywords: Iron phosphate, alkali-ions, Li-ion, Na-ion, K-ion, sluggish reactions, electrochemical strains, chemo-mechanics.

6.1 Introduction

Development of cathode structures suitable for Na-ion and K-ion batteries is still one of the major challenges on the way to the design of next-generation alkali metal-ion batteries. Although Li, Na and K belong to the same alkali metal group with a single charge in their cation form, intercalation of Na^+ and K^+ ions in electrodes is difficult since ionic radii of Na^+ (1.02 Å) and K^+ (1.38 Å) are larger than that of Li^+ (0.76 Å)[109]. Therefore, physical, and electrochemical behavior of the cathode materials in response to Na^+ and K^+ ion intercalation is expected to be fundamentally different from the response to Li^+ ion. However, there is not much known about how electrochemical reactions and the transport of ions that take place in cathode materials with different alkali metal ions. There have been several studies focusing on electrochemical characterization and investigation of the structural changes in the electrode materials[48–50,52,110,111]. A lack of insight into these reaction-transport mechanisms limits the design of novel cathode materials for Na-ion and K-ion batteries. Therefore, comparative studies between Li-ion, Na-ion and K-ion battery cathodes are critical to identify fundamental similarities and differences during intercalation.

Even modest expansions in brittle cathodes can cause particle fracturing in a larger crystalline-size scale[20,55–57,69]. Intercalation of larger ions can cause structural collapse and amorphization induced by continuous accumulation of strains and distortions[53,54,112]. Dislocation activity has been observed during electrochemical delithiation of micron size $LiFePO_4$ particles, although the lattice strains were only around %5 for $LiFePO_4$[113]. Synchrotron radiation powder X-ray diffraction and pair distribution function analysis demonstrated the formation of amorphous phases in iron phosphate electrodes during Na intercalation[20]. Islam *et al.*[90] discussed the effect of lattice strain on the ion condition and defect properties of $LiFePO_4$ and $NaFePO_4$ using atomistic simulations. The calculations suggest that tensile strains generated perpendicularly to the migration channels can improve the intercalation kinetics in polyanionic compounds cathodes[90]. Lattice strain induced by large Na^+ ion intercalation into Na_xCuS structure causes crystallographic tuning and deviation of

68

reaction pathways from the thermodynamic equilibrium[114]. K^+ ion insertion into $FePO_4$ electrode resulted in amorphization or severe crystallinity lowering in crystalline $FePO_4$ electrode[96]. Amorphization of layered manganese oxide ($AMnO_2$) is also observed upon Na^+ and K^+ ion intercalation[112]. Recent TEM studies show a slight amorphization in the iron phosphate electrode upon Na intercalation[20] whereas K ions cause amorphization in the crystal structure of iron phosphate[14]. Although the amorphization in the structure can be easily identified by conventional diffraction or electron microscopy techniques, quantitative analysis of the physical changes in the structure during and after amorphization while cycling the battery electrode is critical. Recently, we developed a new experimental approach to monitor dynamic physical and structural changes in the amorphous phase of the electrodes by combining *in situ* strain measurements via digital image correlation (DIC) and in-operando XRD techniques[115]. The study detected the redox chemistry and the associated electrochemical strains in the amorphous phases of the iron phosphate electrode during K ion intercalation[115].

In this work, we compare the *operando* physical and electrochemical responses of the host cathode electrode upon intercalation of Li, Na and K ions using DIC and electrochemical methods. Iron phosphate was selected as a model system because it allows intercalation of Li, Na and K ions[67,68]. Chemo-mechanical strains were observed to increase linearly with Li and Na intercalation. However, strain development shows a non-linear increase with K intercalation. Strain rates were more constant and lower in value during Li intercalation. Our study provides a quantitative analysis into the electrochemical strains causing irreversible deformations in the crystalline iron phosphate electrode. More importantly, we show that although the net value of electrochemical strains are similar with Na and K ion intercalation, the kinetics of strain development is different for various ions.

6.2 Materials and Methods

Composite electrodes were prepared by mixing pristine lithium iron phosphate (LiFePO$_4$, LFP, Hanwha Chemical) with sodium carboxymethyl cellulose (binder, CMC, Aldrich) and conductive additive (carbon black, Alfa Aesar) in 8:1:1 mass ratio. Iron phosphate (FePO$_4$, FP) composite electrode was formed by electrochemical displacement technique using a pristine LFP composite electrode[67,68,107,115] via galvanostatic cycle at a rate of C/10. FePO$_4$ electrodes were charged / discharged with Li, Na or K ions by galvanostatic cycles at C/25 rate against Li, Na or K counter electrodes, respectively. The iron phosphate electrodes were charged and discharged at C/25 rate, based on a theoretical capacity of 170 mAh/g for LiFePO$_4$, 154 mAh/g for NaFePO$_4$ and 131 mAh/g for KFePO$_4$. The following salts and solvents were used to prepare electrolytes: 1 M LiClO$_4$ in 1:1 (v:v) EC:DMC for Li intercalation, 1 M NaClO$_4$ in 1:1 (v:v) EC:DMC for Na intercalation. 0.5 M KPF$_6$ in 1:1 (v:v) EC:DMC or EC:PC electrolytes were used for K intercalation. DIC technique was used to probe *in situ* strain generation during battery cycling. The natural surface features of the composite electrode were used as a speckle pattern suitable for the calculations of displacement fields and their resultant strain distribution on the electrode surface. A detailed description of the technique and custom battery cell was provided in our previous publication[37].

6.3 Results and Discussion

6.3.1 First cycle

Li, Na and K ions are intercalated into iron phosphate electrode at C/25 rate while monitoring *in situ* strain generation in the electrode. Voltage and electrochemical strains during the first cycle are plotted against the state of discharge (SOD) or state of charge (SOC) during Li, Na and K ions intercalation / de-intercalation, respectively. (**Figure 27**). SOD /SOC is calculated by dividing practical capacity measured in the experiment by theoretical capacity of LiFePO$_4$, LiFePO$_4$ or KFePO$_4$. A single voltage plateau is observed during Li and Na intercalation into iron phosphate at

around 3.41V (vs Li/Li$^{0/+}$) and 2.81V (vs Na/Na$^{0/+}$), respectively. A two-phase reaction between

iron phosphate and LiFePO$_4$ or NaFePO$_4$ results in a single potential plateau during the

galvanostatic discharge cycles[67,68]. The LiFePO$_4$ electrode showed a flat potential plateau around

3.44 V vs Li/Li$^{0/+}$. NaFePO$_4$ electrode showed two distinct plateaus at around 2.93 and 3.21 V vs

Na/Na$^{0/+}$. The two potential plateaus during desodation are attributed to the formation of

Na$_{0.7}$FePO$_4$ reaction intermediate during transition of NaFePO$_4$ phase to FePO$_4$ phase[68]. In the case

of K intercalation / de-intercalation, potential profiles did not show any distinct plateau during

intercalation of K ions into iron phosphate. Similar potential evolution in two different electrolyte

systems ensures that the electrochemical behavior is due to K-ion intercalation/ de-intercalation in

the electrode. Also, a similar potential profile was reported when K ions were intercalated into the

amorphous iron phosphate[108]. A recent *in situ* XRD study also demonstrated the amorphization of

the crystalline iron phosphate during the intercalation of K ions[115].

The corresponding electrochemical strains in the electrodes upon Li, Na and K intercalation are

shown in **Figure 27**B and E. The electrode expanded by almost 0.65% and 2.53 % at the end of the

first discharge of Li and Na ions, respectively. K ions were only able to intercalate into electrode

structure up to a SOD of *ca.* 0.30, resulting in 0.15% strain generation. In the case of charge

reactions, extraction of Li and Na ions from LiFePO$_4$ and NaFePO$_4$ resulted in -0.30 and -1.21%

contraction. During the removal of K ions, potassium iron phosphate experienced -0.40% reduction

in the electrochemical strains at 0.3 SOD. The electrode experiences -0.12, and -0.40% strain

generation at 0.3 SOD during Li and Na ion intercalation. The NaFePO$_4$ and K$_z$FePO$_4$ electrodes

undergo similar strain generation when the same amount of Na or K ions were removed from or

inserted into NaFePO$_4$ and K$_z$FePO$_4$ electrodes, respectively. Overall, the slope of strain build up

changes dramatically during K ion intercalation, whereas strain evolutions during Li intercalation

show a lower degree of nonlinearity during the first discharge cycle only. The slope of strains

increased during Na ion insertion, however strain rate become constant during Na extraction in the first cycle.
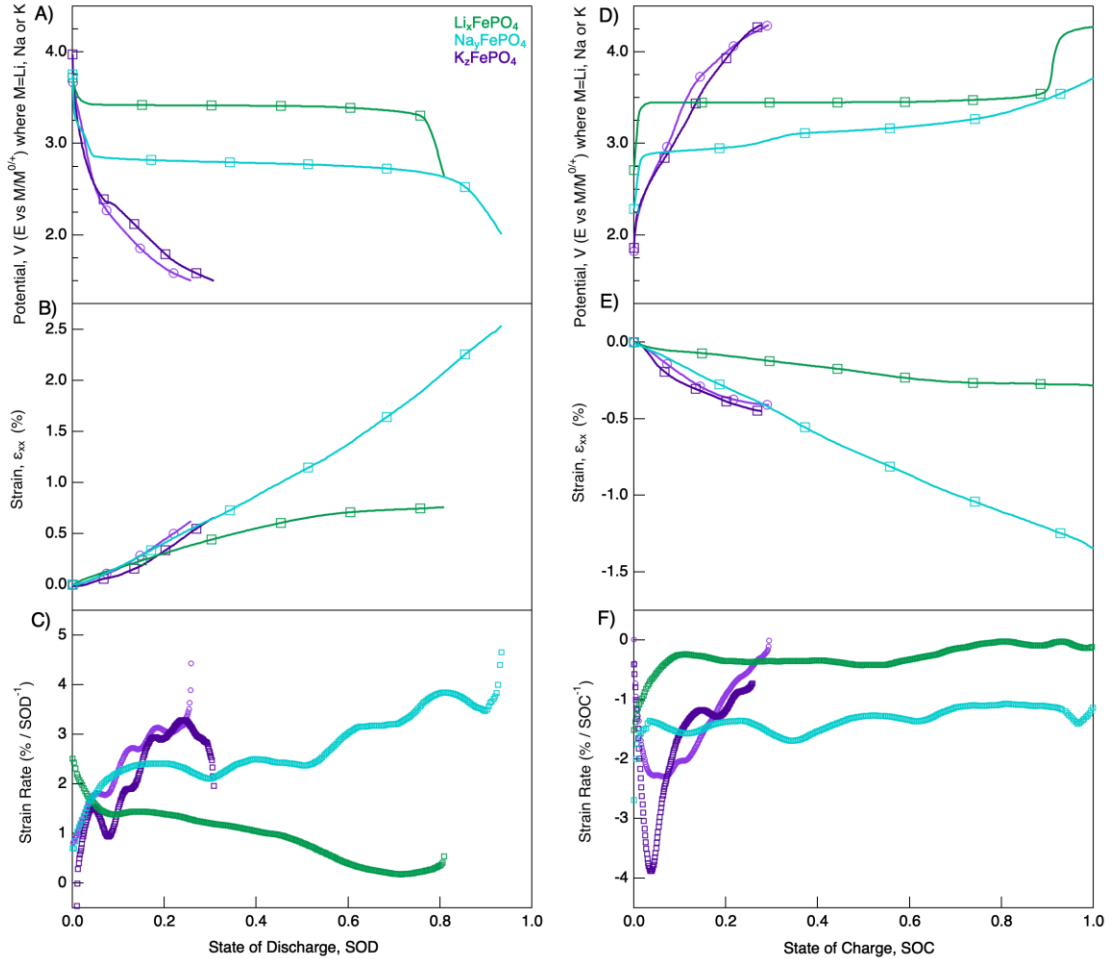
Figure 27. Potential evolution, strain generation and strain rates with respect to state of discharge (A, B, C) and charge (D, E, F) of Li (green), Na (blue) and K (purple) ions into FePO$_4$ electrode during the first cycle. The square and spherical symbol show when electrode is cycled either in EC:DMC or EC:PC solvents, respectively. Strain set to zero at the beginning of each charge / discharge cycles.

Since SOD / SOC during discharge and charge of K ions were less than 0.35, **Figure C1** is limited to 0.35 SOC / SOD for better comparison between Li, Na and K intercalation behavior during the first cycle. The slope of the strains was progressively increased as more potassium ions were intercalated into the electrode. We determined strain rates during charge and discharge cycles by calculating the derivative of electrochemical strains with respect to the state-of-discharge / charge. Between 0.05 and 0.35 of SOD, the strain rates for Li and Na intercalation into iron phosphate were

about 1.40 and 2.40 %-SOD^{-1}, respectively. Strain rate during Na ion intercalation become around 3.5%-SOD^{-1} at the end of the discharge. On the other hand, the strain rates continuously increased as more K ions were intercalated into iron phosphate and reached to around 3.2 %-SOD^{-1} when the voltage reached 1.5V vs K/K$^{0/+}$ at the end of the discharge cycle. During the first charge, strain rates drastically reduced from about -3 %-SOC^{-1} to almost 0.5%-SOC^{-1} during K extraction from K$_z$FePO$_4$. On the other hand, extraction of Na and Li from NaFePO$_4$ and LiFePO$_4$ shows constant strain rates at around -0.35 and -1.35 %-SOC^{-1}, respectively.

6.3.2 Subsequent Cycles

Figure 28 shows the voltage profile and strain generation during the 4th cycle. The 2nd and 3rd cycle data were also plotted in **Figure C2**-**Figure C6**. Overall, the potential profiles during the subsequent charge / discharge cycle of Li, Na and K ions show very similar behavior compared with the 1st cycles. A single potential plateau was observed during both charge and discharge of Li ions in LiFePO$_4$ cathode. Charge cycles during Na extraction showed two distinct potential plateaus and Na intercalation resulted in a single potential plateau in NaFePO$_4$. Again, potential profiles did not show any distinct plateaus during subsequent charge / discharge cycles of K ions in K$_z$FePO$_4$ cathode.

Electrochemical strains showed a nearly linear increase with Li and Na intercalation. However, strain generation data showed nonlinear increase during K ion intercalation into K$_z$FePO$_4$. Na and K intercalation resulted in much larger electrochemical strains in the electrode compared to the Li intercalation due to their comparably larger ion sizes. It is interesting that the electrode experiences almost the same amount of strain generation during Na and K ion intercalation when the same number of ions are inserted into or removed from the electrode structure. We, again, calculated the strain rates during Li, Na and K intercalation into the electrode structure. Similar to the first cycle, the strain rate continuously increased during K ion intercalation at the 4th discharge cycle. However,
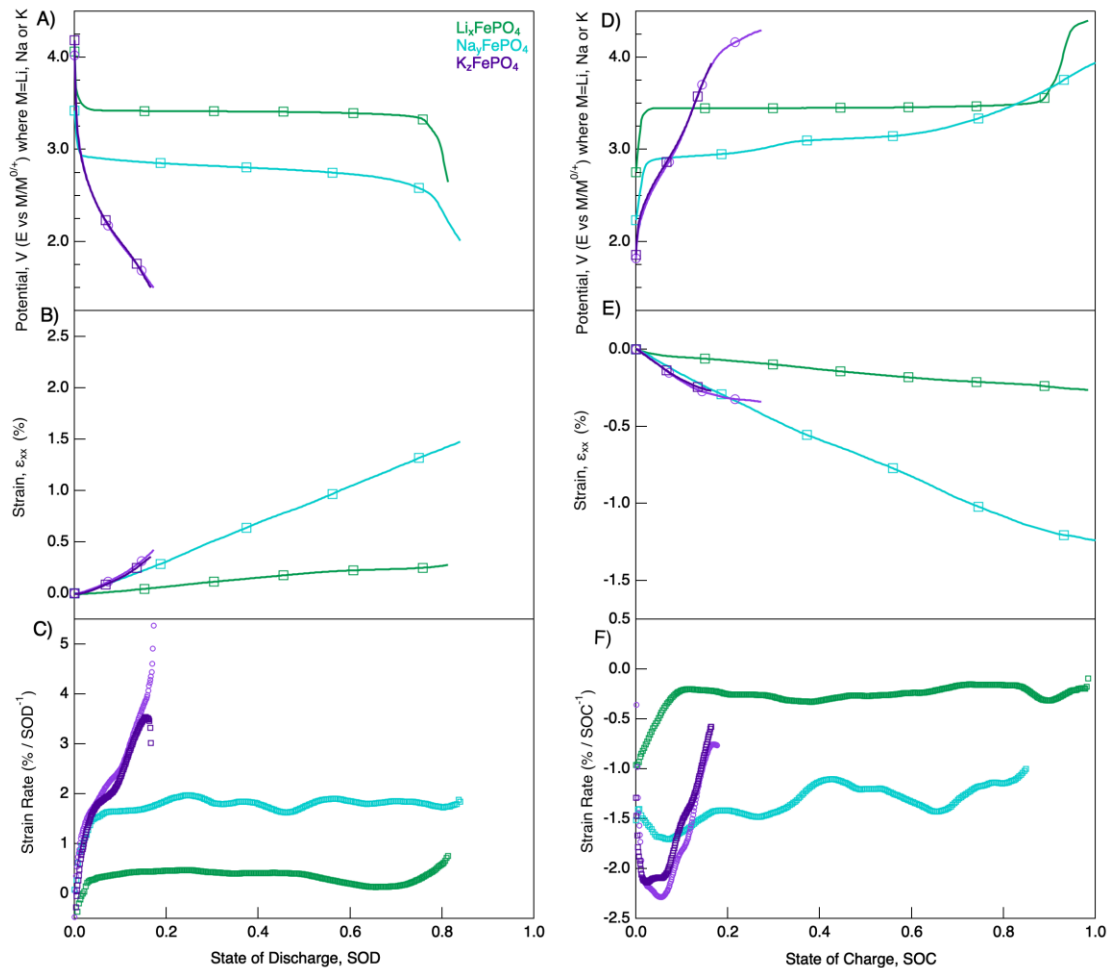
Figure 28. Potential evolution, strain generation and strain rates with respect to state of discharge (A, B, C) and charge (D, E, F) of Li (green), Na (blue) and K (purple) ions into FePO$_4$ electrode during the fourth cycle. The square and spherical symbol show when electrode is cycled either in EC:DMC or EC:PC solvents, respectively.

the values of calculated strain rates were almost constant during charge / discharge cycles of Li and Na ions in the electrode. Strain rates during K ion intercalation clearly demonstrated a major difference in comparison with strain rates during Li and Na intercalation into iron phosphate electrode.

Overall, lithium intercalation into the iron phosphate results in the least strain generation in the electrode structure compared to the Na$^+$ ion and K$^+$ ion intercalation. This behavior was expected as the Li ions is the smallest in ionic size, therefore results in less expansion in the crystalline structure during discharge. During the first discharge, Na ion intercalation in the crystalline iron

phosphate resulted in a steady increase in strain rate, which becomes almost 3.5%-SOD^{-1} at the end of the first discharge. Surprisingly, the rate of strains at the end of the first discharge was very similar upon Na and K ion intercalation. In the subsequent cycles, Na-ion intercalation cause much larger strains in the electrode due to larger discharge capacities in comparison with K-ion intercalation. The strain rates were almost constant around 2%-SOD^{-1} in the subsequent discharge cycles during Na insertion. This is quite interesting behavior. Previously, Xiang et al.[20] reported a loss of crystallinity in the iron phosphate electrode during the first discharge cycle by *in situ* XRD measurements supported by ex-situ TEM analysis. They associated the loss of crystallinity in the first discharge cycle to the formation of amorphous phases in the iron phosphate electrode. Beyond the first discharge cycle, their XRD analysis demonstrated the preservation of crystallinity in the iron phosphate electrode[20]. This study is well-aligned with our results with the progressive strain rate evolution only observed during the first discharge of Na ion intercalation. In the case of K ion intercalation, the steady increase in the strain rates are observed in the subsequent cycles too. XRD studies on K ion intercalation into iron phosphate demonstrated amorphization in the crystalline structure[96,115]. Therefore, progressive evolution of the strain rates in the electrodes is likely due to the occurrence of plastic deformation in the electrode structure. Constant strain rates during Li and Na intercalation can be interpreted as preserving crystalline structure while removing these ions from the host structure. Sharp changes in strain rates during K insertion and removal from the electrode results in a state-of-charge (discharge) dependent nonlinear strain evolution and deformations in the electrode.

6.3.3 Potential-Dependent Mechanical Behavior

To further elucidate the difference between the electrochemical deformation behaviors observed in the electrodes, we further investigated the redox chemistry and associated mechanical deformations in the electrode. Capacity and strain derivatives in the FePO$_4$ electrode during Li, Na and K intercalation were calculated to evaluate electrochemical reaction processes and structural changes

in the electrode. The derivatives in the first two cycles are shown in **Figure 29**. Strain and capacity derivatives during the 3rd and 4th cycles are shown in the **Figure C7**. The electrochemical potentials in Na and K ion batteries were measured against the reduction potential of Na and K metals.

Capacity and strain derivative analyses demonstrated the fundamental differences in intercalation mechanism of Li-ion, Na-ion and K-ion into iron phosphate. During Li and Na intercalation, the shape and location of strain derivative curves are almost identical to the capacity derivatives during the four cycles. Capacity and strain derivative peaks during Li and Na intercalation occurred at potentials where redox reactions and associated phase transformations in the electrode structure have been reported before[67,68]. Reversible behavior of the derivatives in each cycle suggests that the redox potentials do not change significantly over the subsequent cycles. Li-ion intercalation
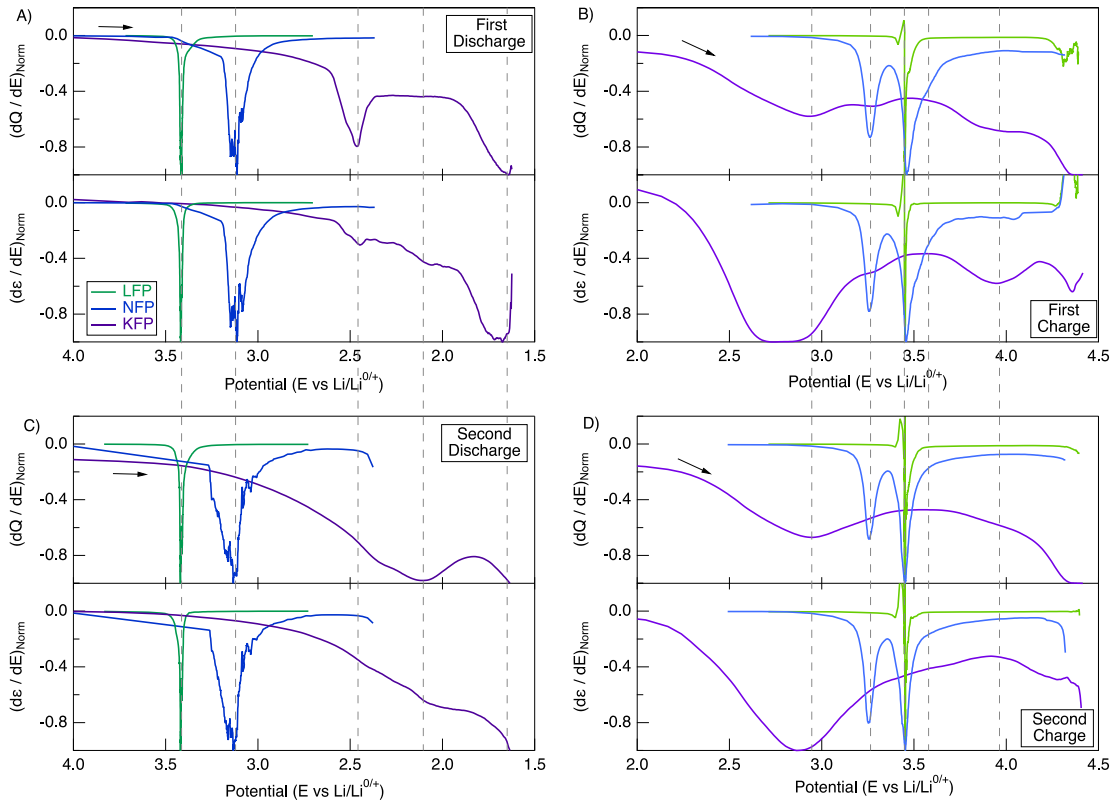
Figure 29. Normalized derivatives of capacity (dQ/dE) and strains (de/dE) with respect to potential for intercalation of Li (green), Na (blue) and K (purple) ions into FePO$_4$ during 1st (A, B) and 2nd (C, D) discharge and charge cycles. Derivatives are normalized by dividing the maximum nominal values in each charge and discharge cycles.

took place in a narrow potential range as demonstrated by sharp capacity and strain derivatives in **Figure 29**. The observation of broader peaks in capacity and strain derivatives during Na-ion intercalation suggests the slower intercalation in comparison to Li-ions. In the case of K ion intercalation, there was a significant difference in terms of the evolution of capacity and strain derivatives. First, irreversible derivative peaks of strain and capacity derivative peaks were observed during the first discharge of K ions at around 2.3V and 1.55V. In the subsequent discharge cycles, very broad capacity peaks were observed at around 1.9V. Strain derivatives did not show any characteristic peaks except change in the rate of strain derivatives at around 1.9V. This behavior suggests the structural resistance towards the intercalation of K-ions into iron phosphate. During the charge cycles and upon K ion extraction from the electrode, broad capacity and strain derivative peaks were observed at around 2.75V during the extraction of K ions from the electrode. A well-defined and reversible derivative peak during extraction of K ions points to the slower reaction kinetics during the phase transformation in the electrode structure.

6.4 Conclusion

In this work, we compared the electrochemical and mechanical response of the iron phosphate cathodes upon Li, Na and K ion intercalation by using electrochemical techniques and *in situ* digital image correlation. Iron phosphate model electrodes were prepared by electrochemical displacement technique in order to ensure identical morphology, structure and chemistry in the pristine iron phosphate electrodes. Strain evolution during Li and Na intercalation results in more linear dependence on the state of charge / discharge with the exception of the first discharge cycle of Na ions. However, strains generated in the electrode shows nonlinear behavior during insertion / extraction of K ions. When the same amount of K and Na ions were intercalated, similar chemo-mechanical expansions were observed. When the same amount of ions are intercalated into the electrode, the least volumetric expansions were observed for Li-ion insertion. The electrode experienced larger magnitudes of strains upon Na ion intercalation at the end of discharge cycles.

However, strain rate calculations showed that K ion intercalation results in a progressive increase in the strain rate, whereas Li and Na intercalation induce nearly constant strain rates. Potential-dependent behaviors also demonstrate more sluggish redox reactions during K intercalation, compared to the Li and Na intercalation. Our results shows that strain rates are critical factor for the amorphization of the crystalline securer, rather than the absolute value of electrochemical strains. These observations provide a fundamental insight into the impact of alkali ions on the redox chemistry and associated chemo-mechanical deformations.

CHAPTER VII

ELUCIDATING CYCLING RATE-DEPENDENT ELECTROCHEMICAL STRAINS IN

SODIUM IRON PHOSPHATE CATHODES FOR Na-ION BATTERIES

Bertan Özdogru,‡[1] Hannah Dykes,‡[1] Darrell Gregory,[1] Damien Saurel,[2] Vijayakumar

Murugesan,[3] Montse Casas-Cabanas[2] and Ö. Özgür Çapraz[1]

1) The School of Chemical Engineering, Oklahoma State University, Stillwater, OK 74078.

2) CIC EnergiGUNE, Parque Tecnológico de Álava, 01510, Vitoria-Gasteiz, Álava, Spain

3) Joint Center for Energy Storage Research (JCESR), Pacific Northwest National Laboratory,

902 Battelle Blvd, Richland, WA 99354

‡: These authors contributed equally to this work.

Note: This article first published in *Journal of Power Sources 507 (2021): 230297.* Both Hannah
Dykes and I are first authors on this paper. I have prepared slurries and perform the strain
measurements. The galvanostatic intermittent titration measurement (GITT) was performed by
Darrell Gregory. Mathematical modelling of the spherical cathode particle was performed by
Hannah Dykes. Ömer Özgür Çapraz conceived the idea and supervised the work.

ABSTRACT

Battery electrodes materials undergo significant mechanical instabilities which affects their longevity and exert rate-limitations during the cycling process. In this study, we investigate the rate-dependent mechanical response of sodium iron phosphate ($NaFePO_4$, NFP) cathodes during Na intercalation via galvanostatic cycling at different rates by employing digital image correlation, electrochemical methods, and mathematical model. The mechanical behavior of the electrode shows strong dependance on the applied scan rate. At slower rates, electrode shows asymmetrical strain generation between anodic and cathodic cycles, which is attributed to the formation of cathode-electrolyte interface layers. The electrode undergoes smaller strain generation when cycled at slower rates when the same amount of Na ions is removed or inserted into the electrode. A mathematical model was developed to predict strain evolution in the composite electrode as well as the concentration profile of the Na ions in the electrode particles. Rate-dependent and time-dependent factors on the strain generation in the electrode are attributed to the capacity-dependent intercalation strains, rate-dependent mismatch strains, and time-dependent irreversible strains. The combination of in situ strain measurements with the analytical model provided new insight into the electrochemically induced mechanical deformations in Na-ion cathode electrodes.

7.1 Introduction

Recent concerns revolving around the relative scarcity and cost of lithium have resulted in increasing interest in rechargeable Na-ion batteries[116,117]. Sodium is a far more abundant material than lithium and is more evenly distributed throughout the earth crust[118]. However, Na-ion batteries suffer from low-capacity retention due to chemo-mechanical degradations in the electrodes such as the decomposition of organic electrolytes on the surface of the electrode, continuous volumetric changes in the electrode constrained by current collectors, and mechanical damages in the electrodes[14,119]. Organic electrolytes decompose on the electrode surface during ion intercalation, causing the formation of a resistive surface layer on the electrode. Phase transitions commonly occur as Na ions intercalate into or out of the host lattice which creates volume mismatches. The associated misfit strains can produce plastic deformation or amorphization in the electrode material and have negative impacts on reversible ion insertion and extraction processes[20,120]. These chemo-mechanical degradations can be further exacerbated by the larger ionic radius of Na cations (1.02 Å) and their reactivity towards electrolyte species[53]. Also, it is expected that a cathode electrode would be prone to mechanical deformations during Na ion intercalation at faster rates due to kinetic limitation associated with slower Na ion diffusion. Although these chemo-mechanical deformations have been intensively reported for Li-ion battery electrodes, the physical response of the electrode upon Na intercalation is expected to be different than ones during Li intercalation. Therefore, further studies are required to understand the impact of the Na ions on the mechanical stability of electrodes.

Structural and interfacial instabilities in Li-ion battery electrodes have been studied by using an analytical mathematical model and various advanced characterization techniques such as electron microscopy[121–128], atomic force microscopy[129–133], in-situ XRD, and X-ray tomography[134–136], dilatometry[137,138], digital image correlation[36,107], and *in-situ* curvature measurements[139,140]. Transport-mechanics couplings in the electrified interfaces and bulk behavior of battery electrodes

have been investigated by developing a continuum-based model for Li-ion batteries. These models enable the prediction of intercalation behavior of Li-ions under various factors such as surface tension, scan-rate, and morphology of the electrode[22,141–146]. The physical response of the Li-ion battery electrodes due to chemo-mechanical deformations has been characterized experimentally by monitoring stress and strain evolutions in the electrode via digital image correlation and curvature measurements. These in situ mechanical measurements shed light on complex reaction processes controlling the stability of electrode structure as well as its surface with electrolyte[36,107,139,140,147]. However, chemo-mechanical instabilities associated with interfacial and structural deformations in the cathode electrodes during Na ion intercalation are not well known.

In this study, we chose sodium iron phosphate cathode to study rate-dependent and time-dependent deformations by utilizing in situ electrochemical strains, electrochemical techniques, and a mathematical model. Olivine-type sodium iron phosphate ($NaFePO_4$, NFP) is structurally analogous to the Lithium iron phosphate ($LiFePO_4$, LFP) electrode, which is an inexpensive and environmentally benign cathode material widely used in commercial Li-ion batteries. Due to the performance of the iron phosphate framework in Li-ion batteries, NFP has attracted much attention as a cathode electrode for Na-ion batteries. NFP has a theoretical capacity of 154 mAh g^{-1}. Michaelis group investigated the intercalation kinetics and electrochemical performance of NFP by using the electrochemical displacement technique[67,68]. Casas-Cabanas group monitored reaction mechanisms and associated structural deformations in the NFP electrodes via in situ x-ray diffractions[32,48,54,64,79]. Previously, we developed a methodology to tackle in situ electrochemical strain evolution in sodium iron phosphate electrodes using digital image correlation[107].

The goal of the study is to explore the rate and time effect on the mechanical behavior of the composite sodium iron phosphate cathode. To achieve it, we experimentally monitor in situ strain evolution in the electrode at different rates. In situ strains are monitored using the optical, full-field digital image correlation (DIC) technique. As expected, sodium intercalation causes volumetric

expansions in the composite electrode and the volume of the electrode shrinks during the removal of Na ions. Although a large amount of the irreversible strain was detected during the first cycle, strains become reversible in the subsequent cycles. Noticeably larger expansions are observed in the composite electrode when cycled at faster scan rates. Strain evolution in the composite electrode is predicted based on the elastic properties of the composite electrode and atomic-scale changes in the crystal structures. Concentration gradients and mismatch strains inside the particles are also predicted based on the transport model. The experimental and modeling studies demonstrate the mechanical penalty in the $NaFePO_4$ composite electrode at faster rates.

7.2 Materials and Methods

7.2.1 Material Preparation

Composite electrodes and electrolytes were prepared by following the procedure described previously[107]. Briefly, sodium carboxymethyl cellulose (binder, CMC, average MW ~700,000, Aldrich) and ultra-pure water mixed with 1:40 mass ratio and homogenized. Then, lithium iron phosphate (active material, LFP, Hanwha Chemical) and Super P (conductive additive, carbon black, >99%, metal basis, Alfa Aesar) were added to the above solution. The average particle size of LFP used in the study was 250 nm, determined by SEM. Final LFP: SuperP: CMC: Water mass ratio was 8:1:1:40. This slurry was mixed for 30 minutes with Thinky centrifugal mixer at 2000 rpm until completely homogenizes. To prepare the free-standing electrodes, the slurry was cast on copper foil (9 µm thick, >99.99%, MTI) and a doctor blade was used to control the slurry thickness. The casted slurry was air-dried ad ambient condition for 16 h. Dried electrodes are carefully removed from the surface to create the free-standing electrodes used in the strain measurements. For coin cell and GITT measurements, the same slurry was prepared, and it was cast on aluminum foil (15 µm thick, MTI) with a doctor blade and air-dried for 16 h.

The electrolyte solution was prepared inside a glove box under an argon atmosphere (MB-Unilab Pro SP, MBRAUN). Oxygen and water contents were kept below 1 ppm all the time. Ethylene carbonate (EC, anhydrous, 99%, Acros Organics) and dimethyl carbonate (DMC, anhydrous, >99%, Aldrich) were mixed in a 1:1 volume ratio. 1 M sodium perchlorate ($NaClO_4$, ACS grade, >98%, Aldrich) was added to the above EC/DMC solution.

Sodium cubes immersed in mineral oil (Na, 99.9%, metal basis, Sigma Aldrich) were cleaned with hexane inside the glove box. Cleaned Na cubes were stored in 1:1 (v:v) EC:DMC solution for future use. Before studies, Na cubes were removed from the solvent solution and dried with filter paper. A stainless-steel scalpel is used to clean the oxidized surface. The cleaned piece was then placed inside a polyethylene bag and rolled into the shape of a foil using a rolling pin. Flattened Na foil was then placed into the battery cell as a counter electrode.

7.2.2 Electrochemical Cycling

Electrochemical displacement technique was used to form iron phosphate (FP) composite electrode using pristine LFP composite electrode[67,68,107]. Electrochemical delithiation of the pristine LFP electrode was done by applying a positive current at C/10 rate to 4.0 V vs Na counter electrode. FP composite electrodes were cycled against Na counter electrode in 1 M NaClO4 in 1:1 (v:v) EC:DMC electrolyte between 2.0-4.0 V. We provided further details of the electrochemical displacement technique in the Supplementary information by conducting X-ray diffraction analysis and in situ strain measurements. The electrodes were cycled at C/25, C/10, C/4 and 1C rates. GITT measurements were carried out using a custom Swagelok coin cell system. Pristine LFP electrode cast on aluminum foil assembled into the custom cell with or Na counter electrode and electrolyte. A Celgrad 2044 polymer separator was used to separate both electrodes. Before GITT measurements, cells were cycled at a C/10 rate for 5 cycles. GITT measurements carried out with a series of current pulses at C/25 for 1 h, followed by a 10 h relaxation period.

7.2.3 Strain Measurements

A detailed description of the custom battery cell was provided in our previous publications[37]. Polychlorotrifluoroethylene (PCTFE, Plastics International) was used to make the main body of the custom battery cell and the electrode holders. Optical access was achieved by a quartz window (99.995 % SiO2, 1/16 in thick, 2 in diameter, McMaster-Carr). This window was placed on the top of the custom cell and Viton O-rings (Grainger) used to seal the cell. Strain analysis was conducted by taking images of the freestanding electrode throughout the electrochemical cycling periods. Grasshopper3 5.0 MP camera (Sony IMX250, resolution, 2448 (w)*2048(h) pixel) with 12.0X adjustable zoom lens (NAVITAR) for an effective resolution of 0.873 µm/pixel was used for image capture. Illumination of the freestanding electrode was achieved with a single constant high-intensity LED light source (Amazon). Depending on the cycling rate, images were captured every 10 min, 2 min, and 0.25 min for galvanostatic cycling at C/25, C/10, and C rates, respectively. A lab-made LabVIEW program was used to capture the images. The natural speckle pattern of the LFP composite electrode was used to calculate the strain generation on the electrode using Digital Image Correlation (DIC). Full-field strain measurements were performed on an area of interest of 750 µm(w) x 500 µm(h) using Vic2D software with a subset size of 111 x 111 pixels and a step size of 15. Strains were synchronized with the electrochemical response of the electrodes (current and voltage) using a lab-made MATLAB program.

7.3 Results and Discussion

7.3.1 Representative Electrode Response during Na$^+$ ion Intercalation

Figure 30A shows the representative electrochemical behavior of a sodium iron phosphate (NFP) composite electrode cycled galvanostatically at a C/25 rate against a sodium counter electrode for four cycles. Iron phosphate composite electrodes were formed by electrochemical displacement of Li ions from pristine lithium iron phosphate composite electrode using the methodology described
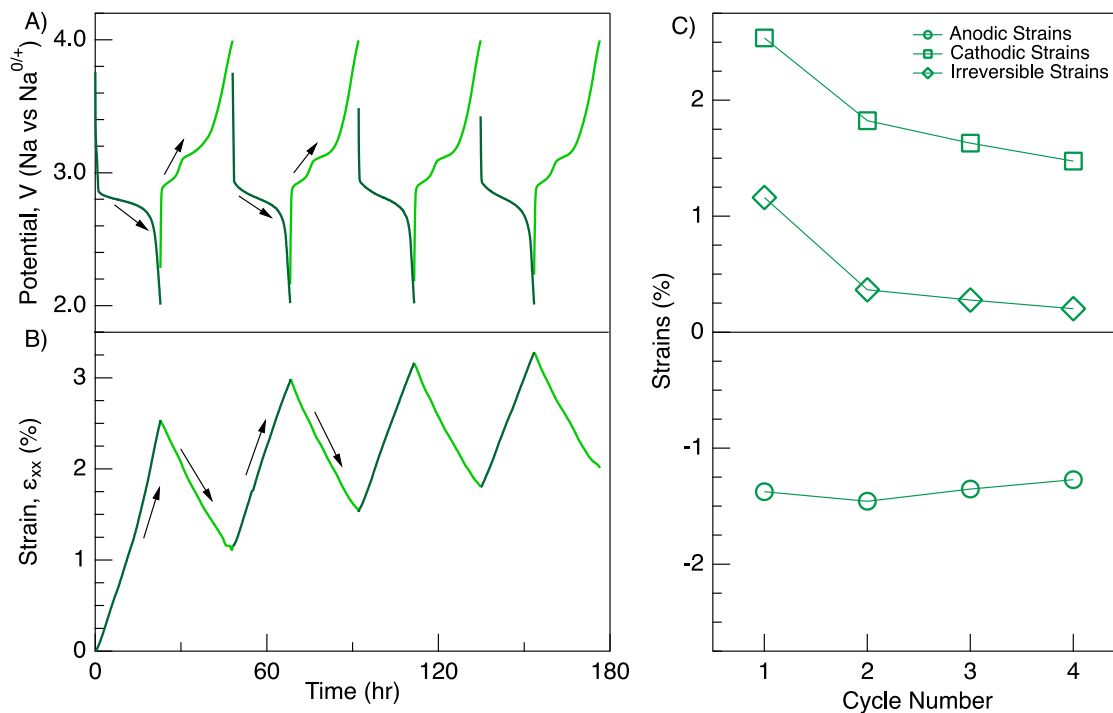
Figure 30. A) Voltage and B) strain evolution in iron phosphate composite electrode during sodium intercalation cycled at C/25 in 1 M NaClO$_4$ in EC/DMC electrolyte. C) Corresponding anodic, cathodic, and irreversible strain generations.

in our previous publication[107]. Voltage and strain evolution during electrochemical delithiation of pristine LFP and resulting crystalline structure change can be seen in **Figure D1**. The sodiation of the iron phosphate in the first discharge resulted in 144mAh g^{-1} discharge capacity, which is close to the theoretical capacity of sodium iron phosphate (154 mAh g^{-1})[67,68]. The electrode showed a very flat potential plateau around 2.85V during the sodiation of iron phosphate in the first discharge. The discharge capacity decreased to 138 and 130 mAh g^{-1} in the second and fourth discharge cycles. Charge capacities during the first, second, and fourth cycles were calculated to be 174, 164, and 158 mAh g^{-1}, respectively. Two distinct potential plateaus at around 2.88 and 3.10 V were recorded during the first charge (desodiation). The evolution of the potential plateaus in the subsequent cycles were like the first cycle. A similar potential response during Na ion intercalation of NaFePO$_4$ electrodes via galvanostatic cycling was reported in the literature[67,68].

The corresponding strain evolution in the sodium iron phosphate composite electrode cycled at C/25 rate is shown in **Figure 30**B. Electrochemical strains demonstrated a linear relationship with galvanostatic charge/discharge time at all cycle numbers. As expected, electrochemical strains increased and decreased during the discharge and charge cycles, respectively. Strains were categorized as "anodic", "cathodic" and "irreversible strain" to evaluate their progression with cycle numbers[107]. Anodic and cathodic strain values were shifted to start from zero at the beginning of each charge/discharge cycle to calculate strain generation in each cycle. The strain value at each cycle was labeled as "irreversible strain" and it was calculated by subtracting the cathodic strain from anodic strains for each cycle. During the first discharge cycle, the insertion of Na ions into iron phosphate resulted in 2.43% volume expansion in the NFP composite electrode. Cathodic strain progressively decreased from 2.43% at 1st discharge to 1.48% at 2nd discharge. The cathodic strains became 1.34 and 1.26% at the end of the 3rd and 4th discharge cycle, respectively. The removal of Na ions during the first charge cycle caused a reduction in electrode volume, generating about $-1.34 \pm 0.1\%$ anodic strain in the first charge cycle. However, there is an asymmetrical strain evolution in magnitude between charge and discharge cycles, causing mechanical irreversibility between anodic and cathodic cycles. At the end of the first cycle, the electrode did not return to its original size, which results in 1.16% irreversible strains. In the subsequent cycles, the generation of the irreversible strains at each cycle reduced slowly from 0.36% at the end of the second cycle to 0.20 % at the end of the fourth cycle.

Strain and capacity derivatives with respect to potential are calculated to investigate the reversible changes in the electrode during Na ion intercalation. The angstrom-scale changes in the electrode structure during metal ion intercalation induce macroscale volumetric expansions in the composite electrode. Previous studies demonstrated a good correlation between phase transformations and the evolution of potential-dependent strain rates in the composite graphite, lithium iron phosphate, and lithium manganese oxide electrodes for Li-ion batteries[33,34,38,44,107]. The location of strain derivative

peaks in these studies matches very well with the current peaks in cyclic voltammetry or the capacity derivative peaks in galvanostatic cycling. Similar to the previous studies, the strain derivatives, $d\varepsilon/dE$ and capacity derivatives, dQ/dE were calculated with respect to potential. **Figure 31** shows strain and capacity derivatives during fourth charge and discharge cycles at C/25 rate. Two characteristic peaks in capacity derivatives are observed during fourth charge cycle at 2.92 and 3.11 V in **Figure 31**. A well-defined two peaks in the strain derivative matches with the corresponding peaks in the capacity derivative within ±0.02 V. Two peaks in the capacity derivatives correspond to the appearance of intermediate $Na_{0.7}FePO_4$ during transition of $NaFePO_4$ phase to $FePO_4$ phase[20,32,48]. A similar evolution in strain and capacity derivatives is also observed in the earlier desodiation cycles too (**Figure D5**). During discharge, two overlapping 2-phase reactions $FePO_4$ - $Na_{2/3}FePO_4$ and $Na_{2/3}FePO_4$ – $NaFePO_4$ take place in potentials close to each other, therefore they merged into a single plateau with the overlap of the two reactions, leading to
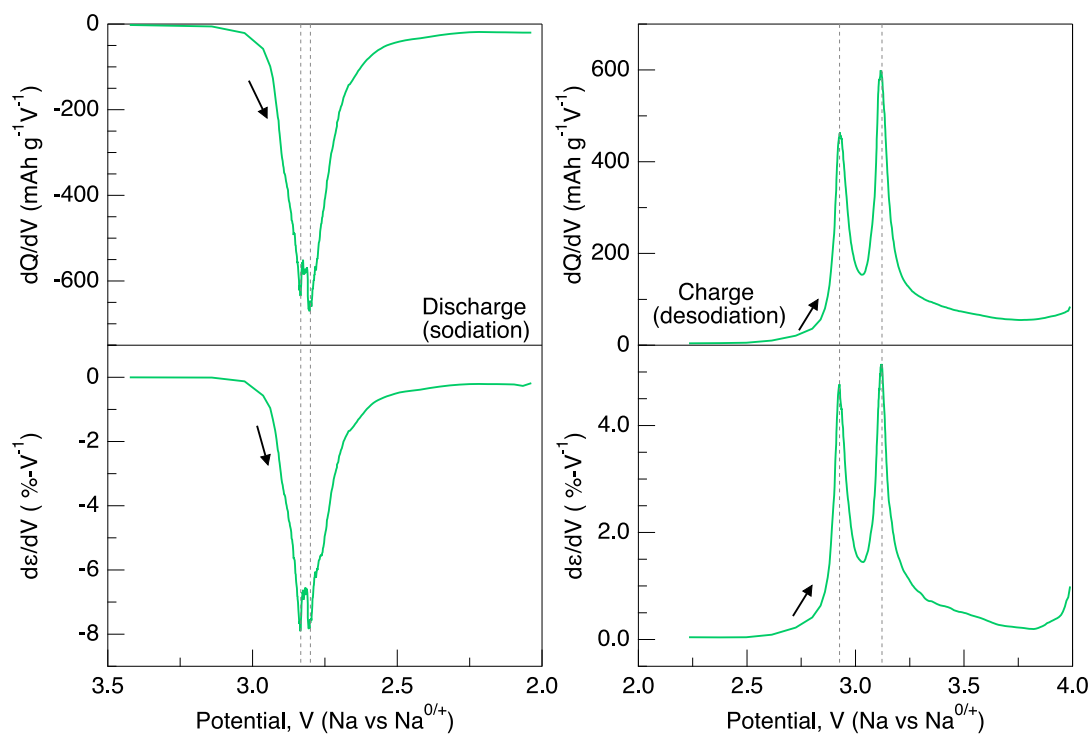
Figure 31. Capacity derivatives and strain derivatives in $NaFePO_4$ composite electrode cycled at C/25 during sodiation (left size) and desodiation (right side) in 1 M $NaClO_4$ in EC/DMC electrolyte during 4th cycle.

3 phase coexistence at half discharge[32,54,64]. Our measurements at a slow rate showed that there are almost two capacity and strain peaks observed during the fourth discharge cycle in 2.80 and 2.84 V, and these peaks were separated with a very narrow potential window.

In general, the electrode experiences reversible and irreversible deformations during Na ion intercalation. The irreversible physical response of the electrodes has been attributed to the formation of cathode – electrolyte interface (CEI), the dissolution of transition metal ions, and the generation of defects in the crystalline structure[14,119]. Reversible deformations in the Na-ion electrodes are correlated with the changing lattice parameters as alkali metal ions are intercalated into and deintercalated from the electrode[104,107]. In the next section, the role of scan rate and intercalation time on the physical response of the sodium iron phosphate electrode is investigated to elaborate these reversible and irreversible changes in the sodium iron phosphate electrode. We will discuss how rate and intercalation time impacts the irreversible behavior of electrode as well as intercalation mechanics.

7.3.2 Electrochemical Strain Generation at Different C-Rates

NFP cathodes were cycled at C/10, C/4, 1C and 2C scan rates while monitoring in situ strain evolutions in the composite electrode (**Figure D4**). Single potential plateaus are observed during the insertion of Na ions at 2.82, 2.68, and 2.44 V for C/10, C/4, and 1C rates, respectively. There was no clear potential plateau observed for the electrode cycled at 2C rate, it is likely due to the low charge / discharge capacity of the electrode when cycled at 2C rate. Discharge capacities in the first cycle were 142, 125, 83.9 and 20.4 mAh g^{-1} at C/10, C/4, 1C and 2C rates, respectively. Two distinct potential plateaus were clearly observed when the electrode was charged at C/10 and C/4 rates. These two potential plateaus are corresponding to the appearance of intermediate Na$_{0.7}$FePO$_4$ during the transition of the NaFePO$_4$ phase to FePO$_4$ phase[20,32,48]. However, these potential plateaus became less pronounced in the subsequent cycles when the electrode is cycled at

a 1C and 2C rates rate (**Figure D2** and **Figure D3**). The overpotential is calculated by subtracting

a potential at beginning of the first plateau during charge (marked with circle times symbol on the

Figure D4) from the potential at the beginning of the single plateau during discharge (marked with

asterisk symbol on the **Figure D4**). The overpotential in the first cycle were 0.02, 0.10, 0.27, 0.65

and 1.03V at C/25, C/10, C/4, 1C and 2C rates, respectively. The increase in potential hysteresis at

higher scan rates has been observed for other cathode materials during Li and Na intercalation[148,149].

Previous experimental studies, as well as mathematical models also showed the increase in the

overpotential with increasing scan rates[48,52,150]. For sodium, both reaction kinetics and diffusion

rates are sluggish compared to lithium. This, in turn, increases the overpotentials required to insert

or remove sodium from the $FePO_4$ structure, especially at higher scan rates.

Figure D4 shows the electrochemical strain evolution in the composite sodium iron phosphate

electrode cycled at C/10, C/4, 1C and 2C rates. Electrochemical strains demonstrated a linear

relationship with galvanostatic charging / discharging at all different scan rates. The progression of

anodic, cathodic, and irreversible strain generation with cycle numbers at different scan rates are

plotted in **Figure 32**. The cathodic strain became 2.31, 2.25, 1.27% and 0.28% at the end of the

first discharge cycle at C/10, C/4, 1C and 2C rates, respectively. During the first charge cycle, -

1.31, -1.22, -0.57%   and -0.15% anodic strains are generated at C/10, C/4, 1C and 2C rates,

respectively. In the subsequent cycles, the average anodic strains became -0.46, -1.05, and -1.16%

within the margin of 0.02% at C/10, C/4, and 1C rates, respectively. Like C/25 rate, slightly

asymmetrical strain evolution in magnitude was detected between charge and discharge cycles

when the electrode cycled at C/10. Interestingly, the cathodic and anodic strain increased by the

cycle number at 2C rate with cycle number, while irreversible strains was below 0.1%. Irreversible

strains at the end of the first cycle were 1.00, 1.03, 0.70 and 0.13% at C/10, C/4, 1C and 2C rates,

respectively. Irreversible strains decreased rapidly in the subsequent cycles. The generated

irreversible strains in the third cycle were 0.19, 0.13, 0.05% and 0.05% for C/10, C/4, 1C and 2C rates, respectively.
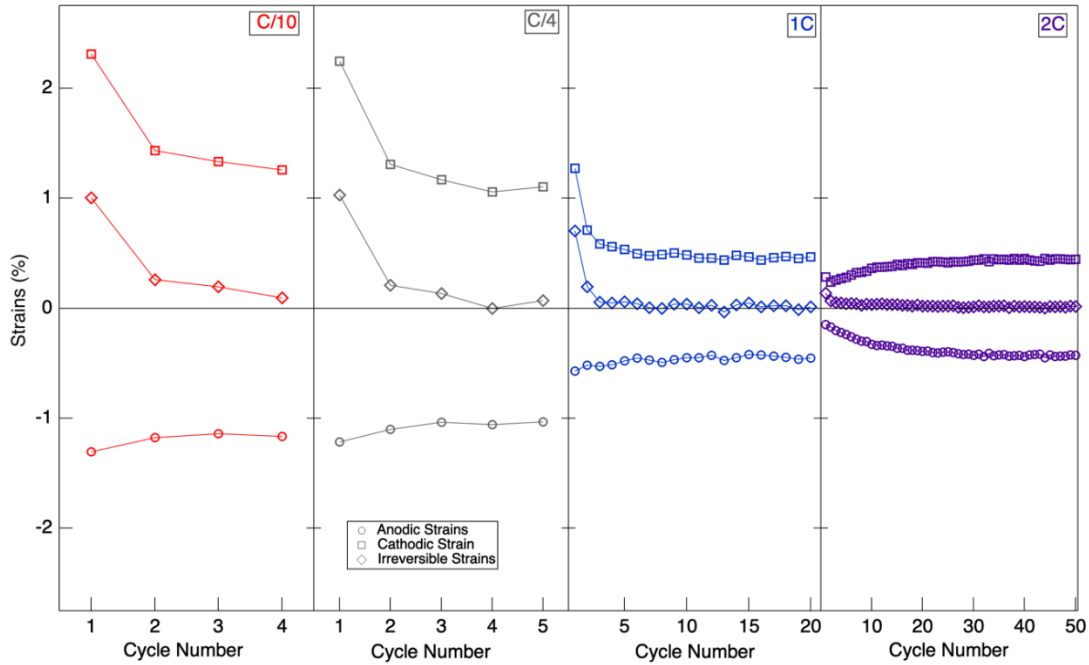
Figure 32. Anodic, cathodic, and irreversible strain at C/10 (red color), C/4 (grey color), 1C (blue color) and 2C (purple) rates.

The total amount of sodium ions displaced during cycling directly influences the strain evolution in the electrode. Previous studies on Li-ion electrodes showed a linear relationship between the capacity and strain evolution in graphite anode and lithium manganese oxide cathode materials[34,38]. In situ stress and XRD studies on lithium manganese oxide[35] graphite[151], lithium cobalt oxide[152], and lithium iron phosphate[32] showed the linear relationship between capacity and physical response of electrodes. To better understand the rate-dependent strain generation in the composite sodium iron phosphate cathode, electrochemical strains during the fourth charge and discharge cycles at different rates are plotted with respect to capacity in **Figure 33**. Strain values were shifted to zero at the beginning of each charge and discharge cycle to calculate strain generation in each cycle. The strain increases almost linearly with respect to charge and discharge capacities at all scan rates. However, the rate of the electrochemical strains with respect to capacity depends on the applied scan rate. For example, when the sodium ions are intercalated into the electrode until the discharge
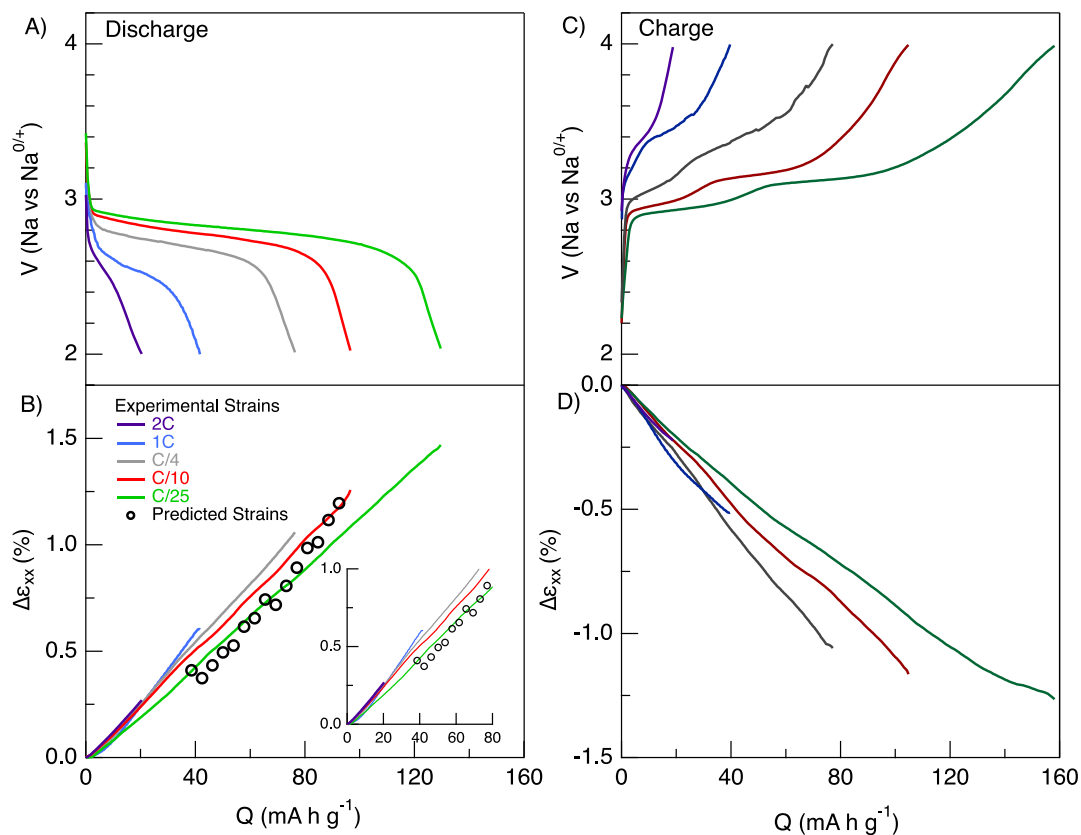
Figure 33. Voltage and strain evolution in iron phosphate composite electrode during sodium intercalation in 1 M NaClO$_4$ in EC/DMC electrolyte at different scan rates during the 4th cycle. Dotted points indicate the predicted strains calculated from the mathematical model.

capacity becomes 40 mAh g^{-1}, the composite electrode expands 0.426, 0.505, 0.540, and 0.589% when cycled at C/25, C/10, C/4, and 1C rates, respectively. The slope of the strains with respect to the state of discharge (SOD) is calculated as 1.75, 1.99, 2.13, 2.04 and 2.25 at C/25, C/10, C/4, 1C and 2C rates, respectively. When considering the same charge capacity, the electrode volume also shrinks greater at faster rates. Strain and capacity relationships during the third cycle are also compared at different scan rates in the **Figure D10**. The distinct difference in the electrochemical strain evolution during charge is clearly observed for the third charge cycle too. The magnitude of electrochemical strains was slightly higher at faster rates in the third charge cycle. The electrode experience larger strains at faster scan rates although the same amount of sodium ions is inserted into or extracted from the electrode. However, it is important note that the additional strains at

higher rates compared to the slower rates are more pronounced during charge cycles compared to discharge cycles.

Overall, there are two distinct rate-dependent physical responses of the composite NFP electrode. The first one is asymmetrical strain evolution between charge and discharge cycles at slower rates. The electrode demonstrated a more symmetrical strain evolution between charge and discharge rates when cycled at faster rates, which leads to smaller irreversible strain generation in each cycle (**Figure 32**). Another distinct physical behavior of the electrode is the rate-dependent strains with respect to capacity. When the same amount of sodium is inserted into or removed from the electrode, the electrode undergoes larger volumetric changes at faster rates. To shed light on these discrepancies, we will discuss the possible factors, such as the progression of cathode-electrolyte interface (CEI) formation, and the transport-mechanics coupling of Na ions in the cathode particles, on the rate- and time-dependent electrochemical strains.

7.3.3 Progression of Irreversible Strains

Irreversible deformations in the electrodes have been attributed to the dissolution of transition metal from the structure of the electrode[153], vacancy formations in the crystalline structure, and the formation of CEI layers[21]. To differentiate these factors on the irreversible strains at different rates,
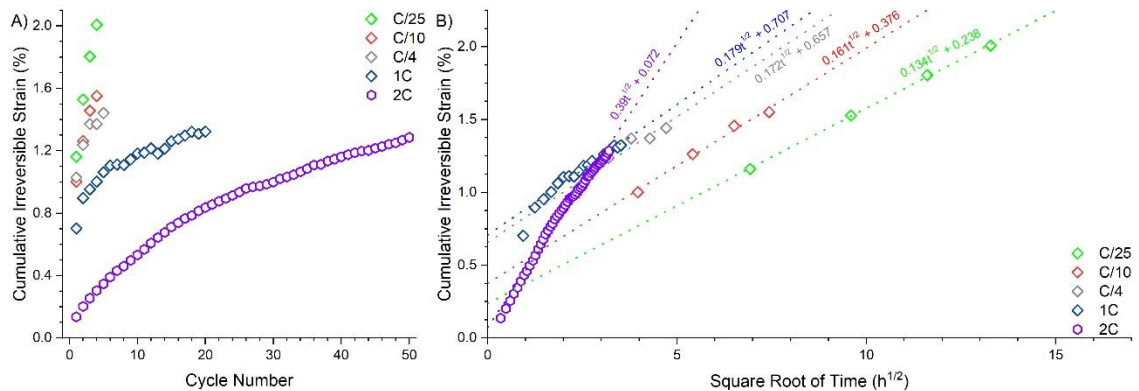
Figure 34. Cumulative irreversible strains in the composite NFP electrode cycled at 2C (purple), 1C (blue), C/4 (grey), C/10 (red), and C/25 (green) rates. The cumulative irreversible strains are plotted with respect to (A) cycle number and (B) square root of cycling time. Dash lines represent the fitted data with the fitted equation.

the cumulative irreversible strains were plotted with respect to cycle number (**Figure 34**A). If the dominant force on the irreversible deformation is the dissolution of iron metal from the $NaFePO_4$ structure, we expect to observe negative irreversible strains with increasing cycle numbers. Zhao et. al showed the reduction in strains in lithium manganese oxide cathodes due to the dissolution of manganese into electrolyte[154]. Since the cumulative irreversible strains increased with cycle number for all scan rates, it is unlikely that the dissolution of iron dominates the irreversible behavior in the sodium iron phosphate electrode.

Another factor contributing to irreversible deformation could be the formation of vacancies in the crystal structure of the electrode. Unexpected compressive stress generation was observed during the first delithiation cycle in lithium manganese oxide cathode[35] and the irreversible behavior was associated with the formation of oxygen vacancies in the electrode structure. Large irreversible strains were detected in the first cycle of lithium intercalation into lithium iron phosphate and lithium manganese oxide electrodes[37,107]. **Figure 34** demonstrates the large deformations only in the first cycle in sodium iron phosphate cathode at all scan rates. Although the generation of oxygen vacancies may contribute to the irreversible behavior of sodium iron phosphate in the first cycle, they are unlikely to cause the progressive evolution of irreversible strains with increasing cycle numbers.

The formation of cathode – electrolyte interface (CEI) layers is a well-known phenomenon causing irreversible deformation in the alkali-metal ion battery electrodes. Oxidation of electrolyte species at high voltages and interaction between electrolyte and cathode can cause the formation of organic and inorganic layers on the cathode surface[14,119]. Smith et al. previously demonstrated that the thickness of the solid-electrolyte interface layer increases approximately with the square root of time on graphite electrode in Li-ion batteries[155]. Cycle time and operational temperature dominate the solid-electrolyte interface growth rate, not the cycle number[155–157]. Also, a continuum-based mathematical model predicted the growth rate of solid-electrolyte interface layers with the square

root of time[158]. Previously, we observed a linear relationship between cumulative irreversible strains and the square root of time for graphite anode and lithium manganese oxide cathodes for Li-ion batteries. The irreversible strains were associated with the electrolyte decomposition on the surface of the electrodes[37,104].

To shed light on irreversible strains on the sodium iron phosphate electrode, the cumulative irreversible strains were plotted against the square root of time (**Figure 34**B). A linear relationship between cumulative irreversible strain generation and the square root of time is observed for all scan rates. Interestingly, the electrode undergoes larger cumulative irreversible strain generation at faster rates when cycled for the same amount of time. As a result, the rate of irreversible strain with respect to the square root of time increases from $0.134\ hr^{-0.5}$ at C/25 to $0.179\ hr^{-0.5}$ at 1C. The slope was calculated as $0.390\ hr^{-0.5}$ at 2C rate. Attia et al. also demonstrated a similar correlation between the rate of solid electrolyte interface growth and nominal C-rate for Li-ion graphite electrode[159].

If we assume that the growth of CEI layers on the electrode causes an overall increase in the size of the sodium iron phosphate particles, then this deformation on the electrode surface will lead to irreversible macroscopic expansions of the electrode. Based on this assumption, we previously estimated the thickness of the decomposition products for Li-ion graphite composite electrode using the following equation;

$$h_{CEI} = 0.5\ D_{particle}\varepsilon_{irr}$$

where h_{CEI}, $D_{particle}$, and ε_{irr} denote the thickness of the CEI layer, the original size of the particle diameter, and generated irreversible strains, respectively[104]. The average particle size in the composite sodium iron phosphate cathode is about 250 nm. With the given irreversible strains of 1-2% on the electrode, the thickness of the CEI layer is estimated to be ca. 1.25 – 2.5 nm. Previous studies based on X-ray photoelectron spectroscopy detected a few nanometer-thick layer of CEI on

lithium iron phosphate and nickel manganese cobalt oxide cathodes[156,160]. Therefore, the estimated thickness of CEI from the strain measurements is consistent with the experimentally measured CEI thickness.

To summarize this section, the irreversible strains increase linearly with the square root of time for all scan rates. This correlation between irreversible deformations and time suggests the contribution of the CEI growth on the irreversible strains. Since the rate of decomposition on the electrode surface is time-dependent, the irreversibility causes asymmetrical strain response between anodic and cathodic cycles at slower rates. The growth of the CEI layer contributes to irreversible positive strain evolution in the electrode. In addition to intercalation-induced strain, if the CEI growth is the only irreversible factor causing strains in the electrode, then it was expected to observe more positive strain generation during sodiation and less negative strains during desodiation at the slower rates, compared to the behavior of electrode cycled at faster rates because of the difference in intercalation time. However, this cannot simply explain the rate-dependent strain profiles observed in **Figure 33** and **Figure D10**. Local volume mismatch between separated phases in the electrode structure and mismatch strains due to rate-dependent concentration gradients in the electrode might also contribute to the rate-dependent strain behavior. In the following section, we will discuss the factor of diffusion-limitations at faster rates and their impact on the strain evolution in the electrode.

7.3.4 Predicted Strains in Composite Electrode

A typical composite electrode consists of active materials, conductive carbon, and polymeric binders. Conductive carbon and polymeric binders do not intercalate with ions, their function is to provide conductive network and mechanical strength in the composite electrodes[161,162]. During battery operation, electrochemical strains in the active materials during ion intercalation (e.g. $NaFePO_4$) governs the volumetric changes in the composite electrode. Previously, the expansions in the Li-ion battery composite electrodes were estimated by considering the volumetric changes

in the active particles and calculating the elastic properties of the composite electrode[163,164]. The model assumes that lithium ions are uniformly distributed in the active particles. The model only considers elastic and reversible deformations upon reversible Li^+ ion intercalation. Also, the impact of side reactions, defect formations, plastic deformations, and the formation of the cathode-electrolyte interface are not included in the model calculation. The individual active materials might show anisotropic behaviors, however, the randomly distributed active materials in the composite network leads to isotropic behaviors in the composite electrodes at the length scales considered in the model. The predicted strains showed good correlations with the experimentally measured composite strains in Li-ion batteries when the electrodes were cycled at slow scan rates[163,164]. Sodium-intercalation induced strain in the composite $NaFePO_4$ electrode is calculated by adjusting the previous composite model for Na-ion batteries. Strains in composite electrode, ϵ_{ce} is computed as,

$$\varepsilon_{ce} = \varepsilon_{NFP}\phi_{NFP} + \left(\frac{\varepsilon_{NFP}}{\frac{1}{K_{pm}} - \frac{1}{K_{NFP}}}\right)\left(\frac{1}{K_e} - \frac{1}{K_{average}}\right)$$

Elastic properties of the composite electrode such as bulk modulus, K, are calculated by using open cell theory for anisotropic porous solid end S-combining rule[165]. The volumetric fraction of the NFP particles, ϕ_{NFP}, in the composite electrode is calculated by measuring the porosity of the composite electrode. The model and porosity calculations are described in the supporting information. Calculation of the strains in the composite electrode requires information about the linear strains in the NFP particles, ε_{NFP}, during Na^+ ion intercalation. Changes in the lattice parameters can be used to calculate linear strains in the NFP particles. Previously, Casas-Cabanas and her group intensively investigated the structural changes in the olivine $NaFePO_4$ during charging / discharging by using synchrotron X-ray diffraction experiments[32,48,54,64,79]. The intensity of the low angle diffraction peaks of the phases, unit cell parameters and cell volumes is plotted

with respect to Na content in the electrode discharged at C/66 rate in **Figure D11** and **Figure D12** using the previously published XRD study[48]

Linear strain in the sodium iron phosphate electrodes was calculated from the changes in the cell volume of the electrode particles with respect to SOD. The predicted strains in the unconstrained composite electrode are compared with the experimentally measured strains during discharging at different scan rates in **Figure 33**B. In the calculations, the predicted strains were calculated between SOD of $0.25 - 0.65$ to avoid the three-phase region at around 0.65 state of discharge. The corresponding discharge capacity at 0.25 SOD is 38.5 mAh g^{-1}. The predicted strains were shifted by 0.41% to provide a better comparison with the experimentally measured strains. The model predictions resemble the experimentally measured strains at slow scan rates until discharge capacity becomes 80 mAh g^{-1}. Note that the model assumes uniform sodiation of the sodium iron phosphate electrode and it is incapable of incorporating possible mismatch strains associated with large concentration gradients at faster scan rates. We hypothesize that the diffusion-limited concentration profile of Na ions in the electrode particles causes mismatch strains at faster scan rates. To further investigate, we calculate the concentration gradients and mismatch strain profiles in the electrode particle using Fick's law.

7.3.5 Predicted Na Concentration and Mismatch Strains in the Electrode Particle

An analytical model based on Fick's law and elastic deformation was developed to stimulate the concentration profile of Li ions and stress generation in various shapes and orientations of Li-ion battery electrodes[22,120,142,143,166–168]. We adopted previous diffusion-mechanics models of Li-ion batteries into Na-ion batteries to compute the Na concentration gradient and mismatch strains in spherical $NaFePO_4$ particles. In the olivine $NaFePO_4$ structure, FeO_6 octahedra connect with neighbor FeO_6 by sharing corner in the ab plane, whereas PO_4 tetrahedra shares corners and edges with the FeO_6 octahedra. The structure provides open channels along the a-axis and b-axis for Na

ions. We consider a simple problem of diffusion of Na ions within the sphere shape of particles with the radius, r. From SEM images, the average radius of the particles was around 125 nm. The concentration of sodium in the particle is governed by time-dependent Fick's law[143];

$$\frac{\partial c}{\partial t} = \frac{D}{r^2}\frac{\partial}{\partial r}\left(r^2\frac{\partial c}{\partial r}\right)$$

The primary driving force for sodium diffusion is the concentration gradient. GITT measurements were performed to calculate the diffusion coefficient of the sodium in the $NaFePO_4$ particles (Supp. Information). The diffusion coefficient varies between $1 \times 10^{-14}\ cm^2/s$ and $1 \times 10^{-17}\ cm^2/s$ during intercalation of Na ions. In the calculations, we assume constant diffusivity of $2 \times 10^{-15}\ cm^2/s$ and the stress-induced diffusion is neglected. Initial and boundary conditions are given by;

$$C(r, 0) = 0 \text{ for } 0 \leq r \leq R$$

$$D\frac{\partial C(0,t)}{\partial t} = 0 \text{ for } t \geq 0$$

$$D\frac{\partial C(R,t)}{\partial t} = \frac{I}{F} \text{ for } t \geq 0$$

At the surface of the electrode, current density, I is constant under galvanostatic discharging and it can be defined with the galvanostatic discharge rate as $I = (C - rate)\frac{\alpha\rho R}{3}$ where α and ρ denote theoretical capacity and density of the electrode, respectively. The C-rate represents the amount of time it takes to discharge the battery with respect to its theoretical capacity. C_{max} is the maximum concentration of sodium in the $NaFePO_4$. In **Figure 33**, the state of discharge at the end of the discharge was 0.27, 0.50, 0.62, and 0.84 when the electrode was cycled at 1C, C/4, C/10, and C/25 rates, respectively. To simulate the concentration gradients and mismatch strains, the electrode particles are discharged until the average SOD in the particle reached the experimentally observed SOD for four different scan rates in **Figure 30** and the **Figure D4**. As a reference point, the

concentration profile of sodium is also computed when cycled at C/100 until 0.95 SOD. The

concentration profile of sodium inside the electrode particles is estimated by solving the partial

differential diffusion equation using the MATLAB PDEPE toolbox.

Figure 35 shows the distribution of sodium at different C-rates. At slower rates (C/100 and C/25),

sodium is almost uniformly distributed along the particle radius. When the scan rate increased

further, the concentration of sodium near the particle surface differs significantly from the

concentration in the center of the particles. As a result, a large sodium concentration gradient is
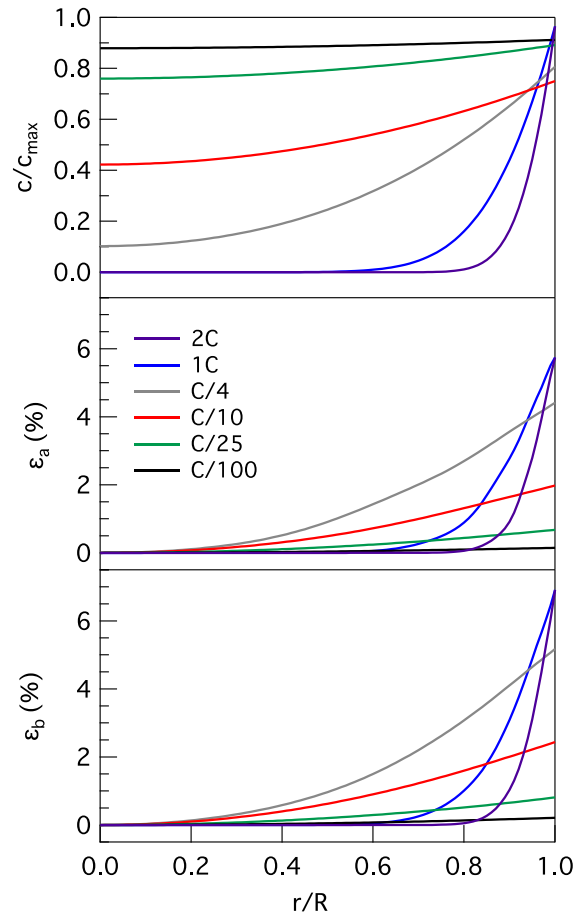
Figure 35. Na Concentration and Mismatch Strains in Electrode Particle: The sodium concentration profiles and the mismatch strains at five different scan rates. In the calculations, it is assumed that the electrode particles are discharged until 0.15, 0.27, 0.50, 0.62, 0.84 and 0.9% state of discharge for 2C, 1C, C/4, C/10, C/25 and C/100. The state of discharge values for each rate is chosen based on experimentally measured electrode capacity in **Figure 34**.

observed near the electrode surface at faster rates. We calculate the deformation mismatch due to

the inhomogeneous distribution of sodium inside the electrode particle by following the previous elastic model developed for Li-ion batteries[22]. Mismatch strains are calculated as

$$\varepsilon(r) = \frac{l(r) - l|_{r=0}}{l|_{r=0}}$$

Concentration dependent-lattice parameters among the a-axis and b-axis are used to calculate strains. Shortly, the estimated concentration profiles throughout the radius of the electrode particle were converted into radius and time-dependent SOD and match with the lattice parameter in the a-axis and b-axis from the **Figure D11**. Steep concentration gradients at faster scan rates result in the generation of large mismatch strains in the electrode particle.

Table 2. Average concentration in the electrode particle C_{ave}, and mismatch strains in the particle along a-axis ($\varepsilon_{a,ave}$) and b-axis ($\varepsilon_{b,ave}$).

C-rates	2C	1C	C/4	C/10	C/25	C/100
$\bar{C}_{ave}$	0.15	0.30	0.53	0.63	0.84	0.89
$\varepsilon_{a,ave} / \bar{C}_{ave}$	6.17	6.19	5.21	2.08	0.53	0.10
$\varepsilon_{b,ave} / \bar{C}_{ave}$	6.91	7.00	5.95	2.55	0.63	0.14

The average concentration in the electrode particle ($\bar{C}_{ave}$, where $\bar{C}_{ave} = C/C_{max}$), average mismatch strains in the particle along a-axis ($\varepsilon_{a,ave}$) and b-axis ($\varepsilon_{b,ave}$) are calculated from the simulation and tabulated in **Table 2**. Average values are calculated via $\Phi_{ave} = \frac{\int_0^R \Phi dr}{\int_0^R dr}$ where $\Phi = \bar{C}_{ave}, \varepsilon_a$ or ε_b. Average predicted Na concentrations in the electrode particle at different rates are in good agreement with the experimentally measured Na content in the composite electrode (**Figure 33**). The average mismatch strain evolution per charge is greater in magnitude when the electrode is cycled at faster rates. These mismatch strains in the electrode particle leads to additional macroscopic expansions of the composite electrode at faster rates.

101

7.3.6 Factors Contribution Electrochemical Strains in NaFePO$_4$ Electrode

Intercalation of Na ions generates electrochemical strain generation in the composite electrode (**Figure 30**). Strain derivatives during charge / discharge cycles match well with the capacity derivatives, which points out that the phase transformation in the electrode causes potential-dependent strain rate changes in the electrode (**Figure 31**). Strains also show very linear dependence on the capacity. Predicted composite strains based on anisotropic porous solid end S-combining rule also agrees well with the electrochemically measured strains at C/25 rate (**Figure 33**). The measurements also point out to irreversible and rate-dependent strain generation factors in the electrode in addition to the intercalation-induced electrochemical strains. First, large amount of irreversible strain generations is detected in the early cycle (**Figure 32**). Cumulative irreversible strain shows a linear dependence with the square root of the cycle time (**Figure 34**). When irreversible strain generation becomes negligible small in the subsequent cycles compared to the intercalation-induced strains, the electrode experiences a slightly larger expansion when cycled at the faster rate (**Figure 33**). This behavior suggests the rate-dependent strain evolution in the composite electrode. In summary, strains in the composite sodium iron phosphate electrode, ε_c can be defined as

$$\varepsilon_c = \varepsilon_i(Q) + \varepsilon_M(\nu) + \varepsilon_{\Delta-phase} + \varepsilon_{CEI}(t) + \varepsilon_{other}$$

where $\varepsilon_i(Q)$ is the capacity-dependent intercalation-induced strains, $\varepsilon_M(\nu)$ is the rate-dependent mismatch strains due to concentration gradients, $\varepsilon_{\Delta-phase}$ is mismatch strains due to the volume mismatch between separated phases in the electrode structure, $\varepsilon_{CEI}(t)$ is time-dependent, CEI-induced irreversible strains. ε_{other} is the strain generation due to the combination of other irreversible deformations such as oxygen vacancies, dissolution of iron, and irreversible structural or microstructural changes (e.g. cracks). Experimentally measured and predicted composite strains in **Figure 33** indicate the linear relationship between intercalation-induced strains, $\varepsilon_i(Q)$ and the

electrode capacity. Time-dependent cumulative irreversible strains in **Figure 34** points out the contribution of CEI growth on the irreversible deformation, $\varepsilon_{CEI}(t)$. Large irreversible strains are detected during the first cycle at any scan rates (**Figure 30** and **Figure D4**) and it can be associated with either $\varepsilon_{CEI}(t)$ and/or ε_{other}.

Rate-dependent strain rates with respect to capacity in **Figure 35** is associated with the generation of mismatch strains in the electrode. Mismatch strains, $\varepsilon_M(\nu)$, can be generated due to rate-dependent concentration gradients in the electrode particle and volume mismatch between two separate phases in the electrode. The energy accommodation during mechanical deformations in the electrode widens the potential gap between the electrochemical redox reactions, which leads to higher potential hysteresis[21]. Zhu and Wang calculated the strain accommodation energy for LiFePO$_4$ electrodes with 40-nm and 100-nm particle sizes. The bigger particles require large potential hysteresis to accommodate the volume differences between Li-rich and Li-poor phases[169]. Synchrotron X-ray diffraction and pair distribution function analysis suggest NaFePO$_4$ accommodates discontinuous volume changes in the electrode by forming short-range amorphous phases[20]. Operando synchrotron study also suggested the formation of mismatch strains on NaFePO$_4$ cathodes induces cost of mechanical energy, which causes larger potential hysteresis between redox reactions[95]. The analytical model predicted sharper concentration gradients and localized strain generation near the electrode surface during Li-ion intercalation electrode[22,141–146]. In situ stress measurements and finite strain model demonstrated local stress gradients near the Si thin film electrode surface due to sharp concentration gradients near surface[170,171]. In our study, the transport model only simulates the rate-induced concentration gradient within the solid solution (**Figure 35**). The model predicts sharp concentration gradients of Na near the electrode surface at higher rates, which contributes to greater mismatch strains (**Table 2**). It should be noted that large concentration gradients impede the volume mismatch between two separate phases in the electrode.

Although predicted strain values do not incorporate the phase separation factor, it demonstrates the contribution of sharp concentration gradients at faster rates on the mismatch strains.

7.4 Conclusion

A better understanding of the rate effect on electrode mechanics is required to develop new electrodes with better rate-capabilities. In this work, we interrogated the impact of scan rate on electrochemical strain generations in the $NaFePO_4$ composite cathode for Na-ion batteries. Digital image correlation was used to monitor strain generation in the composite cathode during cycling at different scan rates. A large irreversible strain is observed in the first cycle at all scan rates. A linear relationship between electrode capacity and strain evolution is observed at all scan rates. Asymmetrical strain evolution between anodic and cathodic cycles is observed at slower rates and it was attributed to the generation of time-dependent irreversible strains due to CEI growth. The rate of increase in the cumulative irreversible strain was greater when the electrode cycled at faster rates. The remarkably larger intercalation-induced strain evolution is observed in the composite electrode when cycled at faster scan rates. Experimental strain measurements were compared with the predictions from an analytical model for composite electrodes based on uniform elastic deformations and intercalation-induced structural changes in the NFP particles. A transport-mechanics model is developed to predict the concentration profile of Na in the electrode particles and associated mismatch strains at different scan rates. Our study demonstrated the scan rate-dependent and time-dependent additional volumetric changes in the electrode due to the formation of CEI layers and mismatch strains. When considering commercial electrodes being constrained by current collectors and battery packing, these constrained electrodes will be more prone to mechanical degradations at faster rates due to larger electrochemical strains. Mechanical instabilities in the electrode particles will shorten the lifetime and worsen the performance of the battery electrodes.

CHAPTER VIII

RATE-DEPENDENT ELECTROCHEMICAL STRAIN GENERATION IN COMPOSITE

IRON PHOSPHATE CATHODES IN Li-ION BATTERIES

Bertan Özdogru, Vijayakumar Murugesan, and Ömer Özgür Çapraz

1) The School of Chemical Engineering, Oklahoma State University, Stillwater, OK 74078

2) Joint Center for Energy Storage Research, Pacific Northwestern National Laboratory, 902 Battelle Blvd, Richland, WA 99354

ABSTRACT

The performance of battery electrodes is significantly impacted by chemo-mechanical instabilities at faster charge/discharge rates. This study reports rate-dependent mechanical deformations in the $LiFePO_4$ cathodes during battery cycling by synchronizing in situ digital image correlation and electrochemical techniques. The electrode undergoes larger mechanical deformations in the early cycles and irreversible strains become negligible at the subsequent cycles. Cumulative irreversible strains show a linear relationship with the square root of cycling time, and the slope of the cumulative irreversible strains is greater at faster rates. The study compares the irreversible strains in $LiFePO_4$ for Li-ion batteries with its analogous $NaFePO_4$ cathodes for Na-ion batteries. Rate-dependent mechanical deformations are reported as $LiFePO_4$ electrode undergoes larger strains per capacity at faster rates. Pulsed current charge/discharge experiments coupled with strain measurements suggest a delay in the phase transformations at faster rates. The study provides new insights about rate-dependent chemo-mechanical deformations in the $LiFePO_4$ electrodes.

Keywords: Rate-dependent deformations, fast charging, irreversible deformations, digital image correlation, Lithium Iron Phosphate

8.1 Introduction

Rechargeable lithium-ion batteries have been widely used to provide power to portable electronics since their commercialization in the early 1990s[172]. In recent years, there has been a growing interest to power electric vehicles with Li-ion batteries[173]. The fast-charging ability of Li-ion batteries with long cycle life is desirable for electric vehicle applications. However, the electrodes suffer from chemo-mechanical instabilities associated with the formation of cathode-electrolyte interface (CEI) layer and particle fracture[174,175]. Cathode materials undergo repeated volumetric changes during Li intercalation, which eventually leads to mechanical degradations in the brittle cathodes and further electrolyte decomposition on the fresh cathode surfaces after fractures[21,62,176]. Fast charging intensifies the chemo-mechanical deformations due to the diffusion-limitations in the electrode and disruptions in the phase transformation pathways in the cathode structure. In this study, we choose to investigate the rate-dependent chemo-mechanical deformations in lithium iron phosphate (LiFePO$_4$, LFP) cathodes. LFP is an environmentally benign cathode material with lower cost compared to lithium metal oxide cathodes, and LFP has a promising ability for fast-charging[69,177,178]. LFP cathodes have been widely used in electrical vehicle applications, where fast charging ability plays an important role on battery material selection[179].

Phase transformation dynamics in LFP has received great interest due to its ability for fast charging / discharging. In general, the phase transformation of the lithium iron phosphate to iron phosphate during delithiation induces 6.8% volumetric reduction[81]. During the Li insertion and removal processes, the repeated volumetric changes result in mechanical fracture in the LFP electrodes[174,175]. Phase transition impacts the misfit strains between the boundaries of Li-poor and Li-rich phases in the electrode. A high-resolution transmission electron microcopy study reported that the phase boundary migration mechanisms in lithium iron phosphate electrodes were associated with the relaxation of the elastic strains in the phase boundaries[113]. There are several mechanisms proposed for the phase transformation in lithium iron phosphate such as shrinking core[150,180], domino

cascade[75,82] and nonequilibrium solid solution[31,71,80,83,85,181–183]. These studies indicate the impact of the particle size and charge/discharge rates on the phase transition in the electrode. Also, operando X-Ray diffraction (XRD) measurements revealed the formation of the intermediate Li_xFePO_4 (where $0.6<x<0.75$) at the faster rates[85,183,184]. Asymmetric phase transition behavior between lithiation and delithiation processes in the electrode was reported by scanning transmission X-Ray microscopy and operando XRD studies[80,185]. Despite the extensive literature reports on the dynamic changes in material chemistry of LFP electrodes during cycling, there is still little understanding about how rate-dependent phase transformations in LFP electrode impact the chemo-mechanical stability of the electrodes at faster rates.

To fill this gap, we utilize digital image correlation (DIC) coupled with electrochemical techniques in order to probe strain generation in the LFP electrode during cycling. DIC technique has been utilized to investigate the chemo-mechanical deformation mechanisms in various electrode material chemistries materials for alkali metal ion batteries[33,98,115,186]. Strain evolution during battery operation was monitored using an in-situ, optical, full-field digital image correlation technique. Iron phosphate composite electrode was prepared from lithium iron phosphate composite electrode using electrochemical displacement method. Our results indicate that a large irreversible deformation in LFP electrode is observed during the early cycles regardless of cycling rate. Irreversible strain generation reduces significantly with the subsequent cycles. Analysis on the cumulative irreversible strain generation shows linearity with square root of experimental time, and the slope of the cumulative strain generation with respect to the square root of time is higher with higher scan rates. In order to understand the phase transformation mechanism at different cycling rates, pulsed current measurements with resting periods were carried out at| different C-rates while monitoring in situ strains in the electrode. Pulsed current experiments pointed out the delay in the phase transformation at faster rates. This study provides new insights into the effect of cycling rate on the chemo-mechanical degradation of LFP cathodes during lithium intercalation.

8.2 Results and Discussion

8.2.1 Electrochemical and Mechanical Behavior of Iron Phosphate

Figure 36 shows the potential evolution and the corresponding strain evolution in iron phosphate composite electrode during the charge/discharge cycles. The iron phosphate electrodes were galvanostatic cycled at C/25 rate between 2.6-4.4 V for five cycles. During the discharge (lithiation) and charge (delithiation), flat potential plateaus are observed around 3.42 and 3.45V, respectively. Single potential plateaus during charge / discharge cycles were associated with the two-phase transition between Li-rich $LiFePO_4$ and Li-poor $FePO_4$ phases[72–75]. Charge and discharge capacities were about 150 and 177 mAh/g, which are close to the theoretical capacity (170 mAh/g). Lithium insertion into $FePO_4$ caused generation of 0.61% strains in the electrode during the first discharge. Extraction of the Li during charge cycles resulted in the contraction of the electrode's volume. The electrode did not return to its original state and 0.27% irreversible strains were observed at the end of first cycle. The irreversible deformations became 0.57% strains by the end of the fifth cycle.

In order to investigate the rate-dependent mechanical behavior of the electrode, LFP electrodes were charged/discharged at various scan rates. **Figure 37** shows the potential evolution and associated strain generation in the electrode cycled at 2.5C, 1C, C/4, and C/10 rates. Single flat plateaus were observed during each delithiation and lithiation flat potential plateaus were observed during each delithiation and lithiation cycle at all rates, which indicates an expected two-phase reaction between $LiFePO_4$ and $FePO_4$. The discharge capacities at the 5th cycle were 150, 151, 134, and 126 mAh/g for C/10, C/4, 1C, and 2.5C rates, respectively. Due to transport limitations, the discharge capacity reduced as scan rate increased. Potential plateaus during the 5th charge cycle were about 3.46, 3.47, 3.54, and 3.73V for C/10, C/4, 1C, and 2.5C rates, respectively. The potential hysteresis is calculated by subtracting the potential plateau during charge (marked with circle times symbol) from the potential plateau during discharge (marked with circle times symbol)[187]. The

potential hysteresis in the 5th cycle were about 50, 70, 240, and 520 mV for C/10, C/4, 1C, and 2.5C rates, respectively. The increase in the potential hysteresis at faster rates was associated with the solid diffusion limitations at higher rates[150,188]. At all scan rates, the electrode undergoes volumetric expansions during Li insertion and negative strains were generated because of Li extraction from the electrode.
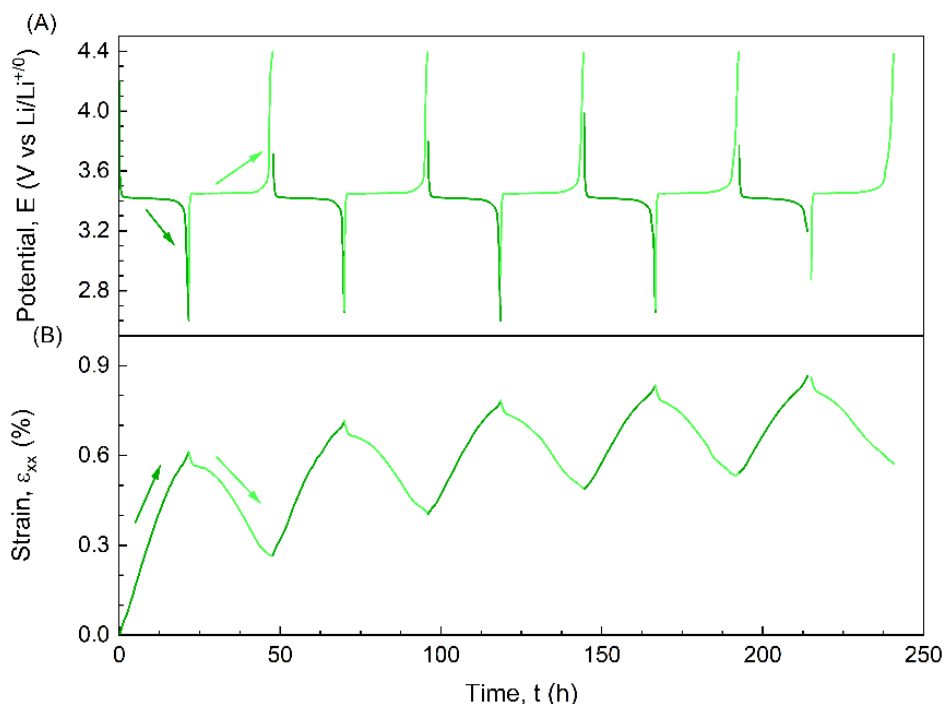
Figure 36. (A) Potential and (B) strain evolution in iron phosphate composite electrode during cycling between 2.6-4.4 V against Li counter electrode at C/25 rate with 1 M $LiClO_4$ in 1:1 EC:DMC.

Figure 36 and **Figure 37** indicate that the magnitude of the strains depends on the cycle number and the applied scan rates. Strain values are shifted to start from zero at the beginning of each charge and discharge cycle. Strain generation during Li insertion and extraction is called "discharge strain" and "charge strain", respectively. Strain value at the end of each cycle is labeled as "irreversible strain," and it is calculated by subtracting the cathodic strain from anodic strains for each cycle. These strains and the capacities for each of the charge / discharge cycles were tabulated in Supp. Table 1-5. Charge, discharge, and irreversible strains were also plotted with respect to cycle number at different rates in Supp. Fig 2. Overall, larger strain generation is observed in the

110
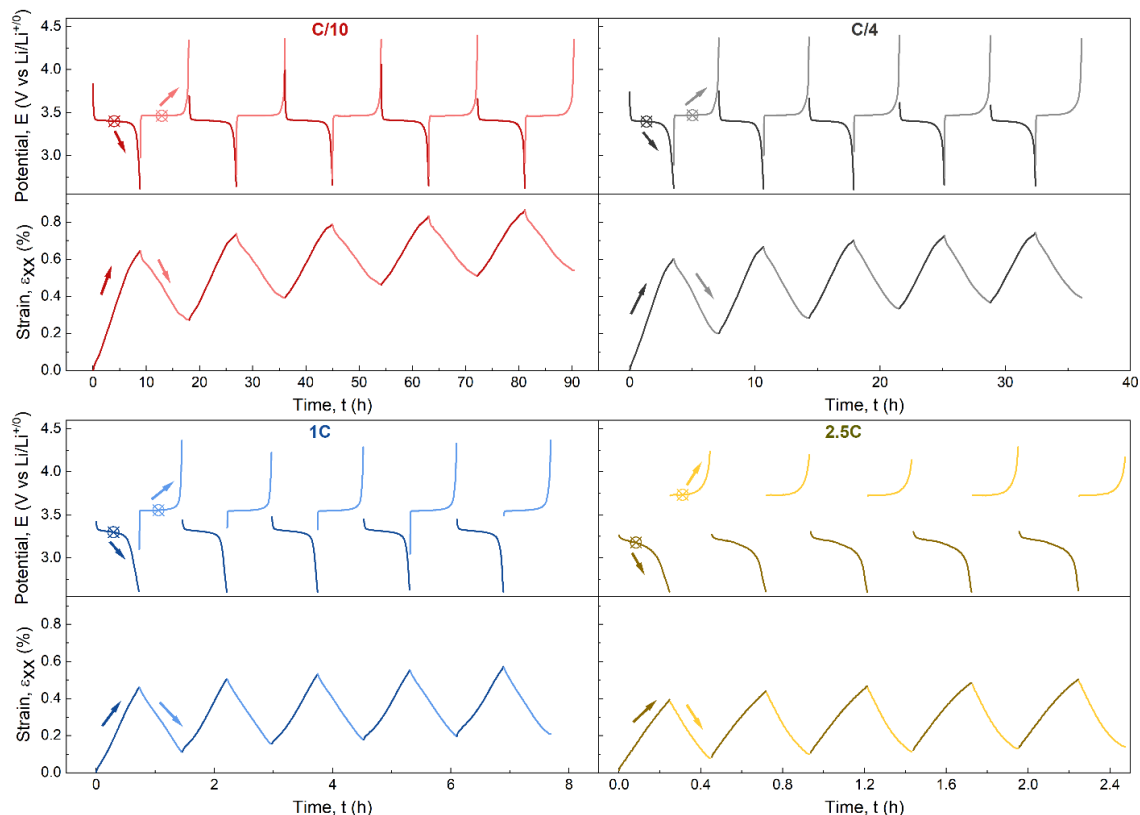
Figure 37. Potential and strain evolution in FP composite electrode during cycling between 2.6-4.4 V against Li counter electrode at different scan rates with 1 M LiClO$_4$ in 1:1 EC:DMC during first five cycles.

first discharge cycle compared to the discharge strains in the subsequent cycles. Similarly, the charge strains also reduced with the cycle numbers. As a result, strain generations became more reversible, and generation of irreversible strains reduced at the later cycles as shown in **Figure E1** and **Figure E2**.

To better depict the rate-dependent mechanical behavior of the LFP electrode, the strain generation and potential evolution in the electrode during the fifth cycle were plotted against charge/discharge capacities for all rates in **Figure 38**. Similar behavior is also observed for the early cycles in **Figure E3**-**Figure E6**. Electrochemical strains are set to zero at the beginning of charge and discharge cycles. The total amount of displaced Li ions in the electrode influences the strain generation in the electrode. The strains increased during the discharge cycle as a result of Li$^+$ ion insertion into the structure. Similarly, the strains decreased when the Li$^+$ ions were extracted from the electrode.

111
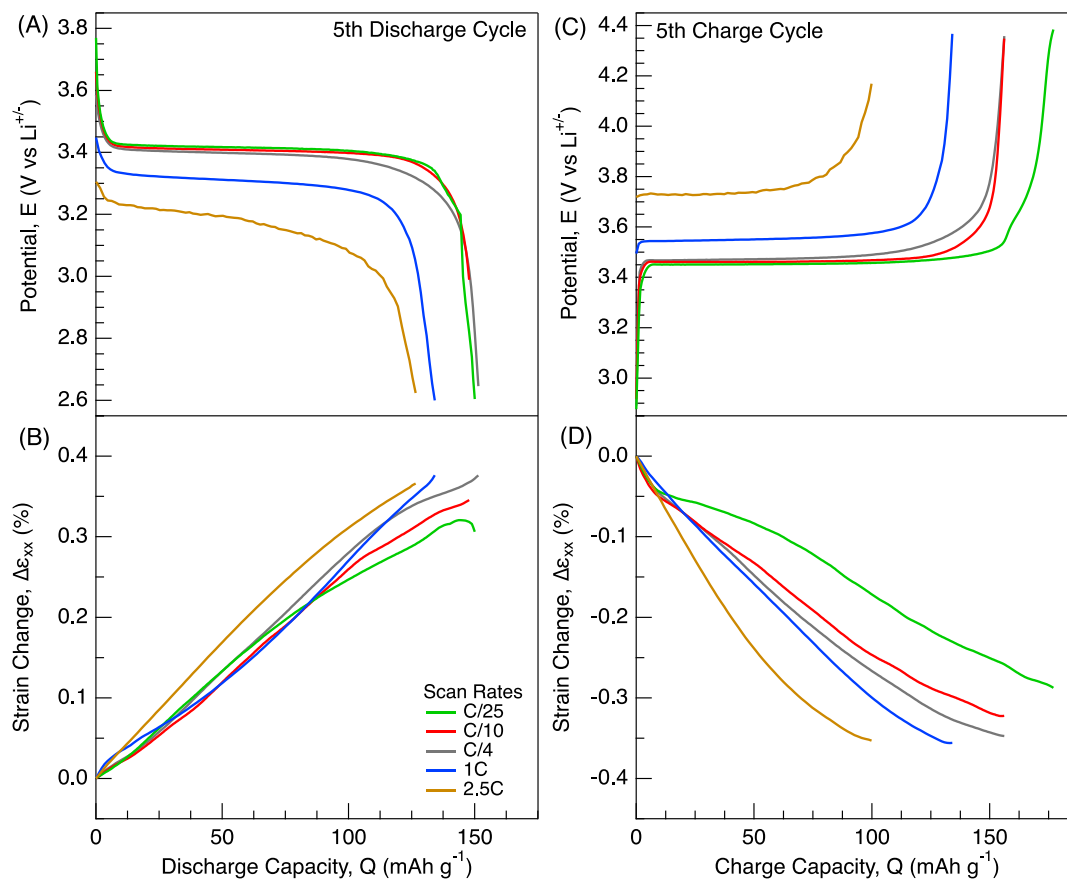
Figure 38. (a,c) Potential and (b,d) strain evolution in lithium iron phosphate electrode cycled at different scan rates during the 5th cycle for (a,b) discharge and (c,d) charge cycles. Strain evolution during discharge and charge cycles set to zero at the beginning of discharge and charge cycles, respectively.

However, the rate of the electrochemical strain generation showed a strong dependence on the applied scan rate, especially on the charge cycles. For example, when the charge capacity of the electrode was 100 mAh/g, the corresponding electrochemical strains in the electrode were -0.17, -0.25, -0.27, -0.30, and -0.35% at C/25, C/10, C/4, 1C and 2.5C rates, respectively.

Overall, in situ strain measurements indicate two major factors effecting the mechanical response of the LFP electrodes. The first characteristic behavior is the cycle-number dependent strain evolution in the electrode. Large irreversible strains are observed in the early cycles and the irreversible mechanical deformations are reduced in the subsequent cycles. Large strain generation was observed during the first lithiation cycle at any rate. The second major factor is the rate-

dependent mechanical deformations in the electrode. At faster rates, larger strain generation is recorded in the composite electrode when the same amount of Li^+ ions are removed from and inserted into the electrode. This rate-dependent behaviour is especially amplified during the charge cycles. In the following sections, we will discuss the potential sources for the irreversible mechanical deformations and rate-dependent mechanical deformations in the composite electrode.

8.2.2 Cycle Number-Dependent Irreversible Deformations in the Iron Phosphate Electrode

Li-ion battery electrodes experience irreversible deformations during early cycles due to several chemo-mechanical degradations such as the formation of solid-electrolyte interface (SEI) layers on the electrode surface and the dissolution of transition metals from the electrode structure into the electrolyte. Governing mechanisms behind these deformations occur under different conditions and depend on the chemistry of the electrode and electrolyte materials.

Dissolution of the transition metals (TMs) has been investigated for metal oxide and olivine-type cathodes. During the Li intercalation, TMs are expected to remain in the cathode structure. However, TMs in the near surface of the cathodes may dissolve into electrolyte[189]. The dissolution of the TMs is one of the biggest reasons behind the capacity loss especially in transition metal oxide cathodes[154,190]. The olivine-type structure of the $LiFePO_4$ provides more protection to stabilize Fe in the crystalline structure. If dissolution of the iron in the LFP cathode in our study is a dominant factor for the irreversible strains in the early cycles, then, it is expected that the volume of the electrode reduces as a result of the loss of active materials from the electrode. However, the irreversible strains are positive, indicating the irreversible expansions in the electrode volume. Aurbach et al. showed that dissolution of Fe ion is negligible in $LiFePO_4$ cathodes cycled in $LiClO_4$ salt-containing electrolytes, even at elevated temperature[191]. Therefore, the dissolution of the Fe ions cannot be the primary force behind the irreversible strains in **Figure 36** and **Figure 37**. [98]
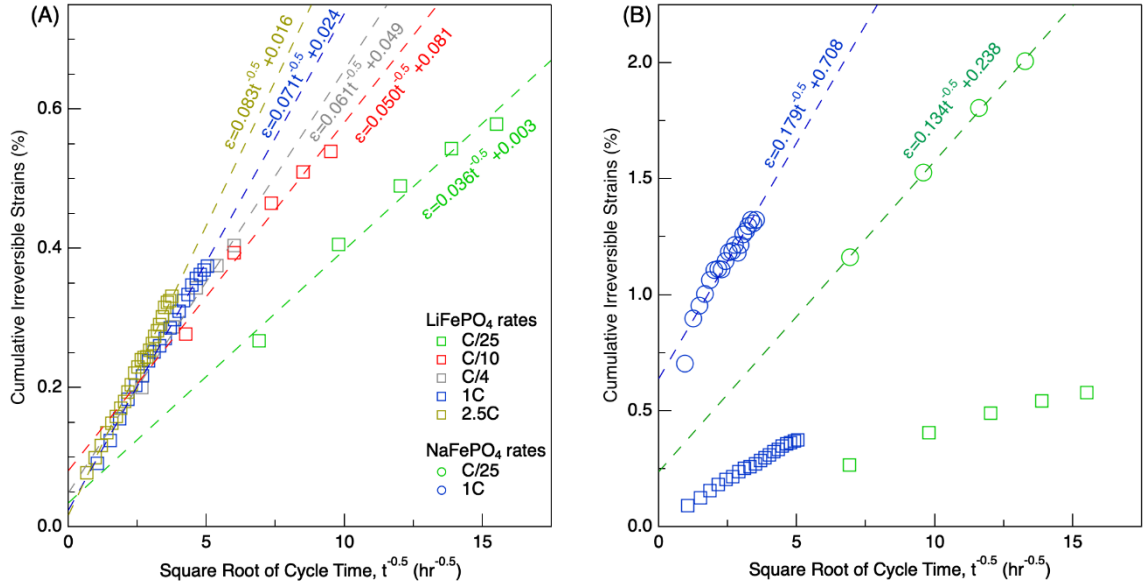
Figure 39. Cumulative irreversible strain evolution in composite lithium iron phosphate electrode at different cycling rates plotted against the square root of time. (a) lithium iron phosphate electrodes cycled at C/25 (green), C/10 (red), C/4 (gray), 1C (blue) and 2.5C (orange) rates. (b) Comparison of cumulative irreversible strain evolution in LiFePO4 and NaFePO4 electrodes cycled at C/25 and 1C rates. Plots for NaFePO4 electrodes are reproduced from our previous publication[98]. Dash lines represent the linear fitting of the data with the fitted equation

Formation of cathode-electrolyte interface (CEI) can be responsible for irreversible mechanical deformations in the electrode. CEI layers could form due to the electrochemical oxidation of electrolyte species at higher voltages, and chemical reactions between electrolyte species and cathode electrode[192–195]. Similarly, the electrochemical reduction of electrolyte species at lower voltages causes the formation of solid-electrolyte interface (SEI) layers on the anode electrodes. Previous in situ DIC study coupled with electron microscopy demonstrated the correlation between irreversible strains in the early cycles with the formation of SEI layers on the Li-ion graphite electrodes[104]. Also, the combination of in situ DIC with impedance spectroscopy study associated the irreversible strain generation during the initials cycles with the formation of CEI layers on the lithium manganese cathode[37]. Dahn and his group showed that thickness of the SEI and CEI layers increases approximately with the square root of time ($t^{-0.5}$) on graphite and NMC electrodes for Li-ion batteries, respectively[155,196]. More importantly, studies indicate that SEI/CEI growth rate is controlled by the cycle time and operational conditions (e.g. temperature and potential window),

not by cycle number[155–157,196]. The linear relationship between cumulative irreversible strains and $t^{-0.5}$ was observed for lithium manganese oxide, sodium iron phosphate and graphite composite electrodes[37,98,104].

If the CEI formation contributes to the irreversible strains in lithium iron phosphate cathode, then we expect to observe similar linear relationship between cumulative irreversible strains with $t^{-0.5}$. The cumulative irreversible strains were calculated from **Figure 36** and **Figure 37** for different rates, and they are plotted against the square root of cycle time in **Figure 39**A. Cumulative irreversible strains in LFP cathodes linearly increase with $t^{-0.5}$. Slope of cumulative strain increases with scan rate, from 0.036 $hr^{1/2}$ at C/25 to 0.071 $hr^{1/2}$ at 1C. Rate-dependent SEI growth was also reported for graphite electrode in Li-ion batteries[159]. We previously investigated the rate-dependent irreversible mechanical deformations in sodium iron phosphate cathodes for Na-ion batteries[98]. Our study also showed a similar relationship between cumulative irreversible strains with $t^{-0.5}$. In **Figure 39**B, we compared the irreversible strain generations in $LiFePO_4$ and $NaFePO_4$ cathodes cycled at 1C and C/25 rates. In both cases, the slope increases at the higher C-rates. When comparing the irreversible strains per $t^{-0.5}$ at the same rates, the slopes are greater in $NaFePO_4$ cathode compared to $LiFePO_4$. This indicates the formation of thicker CEI layers on the iron phosphate cathodes in Na chemistry compared to in Li chemistry. Previous XPS studies on antimony anodes also indicated the formation of thicker SEI layers during Na-ion intercalation compared to the Li-ion intercalation[197,198].

8.2.3 Rate-Dependent Electrochemical Strains:

Li-ion intercalation into the cathodes involves the diffusion of Li in the cathode and structural changes associated with the phase transformations in the electrode structure. As discussed before, several different phase transformation mechanisms are proposed for lithium iron phosphate, such as shrinking core[150,180], domino cascade[75,82] and nonequilibrium solid solution[31,71,80,83,85,181–183].

These studies indicate the impact of the particle size and charge/discharge rates on the phase transition in the electrode. In general, LFP electrodes with a diameter larger than ca. 100 nm undergo phase transformation between Li-rich Li_xFePO_4 and Li-poor $Li_{1-x}FePO_4$ phases with a sharp interface[71,72,84–86]. The Li transport in the electrode could be impacted by the sharp interface between the growing and shrinking domains during phase transformation[199]. Also, at faster charge / discharge rates, intercalation could be limited by the low diffusivity of the Li-ions in the electrode[22,142]. The average size of the iron phosphate particles is approximately 250 nm in our study and the phase change is manifested via a potential plateau during both lithiation/delithiation process.

Volumetric changes in the crystalline structure are a result of the lattice mismatch between the consumed phases and the created new phases in the electrode. Previous studies showed the correlation between nanoscale changes in the crystalline structure during phase transformation with the microscale changes in the electrochemical strain in electrodes during Li-ion, Na-ion, and K-ion intercalations[98,104,115]. In these studies, capacity and strain derivatives were calculated with respect to electrochemical potential. The shape and the location of the strain derivatives resemble the capacity derivatives for galvanostatic cycling and current evolution for cyclic voltammetry. In this study, we also calculated the strain and capacity derivatives at different rates in **Figure 40**. Strain and capacity derivatives for different cycle numbers and scan rates are also plotted in **Figure E7**-**Figure E11**. Both strain and capacity derivatives demonstrate a very sharp and narrow peak derivative when cycled at C/25 rate. It can be associated with the two-phase structure with the sharp interface in the electrode during phase transformation at the slower rate[81]. The minima of the strain derivatives match with the capacity derivatives within 0.01 V. The shape of the strain derivatives and capacity derivatives also resemble each other. At the faster rates, the potential location of the derivative peaks becomes wider between charge and discharge cycles. Both strain and capacity derivatives become broader at faster rates. Strain derivative analysis suggests that higher C-rates

could impact the phase transformation pathways, causing the delay or limited intercalation capacity in the electrode. We have also analyzed the contour plots of the electrodes to understand how the strain is generated on the free-standing electrode. When the electrode is cycled at slow scan rate (C/25), shown in Supp. Fig. 12, strain is homogeneously distributed over the whole region of interest. However, at faster scan rates (1C), shown in Supp. Fig. 13, localized strain evolution can be seen during cycling, which can be related to delayed phase transformations at higher scan rates.

In order to probe the possible delay in the phase transformations and associated mechanical response in the electrode, we monitor in situ electrochemical strain in the electrode via pulsed current charge/discharge method. **Figure 41** shows the potential and strain evolution during C/25 and C/4 rates for pulse current measurements. In the pulsed current experiments, first, electrodes were cycled for five cycles at either C/25 or C/4 rates. The fifth cycle is called the uninterrupted charge/discharge cycle. Then, pulsed current was applied to the electrodes equivalent to C/25 (at 6.8 mA g^{-1}) and C/4 rates (at 42.5 mA g^{-1}) for 150 and 24 min, respectively. Between current pulses at 6.8 mA g^{-1} and 42.5 mA g^{-1}, electrodes were at open circuit for 150 min and 300 min, respectively. **Figure 41**A and **Figure 41**C shows the potential and strain evolution during uninterrupted and pulsed current measurements for the electrode cycled at C/25. At this rate, the potential evolution and specific capacity shows similarities between uninterrupted and pulsed current charge/discharge cycles. Magnitude and evolution of electrochemical strains in the electrode show similarity between uninterrupted and pulsed current charge/discharge cycles. This similarity indicates the homogeneous phase transition between LFP and FP at slower scan rates.

Electrode was also charged/discharged via uninterrupted and pulsed current measurements at C/4 rate in **Figure 41**B and **Figure 41**D. Interestingly, overall charge and discharge capacities in the electrode were almost 15% greater in the pulsed current experiment compared to the uninterrupted one. The slope of the strains with respect to charge/discharge capacities was lower when the
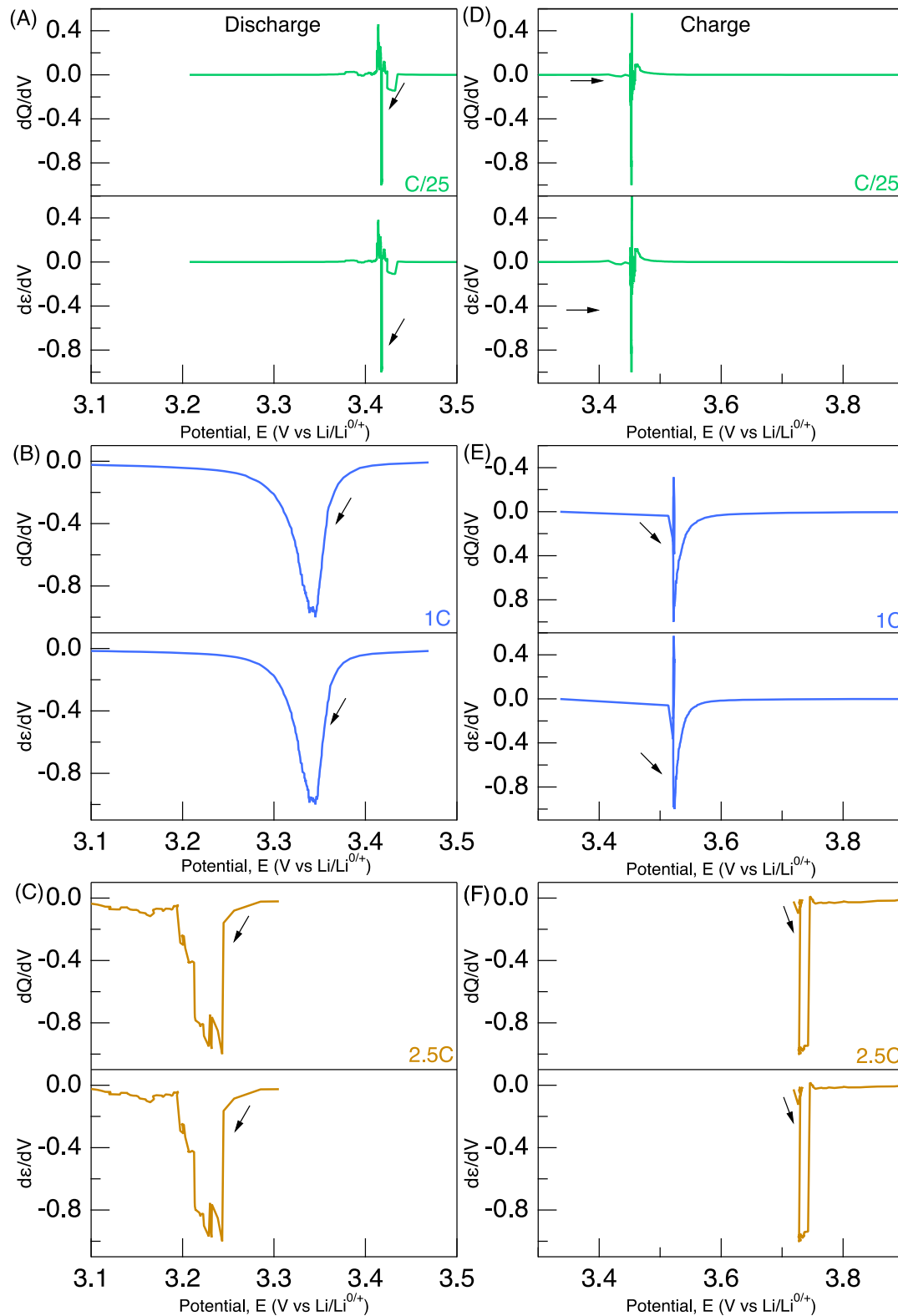
Figure 40. Capacity derivatives (dQ/dV, mAh g^{-1} V^{-1}) and strain derivatives (de/dV, %-V^{-1}) for 5th charge and discharge cycles at either C/25, 1C or 2.5C rate. The derivatives were normalized between by dividing them by the maximum value.

electrode was cycled via pulsed current measurement compared to the uninterrupted one. The lower slope indicates that the electrode undergoes less strain generation when the electrode was permitted to relax after pulsed current charge/discharge periods. During the relaxation period, the electrode is allowed to reach a quasi-equilibrium. **Figure 42** shows the strain evolution in the electrode during resting periods after the pulsed current charge/discharge at C/25 or C/4 rates. The strain evolution during the open circuit resting periods was found to be greater when the electrode was charged/discharged via pulsed current method compared to the uninterrupted one. The distinct
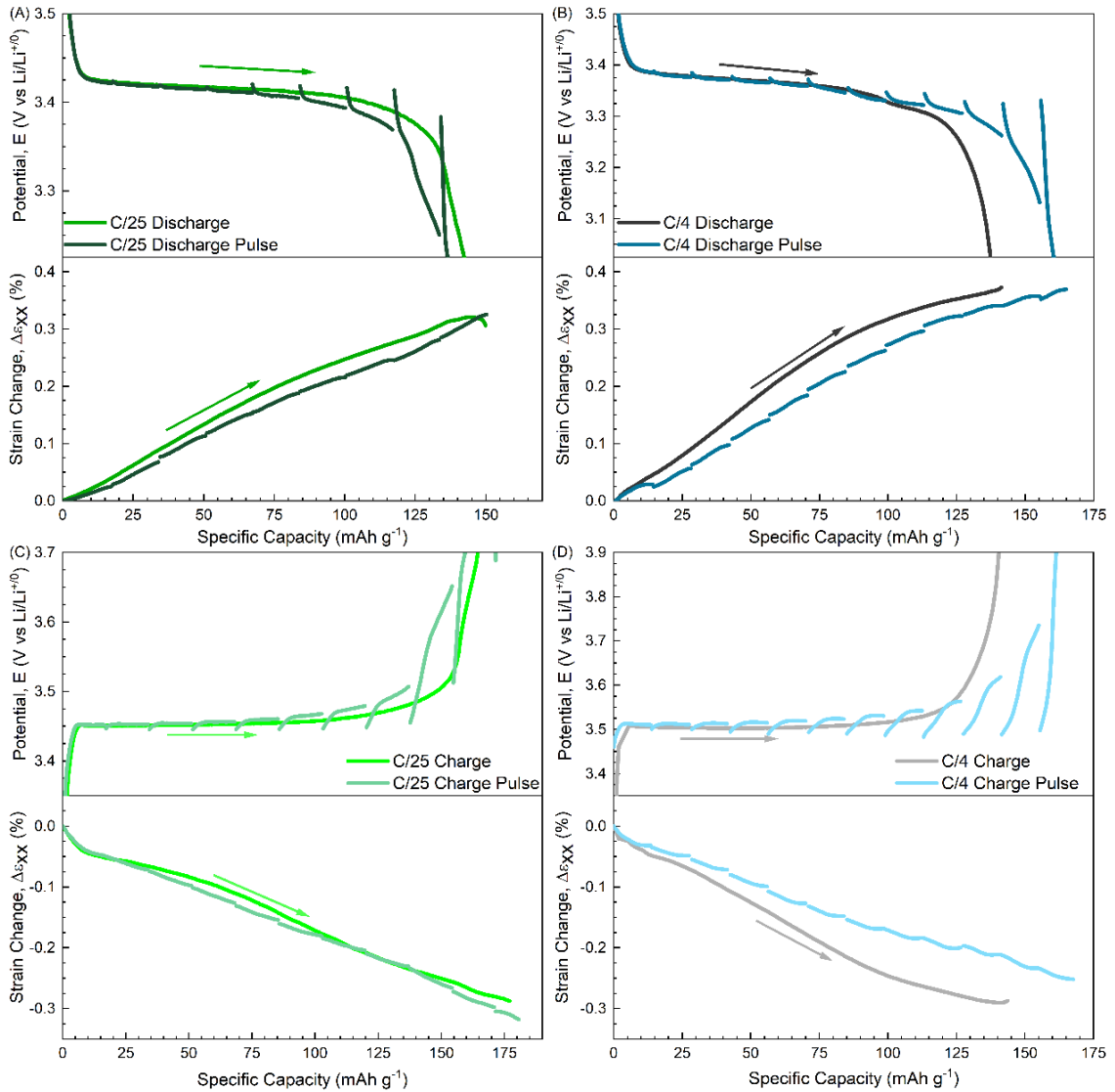
Figure 41. Potential and strain evolution during pulsed current measurements. Electrodes initially cycled at (a,c) C/25 and (b,d) C/4 rates for five cycles. Pulsed current was applied to the electrodes equivalent to (a,c) C/25 (6.8 mA g^{-1}) and (b,d) C/4 rates (42.5 mA g^{-1}) for 150 and 24 min.

119

difference in the mechanical relaxation of the electrode at faster rates further indicates the peculiar phase transformations in the iron phosphate electrodes at faster rates.

In situ XRD studies[71,85] showed that at slower scan rates, delithiation of LFP to FP follows the nucleation process. However, at higher scan rates, delithiation follows nonequilibrium solid solution by forming metastable Li_xFePO_4 phases. When these particles are relaxed, the particles phase separate into their equilibrium state with only single particle LFP and FP present. X-ray diffraction and X-ray absorption spectroscopy studies showed that the formation of the transient state phase leads to lag in the phase transformation between Li-rich and Li-poor phases[31]. Hess et al[200] employed a novel operando X-ray diffraction-electrochemical impedance spectroscopy and showed the presence of solid solution phases at faster scan rates. Moreover, at the end of
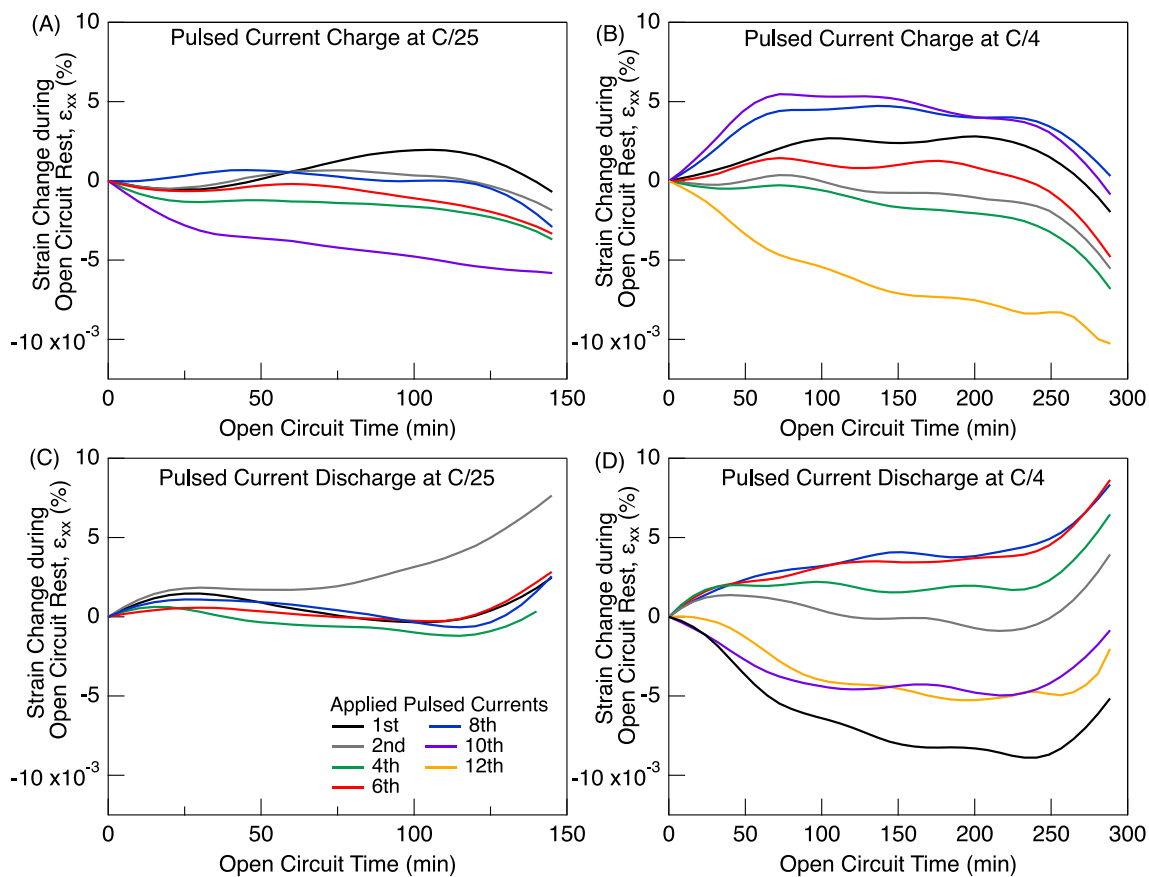
Figure 42. Strain change during the open circuit rest period after pulsed current charge / discharge periods at C/4 or C/25. Lines are colored to demonstrate the open circuit strains for the applied pulsed currents with sequence in **Figure 41**.

charge/discharge, the majority of the intermediate product stays in metastable form and slowly converts into its single phase LFP or FP particles. This behavior was also observed by Chang et al[201], when intermittent resting was employed at the end of discharge and charge, where no LFP or FP phases were observed prior to discharge and charge resting, respectively. Therefore, rate-dependent strain evolutions (**Figure 38**) and pulsed current charge/discharge experiments in **Figure 41** and **Figure 42** are in good agreement with the literature. Our study demonstrates the impact of the peculiar phase transformations at faster rates on the mechanical behavior of the iron phosphate cathodes for Li-ion batteries.

8.3 Conclusion

A better understanding of the rate-dependent chemo-mechanical behavior of the lithium iron phosphate (LFP) cathodes is necessary for their employment for fast charging applications. In this study, we investigated in situ electrochemical strain evolution in the composite LFP electrodes cycled at various rates. Digital image correlation was employed to monitor electrochemical strains in the composite electrode. Time-dependent and rate-dependent strain evolutions were identified in LFP electrodes. Strain generation during the first discharge was greater than the subsequent cycles at any scan rate. Strains became more reversible at the subsequent cycles. Cumulative irreversible strains showed linear relationship with the square root of cycle time. The slope of the cumulative irreversible strains was greater at faster rates. We also compared the irreversible strain generation in LFP cathodes with our previous study on $NaFePO_4$ cathodes. Na-ion intercalation induces much larger cumulative irreversible strains per cycle in the iron phosphate electrode compared to the Li-ion intercalation. Rate-dependent strains were investigated at the later cycles where irreversible strains almost become negligible. Larger strain evolution per discharge/charge capacity were recorded when the electrode was cycled at faster rates. Pulsed current discharge/charge experiments were performed to investigate the rate-dependent mechanical behavior of the LFP electrodes. Strain measurements during the open circuit periods after applied

pulsed current indicated the mechanical relaxations in the electrode when cycled at higher currents. The rate-dependent mechanical deformations in the $LiFePO_4$ are associated with the phase delays and metastable phase formations at faster rates. The outcome of this study sheds light into rate-dependent deformations in the $LiFePO_4$ electrodes, which is crucial understanding to improve the electrochemical performance of $LiFePO_4$ electrodes at faster charge / discharge applications.

CHAPTER IX

THE COUPLING BETWEEN VOLTAGE PROFILES AND MECHANICAL

DEFORMATIONS IN LAGP SOLID ELECTROLYTE DURING Li PLATING AND

STRIPPING

Bertan Ozdogru[1], Shubhankar Padwal[2], Batuhan Bal[1], Sandip Harimkar[2], Behrad Koohbor[3], Ömer Özgür Çapraz[1]

1) The School of Chemical Engineering, Oklahoma State University, Stillwater, OK 74078

2) The School of Mechanical and Aerospace Engineering, Oklahoma State University, Stillwater, OK 74078

3) Department of Mechanical Engineering, Rowan University, 201 Mullica Hill Rd., Glassboro, NJ 08028

ABSTRACT

Solid electrolytes show a great promise to use Li metal as an anode for high-energy all-solid-state batteries. However, the practical performance of these batteries suffers from severe chemo-mechanical degradation at the solid electrolyte – Li metal electrode interface. It is critical to understand the governing forces behind the chemical and mechanical deformations during battery operation. The buried interface between Li metal and solid electrolyte present challenges to probe dynamic changes in the interface during battery cycling. In this study, we establish in operando experimental system by utilizing digital image correlation (DIC). In operando DIC measurements provided temporal and spatial resolution of the chemo-mechanical deformations in LAGP solid electrolyte during the symmetrical cell cycling. The study reports experimental evidence for the correlation between overpotentials and mechanical deformations in the interface. The increase in strains in the interphase layer coincides with increase in overpotential. At the later cycles, large shear strains (~0.75%) were generated in the middle of the solid electrolyte where fractures were detected by ex-situ micro-X-ray computed tomography. This work highlights the mechanical deformations in LAGP / Li interface and its coupling with the electrochemical behavior of the battery.

Keywords: solid electrolyte, LAGP, interfacial deformations, strains, chemo-mechanical instabilities, overpotentials, fracture

9.1 Introduction

Rechargeable Li-ion batteries with organic liquid electrolytes have been widely used in portable electronics since their first commercialization in the early 1990s[202]. However, demanding applications such as electrical vehicles require batteries with much higher energy density than Li-ion batteries. Replacing organic liquid electrolytes with the solid electrolyte helps to eliminate the fire hazard to improve the safety, and in addition, it offers a promising way to increase the energy density by allowing the utilization of Li metal as an anode material. Despite the growing interest in solid electrolyte-based Li metal batteries, the utilization of the technology is still hindered by solid-solid interactions and chemo-mechanical instabilities in all-solid-state batteries[203,204].

Chemo-mechanical instabilities may originate from penetration of Li metal towards solid electrolyte, the formation of interphase layer in the vicinity of solid electrolyte – electrode, and void formation and associated contact loss between electrode and electrolyte[203–205]. Understanding the driving forces behind these instability mechanisms and their coupling with the electrochemical performance of the all-solid-state batteries is required to engineer the properties of solid electrolytes and the interface between electrode – solid electrolytes. However, the buried nature of the solid-solid interface makes it a challenge to probe the so-called chemo-mechanical deformation using in operando techniques. Various characterization techniques have been adopted to investigate these chemo-mechanical deformations in the solid electrolyte – electrode interface such as optical microscopy[206], X-ray computed tomography[207–209], Raman spectroscopy[210], scanning electron microscopy[211], transmission electron microscopy[212], in situ X-ray photoelectron spectroscopy[213], and in situ neutron diffraction[214].

Here, we demonstrate a new experimental approach to monitor dynamic physical changes and their resultant mechanical variations in solid electrolytes by utilizing in operando strain measurements via digital image correlation (DIC). These in operando experiments are supported by

electrochemical measurements and ex-situ micro-X-ray computed tomography (Micro-CT) analyses. $Li_{1.5}Al_{0.5}Ge_{1.5}P_3O_{12}$ (LAGP) solid electrolyte is selected as a model system. DIC technique has been used to investigate reversible and irreversible strain generation in the battery electrodes due to phase transformations[33,115,215] and a formation of solid-electrolyte interface[37,104]. Recently, Koohbor et al. applied DIC technique to monitor spatial deformations in the solid electrolyte – Au electrode interface[216]. Building on it, we utilized the DIC technique to monitor strain generation in LAGP solid electrolyte and at the interface between LAGP – Li metal electrode during Li plating and stripping. In operando DIC measurements provided spatial and temporal development of the chemo-mechanical strains in the interphase layer. The study provides experimental evidence for the relationship between mechanical deformations in the interphase layer and the overpotential. Fractures in the solid electrolyte were found by ex-situ Micro-CT analysis and the location of the fractures coincides with the areas wherein large shear strains were generated. Counterintuitively these shear bands were formed away from the SE/electrode interface but near the middle of the solid electrolyte.
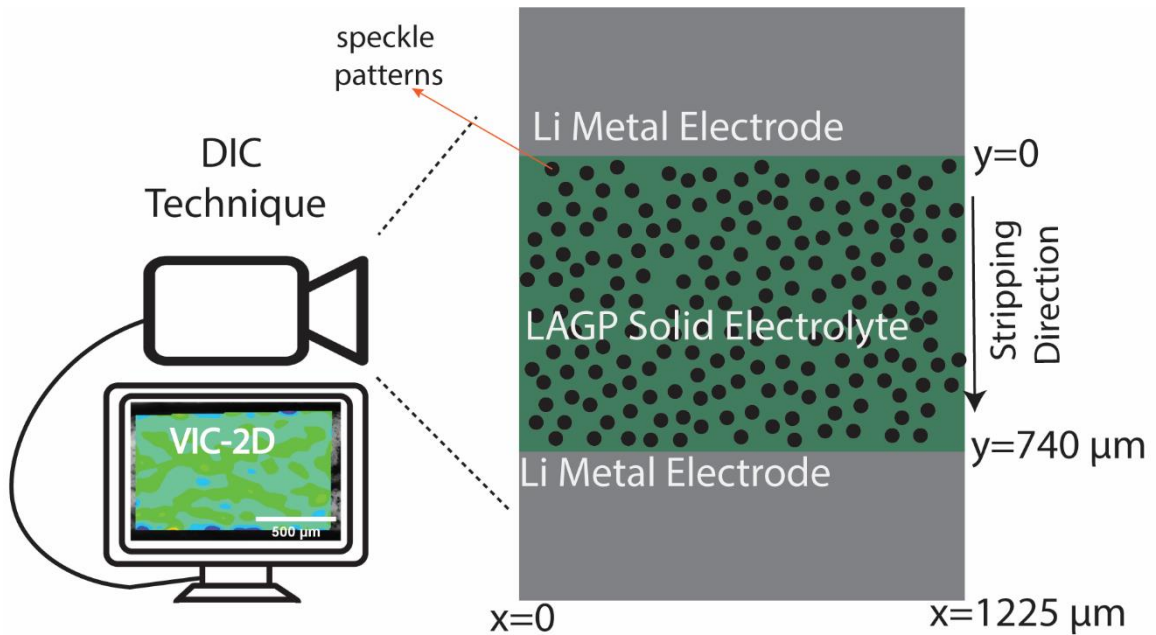
Figure 43. Schematic of in operando strain measurement for solid electrolytes.

9.2 Results and Discussion

Figure 43 demonstrates the schematics of the experimental setup for in operando strain measurements on LAGP solid electrolytes during battery cycling and the details of the system can be found in **Figure F1**. A symmetrical Li | LAGP | Li cell was cycled by applying constant current density. In operando strain measurements were performed to monitor deformations in electrode-solid electrolyte interface during battery cycling. Details of the sample preparation can be found in the Experimental Section in Appendix F. **Figure 44** shows the galvanostatic voltage profiles during 3rd (at 1 $\mu A/cm^2$), 6th (at 2 $\mu A/cm^2$), 17th (at 8 $\mu A/cm^2$) and 21st (at 16 $\mu A/cm^2$) stripping cycles where Li is stripped from the upper Li metal electrode and plated on the bottom one in **Figure 43**. The applied current density was selected based on the electrochemical performance of the LAGP solid electrolyte in the strain custom cell and similar current densities were previously used for other solid electrolyte system[217]. The voltages showed a flat profile at around 0.04 and 0.08V when Li was stripped at 1 and 2 $\mu A/cm^2$, respectively. When cycled at 8 $\mu A/cm^2$ for 4 hours, the voltage profile demonstrated an increase from 0.32 to 0.38V with the total 32 $\mu Ah/cm^2$ charge being transferred. At 16 $\mu A/cm^2$, the voltage profile rapidly increased from 1.27 to 2.56 V.

Figure 44B shows the corresponding contour plots for normal vertical strains, ε_{yy} on the LAGP solid electrolyte at the end of the stripping cycles. A negligible amount of strains development was observed at the end of the third stripping cycle at 1 $\mu A/cm^2$. When the current density was increased to 2 $\mu A/cm^2$ while keeping the total charge transferred to be the same, interphase formation and associated chemo-mechanical strains were detected in the interface of LAGP – Li metal electrodes. Non-homogeneously distributed negative strains were generated at the top interface, while positive strains were observed on the bottom interface. At 8 $\mu A/cm^2$, strains further propagated towards the solid electrolyte and a strain generation in the middle of the solid

electrolyte was observed. Propagation of mechanical deformation and the interphase formation towards the solid electrolyte became more pronounced when current was 16 $\mu A/cm^2$.
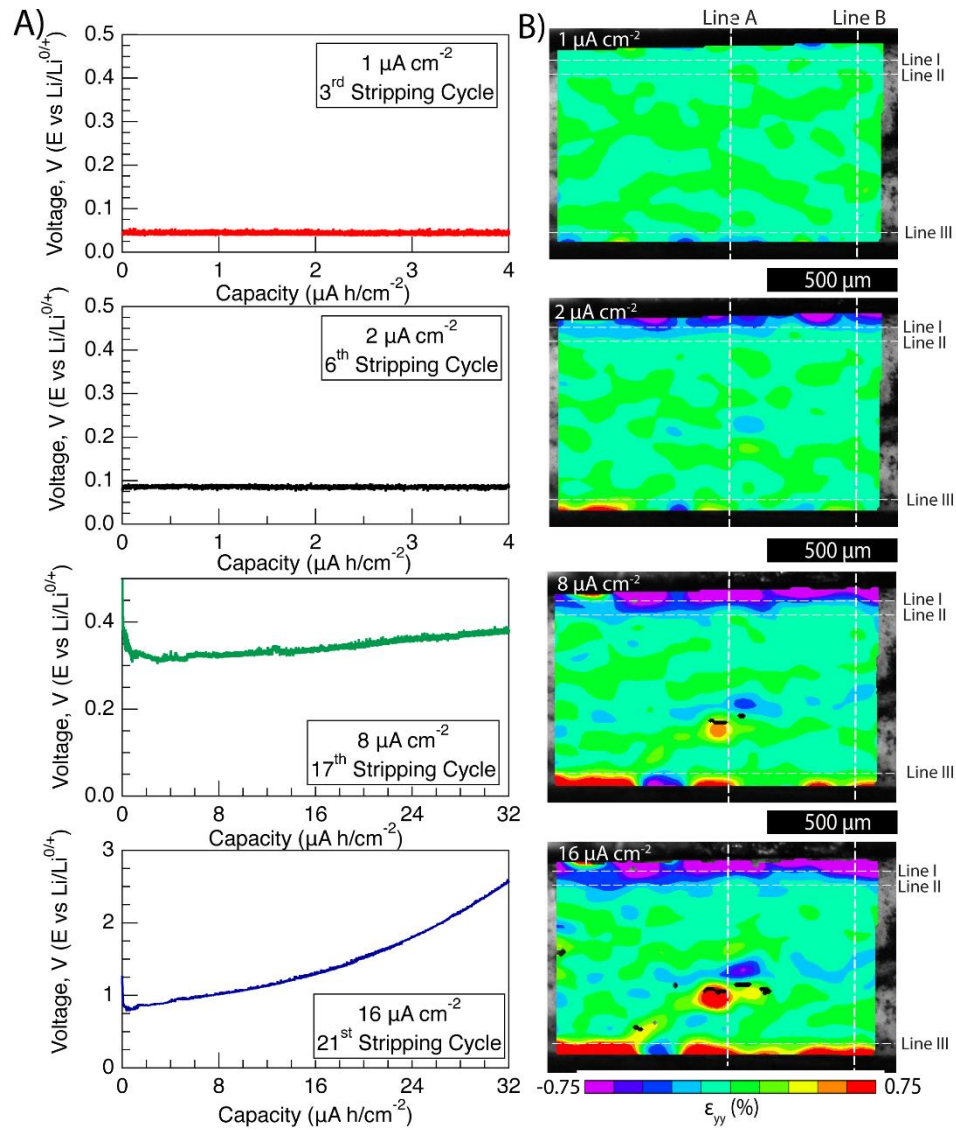
Figure 44. A) Voltage evolution profile with respect capacity when Li was stripped from the top Li metal electrode at 1, 2 , 8 and 16 μA/cm². B) Contour plots of normal strain, $\mathcal{E}_{yy}$ at the end of the corresponding stripping cycle.

To demonstrate the chemo-mechanical strains quantitively, the strain evolution along the thickness of solid electrolyte (vertical lines A and B) and along the width of the solid electrolyte (horizontal lines I, II and III) are plotted in **Figure 45**A and **Figure 45**B, respectively. Normal strains on the vertical line A and B demonstrate the evolution of the interphase formation when the symmetrical cell was cycled under different current densities. As the current density was increased, the

interfacial deformations reached almost -2.25% in some areas in the LAGP – top Li metal interface. The negative strains could be associated with the formation of voids at the top Li-LAGP interface because of the Li stripping process. The presence of these voids will possibly weaken the mechanical load-bearing capacity of LAGP at areas close to the top interface and reduce the contact area between LAGP SE and Li electrode[211,212]. At the same time, positive strains at the opposite side indicate the expansions in the interphase of LAGP – bottom Li metal which could be due to Li penetration and / or amorphization in LAGP. Li plating can penetrate in ceramic solid electrolytes, causing the expansions in the interphase of solid electrolyte – Li metal[204,206,211]. Reaction between Li and LAGP solid electrolyte causes volume expansions due to amorphization of the LAGP interphase[209,218]. The depth profile of strains on the vertical lines suggests that the interphase formation is about 75 micrometers thick. Previous studies on LLZO and LAGP solid electrolytes also reported around 50-90 micron-thick interphase formation between Li metal and solid electrolyte[209,218]. Generation of normal strains in the center of the solid electrolyte was recorded at higher current densities in the vertical lines. We will discuss these deformations in the solid electrolyte and how it impacts the electrochemical behavior in the later section.

The strain profiles on the horizontal lines in **Figure 45**B provide information about the strain magnitudes 50 and 100 microns away from the interface of LAGP-Li metal electrodes. Strains measured at the end of the 3rd stripping cycle at 1 $\mu A/cm^2$ were negligible. Normal strains, ε_{yy} along the horizontal line I, II and III became noticeably large at the 6th cycle at 2 $\mu A/cm^2$. Normal strains, ε_{yy} further increased by the end of the 17th cycle at 8 $\mu A/cm^2$. The strain patterns on the horizontal lines show heterogenous Li plating and stripping in the LAGP / Li metal interface. The interfacial deformations became more heterogonous by increasing the applied current density. For example, on line III, the minimum strains are on the same location regardless of the applied current density and cycle number. However, the magnitude of the strains in the neighboring areas increased with increasing current density. The strain measurements in **Figure 44** and **Figure 45** demonstrate
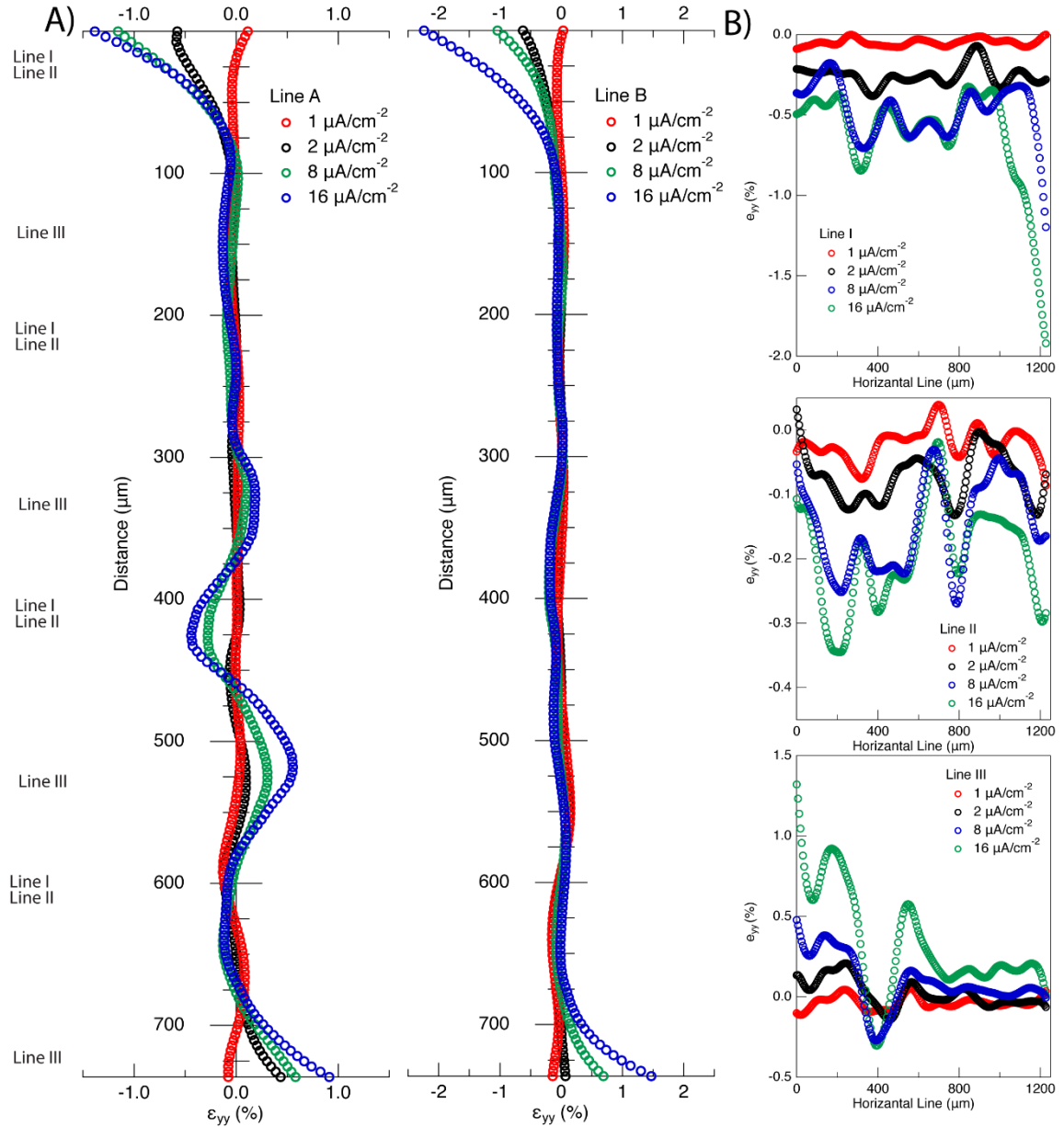
Figure 45. A) Normal strains, ε_{yy} along the line A and line B for four different current densities from figure 2. B) normal strains, ε_{yy} along the horizontal lines I, II and III. Line I and II are 50 and 100 μm away from the upper Li metal / LAGP electrolyte in Figure 2, respectively. Line III is 50 μm away from the below Li metal / LAGP electrolyte.

the impact of the early non-uniform deformations on the spatial distribution of Li plating and stripping on the solid electrolyte – electrode interface[211,219]. Surface roughness in the Li anode – solid electrolyte interface distorts the electrical field distribution during battery cycling and leads to uneven electrodeposition of Li metals[220]. The heterogeneity in the interface increases with the subsequent cycles due to uneven electrodeposition and stripping. The surface roughness of the solid
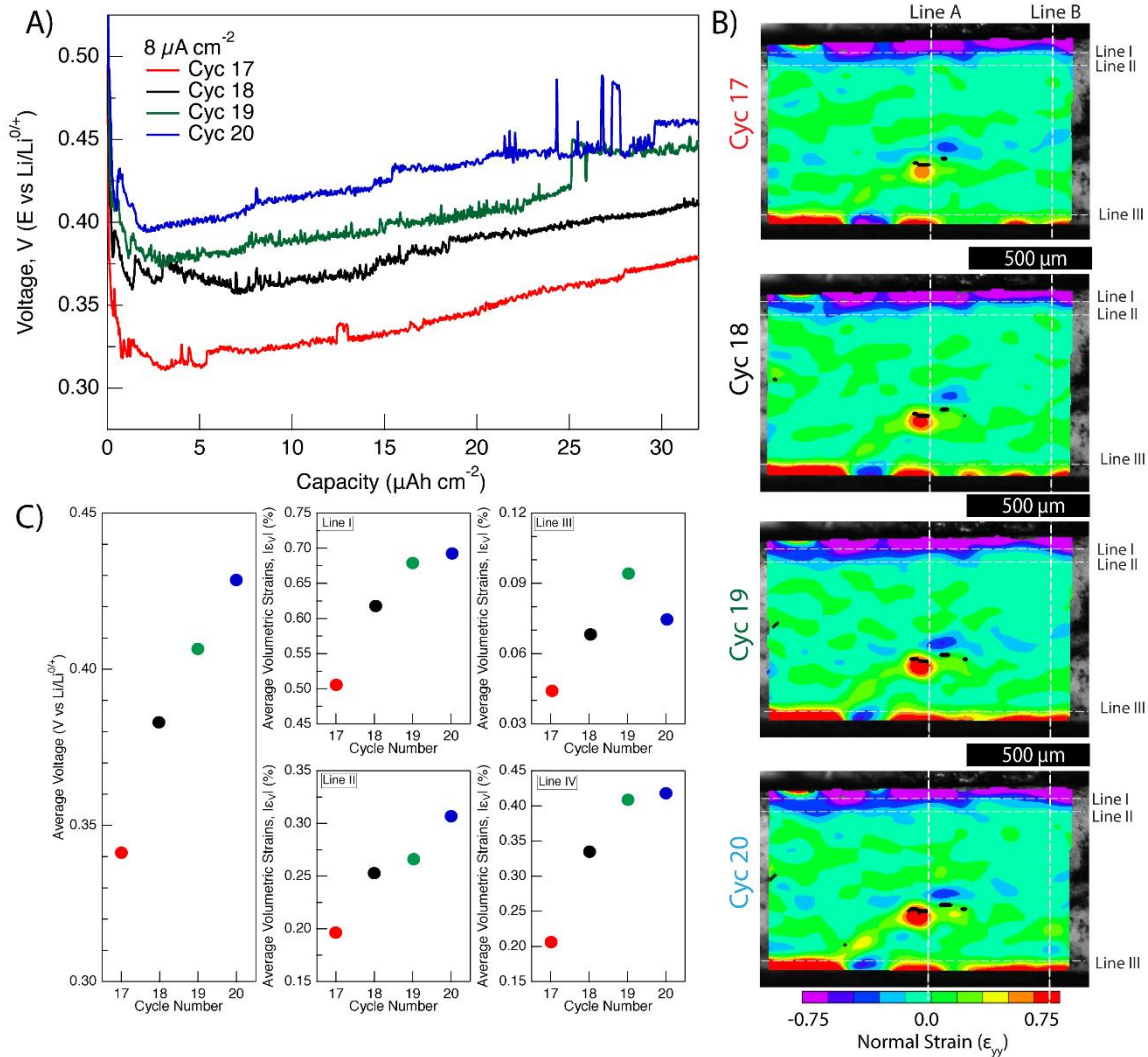
Figure 46. A) Voltage evolution during stripping cycles at 8 μA/cm^2. B) Contour plots of normal strain, ε_{yy} at the end of the corresponding stripping cycle. C) Average voltages from Fig 4A and average normal strains, ε_v along the horizontal lines I, II, III and IV. Line I and II are 50 and 100 μm away from the upper Li metal / LAGP electrolyte, respectively. Line III and IV are 50 and 25 μm away from the bottom Li metal / LAGP electrolyte, respectively.

electrolyte in this study was measured as about 300 nm (**Figure F2**B). Therefore, the strain measurements point out the importance of the interfacial morphology of the solid electrolytes (e.g., surface roughness) and their impact on the interfacial deformations in the subsequent cycles.

To understand the relationship between overpotential and the chemo-mechanical strains in the interphase, Li ions were stripped and plated at the same current density for consecutive cycles at 8 $\mu A/cm^2$. **Figure 46**A shows an increase in the voltage with the cycle number. The average value

of the voltage during each stripping cycle also increases with subsequent cycles. Contour plots of normal strain, ε_{yy} at the end of the corresponding stripping cycles are shown in **Figure 46**B. The depth of the strained layers near Li metal / LAGP interface increases slightly with the subsequent cycles (**Figure F4** and **Figure F5**). Strains profiles for ε_{xx} and ε_{yy} components on the horizontal lines I, II and III were plotted in **Figure F6**-**Figure F8**. Assuming symmetry about the y-axis, the strain components ε_{xx} and ε_{zz} can be taken to be equal (or at least close) in value. Volumetric strains developed at any given location across the SE thickness could then be calculated $\varepsilon_V = 2\varepsilon_{xx} + \varepsilon_{yy}$. Considering the dominance of ε_{yy} values over those of ε_{xx}, volumetric strain is expected to have the same sign as ε_{yy} strain component. The calculated volumetric strains along the horizontal lines are plotted in **Figure F9**. The average ε_V is calculated along each horizontal line for each cycle as shown in **Figure 46**C. Overall, both average voltage and average strains increased with the subsequent cycles. This suggests a direct correlation between the interfacial deformations and the mechanical overpotential.

At the LAGP – Li electrode interface, the electrochemical redox reactions are $Li \leftrightarrow Li^+ + e^-$. In the **Figure 46**, the Li metal is oxidized at the top Li metal / LAGP interface, and it is reduced at the bottom Li metal / LAGP interface. The overpotential is the summation of the electrical overpotential, $\eta_\emptyset$ and the mechanical overpotential, η_σ. The electrical potential can be defined as.

$$\eta_\emptyset = \emptyset_s - \emptyset_e - U$$

where $\emptyset$ is the electrical potential and U is the equilibrium potential. The contribution of stress on the overpotential has been discussed for alloy-type anodes and lithium iron phosphate cathode in organic liquid electrolytes for Li-ion batteries[21,148,169,221]. Recently, Mistry and Mukherjee[222] developed the mathematical expressions for the mechanical overpotential, η_σ by also considering deformations in solid electrolyte particles as well as the electrode.

$$\eta_\sigma = \left\{ \Omega_{Li^+} \sigma_{h,e} - \Omega_{Li} \sigma_{h,Li} \right\} / F$$

where Ω_{Li^+} is the partial volume of Li^+ in the solid electrolyte, Ω_{Li} is the molar volume of Li and σ_h is the hydrostatic stress. The Butler-Volmer relationship correlates the overpotential, η with the Faradaic reaction current. If the electrical overpotential impacts the anodic and cathodic reactions equally but mechanical overpotential selectively contributes to the anodic reaction, then the Butler-Volmer relationship becomes[223,224];

$$i = i_o \left(exp\left(\frac{F\eta_\sigma}{RT}\right) exp\left(\frac{F\eta_\varnothing}{2RT}\right) - exp\left(\frac{-F\eta_\varnothing}{2RT}\right) \right)$$

where i_o is the exchange current density, α_a and α_c are the charge transfer coefficients, F is the Faraday's constant, R is the gas constant, and T is temperature. The mathematical model based on the updated Butler-Volmer relationship predicted the contribution of the hydrostatic stress in the solid electrolyte particles in overpotentials for all-solid-state batteries[222]. While the present results only show the evolution of chemo-mechanical strains, a simple stress analysis can be conducted to highlight the role of hydrostatic stresses as well. A correlation between volumetric strain and hydrostatic stress can be easily established using the well-known linear elastic mechanics as $\sigma_h = K\varepsilon_V$ where K denotes the bulk modulus of the solid electrolyte material. Bulk modulus can be calculated via $K = E/[3(1 - 2v)]$. Elastic modulus, E and Poisson's ratio, v for LAGP were reported as 144 GPa and 0.25, respectively[225]. When considering the relationship between stress and strains, our experimental measurements on the correlation between overpotential and strains in the interphase layer aligns very well with the predictions in the mathematical model. The nonuniform growth of the interphase layer accelerates at higher currents, which leads to the chemo-mechanical failure in the solid electrolytes[206,218]. The surface overpotentials can also be impacted by the contact loss between solid electrolyte and Li metal electrode, charge transfer resistance at the interface, and transport rate of Li ions in the solid electrolyte[212,226]. Evolution of overpotential

133
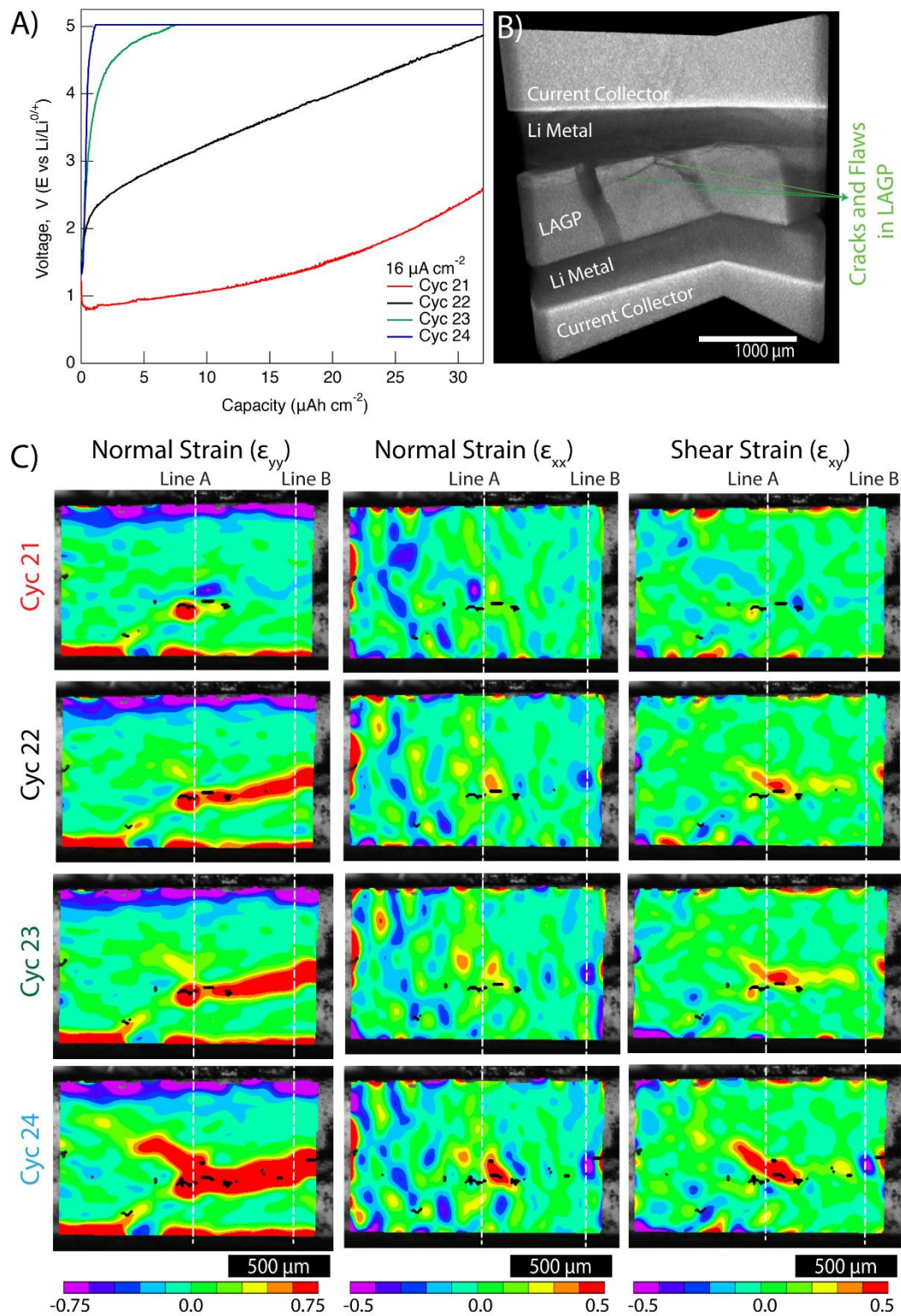
Figure 47. A) Voltage evolution during stripping cycles at 16 μA/cm^2 , B) 3-D X-ray microcomputed tomography (Micro-CT) image of the Li metal - LAGP solid electrolyte – Li metal after cycling. Large cracks and flaws are observed in the LAGP electrolyte. C) Contour plots of normal strains, ε_{yy} and ε_{xx}, and shear strains ε_{xy} at the end of the corresponding stripping cycle.

134

will increase the energy cost for Li plating / stripping processes. The correlation between mechanical deformations and overpotentials during battery cycle indicates the importance of chemo-mechanical stabilities in the interphase.

In order to quantitively analyze the role of strains on the mechanical failures at higher current densities, the Li metals were stripped and plated at 16 $\mu A/cm^2$ for four consecutive cycles (**Figure 47**A). The voltage was set to 5V upper limit. A rapid increase in the voltage profile was observed in the first two consecutive cycles at 16 $\mu A/cm^2$ (cycle 21 and 22). In the last two consecutive cycles, the voltages reached to 5V upper limit. After the electrochemical cycling, an ex-situ Micro-CT image of the solid electrolyte was taken without dissembling the cell. The Micro-CT image in **Figure 47**B shows evidence of cracks and flaws in the LAGP solid electrolyte after cycling.

The associated counter plots for ε_{yy}, ε_{xx} and ε_{xy} strains at the end of each stripping cycle are plotted in **Figure 47**C. The strain evolutions along the thickness of the solid electrolyte (vertical lines A and B) are shown in the **Figure F10** and **Figure F11**. Generation of positive normal strain, ε_{yy} in the middle of the LAGP solid electrolyte is recorded in the 21st stripping cycle. However, the magnitude of the ε_{xx} normal strains and ε_{xy} shear strains were much smaller compared to the ε_{yy} normal strain. In the subsequent cycles, the magnitude and size of the ε_{yy} normal strain became much greater. The ε_{yy} normal strain could be associated with the formation of voids in the solid electrolyte, which can disturb the conduction of the Li ions in the solid electrolyte. At the same time, the magnitude of the shear strains increased dramatically in the middle of the LAGP electrolyte. These mechanical deformations in the middle of the solid electrolyte correspond well with the cracks observed in the Micro CT analysis in **Figure 47**.

9.3 Conclusion

In conclusion, in operando DIC measurements provided temporal and spatial analysis of the chemo-mechanical strains in LAGP solid electrolyte during battery cycling. The depth of the interphase

layer was about 75 microns and the normal strains progressively increased with consecutive cycles and increasing current density. The maximum and minimum value of normal strains were detected between 1.75 and -3.25% in the vicinity of the Li metal anode – LAGP electrolyte. An increase in the average strains in the interphase layer corresponds to the increase in overpotential. The DIC measurement detected the generation of 2.25% normal strains and 0.75% shear strains in the middle of the solid electrolyte, which coincides with the mechanical fracture detected by ex-situ Micro CT. In operando DIC measurements offer promising capabilities to study interfacial instabilities in solid-solid interfaces by probing spatial and temporal resolution of mechanical deformations during all-solid-state battery operation.

CHAPTER X

CONCLUSION AND FUTURE WORK

10.1 General Conclusion

In the Chapter 4, we have first showed that in-situ strain measurement system, which was previously employed to analyze lithium-ion battery electrodes such as graphite[36], lithium manganese oxide[33,37], and lithium iron phosphate[44], is suitable for the investigation of mechanical deformation in sodium-ion battery environment, During the first discharge, we have observed unexpectedly large strain generation with lithium and sodium intercalation. The strain evolution becomes more reversible in the subsequent cycles for both lithium and sodium. Interestingly, expansion in the sodium electrode compared to lithium electrode is much larger compared to unit cell volume difference observed in the previous diffraction studies. We hypothesize that the diffusion limitations, combined with amorphization can cause larger expansion in the case of sodium intercalation. More importantly, we showed that the DIC technique is suitable for alkali metal-ion battery investigations.

Previous studies show that, during potassium intercalation into iron phosphate causes irreversible amorphization of iron phosphate crystalline structure. To investigate the effect of electrochemical redox reactions on the mechanical deformation, in Chapter 5, we combined in-situ XRD and strain techniques to understand the phase evolution and mechanical deformation during potassium intercalation into iron phosphate host structure. Both in-situ XRD and HR-TEM analysis showed

the amorphization of iron phosphate during potassium intercalation. We were able to track the volume changes in the amorphized iron phosphate structure during electrochemical redox reaction, which enables future studies on amorphous electrode materials.

To understand the difference between lithium, sodium, and potassium intercalation, in Chapter 6, we compared the strain evolution for these alkali metal-ions. Except for first discharge, a linear correlation between state of charge/discharge and strain is observed for Li-ion and Na-ion intercalation, while it was nonlinear in the K-ion case. Interestingly, while sodium intercalation resulted with the largest expansion in the composite electrode; when the same number of ions inserted or removed from structure, sodium and potassium showed similar strain evolution. While the absolute strain is larger in Na-ion, strain rates were higher in K-ion. We hypothesized that the strain rate, instead of absolute strain, is the key factor contributing in the amorphization of electrode structure.

To understand the effect of different cycling rate on the iron phosphate host structure during sodium intercalation, in Chapter 7, we cycled electrode via galvanostatic cycling, employing DIC, GITT and mathematical model. We observed a strong dependence on the applied scan rate and mechanical behavior of the electrode. At slower scan rates, an asymmetrical strain generation observed between anodic and cathodic cycles, associated with the formation of CEI layer. Additionally, for the same amount of Na inserted and removed, electrode undergoes smaller strain generation when cycled at slower scan rates. To predict the concentration profile and mismatch strain in electrode particles, a mathematical model was developed.

In Chapter 8, we employed a similar approach that we used in Chapter 7, during lithium intercalation. For all scan rates, at early cycles, larger irreversible strains observed, where they become negligible at later cycles. Per capacity basis, LFP electrode undergoes larger strain generation when cycled at higher scan rates. We have also conducted pulsed current

charge/discharge experiments during in situ strain measurement, where the results suggest a delay in the phase transformation at faster scan rates.

In Chapter 9, we establish an in-situ experimental system by utilizing DIC technique to investigate the chemo-mechanical deformation in LAGP solid electrolyte during symmetric cell cycling. Results showed a correlation between mechanical deformation and overpotential generation in the Li/LAGP interphase. Increase in strain at interphase coincides with the increase in overpotential. We observed large shear strains at the middle of the solid electrolyte at later cycles, where fractures were detected by ex-situ Micro X-Ray CT.

10.2 Future Work

Throughout this dissertation, we showed that in-situ strain measurement system that utilize Digital Image Correlation technique can be utilized for "beyond" Li-ion battery applications. We have shown how lithium, sodium and potassium intercalation changes the strain evolution in iron phosphate composite electrode under different cycling rate. These results are an excellent starting point for the future studies.

Previously, Gribble et al[227] showed the effect of different binders in the graphite anode material for potassium-ion battery application. This study signifies the importance of the chemical stability of different components of composite electrode under sodium and potassium-ion battery conditions. By optimizing the composite electrode composition, by changing the mass ratios as well as its composition, we can optimize the strain evolution in the composite electrodes.

Investigation of amorphous materials and their mechanical response during redox reaction is a crucial step for the commercialization of these technologies. Materials such as hard carbon[228], antimony[229], and tin[230] show amorphous behavior during sodium intercalation/deintercalation, where tin and antimony reversible switch between amorphous and crystalline phases. In the Chapter 5, we showed that, in-situ strain measurement system can quantify the amount of expansion and

shrinkage in the host structure, even after electrode particle amorphized due to potassium intercalation. Future studies will enable the researchers to understand the effect of electrochemical reactions under composite electrode configuration.

Finally, the results obtained for perovskite iron phosphate structure can be extended into other structures such as rock-salt ($LiCoO_2$), and polyanionic compounds (Prussian Blue analogs) will enable the researchers to understand the effects of reactivity and ionic radius of different alkali metal-ions on the same host structure.

REFERENCES

1.   Cecchini, R. & Pelosi, G. From the Historian--Alessandro Volta and his battery. *IEEE Antennas Propag Mag* **34**, 30–37 (1992).

2.   Armand, M. & Tarascon, J. M. Building better batteries. *Nature* vol. 451 652–657 Preprint at https://doi.org/10.1038/451652a (2008).

3.   Ohzuku, T. & Brodd, R. J. An overview of positive-electrode materials for advanced lithium-ion batteries. *J Power Sources* **174**, 449–456 (2007).

4.   John Newman, K. E. T.-A. *Electrochemical Systems, 3rd Edition*. (Wiley-Interscience, 2012).

5.   Fuller, T. F. & Harb, J. N. *Electrochemical engineering*. (Somerset: Wiley, 2018).

6.   Energy Information Administration, U. *Electricity*. www.eia.gov/aeo (2019).

7.   Energy Information Administration, U. Electricity data browser - Net generation for all sectors. https://www.eia.gov/electricity/data/browser/ (2020).

8.   Pramudita, J. C., Sehrawat, D., Goonetilleke, D. & Sharma, N. An Initial Review of the Status of Electrode Materials for Potassium-Ion Batteries. *Advanced Energy Materials* vol. 7 1602911 Preprint at https://doi.org/10.1002/aenm.201602911 (2017).

9.   Ellis, B. L. & Nazar, L. F. Sodium and sodium-ion energy storage batteries. (2012) doi:10.1016/j.cossms.2012.04.002.

10.   Nagelberg, A. S. & Worrell, W. L. A thermodynamic study of sodium-intercalated TaS2 and TiS2. *J Solid State Chem* **29**, 345–354 (1979).

11.   Delmas, C., Braconnier, J. J., Fouassier, C. & Hagenmuller, P. Electrochemical intercalation of sodium in NaxCoO2 bronzes. *Solid State Ion* **3–4**, 165–169 (1981).

12.   West, K., Zachau-Christiansen, B., Jacobsen, T. & Skaarup, S. Sodium insertion in vanadium oxides. *Solid State Ion* **28–30**, 1128–1131 (1988).

13.   Komaba, S. *et al.* Electrochemical Na insertion and solid electrolyte interphase for hard-carbon electrodes and application to Na-ion batteries. *Adv Funct Mater* **21**, 3859–3867 (2011).

14. Kubota, K., Dahbi, M., Hosaka, T., Kumakura, S. & Komaba, S. Towards K-Ion and Na-Ion Batteries as "Beyond Li-Ion". *Chemical Record* **18**, 459–479 (2018).

15. Luo, W. *et al.* Potassium Ion Batteries with Graphitic Materials. *Nano Lett* **15**, 7671–7677 (2015).

16. Kim, H., Ji, H., Wang, J. & Ceder, G. Next-Generation Cathode Materials for Non-aqueous Potassium-Ion Batteries. *Trends in Chemistry* vol. 1 682–692 Preprint at https://doi.org/10.1016/j.trechm.2019.04.007 (2019).

17. Nishimura, K. *et al.* Spinel-type lithium-manganese oxide cathodes for rechargeable lithium batteries. *J Power Sources* **81–82**, 420–424 (1999).

18. Gonzalez, J. *et al.* Three dimensional studies of particle failure in silicon based composite electrodes for lithium ion batteries. *J Power Sources* **269**, 334–343 (2014).

19. Verma, P., Maire, P. & Novák, P. A review of the features and analyses of the solid electrolyte interphase in Li-ion batteries. *Electrochimica Acta* vol. 55 6332–6341 Preprint at https://doi.org/10.1016/j.electacta.2010.05.072 (2010).

20. Xiang, K. *et al.* Accommodating High Transformation Strains in Battery Electrodes via the Formation of Nanoscale Intermediate Phases: Operando Investigation of Olivine NaFePO4. *Nano Lett* **17**, 1696–1702 (2017).

21. Mukhopadhyay, A. & Sheldon, B. W. Deformation and stress in electrode materials for Li-ion batteries. *Prog Mater Sci* **63**, 58–116 (2014).

22. Zhao, K., Pharr, M., Vlassak, J. J. & Suo, Z. Fracture of electrodes in lithium-ion batteries caused by fast charging. *J Appl Phys* **108**, 073517 (2010).

23. Reimers, J. N. & Dahn, J. R. Electrochemical and In Situ X-Ray Diffraction Studies of Lithium Intercalation in Li[sub x]CoO[sub 2]. *Article in Journal of The Electrochemical Society* (1992) doi:10.1149/1.2221184.

24. Mohanty, D. *et al.* Structural transformation of a lithium-rich Li 1.2 Co 0.1 Mn 0.55 Ni 0.15 O 2 cathode during high voltage cycling resolved by in situ X-ray diffraction. (2012) doi:10.1016/j.jpowsour.2012.11.144.

25. Gutiérrez-Kolar, J. S. *et al.* Interpreting Electrochemical and Chemical Sodiation Mechanisms and Kinetics in Tin Antimony Battery Anodes Using in Situ Transmission Electron Microscopy and Computational Methods. *ACS Appl Energy Mater* **2**, 3578–3586 (2019).

26. Mcdowell, M. T. *et al.* In Situ TEM of Two-Phase Lithiation of Amorphous Silicon Nanospheres. (2013) doi:10.1021/nl3044508.

27. Zhang, J., Lu, B., Song, Y. & Ji, X. Diffusion induced stress in layered Li-ion battery electrode plates. *J Power Sources* **209**, 220–227 (2012).

28. Bhandakkar, T. K. & Gao, H. Cohesive modeling of crack nucleation in a cylindrical electrode under axisymmetric diffusion induced stresses. *Int J Solids Struct* **48**, 2304–2309 (2011).

29. Chen, D., Indris, S., Schulz, M., Gamer, B. & Mönig, R. In situ scanning electron microscopy on lithium-ion battery electrodes using an ionic liquid. *J Power Sources* **196**, 6382–6387 (2011).

30. Yoon, I., Abraham, D. P., Lucht, B. L., Bower, A. F. & Guduru, P. R. In Situ Measurement of Solid Electrolyte Interphase Evolution on Silicon Anodes Using Atomic Force Microscopy. *Adv Energy Mater* **6**, 1600099 (2016).

31. Orikasa, Y. *et al.* Phase Transition Analysis between LiFePO 4 and FePO 4 by In-Situ Time-Resolved X-ray Absorption and X-ray Diffraction . *J Electrochem Soc* **160**, A3061–A3065 (2013).

32. Galceran, M. *et al.* The mechanism of NaFePO4 (de)sodiation determined by in situ X-ray diffraction. *Physical Chemistry Chemical Physics* **16**, 8837–8842 (2014).

33. Çapraz, Ö. Ö., Bassett, K. L., Gewirth, A. A. & Sottos, N. R. Electrochemical Stiffness Changes in Lithium Manganese Oxide Electrodes. *Adv Energy Mater* **7**, 1601778 (2017).

34. Tavassol, H., Jones, E. M. C., Sottos, N. R. & Gewirth, A. A. Electrochemical stiffness in lithium-ion batteries. *Nat Mater* **15**, 1182–1188 (2016).

35. Sheth, J. *et al.* In Situ Stress Evolution in Li 1+x Mn 2 O 4 Thin Films during Electrochemical Cycling in Li-Ion Cells . *J Electrochem Soc* **163**, A2524–A2530 (2016).

36. Jones, E. M. C., Silberstein, M. N., White, S. R. & Sottos, N. R. In Situ Measurements of Strains in Composite Battery Electrodes during Electrochemical Cycling. *Exp Mech* **54**, 971–985 (2014).

37. Çapraz, Rajput, S., White, S. & Sottos, N. R. Strain Evolution in Lithium Manganese Oxide Electrodes. *Exp Mech* **58**, 561–571 (2018).

38. Çapraz, Ö. Ö. *et al.* Controlling Expansion in Lithium Manganese Oxide Composite Electrodes via Surface Modification. *J Electrochem Soc* **166**, A2357–A2362 (2019).

39. Lyons, J. S., Liu, J. & Sutton, M. A. High-temperature deformation measurements using digital-image correlation. *Experimental Mechanics 1996 36:1* **36**, 64–70 (1996).

40. Reynolds, A. P. & Duvall, F. Digital Image Correlation for Determination of Weld and Base Metal Constitutive Behavior. *Welding Journal, New York* (1999).

41. Zhang, D., Eggleton, C. D. & Arola, D. D. Evaluating the mechanical behavior of arterial tissue using digital image correlation. *Exp Mech* **42**, 409–416 (2002).

42. Zhang, D. & Arola, D. D. Applications of digital image correlation to biological tissues. *J Biomed Opt* **9**, 691 (2004).

43. Autolab B.V., M. *Galvanostatic Intermittent Titration Technique*. https://www.ecochemie.nl/download/Applicationnotes/Autolab_Application_Note_BAT03.pdf (2014).

44. Bassett, K. L. K. L. *et al.* Cathode/electrolyte interface-dependent changes in stress and strain in lithium iron phosphate composite cathodes. *J Electrochem Soc* **166**, A2707–A2714 (2019).

45. Kammers, A. D. & Daly, S. Digital Image Correlation under Scanning Electron Microscopy: Methodology and Validation. *Exp Mech* **53**, 1743–1761 (2013).

46. Komaba, S. Systematic study on materials for lithium-, sodium-, and potassium-ion batteries. *Electrochemistry* **87**, 312–320 (2019).

47. Ponrouch, A. & Rosa Palacín, M. Post-Li batteries: Promises and challenges. *Philosophical Transactions of the Royal Society A: Mathematical, Physical and Engineering Sciences* **377**, (2019).

48. Saurel, D., Galceran, M., Reynaud, M., Anne, H. & Casas-Cabanas, M. Rate dependence of the reaction mechanism in olivine NaFePO4 Na-ion cathode material. *Int J Energy Res* **42**, 3258–3265 (2018).

49. Walczak, K., Kulka, A., Gędziorowski, B., Gajewska, M. & Molenda, J. Surface investigation of chemically delithiatied FePO4 as a cathode material for sodium ion batteries. *Solid State Ion* **319**, 186–193 (2018).

50. Fang, Y. *et al.* Phosphate Framework Electrode Materials for Sodium Ion Batteries. *Advanced Science* **4**, 1600392 (2017).

51. Rousse, G. *et al.* Rationalization of intercalation potential and redox mechanism for A 2Ti3O7 (A = Li, Na). *Chemistry of Materials* **25**, 4946–4956 (2013).

52. Zhu, Y., Xu, Y., Liu, Y., Luo, C. & Wang, C. Comparison of electrochemical performances of olivine NaFePO4 in sodium-ion batteries and olivine LiFePO4 in lithium-ion batteries. *Nanoscale* **5**, 780–787 (2013).

53. Bonilla, M. R., Lozano, A., Escribano, B., Carrasco, J. & Akhmatskaya, E. Revealing the Mechanism of Sodium Diffusion in NaxFePO4 Using an Improved Force Field. *Journal of Physical Chemistry C* **122**, 8065–8075 (2018).

54. Saracibar, A. *et al.* Investigation of sodium insertion-extraction in olivine Na: XFePO4 (0 ≤ x ≤ 1) using first-principles calculations. *Physical Chemistry Chemical Physics* **18**, 13045–13051 (2016).

55. Dokko, K. *et al.* In situ observation of LiNiO2 single-particle fracture during Li-Ion extraction and insertion. *Electrochemical and Solid-State Letters* **3**, 125–127 (2000).

56. Wang, D., Wu, X., Wang, Z. & Chen, L. Cracking causing cyclic instability of LiFePO4 cathode material. *J Power Sources* **140**, 125–128 (2005).

57. Zhang, Z. *et al.* Dual-doping to suppress cracking in spinel LiMn2O4: A joint theoretical and experimental study. *Physical Chemistry Chemical Physics* **18**, 6893–6900 (2016).

58. Peled, E. & Menkin, S. Review—SEI: Past, Present and Future. *J Electrochem Soc* **164**, A1703–A1719 (2017).

59. Yu, X. & Manthiram, A. Electrode-electrolyte interfaces in lithium-based batteries. *Energy and Environmental Science* vol. 11 527–543 Preprint at https://doi.org/10.1039/c7ee02555f (2018).

60. Xu, K. Nonaqueous liquid electrolytes for lithium-based rechargeable batteries. *Chem Rev* **104**, 4303–4417 (2004).

61. Kabir, M. M. & Demirocak, D. E. Degradation mechanisms in Li-ion batteries: a state-of-the-art review. *Int J Energy Res* **41**, 1963–1986 (2017).

62. Boebinger, M. G. *et al.* Avoiding Fracture in a Conversion Battery Material through Reaction with Larger Ions. *Joule* **2**, 1783–1799 (2018).

63. Cortes, F. J. Q., Boebinger, M. G., Xu, M., Ulvestad, A. & McDowell, M. T. Operando Synchrotron Measurement of Strain Evolution in Individual Alloying Anode Particles within Lithium Batteries. *ACS Energy Lett* **3**, 349–355 (2018).

64. Casas-Cabanas, M. *et al.* Crystal chemistry of Na insertion/deinsertion in FePO 4-NaFePO 4. *J Mater Chem* **22**, 17421–17423 (2012).

65. Zhu, W. *et al.* Application of Operando X-ray Diffractometry in Various Aspects of the Investigations of Lithium/Sodium-Ion Batteries. *Energies* vol. 11 Preprint at https://doi.org/10.3390/en11112963 (2018).

66. Lim, L. Y., Liu, N., Cui, Y. & Toney, M. F. Understanding phase transformation in crystalline Ge anodes for Li-ion batteries. *Chemistry of Materials* **26**, 3739–3746 (2014).

67. Heubner, C., Heiden, S., Schneider, M. & Michaelis, A. In-situ preparation and electrochemical characterization of submicron sized NaFePO4 cathode material for sodium-ion batteries. *Electrochim Acta* **233**, 78–84 (2017).

68. Heubner, C., Heiden, S., Matthey, B., Schneider, M. & Michaelis, A. Sodiation vs. Lithiation of FePO4: A comparative kinetic study. *Electrochim Acta* **216**, 412–419 (2016).

69.   Whiteside, A., Fisher, C. A. J., Parker, S. C. & Saiful Islam, M. Particle shapes and surface structures of olivine NaFePO4 in comparison to LiFePO4. *Physical Chemistry Chemical Physics* **16**, 21788–21794 (2014).

70.   Niu, J. *et al.* In situ observation of random solid solution zone in LiFePO4 electrode. *Nano Lett* **14**, 4005–4010 (2014).

71.   Liu, H. *et al.* Capturing metastable structures during high-rate cycling of LiFePO 4 nanoparticle electrodes. *Science (1979)* **344**, (2014).

72.   Ramana, C. v., Mauger, A., Gendron, F., Julien, C. M. & Zaghib, K. Study of the Li-insertion/extraction process in LiFePO4/FePO4. *J Power Sources* **187**, 555–564 (2009).

73.   Wang, J. J., Chen-Wiegart, Y. C. K. & Wang, J. J. In operando tracking phase transformation evolution of lithium iron phosphate with hard X-ray microscopy. *Nat Commun* **5**, 1–10 (2014).

74.   Li, D. & Zhou, H. Two-phase transition of Li-intercalation compounds in Li-ion batteries. *Materials Today* **17**, 451–463 (2014).

75.   Laffont, L. *et al.* Study of the LiFePO4/FePO4two-phase system by high-resolution electron energy loss spectroscopy. *Chemistry of Materials* **18**, 5520–5529 (2006).

76.   Tang, K., Yu, X., Sun, J., Li, H. & Huang, X. Kinetic analysis on LiFePO4 thin films by CV, GITT, and EIS. *Electrochim Acta* **56**, 4869–4875 (2011).

77.   Koltypin, M., Aurbach, D., Nazar, L. & Ellis, B. On the stability of LiFeP O4 olivine cathodes under various conditions (electrolyte solutions, temperatures). *Electrochemical and Solid-State Letters* **10**, A40–A44 (2007).

78.   Moreau, P., Guyomard, D., Gaubicher, J. & Boucher, F. Structure and stability of sodium intercalated phases in olivine FePO 4. *Chemistry of Materials* **22**, 4126–4128 (2010).

79.   Galceran, M. *et al.* Na-vacancy and charge ordering in Na≈2/3FePO4. *Chemistry of Materials* **26**, 3289–3294 (2014).

80.   Zhang, X. *et al.* Direct view on the phase evolution in individual LiFePO 4 nanoparticles during Li-ion battery cycling. *Nat Commun* **6**, (2015).

81.   Padhi, A. K. Phospho-olivines as Positive-Electrode Materials for Rechargeable Lithium Batteries. *J Electrochem Soc* **144**, 1188 (1997).

82.   Delmas, C., Maccario, M., Croguennec, L., le Cras, F. & Weill, F. Lithium deintercalation in LiFePO4 nanoparticles via a domino-cascade model. *Nat Mater* **7**, 665–671 (2008).

83.   Malik, R., Abdellahi, A. & Ceder, G. A Critical Review of the Li Insertion Mechanisms in LiFePO4 Electrodes. *J Electrochem Soc* **160**, A3179–A3197 (2013).

84.   Delacourt, C., Poizot, P., Tarascon, J. M. & Masquelier, C. The existence of a temperature-driven solid solution in Li xFePO4 for $0 \leq x \leq 1$. *Nat Mater* **4**, 254–260 (2005).

85.   Orikasa, Y. *et al.* Direct observation of a metastable crystal phase of LixFePO 4 under electrochemical phase transition. *J Am Chem Soc* **135**, 5497–5500 (2013).

86.   Lv, W. *et al.* Space matters: Li+ conduction versus strain effect at FePO4/LiFePO4 interface. *Appl Phys Lett* **108**, (2016).

87.   Kao, Y. H. *et al.* Overpotential-dependent phase transformation pathways in lithium iron phosphate battery electrodes. *Chemistry of Materials* **22**, 5845–5855 (2010).

88.   Tang, M., Carter, W. C., Belak, J. F. & Chiang, Y. M. Modeling the competing phase transition pathways in nanoscale olivine electrodes. *Electrochim Acta* **56**, 969–976 (2010).

89.   Tang, M., Carter, W. C. & Chiang, Y.-M. Electrochemically Driven Phase Transitions in Insertion Electrodes for Lithium-Ion Batteries: Examples in Lithium Metal Phosphate Olivines. *Annu Rev Mater Res* **40**, 501–529 (2010).

90.   Tealdi, C., Heath, J. & Islam, M. S. Feeling the strain: Enhancing ionic transport in olivine phosphate cathodes for Li- and Na-ion batteries through strain effects. *J Mater Chem A Mater* **4**, 6998–7004 (2016).

91.   Wei, Z. *et al.* From Crystalline to Amorphous: An Effective Avenue to Engineer High-Performance Electrode Materials for Sodium-Ion Batteries. *Adv Mater Interfaces* **5**, (2018).

92.   Hwang, J. Y., Myung, S. T. & Sun, Y. K. Sodium-ion batteries: Present and future. *Chem Soc Rev* **46**, 3529–3614 (2017).

93.   Pasta, M. *et al.* Full open-framework batteries for stationary energy storage. *Nat Commun* **5**, (2014).

94.   Xiong, F., Tao, H. & Yue, Y. Role of Amorphous Phases in Enhancing Performances of Electrode Materials for Alkali Ion Batteries. *Frontiers in Materials* vol. 6 Preprint at https://doi.org/10.3389/fmats.2019.00328 (2020).

95.   Gaubicher, J. *et al.* Abnormal operando structural behavior of sodium battery material: Influence of dynamic on phase diagram of NaxFePO4. *Electrochem commun* **38**, 104–106 (2014).

96.   Hosaka, T., Shimamura, T., Kubota, K. & Komaba, S. Polyanionic Compounds for Potassium-Ion Batteries. *Chemical Record* **19**, 735–745 (2019).

97.   Jin, T. *et al.* Polyanion-type cathode materials for sodium-ion batteries. *Chem Soc Rev* **49**, 2342–2377 (2020).

98. Özdogru, B. *et al.* Elucidating cycling rate-dependent electrochemical strains in sodium iron phosphate cathodes for Na-ion batteries. *J Power Sources* **507**, (2021).

99. McDowell, M. T., Lee, S. W., Nix, W. D. & Cui, Y. 25th anniversary article: Understanding the lithiation of silicon and other alloying anodes for lithium-ion batteries. *Advanced Materials* vol. 25 4966–4985 Preprint at https://doi.org/10.1002/adma.201301795 (2013).

100. Irisarri, E., Ponrouch, A. & Palacin, M. R. Review—Hard Carbon Negative Electrode Materials for Sodium-Ion Batteries. *J Electrochem Soc* **162**, A2476–A2482 (2015).

101. Li, Y., Lu, Y., Adelhelm, P., Titirici, M. M. & Hu, Y. S. Intercalation chemistry of graphite: Alkali metal ions and beyond. *Chemical Society Reviews* vol. 48 4655–4687 Preprint at https://doi.org/10.1039/c9cs00162j (2019).

102. van der Ven, A., Deng, Z., Banerjee, S. & Ong, S. P. Rechargeable Alkali-Ion Battery Materials: Theory and Computation. *Chemical Reviews* vol. 120 6977–7019 Preprint at https://doi.org/10.1021/acs.chemrev.9b00601 (2020).

103. Hosaka, T., Kubota, K., Hameed, A. S. & Komaba, S. Research Development on K-Ion Batteries. *Chem Rev* (2020) doi:10.1021/acs.chemrev.9b00463.

104. Jones, E. M. C., Çapraz, Ö. Ö., White, S. R. & Sottos, N. R. Reversible and Irreversible Deformation Mechanisms of Composite Graphite Electrodes in Lithium-Ion Batteries. *J Electrochem Soc* **163**, A1965–A1974 (2016).

105. Eastwood, D. S. *et al.* Lithiation-induced dilation mapping in a lithium-ion battery electrode by 3D X-ray microscopy and digital volume correlation. *Adv Energy Mater* **4**, 1300506 (2014).

106. Qi, Y. & Harris, S. J. In Situ Observation of Strains during Lithiation of a Graphite Electrode. *J Electrochem Soc* **157**, A741 (2010).

107. Özdogru, B., Dykes, H., Padwal, S., Harimkar, S. & Çapraz, Ö. Electrochemical strain evolution in iron phosphate composite cathodes during lithium and sodium ion intercalation. *Electrochim Acta* **353**, (2020).

108. Mathew, V. *et al.* Amorphous iron phosphate: Potential host for various charge carrier ions. *NPG Asia Mater* **6**, (2014).

109. Speight, Dr. J. G. *Lange's Handbook of Chemistry*. (McGraw-Hill Education, 2017).

110. Memarzadeh Lotfabad, E., Kalisvaart, P., Kohandehghan, A., Karpuzov, D. & Mitlin, D. Origin of non-SEI related coulombic efficiency loss in carbons tested against Na and Li. *J. Mater. Chem. A* **2**, 19685–19695 (2014).

111. de la Llave, E. *et al.* Comparison between Na-Ion and Li-Ion Cells: Understanding the Critical Role of the Cathodes Stability and the Anodes Pretreatment on the Cells Behavior. *ACS Appl Mater Interfaces* **8**, 1867–1875 (2016).

112. Dai, Z., Mani, U., Tan, H. T. & Yan, Q. Advanced Cathode Materials for Sodium-Ion Batteries: What Determines Our Choices? *Small Methods* **1**, 1700098 (2017).

113. Zhu, Y. *et al.* In situ atomic-scale imaging of phase boundary migration in FePO 4 microparticles during electrochemical lithiation. *Advanced Materials* **25**, 5461–5466 (2013).

114. Park, J. Y. *et al.* Atomic visualization of a non-equilibrium sodiation pathway in copper sulfide. *Nat Commun* **9**, 1–7 (2018).

115. Özdogru, B. *et al.* In Situ Probing Potassium-Ion Intercalation-Induced Amorphization in Crystalline Iron Phosphate Cathode Materials. *Nano Lett* **21**, 7579–7586 (2021).

116. Li, M., Lu, J., Chen, Z. & Amine, K. 30 Years of Lithium-Ion Batteries. *Advanced Materials* **30**, 1–24 (2018).

117. Berckmans, G. *et al.* Cost projection of state of the art lithium-ion batteries for electric vehicles up to 2030. *Energies (Basel)* **10**, (2017).

118. Slater, M. D., Kim, D., Lee, E. & Johnson, C. S. Sodium-ion batteries. *Adv Funct Mater* **23**, 947–958 (2013).

119. Song, J., Xiao, B., Lin, Y., Xu, K. & Li, X. Interphases in Sodium-Ion Batteries. *Advanced Energy Materials* vol. 8 Preprint at https://doi.org/10.1002/aenm.201703082 (2018).

120. Zhao, K., Pharr, M., Cai, S., Vlassak, J. J. & Suo, Z. Large plastic deformation in high-capacity lithium-ion batteries caused by charge and discharge. *Journal of the American Ceramic Society* **94**, s226–s235 (2011).

121. Wang, C. M. *et al.* In situ TEM investigation of congruent phase transition and structural evolution of nanostructured silicon/carbon anode for lithium ion batteries. *Nano Lett* **12**, 1624–1632 (2012).

122. Gu, M. *et al.* In situ TEM study of lithiation behavior of silicon nanoparticles attached to and embedded in a carbon matrix. *ACS Nano* **6**, 8439–8447 (2012).

123. Liu, X. H. *et al.* In situ TEM experiments of electrochemical lithiation and delithiation of individual nanostructures. *Adv Energy Mater* **2**, 722–741 (2012).

124. Xie, H. *et al.* β-SnSb for Sodium Ion Battery Anodes: Phase Transformations Responsible for Enhanced Cycling Stability Revealed by in Situ TEM. *ACS Energy Lett* **3**, 1670–1676 (2018).

125. Lu, X. *et al.* Germanium as a Sodium Ion Battery Material: In Situ TEM Reveals Fast Sodiation Kinetics with High Capacity. *Chemistry of Materials* **28**, 1236–1242 (2016).

126. Yang, Z. *et al.* Facile synthesis and in situ transmission electron microscopy investigation of a highly stable Sb2Te3/C nanocomposite for sodium-ion batteries. *Energy Storage Mater* **9**, 214–220 (2017).

127. Xia, W. *et al.* Probing microstructure and phase evolution of α-MoO3 nanobelts for sodium-ion batteries by in situ transmission electron microscopy. *Nano Energy* **27**, 447–456 (2016).

128. Wang, X. *et al.* In Situ Electron Microscopy Investigation of Sodiation of Titanium Disulfide Nanoflakes. *ACS Nano* **13**, 9421–9430 (2019).

129. Tokranov, A., Sheldon, B. W., Li, C., Minne, S. & Xiao, X. In situ atomic force microscopy study of initial solid electrolyte interphase formation on silicon electrodes for Li-ion batteries. *ACS Appl Mater Interfaces* **6**, 6672–6686 (2014).

130. Demirocak, D. E. & Bhushan, B. In situ atomic force microscopy analysis of morphology and particle size changes in Lithium Iron Phosphate cathode during discharge. *J Colloid Interface Sci* **423**, 151–157 (2014).

131. Park, J. *et al.* In situ atomic force microscopy studies on lithium (de)intercalation- induced morphology changes in LixCoO2 micro-machined thin film electrodesq. *J Power Sources* **222**, 417–425 (2013).

132. Lacey, S. D. *et al.* Atomic force microscopy studies on molybdenum disulfide flakes as sodium-ion anodes. *Nano Lett* **15**, 1018–1024 (2015).

133. Han, M. *et al.* In Situ Atomic Force Microscopic Studies of Single Tin Nanoparticle: Sodiation and Desodiation in Liquid Electrolyte. *ACS Appl Mater Interfaces* **9**, 28620–28626 (2017).

134. Wang, J., Eng, C., Chen-Wiegart, Y. C. K. & Wang, J. Probing three-dimensional sodiation-desodiation equilibrium in sodium-ion batteries by in situ hard X-ray nanotomography. *Nat Commun* **6**, 1–9 (2015).

135. Ou, X. *et al.* In situ X-ray diffraction investigation of CoSe2 anode for Na-ion storage: Effect of cut-off voltage on cycling stability. *Electrochim Acta* **258**, 1387–1396 (2017).

136. Talaie, E., Duffort, V., Smith, H. L., Fultz, B. & Nazar, L. F. Structure of the high voltage phase of layered P2-Na2/3-z[Mn1/2Fe1/2]O2 and the positive effect of Ni substitution on its stability. *Energy Environ Sci* **8**, 2512–2523 (2015).

137. Li, M., Wang, Z., Fu, J., Ma, K. & Detsi, E. In situ electrochemical dilatometry study of capacity fading in nanoporous Ge-based Na-ion battery anodes. *Scr Mater* **164**, 52–56 (2019).

138. Karimi, N., Varzi, A. & Passerini, S. A comprehensive insight into the volumetric response of graphite electrodes upon sodium co-intercalation in ether-based electrolytes. *Electrochim Acta* **304**, 474–486 (2019).

139. Tavassol, H. *et al.* Surface Coverage and SEI Induced Electrochemical Surface Stress Changes during Li Deposition in a Model System for Li-Ion Battery Anodes. *J Electrochem Soc* **160**, A888–A896 (2013).

140. Çapraz, Ö. Ö., Hebert, K. R. & Shrotriya, P. In Situ Stress Measurement During Aluminum Anodizing Using Phase-Shifting Curvature Interferometry. *J Electrochem Soc* **160**, D501–D506 (2013).

141. Cheng, Y. T. & Verbrugge, M. W. The influence of surface mechanics on diffusion induced stresses within spherical nanoparticles. *J Appl Phys* **104**, (2008).

142. Cheng, Y.-T. & Verbrugge, M. W. Diffusion-Induced Stress, Interfacial Charge Transfer, and Criteria for Avoiding Crack Initiation of Electrode Particles. *J Electrochem Soc* **157**, A508 (2010).

143. Cheng, Y. T. & Verbrugge, M. W. Evolution of stress within a spherical insertion electrode particle under potentiostatic and galvanostatic operation. *J Power Sources* **190**, 453–460 (2009).

144. Christensen, J. & Newman, J. A Mathematical Model of Stress Generation and Fracture in Lithium Manganese Oxide. *J Electrochem Soc* **153**, A1019 (2006).

145. Christensen, J. & Newman, J. Stress generation and fracture in lithium insertion materials. *Journal of Solid State Electrochemistry* **10**, 293–319 (2006).

146. Li, G. & Monroe, C. W. Multiscale Lithium-Battery Modeling from Materials to Cells. *Annu Rev Chem Biomol Eng* **11**, 277–310 (2020).

147. Chen, J., Thapa, A. K. & Berfield, T. A. In-situ characterization of strain in lithium battery working electrodes. *J Power Sources* **271**, 406–413 (2014).

148. Lu, B. *et al.* Voltage hysteresis of lithium ion batteries caused by mechanical stress. *Physical Chemistry Chemical Physics* **18**, 4721–4727 (2016).

149. Eum, D. *et al.* Voltage decay and redox asymmetry mitigation by reversible cation migration in lithium-rich layered oxide electrodes. *Nat Mater* **19**, 419–427 (2020).

150. Srinivasan, V. & Newman, J. Discharge Model for the Lithium Iron-Phosphate Electrode. *J Electrochem Soc* **151**, A1517 (2004).

151. Mukhopadhyay, A., Tokranov, A., Sena, K., Xiao, X. & Sheldon, B. W. Thin film graphite electrodes with low stress generation during Li-intercalation. *Carbon N Y* **49**, 2742–2749 (2011).

152. Pyun, S. il, Go, J. Y. & Jang, T. S. An investigation of intercalation-induced stresses generated during lithium transport through Li1-δCoO2 film electrode using a laser beam deflection method. *Electrochim Acta* **49**, 4477–4486 (2004).

153. Iltchev, N., Chen, Y., Okada, S. & Yamaki, J. I. LiFePO4 storage at room and elevated temperatures. in *Journal of Power Sources* vols 119–121 749–754 (2003).

154. Zhao, L. Self-reporting of Mn ion dissolution and self-stabilization of cathode-electrolyte interface in lithium ion batteries. (2020).

155. Smith, A. J., Burns, J. C., Zhao, X., Xiong, D. & Dahn, J. R. A High Precision Coulometry Study of the SEI Growth in Li/Graphite Cells. *J Electrochem Soc* **158**, A447 (2011).

156. Qian, Y. *et al.* Influence of electrolyte additives on the cathode electrolyte interphase (CEI) formation on LiNi1/3Mn1/3Co1/3O2 in half cells with Li metal counter electrode. *J Power Sources* **329**, 31–40 (2016).

157. Wang, A., Kadam, S., Li, H., Shi, S. & Qi, Y. Review on modeling of the anode solid electrolyte interphase (SEI) for lithium-ion batteries. *npj Computational Materials* vol. 4 Preprint at https://doi.org/10.1038/s41524-018-0064-0 (2018).

158. Ploehn, H. J., Ramadass, P. & White, R. E. Solvent Diffusion Model for Aging of Lithium-Ion Battery Cells. *J Electrochem Soc* **151**, A456 (2004).

159. Attia, P. M., Das, S., Harris, S. J., Bazant, M. Z. & Chueh, W. C. Electrochemical Kinetics of SEI Growth on Carbon Black: Part I. Experiments. *Journal of The Electrochemical Society* vol. 166 E97–E106 Preprint at https://doi.org/10.1149/2.0231904jes (2019).

160. Malmgren, S. *et al.* Comparing anode and cathode electrode/electrolyte interface composition and morphology using soft and hard X-ray photoelectron spectroscopy. *Electrochim Acta* **97**, 23–32 (2013).

161. Zheng, H., Yang, R., Liu, G., Song, X. & Battaglia, V. S. Cooperation between active material, polymeric binder and conductive carbon additive in lithium ion battery cathode. *Journal of Physical Chemistry C* **116**, 4875–4882 (2012).

162. Chen, J., Liu, J., Qi, Y., Sun, T. & Li, X. Unveiling the Roles of Binder in the Mechanical Integrity of Electrodes for Lithium-Ion Batteries. *J Electrochem Soc* **160**, A1502–A1509 (2013).

163. Lu, Z. *et al.* Nonfilling carbon coating of porous silicon micrometer-sized particles for high-performance lithium battery anodes. *ACS Nano* **9**, 2540–2547 (2015).

164. Shpigel, N. *et al.* Non-Invasive in Situ Dynamic Monitoring of Elastic Properties of Composite Battery Electrodes by EQCM-D. *Angewandte Chemie - International Edition* **54**, 12353–12356 (2015).

165. McGee, S. & McGullough, R. L. Combining rules for predicting the thermoelastic properties of particulate filled polymers, polymers, polyblends, and foams. *Polym Compos* **2**, 149–161 (1981).

166. Zhang, X., Shyy, W. & Marie Sastry, A. Numerical Simulation of Intercalation-Induced Stress in Li-Ion Battery Electrode Particles. *J Electrochem Soc* **154**, A910 (2007).

167. Woodford, W. H., Chiang, Y.-M. & Carter, W. C. "Electrochemical Shock" of Intercalation Electrodes: A Fracture Mechanics Analysis. *J Electrochem Soc* **157**, A1052 (2010).

168. Bucci, G. *et al.* The Effect of Stress on Battery-Electrode Capacity. *J Electrochem Soc* **164**, A645–A654 (2017).

169. Zhu, Y. & Wang, C. Strain accommodation and potential hysteresis of LiFePO4 cathodes during lithium ion insertion/extraction. *J Power Sources* **196**, 1442–1448 (2011).

170. Soni, S. K., Sheldon, B. W., Xiao, X., Bower, A. F. & Verbrugge, M. W. Diffusion Mediated Lithiation Stresses in Si Thin Film Electrodes. *J Electrochem Soc* **159**, A1520–A1527 (2012).

171. Sethuraman, V. A., Srinivasan, V., Bower, A. F. & Guduru, P. R. *In Situ Measurements of Stress-Potential Coupling in Lithiated Silicon*. *Journal of The Electrochemical Society* vol. 157 (2010).

172. Grey, C. P. & Hall, D. S. Prospects for lithium-ion batteries and beyond—a 2030 vision. *Nat Commun* **11**, 2–5 (2020).

173. Nayak, P. K. *et al.* Review on Challenges and Recent Advances in the Electrochemical Performance of High Capacity Li- and Mn-Rich Cathode Materials for Li-Ion Batteries. *Adv Energy Mater* **8**, 1–16 (2018).

174. Chen, G., Song, X. & Richardson, T. J. Electron microscopy study of the LiFePO 4 to FePO 4 phase transition. *Electrochemical and Solid-State Letters* **9**, 4–8 (2006).

175. Yu, Y. S. *et al.* Dependence on Crystal Size of the Nanoscale Chemical Phase Distribution and Fracture in LixFePO4. *Nano Lett* **15**, 4282–4288 (2015).

176. Xu, Z., Rahman, M. M., Mu, L., Liu, Y. & Lin, F. Chemomechanical behaviors of layered cathode materials in alkali metal ion batteries. *J Mater Chem A Mater* **6**, 21859–21884 (2018).

177. Zubi, G., Dufo-López, R., Carvalho, M. & Pasaoglu, G. The lithium-ion battery: State of the art and future perspectives. *Renewable and Sustainable Energy Reviews* **89**, 292–308 (2018).

178. Nitta, N., Wu, F., Lee, J. T. & Yushin, G. Li-ion battery materials: Present and future. *Materials Today* **18**, 252–264 (2015).

179. Li, J. & Ma, Z.-F. Past and Present of LiFePO4: From Fundamental Research to Industrial Applications. *Chem* **5**, 3–6 (2019).

180. Dargaville, S. & Farrell, T. W. Predicting Active Material Utilization in LiFePO[sub 4] Electrodes Using a Multiscale Mathematical Model. *J Electrochem Soc* **157**, A830 (2010).

181. Takahashi, I. *et al.* Irreversible phase transition between LiFePO4 and FePO4 during high-rate charge-discharge reaction by operando X-ray diffraction. *J Power Sources* **309**, 122–126 (2016).

182. Ouvrard, G. *et al.* Heterogeneous behaviour of the lithium battery composite electrode LiFePO4. *J Power Sources* **229**, 16–21 (2013).

183. Zhang, X. *et al.* Rate-induced solubility and suppression of the first-order phase transition in olivine LiFePO4. *Nano Lett* **14**, 2279–2285 (2014).

184. Koyama, Y. *et al.* Hidden Two-Step Phase Transition and Competing Reaction Pathways in LiFePO4. *Chemistry of Materials* **29**, 2855–2863 (2017).

185. Li, Y. *et al.* Current-induced transition from particle-by-particle to concurrent intercalation in phase-separating battery electrodes. *Nat Mater* **13**, 1149–1156 (2014).

186. Özdogru, B. *et al.* Elucidating cycling rate-dependent electrochemical strains in sodium iron phosphate cathodes for Na-ion batteries. *J Power Sources* **507**, (2021).

187. Liu, C., Neale, Z. G. & Cao, G. Understanding electrochemical potentials of cathode materials in rechargeable batteries. *Materials Today* vol. 19 109–123 Preprint at https://doi.org/10.1016/j.mattod.2015.10.009 (2016).

188. Safari, M. & Delacourt, C. Mathematical Modeling of Lithium Iron Phosphate Electrode: Galvanostatic Charge/Discharge and Path Dependence. *J Electrochem Soc* **158**, A63 (2011).

189. Zhan, C., Wu, T., Lu, J. & Amine, K. Dissolution, migration, and deposition of transition metal ions in Li-ion batteries exemplified by Mn-based cathodes-A critical review. *Energy and Environmental Science* vol. 11 243–257 Preprint at https://doi.org/10.1039/c7ee03122j (2018).

190. Wandt, J. *et al.* Transition metal dissolution and deposition in Li-ion batteries investigated by operando X-ray absorption spectroscopy. *J Mater Chem A Mater* **4**, 18300–18305 (2016).

191. Aurbach, D. *et al.* Review on electrode-electrolyte solution interactions, related to cathode materials for Li-ion batteries. *Journal of Power Sources* vol. 165 491–499 Preprint at https://doi.org/10.1016/j.jpowsour.2006.10.025 (2007).

192. Jow, T. R., Delp, S. A., Allen, J. L., Jones, J.-P. & Smart, M. C. Factors Limiting Li + Charge Transfer Kinetics in Li-Ion Batteries . *J Electrochem Soc* **165**, A361–A367 (2018).

193. Qian, Y. *et al.* How electrolyte additives work in Li-ion batteries. *Energy Storage Mater* **20**, 208–215 (2019).

194. Khodr, Z. *et al.* Electrochemical Study of Functional Additives for Li-Ion Batteries. *J Electrochem Soc* **167**, 120535 (2020).

195. Zhao, L., Chénard, E., Çapraz, Ö. Ö., Sottos, N. R. & White, S. R. Direct Detection of Manganese Ions in Organic Electrolyte by UV-vis Spectroscopy. *J Electrochem Soc* **165**, A345–A348 (2018).

196. Ellis, L. D., Allen, J. P., Hill, I. G. & Dahn, J. R. High-Precision Coulometry Studies of the Impact of Temperature and Time on SEI Formation in Li-Ion Cells. *J Electrochem Soc* **165**, A1529–A1536 (2018).

197. Baggetto, L. *et al.* Intrinsic thermodynamic and kinetic properties of Sb electrodes for Li-ion and Na-ion batteries: Experiment and theory. *J Mater Chem A Mater* **1**, 7985–7994 (2013).

198. Song, J. *et al.* A comparative study of pomegranate Sb@C yolk-shell microspheres as Li and Na-ion battery anodes. *Nanoscale* **11**, 348–355 (2019).

199. Islam, M. S., Driscoll, D. J., Fisher, C. A. J. & Slater, P. R. Atomic-scale investigation of defects, dopants, and lithium transport in the LiFePO4 olivine-type battery material. *Chemistry of Materials* **17**, 5085–5092 (2005).

200. Hess, M., Sasaki, T., Villevieille, C. & Novák, P. Combined operando X-ray diffraction-electrochemical impedance spectroscopy detecting solid solution reactions of LiFePO4 in batteries. *Nat Commun* **6**, (2015).

201. Chang, H. H. *et al.* Study on dynamics of structural transformation during charge/discharge of LiFePO4 cathode. *Electrochem commun* **10**, 335–339 (2008).

202. Goodenough, J. B. & Park, K. S. The Li-ion rechargeable battery: A perspective. *J Am Chem Soc* **135**, 1167–1176 (2013).

203. Banerjee, A., Wang, X., Fang, C., Wu, E. A. & Meng, Y. S. Interfaces and Interphases in All-Solid-State Batteries with Inorganic Solid Electrolytes. *Chem Rev* **120**, 6878–6933 (2020).

204. Lewis, J. A., Tippens, J., Cortes, F. J. Q. & McDowell, M. T. Chemo-Mechanical Challenges in Solid-State Batteries. *Trends Chem* **1**, 845–857 (2019).

205. Cheng, L. *et al.* Garnet Electrolyte Surface Degradation and Recovery. *ACS Appl Energy Mater* **1**, 7244–7252 (2018).

206. Porz, L. *et al.* Mechanism of Lithium Metal Penetration through Inorganic Solid Electrolytes. *Adv Energy Mater* **7**, 1701003 (2017).

207. Otoyama, M. *et al.* Visualization and Control of Chemically Induced Crack Formation in All-Solid-State Lithium-Metal Batteries with Sulfide Electrolyte. *ACS Appl Mater Interfaces* **13**, 5000–5007 (2021).

208. Dixit, M. B. *et al.* In Situ Investigation of Chemomechanical Effects in Thiophosphate Solid Electrolytes. *Matter* **3**, 2138–2159 (2020).

209. Tippens, J. *et al.* Visualizing Chemomechanical Degradation of a Solid-State Battery Electrolyte. *ACS Energy Lett* **4**, 1475–1483 (2019).

210. Nanda, J. *et al.* Unraveling the Nanoscale Heterogeneity of Solid Electrolyte Interphase Using Tip-Enhanced Raman Spectroscopy. *Joule* **3**, 2001–2019 (2019).

211. Kazyak, E. *et al.* Li Penetration in Ceramic Solid Electrolytes: Operando Microscopy Analysis of Morphology, Propagation, and Reversibility. *Matter* **2**, 1025–1048 (2020).

212. Lewis, J. A. *et al.* Linking void and interphase evolution to electrochemistry in solid-state batteries using operando X-ray tomography. *Nat Mater* **20**, 503–510 (2021).

213. Wenzel, S. *et al.* Direct Observation of the Interfacial Instability of the Fast Ionic Conductor Li10GeP2S12 at the Lithium Metal Anode. *Chemistry of Materials* **28**, 2400–2407 (2016).

214. Han, F. *et al.* High electronic conductivity as the origin of lithium dendrite formation within solid electrolytes. *Nat Energy* **4**, 187–196 (2019).

215. Özdogru, B., Koohbor, B. & Çapraz, Ö. Ö. The impact of alkali-ion intercalation on redox chemistry and mechanical deformations: Case study on intercalation of Li, Na, and K ions into FePO 4 cathode . *Electrochemical Science Advances* 1–7 (2021) doi:10.1002/elsa.202100106.

216. Koohbor, B., Sang, L., Çapraz, Ö. Ö., Gewirth, A. A. & Sottos, N. R. In Situ Strain Measurement in Solid-State Li-Ion Battery Electrodes. *J Electrochem Soc* **168**, 010516 (2021).

217. Golozar, M. *et al.* Direct observation of lithium metal dendrites with ceramic solid electrolyte. *Sci Rep* **10**, 1–11 (2020).

218. Lewis, J. A. *et al.* Interphase Morphology between a Solid-State Electrolyte and Lithium Controls Cell Failure. *ACS Energy Lett* **4**, 591–599 (2019).

219. Davis, A. L. *et al.* Rate Limitations in Composite Solid-State Battery Electrodes: Revealing Heterogeneity with Operando Microscopy. *ACS Energy Lett* **6**, 2993–3003 (2021).

220. Tu, Q., Shi, T., Chakravarthy, S. & Ceder, G. Understanding metal propagation in solid electrolytes due to mixed ionic-electronic conduction. *Matter* **4**, 3248–3268 (2021).

221. Sheldon, B. W., Soni, S. K., Xiao, X. & Qi, Y. Stress contributions to solution thermodynamics in Li-Si alloys. *Electrochemical and Solid-State Letters* **15**, A9 (2012).

222. Mistry, A. & Mukherjee, P. P. Molar Volume Mismatch: A Malefactor for Irregular Metallic Electrodeposition with Solid Electrolytes. *J Electrochem Soc* **167**, 082510 (2020).

223. Monroe, C. & Newman, J. The Impact of Elastic Deformation on Deposition Kinetics at Lithium/Polymer Interfaces. *J Electrochem Soc* **152**, A396 (2005).

224. Ganser, M. *et al.* An Extended Formulation of Butler-Volmer Electrochemical Reaction Kinetics Including the Influence of Mechanics. *J Electrochem Soc* **166**, H167–H176 (2019).

225. Cheng, Z. *et al.* Good Solid-State Electrolytes Have Low, Glass-Like Thermal Conductivity. *Small* **17**, 2101693 (2021).

226. Tu, Q., Barroso-Luque, L., Shi, T. & Ceder, G. Electrodeposition and Mechanical Stability at Lithium-Solid Electrolyte Interface during Plating in Solid-State Batteries. *Cell Rep Phys Sci* **1**, 100106 (2020).

227. Gribble, D. A. *et al.* Mechanistic Elucidation of Electronically Conductive PEDOT:PSS Tailored Binder for a Potassium-Ion Battery Graphite Anode: Electrochemical, Mechanical, and Thermal Safety Aspects. *Adv Energy Mater* **12**, 2103439 (2022).

228. Zhang, B. *et al.* Correlation Between Microstructure and Na Storage Behavior in Hard Carbon. *Adv Energy Mater* **6**, 1501588 (2016).

229. Allan, P. K. *et al.* Tracking Sodium-Antimonide Phase Transformations in Sodium-Ion Anodes: Insights from Operando Pair Distribution Function Analysis and Solid-State NMR Spectroscopy. *J Am Chem Soc* **138**, 2352–2365 (2016).

230. Wang, J. W., Liu, X. H., Mao, S. X. & Huang, J. Y. Microstructural evolution of tin nanoparticles during in situ sodium insertion and extraction. *Nano Lett* **12**, 5897–5902 (2012).

231. Weppner, W. & Huggins, R. A. Determination of the Kinetic Parameters of Mixed-Conducting Electrodes and Application to the System Li3Sb. *J Electrochem Soc* **124**, 1569–1578 (1977).

232. Prosini, P. P., Lisi, M., Zane, D. & Pasquali, M. Determination of the chemical diffusion coefficient of lithium in LiFePO4. *Solid State Ion* **148**, 45–51 (2002).

233. Morgan, D., van der Ven, A. & Ceder, G. Li Conductivity in LixMPO4 (M = Mn, Fe, Co, Ni) Olivine Materials. *Electrochemical and Solid-State Letters* **7**, 30–33 (2004).

234. Nishimura, S. I. *et al.* Experimental visualization of lithium diffusion in LixFePO 4. *Nat Mater* **7**, 707–711 (2008).

235. Zhu, Y., Gao, T., Fan, X., Han, F. & Wang, C. Electrochemical Techniques for Intercalation Electrode Materials in Rechargeable Batteries. *Acc Chem Res* **50**, 1022–1031 (2017).

236. de Jong, M. *et al.* Charting the complete elastic properties of inorganic crystalline compounds. *Sci Data* **2**, 1–13 (2015).

237. Zhang, T. & Kamlah, M. Sodium Ion Batteries Particles: Phase-Field Modeling with Coupling of Cahn-Hilliard Equation and Finite Deformation Elasticity. *J Electrochem Soc* **165**, A1997–A2007 (2018).

238. Sigma-Aldrich. Sodium carboxymethyl cellulose average Mw: 90,000. https://www.sigmaaldrich.com/CO/es/product/aldrich/419273%0Ahttps://www.sigmaaldrich.com/catalog/product/aldrich/419273?lang=es&region=ES.

239. Carbon, B. *Carbon Black - Material Safety Data Sheet*. www.cancarb.com/trademarks. (2017).

240. Maricite Mineral Data. http://www.webmineral.com/data/Maricite.shtml#.YXAk__rP3IU.

241. Tong, Z. *et al.* Matchmaker of Marriage between a Li Metal Anode and NASICON-Structured Solid-State Electrolyte: Plastic Crystal Electrolyte and Three-Dimensional Host Structure. *ACS Appl Mater Interfaces* **12**, 44754–44761 (2020).

242. Sutton, M., Mingqi, C., Peters, W., Chao, Y. & McNeill, S. Application of an optimized digital correlation method to planar deformation analysis. *Image Vis Comput* **4**, 143–150 (1986).

243. Zhao, J., Sang, Y. & Duan, F. The state of the art of two-dimensional digital image correlation computational method. *Engineering Reports* **1**, e12038 (2019).

APPENDICES

APPENDIX A

SUPPLEMENTARY INFORMATION FOR ELECTROCHEMICAL STRAIN EVOLUTION IN
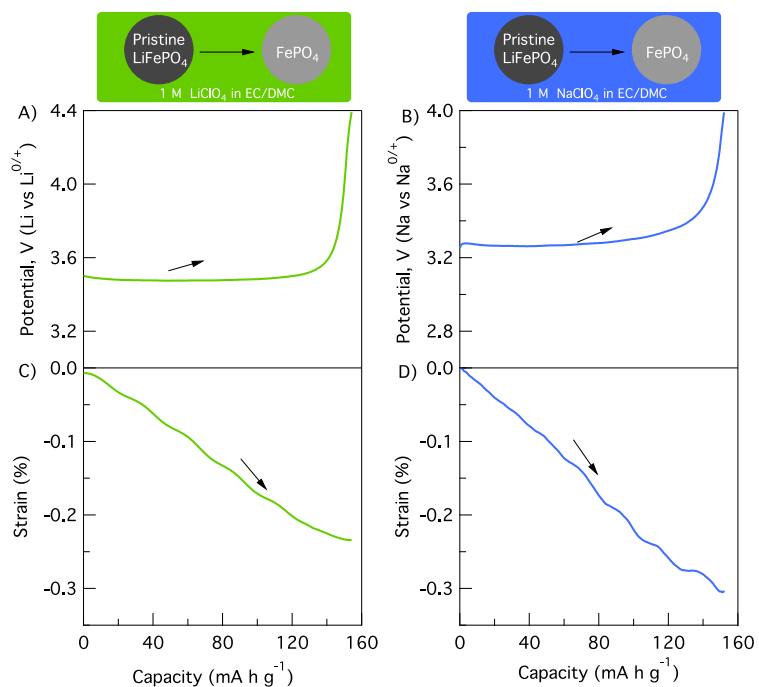IRON PHOSPHATE COMPOSITE CATHODES DURING LITHIUM AND SODIUM ION
INTERCALATION

Figure A1. Formation of iron phosphate, $FePO_4$ electrode by electrochemical delithiation of pristine lithium iron phosphate, $LiFePO_4$ at C/10 against A,C) Li metal counter electrode in 1 M $LiClO_4$ in EC/DMC or B,D) Na metal counter electrode in 1 M Na $NaClO_4$ in EC/DMC.
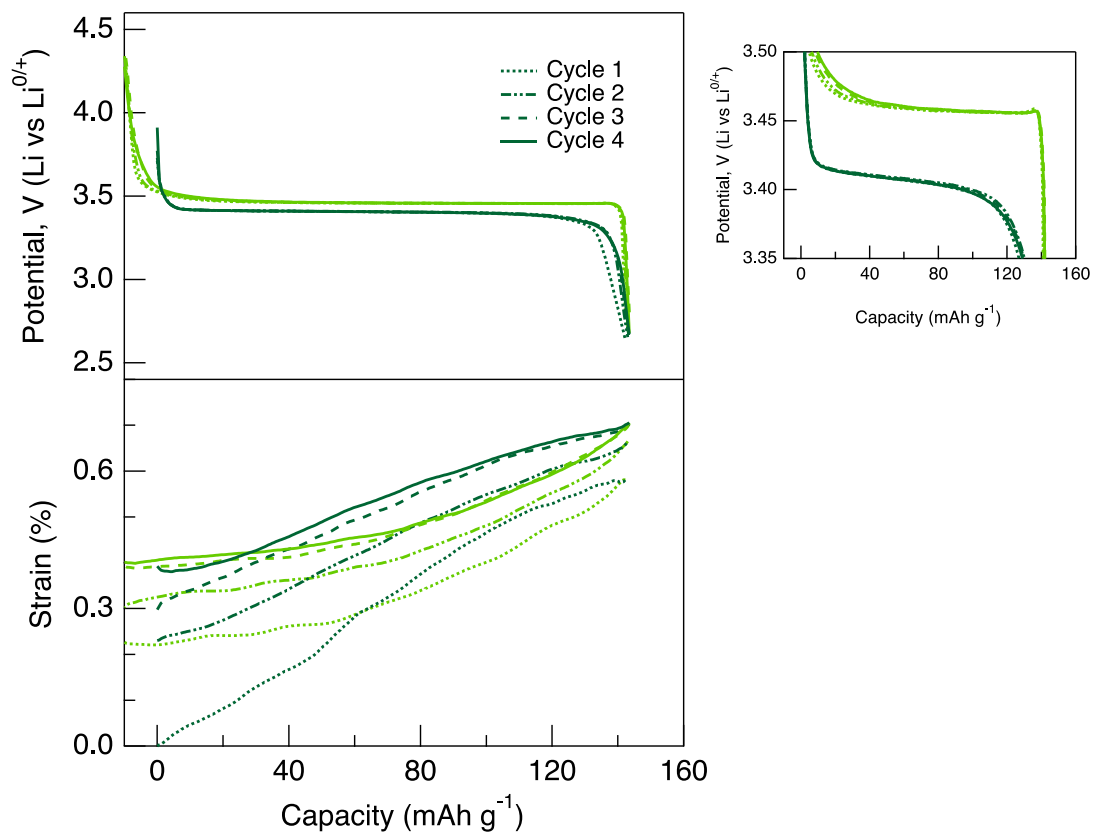
Figure A2. Potential and strain evolution with respect to capacity in LiFePO$_4$ composite electrode during Li intercalation in 1 M LiClO$_4$ in EC/DMC at C/10 rate. Dark and light green lines demonstrate lithiation and delithiation cycles, respectively. The top right figure highlights the potential evolution 3.35 – 3.5 V during sodiation and desodiation at different cycle numbers. The figure is generated from data in **Figure 16**.
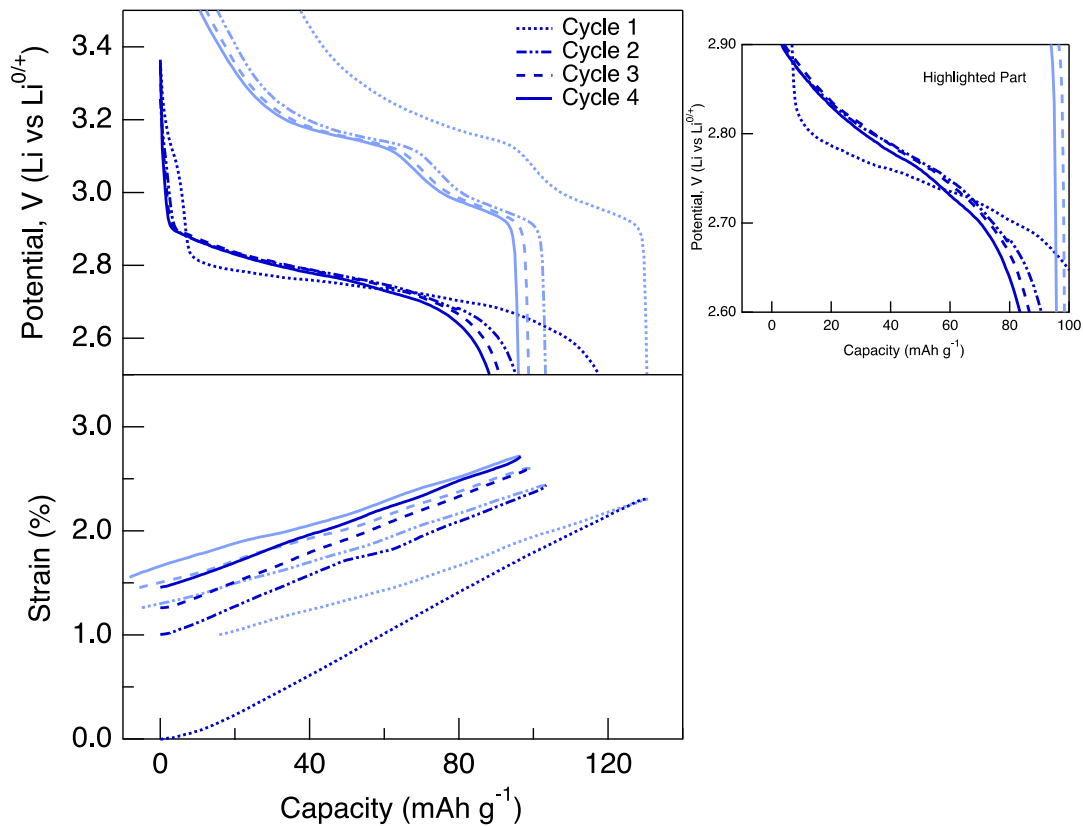
Figure A3. Potential and strain evolution with respect to capacity in NaFePO$_4$ composite electrode during Li intercalation in 1 M NaClO$_4$ in EC/DMC at C/10 rate. Dark and light blue lines demonstrate sodiation and desodiation cycles, respectively. The top right figure highlights the potential evolution between 2.6 – 2.9 V during sodiation at different cycle numbers. The figure is generated from data in **Figure 17**.
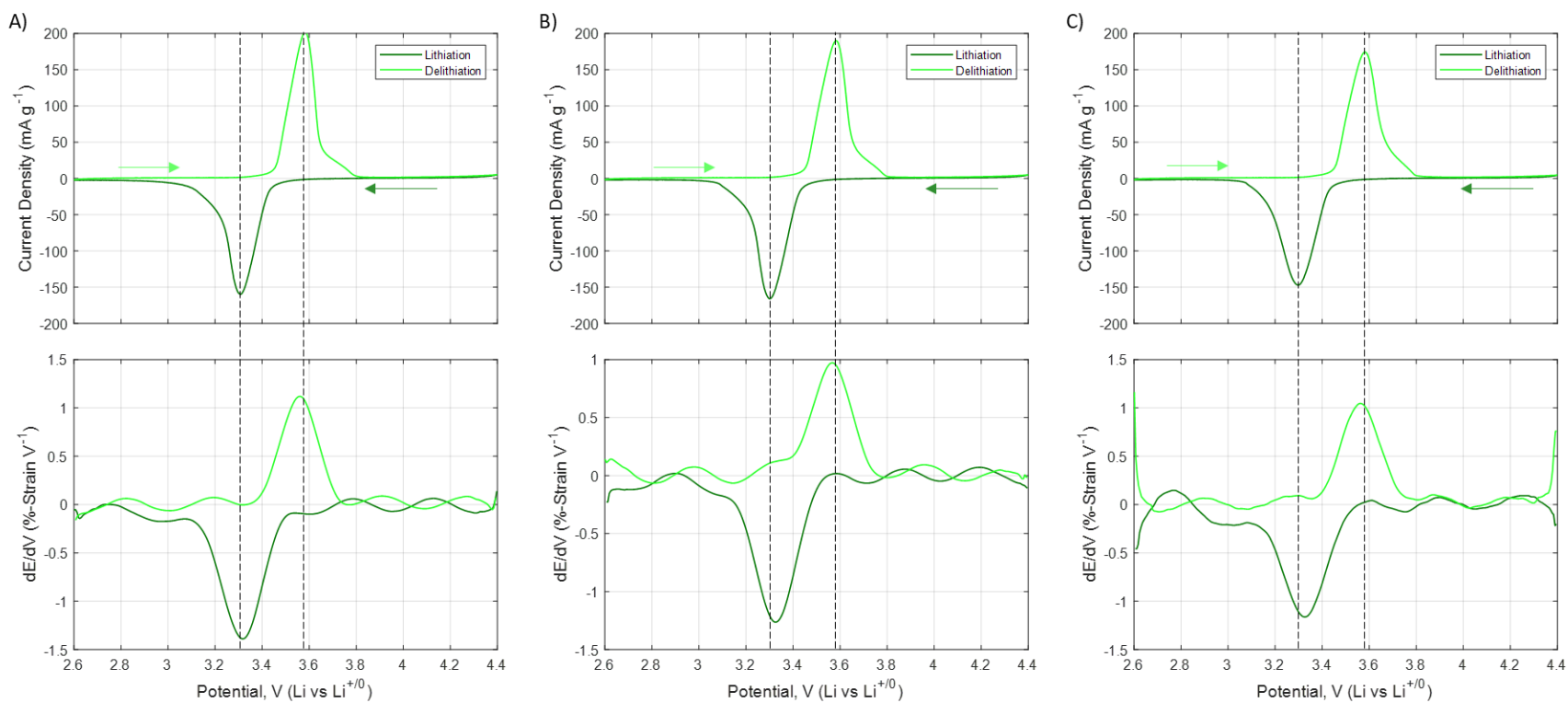
Figure A4. Strain derivatives in LiFePO₄ composite electrode during Li intercalation in 1 M LiClO₄ in EC/DMC for (A) 1ˢᵗ, (B) 2ⁿᵈ, and (C) 3ʳᵈ cycles at 50 µV/s.

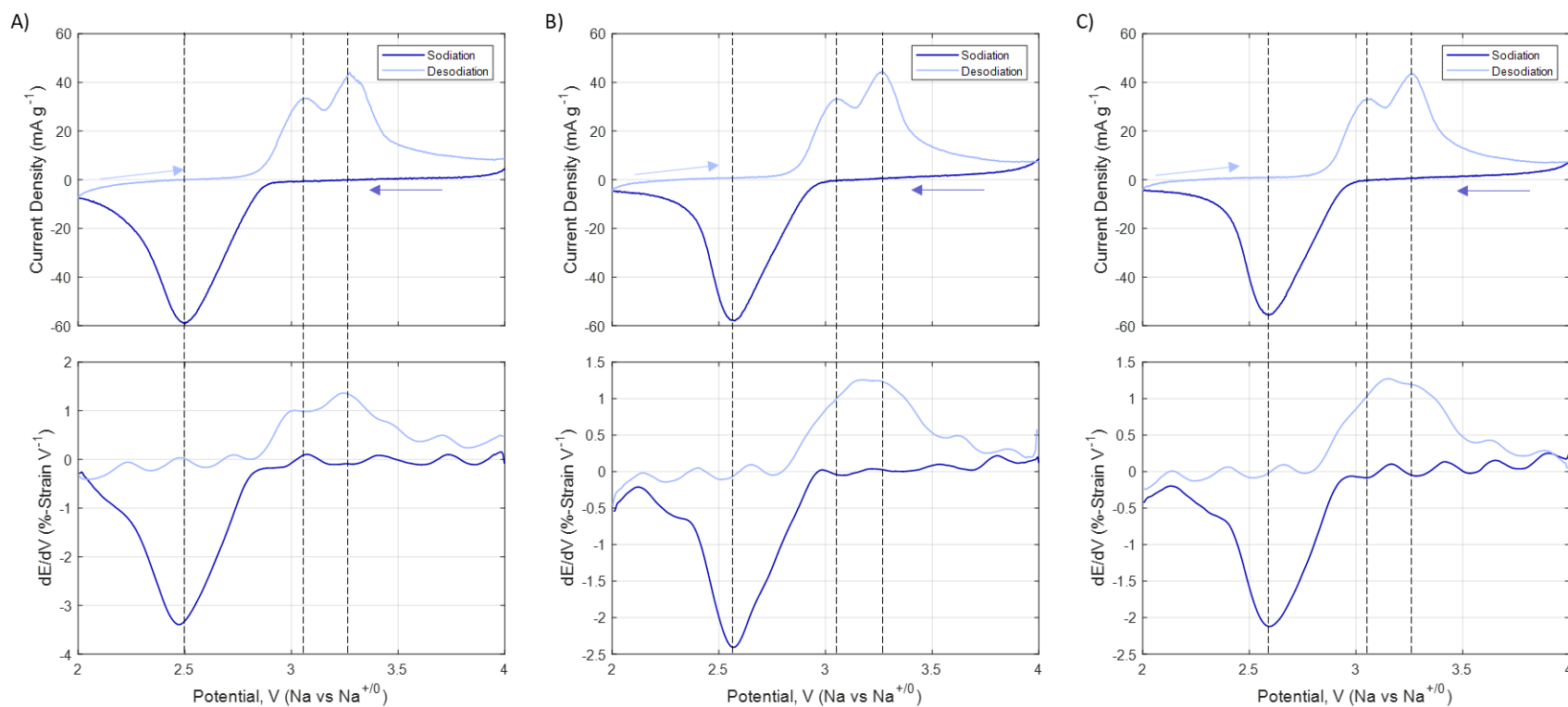**Figure A5.** Strain derivatives in NaFePO₄ composite electrode during Na intercalation in 1 M NaClO₄ in EC/DMC for (A) 1ˢᵗ, (B) 2ⁿᵈ, and (C) 3ʳᵈ cycles at 50 µV/s.
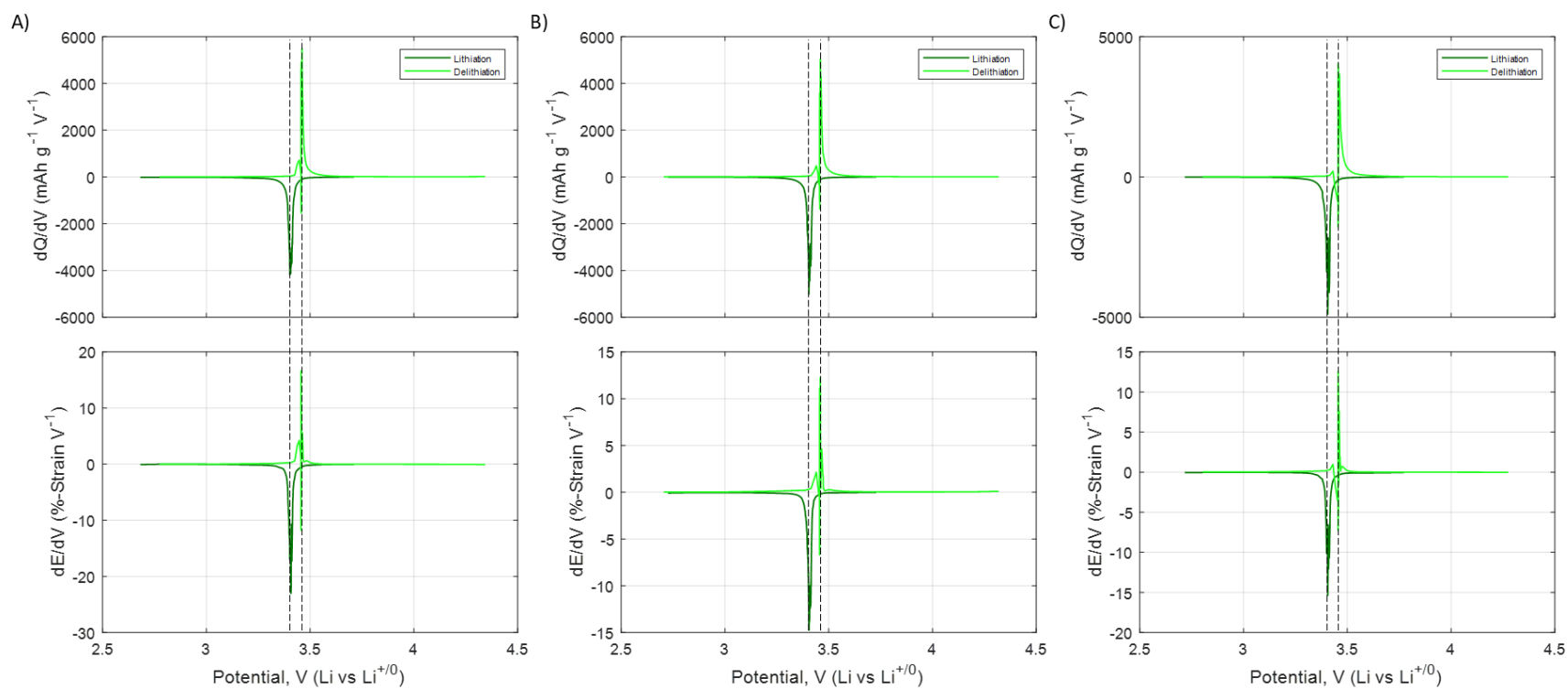
Figure A6. Capacity and strain derivatives in LiFePO$_4$ composite electrode cycled at C/10 rate 1 M LiClO$_4$ in EC/DMC.
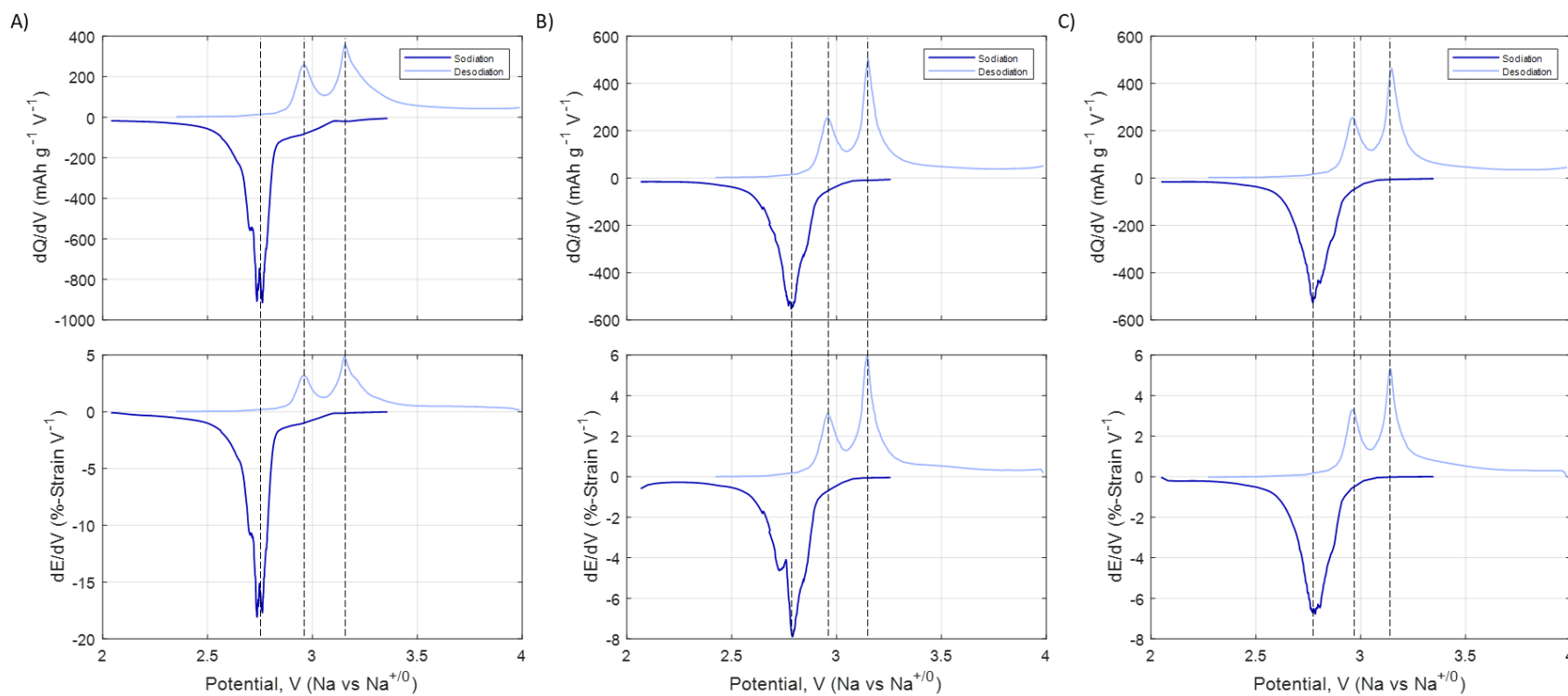
Figure A7. Capacity and strain derivatives in NaFePO₄ composite electrode cycled at C/10 rate 1 M NaClO₄ in EC/DMC.

Table A1. Anodic, cathodic, and irreversible strains during electrochemical cycling of LiFePO$_4$ from individual experiments with average value and error margin. The electrodes were cycled at 50 µV/s in 1 M LiClO$_4$ in EC/DMC. The first cycle starts with the lithiation of FePO$_4$. The average anodic, cathodic, and irreversible strains are plotted in the **Figure 20**a with error bars.

	Cycle Number	Experiment 1	Experiment 2	Experiment 3	Average	Standard Error (+/-)
Cathodic Strains	1	0.683	0.617	0.436	0.578	0.074
	2	0.443	0.525	0.351	0.440	0.050
	3	0.397	0.440	0.312	0.383	0.038
	4	0.338	0.413	0.299	0.350	0.034
Anodic Strains	1	-0.353	-0.381	-0.296	-0.344	0.025
	2	-0.309	-0.373	-0.285	-0.322	0.026
	3	-0.296	-0.344	-0.284	-0.308	0.018
	4	-0.289	-0.342	-0.238	-0.290	0.030
Irreversible Strains	1	0.330	0.235	0.139	0.235	0.055
	2	0.134	0.152	0.066	0.117	0.026
	3	0.101	0.096	0.028	0.075	0.024
	4	0.048	0.072	0.060	0.060	0.007

Table A2. Anodic, cathodic, and irreversible strains during electrochemical cycling of NaFePO$_4$ from individual experiments with average value and error margin. The electrodes were cycled at 50 µV/s in 1 M NaClO$_4$ in EC/DMC. The first cycle starts with the lithiation of FePO$_4$. The average anodic, cathodic, and irreversible strains are plotted in the **Figure 20**b with error bars.

	Cycle Number	Experiment 1	Experiment 2	Experiment 3	Experiment 4	Average	Standard Error (+/-)
Cathodic Strains	1	2.431	3.244	2.346	2.517	2.635	0.206
	2	1.481	1.948	1.391	1.441	1.565	0.129
	3	1.340	1.742	1.294	1.285	1.415	0.109
	4	1.264	1.632	1.203	1.221	1.330	0.102
Anodic Strains	1	-1.155	-1.636	-1.202	-1.347	-1.335	0.108
	2	-1.215	-1.616	-1.227	-1.219	-1.319	0.099
	3	-1.199	-1.555	-1.148	-1.176	-1.270	0.096
	4	-1.144	-1.486	-1.108	-1.138	-1.219	0.089
Irreversible Strains	1	1.277	1.607	1.144	1.171	1.300	0.106
	2	0.266	0.331	0.164	0.222	0.246	0.035
	3	0.141	0.187	0.146	0.109	0.146	0.016
	4	0.120	0.146	0.095	0.083	0.111	0.014

Table A3. Anodic, cathodic, and irreversible strains and capacities during electrochemical cycling of LiFePO$_4$ from individual experiments with average value and error margin. The electrodes were cycled at C/10 in 1 M LiClO$_4$ in EC/DMC. The first cycle starts with the lithiation of FePO$_4$. The average anodic, cathodic, and irreversible strains are plotted in the **Figure 18**c with error bars.

	Cycle Number	Experiment 1	Experiment 2	Average	Standard Error (+/-)
Cathodic Strains	1	0.581	0.673	0.627	0.046
	2	0.435	0.531	0.483	0.048
	3	0.406	0.471	0.438	0.033
	4	0.313	0.423	0.368	0.055
Cathodic Capacity (mA h/g)	1	142.279	149.160	145.719	3.440
	2	142.965	150.186	146.576	3.610
	3	143.483	150.146	146.815	3.332
	4	143.478	150.584	147.031	3.553
Anodic Strains	1	-0.351	-0.439	-0.395	0.044
	2	-0.367	-0.424	-0.396	0.029
	3	-0.311	-0.408	-0.359	0.048
	4	-0.304	-0.371	-0.338	0.034
Anodic Capacity (mA h/g)	1	152.836	154.816	153.826	0.990
	2	153.449	155.853	154.651	1.202
	3	153.294	156.305	154.799	1.505
	4	154.185	156.397	155.291	1.106
Irreversible Strains	1	0.230	0.234	0.232	0.002
	2	0.067	0.106	0.087	0.019
	3	0.095	0.063	0.079	0.016
	4	0.009	0.052	0.030	0.021

Table A4. Anodic, cathodic, and irreversible strains and capacities during electrochemical cycling of NaFePO$_4$ from individual experiments with average value and error margin. The electrodes were cycled at C/10 in 1 M NaClO$_4$ in EC/DMC. The first cycle starts with the lithiation of FePO$_4$. The average anodic, cathodic, and irreversible strains are plotted in the **Figure 18**d with error bars.

	Cycle Number	Experiment 1	Experiment 2	Average	Standard Error (+/-)
Cathodic Strains	1	2.308	2.340	2.324	0.016
	2	1.435	1.499	1.467	0.032
	3	1.333	1.371	1.352	0.019
	4	1.257	1.267	1.262	0.005
Cathodic Capacity (mA h/g)	1	130.633	131.759	131.196	0.563
	2	103.383	104.165	103.774	0.391
	3	99.145	98.826	98.985	0.160
	4	96.533	96.679	96.606	0.073
Anodic Strains	1	-1.306	-1.266	-1.286	0.020
	2	-1.174	-1.255	-1.215	0.040
	3	-1.139	-1.209	-1.174	0.035
	4	-1.164	-1.156	-1.160	0.004
Anodic Capacity (mA h/g)	1	115.653	114.731	115.192	0.461
	2	108.356	105.776	107.066	1.290
	3	105.254	102.675	103.964	1.290
	4	104.732	101.638	103.185	1.547
Irreversible Strains	1	1.002	1.074	1.038	0.036
	2	0.260	0.244	0.252	0.112
	3	0.194	0.162	0.178	0.073
	4	0.094	0.111	0.103	0.045

Table A5. Unit cell parameters and volumetric expansion in electrode particles during Li^+ and Na^+ ion intercalation into iron phosphate. Data is taken from literature[32].

Unit Cell Parameters	$FePO_4$	$LiFePO_4$	$Na_{0.7}FePO_4$	$NaFePO_4$
a (Å)	9.76	10.33	10.29	10.43
b (Å)	5.75	6.00	6.08	6.22
c (Å)	4.75	4.69	4.93	4.94
Volume change vs $FePO_4$ (%)	0.0	6.9	13.5	17.6

APPENDIX B

SUPPLEMENTARY INFORMATION FOR IN SITU PROBING POTASSIUM-ION

INTERCALATION-INDUCED AMORPHIZATION IN CRYSTALLINE IRON PHOSPHATE

CATHODE MATERIALS

EXPERIMENTAL

Sample Preparation: Composite electrodes were prepared by mixing active material with binder and conductive carbon in 8:1:1 mass ratio. Initially, sodium carboxymethyl cellulose (binder, CMC, average MW ~700,000, Aldrich) was dissolved in ultra-pure water with a 1:40 mass ratio. Then, the pristine lithium iron phosphate (active material, $LiFePO_4$, LFP, Hanwha Chemical) and Super P (conductive additive, carbon black, >99%, metal basis, Alfa Aesar) were added to the binder solution. Scanning electron microscopy (SEM) images of the electrode particle are shown in the **Figure B1**. The average particle size of LFP particles was measured by SEM as 219±78 nm (**Figure B2**). Particle size ranges from 100 nm to 400 nm. The slurry was mixed for 30 minutes with Thinky centrifugal mixer at 2000 RPM mixing speed. Composite electrodes were cast onto the copper foil (9 µm thick, >99.99%, MTI) with a doctor blade to control the slurry thickness. The slurry was then dried under ambient conditions for 16 h. Dried electrodes were carefully peeled off to create the freestanding electrode for strain measurements.

Electrolyte solution was prepared by mixing ethylene carbonate (EC, anhydrous, 99%, Acros Organics) and dimethyl carbonate (DMC, anhydrous, >99%, Aldrich) in 1:1 volume ratio inside the glovebox under an argon atmosphere. Oxygen and water content inside the glovebox kept below 1 ppm all the time. 1 M lithium perchlorate (LiClO$_4$, battery grade, dry, 99.99%< Aldrich) or 0.5 M KPF$_6$ (99% min, Alfa Aesar) was added to the EC/DMC solution for Li, Na or K intercalation, respectively.

Li foils (99.9% metal basis, Alfa Aesar) were used as purchased without proceeding any further treatment and were kept inside the argon-filled glove box. Potassium chunks (98%, Acros Organics), immersed in mineral oil, were cleaned with hexane inside the glovebox. Cleaned K chunks were stored in EC:DMC solution in a 1:1 volume ratio for future use. Prior to custom cell assembly, K chunks were removed from the solvent solution, dried with a filter paper, and cut into
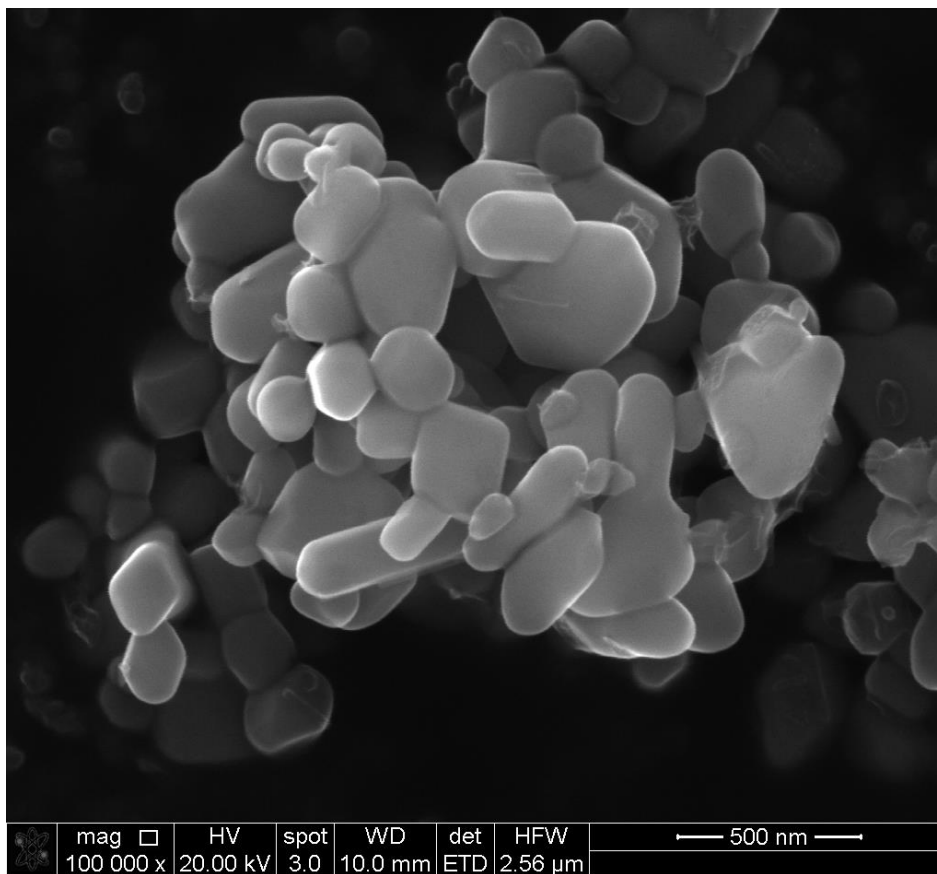
Figure B1. SEM image of the pristine electrode particles

172

pieces with a stainless-steel scalpel. The cut piece was placed inside a polyethylene bag and rolled into the shape of a foil using a rolling pin. Flattened K foil was then placed into the battery cell as a counter electrode.

***Battery Cycling*:** Iron phosphate (FP) composite electrode was formed by electrochemical displacement technique using a pristine LFP composite electrode[67,68]. The pristine LFP electrode was electrochemically delithiated via galvanostatic cycle against K counter electrode at a rate of C/25. For potassium intercalation, FP composite electrodes were cycled against K counter electrode in 0.5 M KPF_6 in 1:1 (v:v) EC:DMC electrolyte between 1.5-4.3 V. The electrodes were cycled via galvanostatic cycle at C/25 rate.

In-operando XRD Measurements: X-ray diffractometer (SmartLab, Rigaku) equipped with an in-operando battery cell was employed for the XRD analysis. LFP slurry was drop-casted directly on Beryllium window and dried overnight in ambient condition. The loading of LFP was measured to be approximately 2 mg/cm^2. With the prepared LFP cathode, the in-operando battery cell was assembled in Ar filled glove box where moisture and oxygen level were controlled to be below 0.5ppm. K metal electrode and electrolyte were prepared in a same manner described above. Two glass fiber separators were used between the K metal anode and LFP cathode. The XRD patterns were continuously collected over the electrochemical displacement process at C/10 up to 4.3V and subsequent discharge/change cycling process at C/25 between 1.5~4.3V (1C=141 mAh/g of active material). The XRD scan range (2θ) was between 28° and 38°, in which all the main peaks of LFP and FP can be observed. Every scan took approximately 20 minutes. The step width used in the XRD measurement was 0.01°.

High Resolution Transmission Electron Microscopy Measurements: The sample preparation for high-resolution transmission electron microscopy (HRTEM) was performed using a FEI Helios Hydra UX Focused Ion Beam-Scanning Electron Microscope (SEM) using Xe ions, outfitted with

an Oxford Instruments X-ray Energy Dispersive Spectroscopy (EDS) system for compositional analysis. An aberration-corrected TEM (Titan 80-300 Scanning TEM/ STEM from Thermo Fisher Scientific, USA) equipped with a high-angle annular dark-field (HAADF) detector and an EDS system was employed at 300 kV for bright-field (BF), HRTEM, high angle annular dark field (HAADF) STEM, selected area electron diffraction (SAED), and composition analysis.
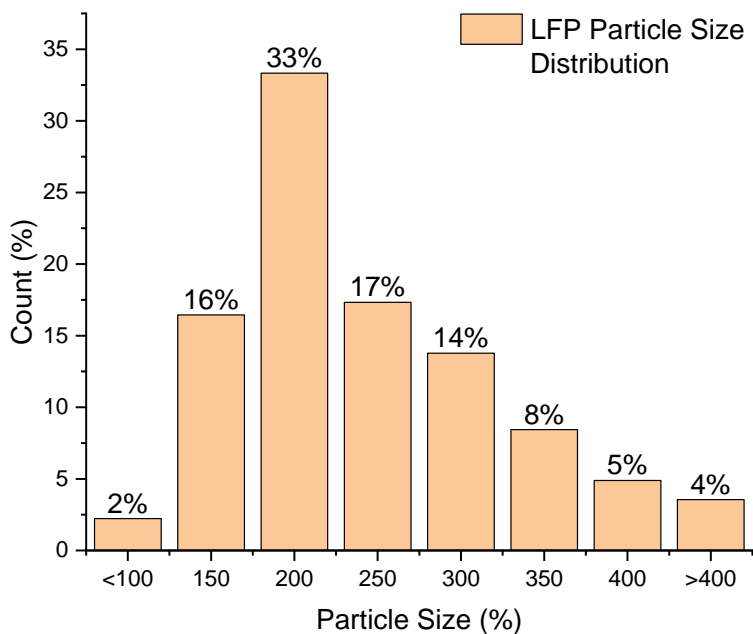

Figure B2. Particle size distribution of Lithium Iron Phosphate cathode particles from 225 particles.

Strain Measurements: A detailed description of the custom battery cell was described in our previous publication[36,37]. **Figure B3** shows the experimental setup and custom battery cell for the in-situ strain measurement system. The main body of the custom battery cell and the electrode holders were made from polychlorotrifluoroethylene (PCTFE, Plastics International). For optical access, a quartz window (99.995 % SiO_2, 1/16 in thick, 2 in diameter, McMaster-Carr) was placed on the top of the custom cell and sealed with Viton O-rings (Grainger).

Analysis of the strain generation was carried out by taking images of the freestanding electrode throughout the electrochemical cycling periods. Images were captured with Grasshopper3 5.0 MP camera (Sony IMX250, resolution, 2448w x 2048h pixel) with 12.0X adjustable zoom lens

(NAVITAR) for an effective resolution of 0.873 µm/pixel when using 4.0X setting on the adjustable zoom lens. A LED light source (Amazon) was used for illumination of the electrode surface. Images were captured using a lab made LabView program every 2 minutes during galvanostatic cycling at C/25. Captured images during electrochemical cycling were analyzed by Vic-2D Digital Image Correlation software. The software tracks the changes in the speckle pattern positions on the electrode surface, taking the initial image as reference, to calculate the strain evolution during the experiment. The natural speckle pattern of the LFP composite electrode was used to calculate strain generation on the electrode using Digital Image Correlation. Full-field strain measurements were performed on an area of interest of 750 µm x 500 µm. Strains were synchronized with the electrochemical response of the electrodes (current and voltage) using a lab-made MATLAB program. An example calculation of in situ strains on the composite electrode is shown in the **Figure B4**. Counter plots shows the homogeneous average of the individual particle response. For each image captured during cycling, ε_{xx} is averaged over the area of the region of interest.
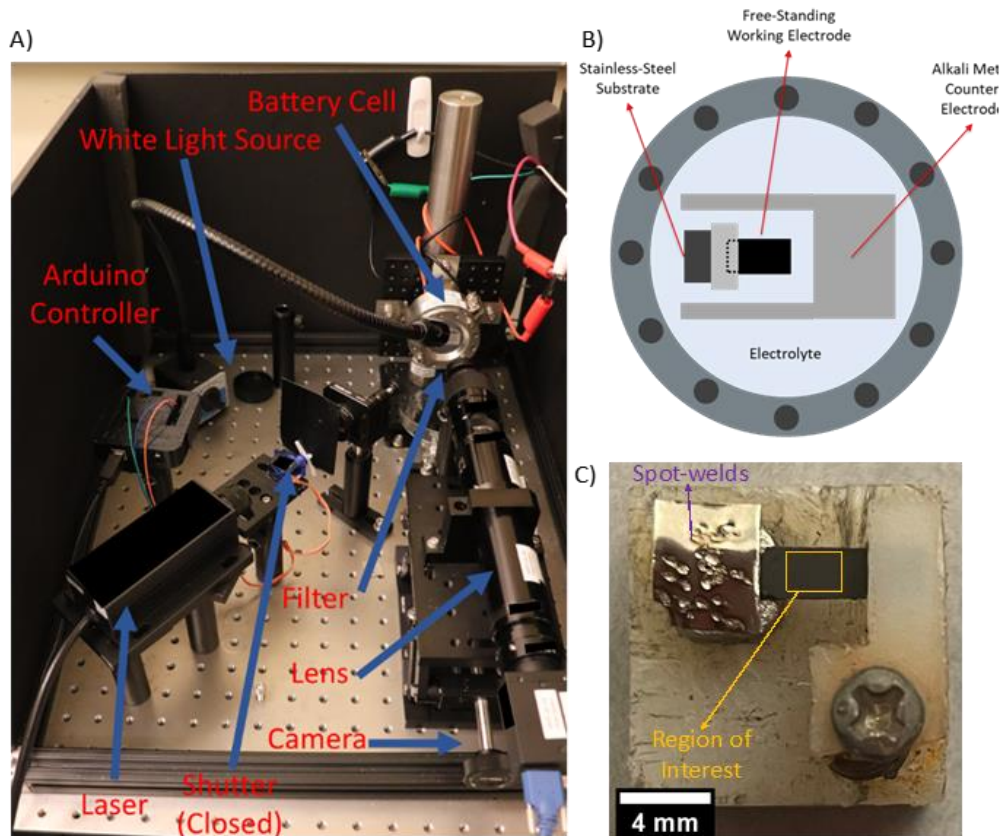
Figure B3. A) In-situ strain measurement setup and its components. B) Schematic view of the custom cell. C) Magnified view of a composite electrode spot welded on the stainless steel. The orange marked area on the Figure C is the region of interest for the strain analysis.
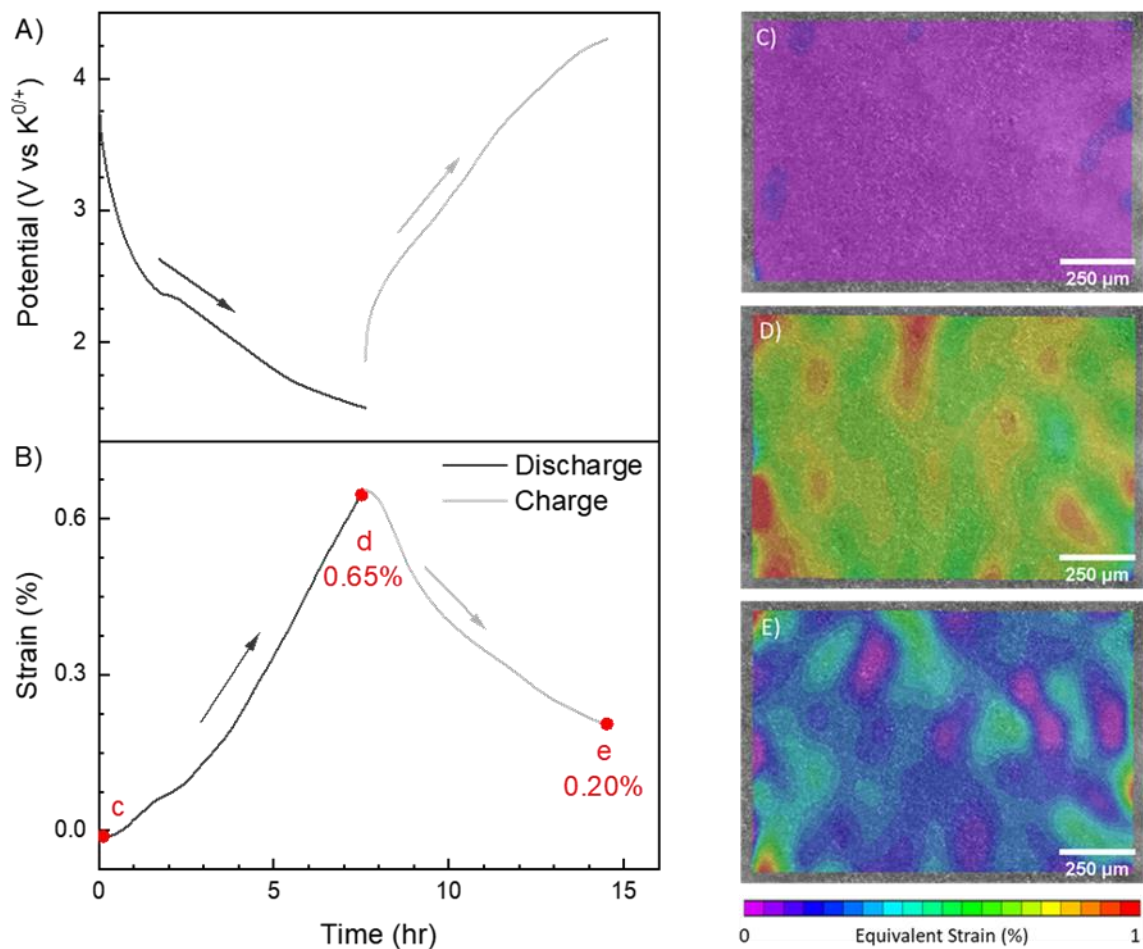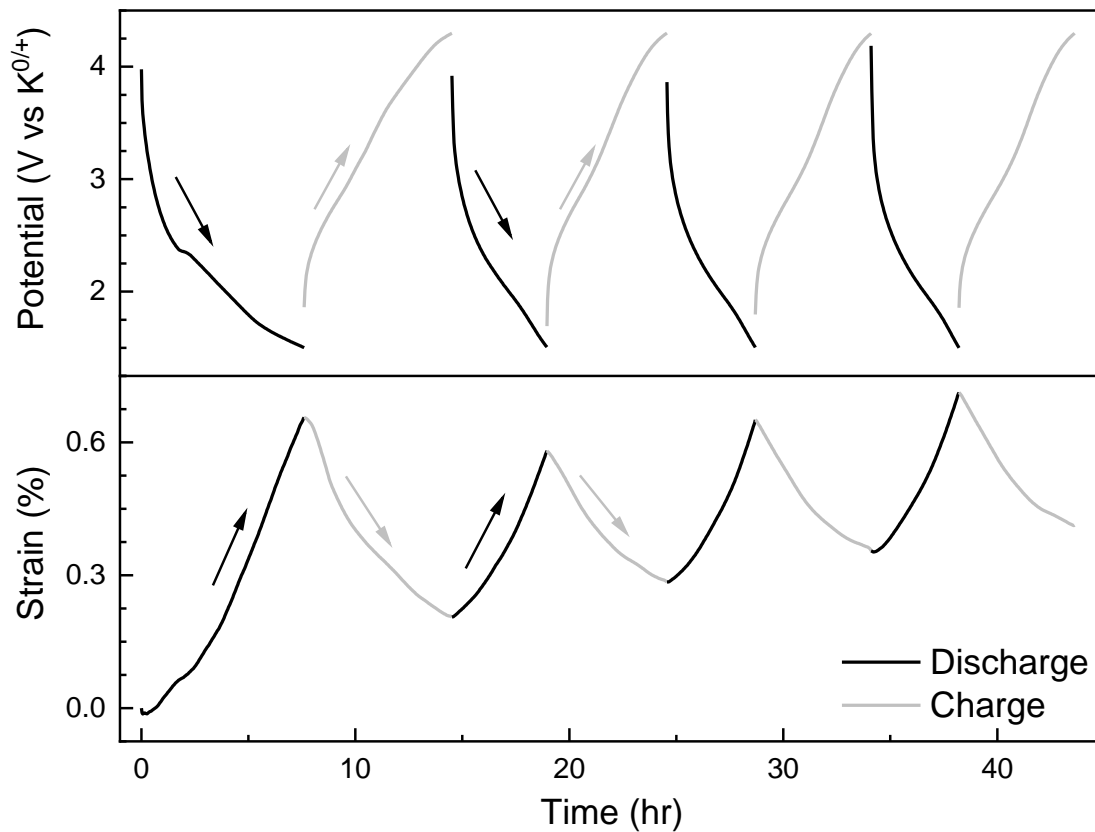
**Figure B4.** (A) Voltage and (B) strain evolution in iron phosphate electrode for potassium intercalation at C/25 rate with 0.5M KPF$_6$ in EC/DMC electrolyte during first cycle. DIC contour plots show the equivalent strain generation for (C) at the beginning of discharge, (D) at the end of 1st discharge and (E) at the end of first charge.

Table B1. Interplanar spacing in iron phosphate electrode structure upon potassium intercalation during first discharge cycle.

(hkl)		(311)	(121)	(211)	(020)
Before Discharge	**2θ**	36.47	37.2	30.06	30.63
	d (nm)	0.246	0.242	0.297	0.292
After Discharge	**2θ**	36.4	37.1	29.94	30.53
	d (nm)	0.247	0.242	0.298	0.293
Change	**Δd (pm)**	+0.457	+0.628	+1.163	+0.932

Figure B5. Voltage and strain evolution in iron phosphate electrode during potassium intercalation at C/25 rate in 0.5M KPF$_6$ in EC/DMC electrolyte
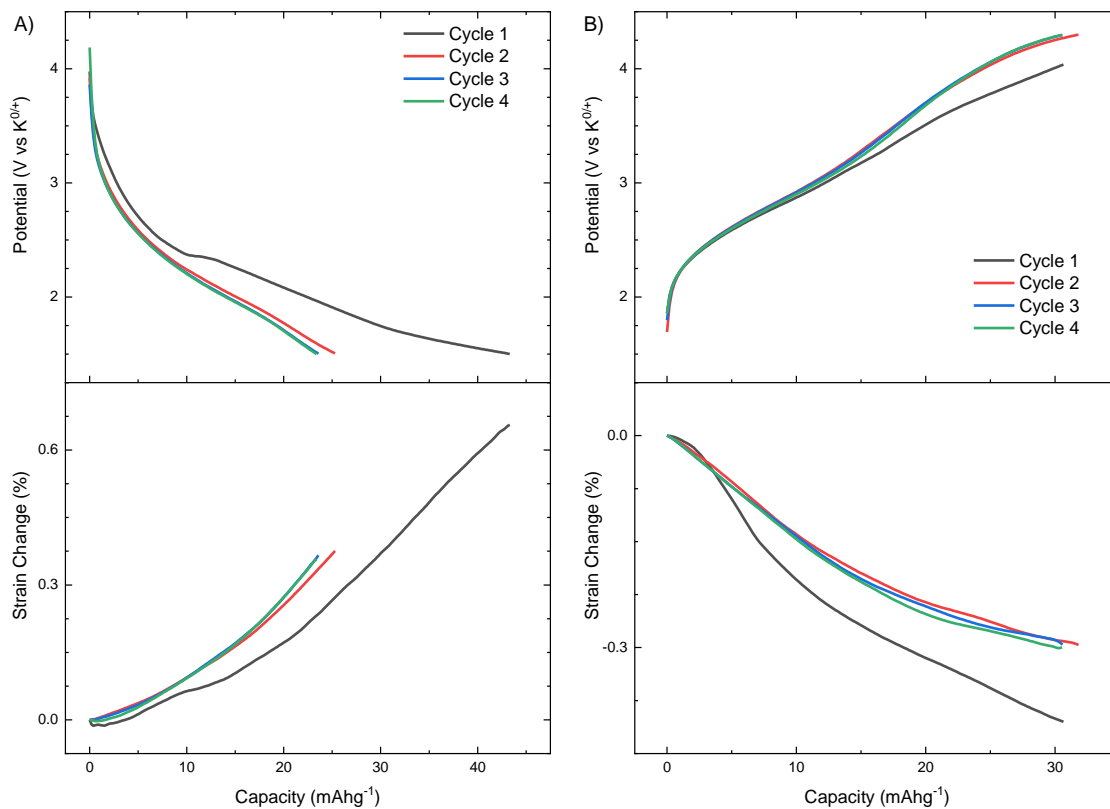
Figure B6. Change in strain versus (A) discharge and (B) charge capacity in iron phosphate during potassium intercalation at C/25 rate in 0.5M KPF_6 in EC/DMC electrolyte. Strain values are set to zero at the beginning of each charge and discharge cycles for better comparison.
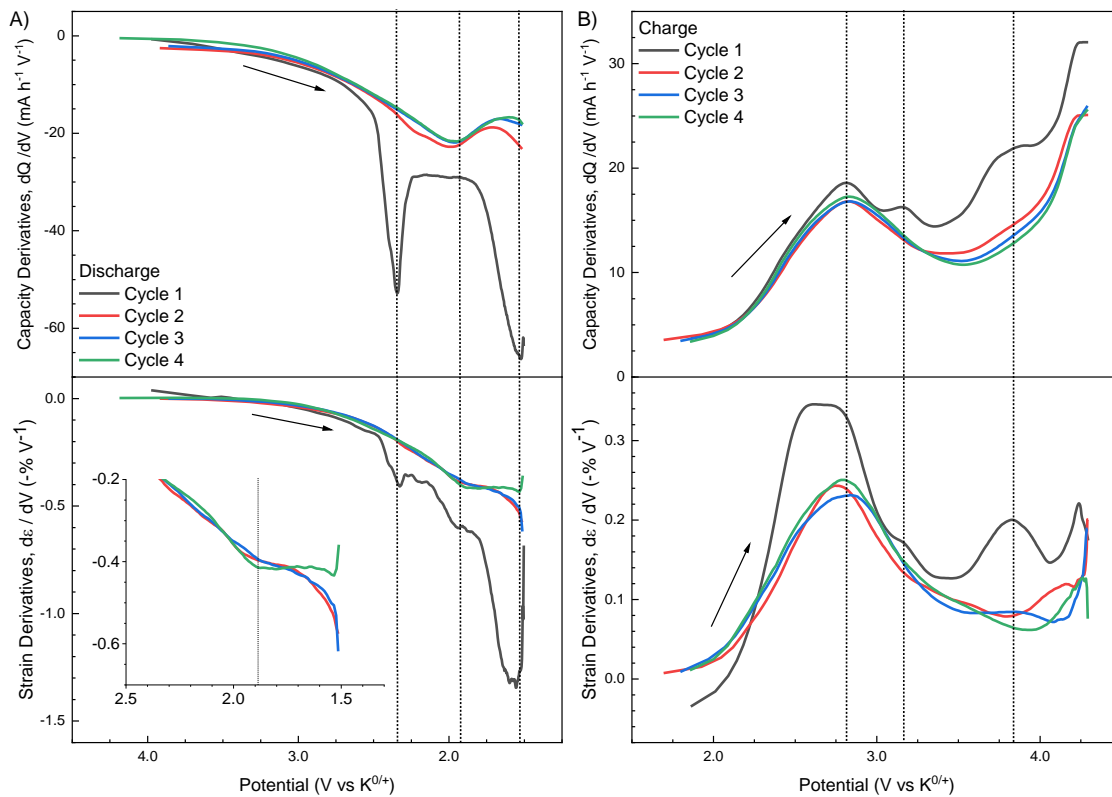
Figure B7. Capacity and strain derivatives in iron phosphate electrode during potassium intercalation for (A) discharge and (B) charge at C/25 rate in 0.5M KPF$_6$ in EC/DMC electrolyte

Control Experiment: First, the LFP electrode is delithiated against Li counter metal in LiClO4 in EC:DMC electrolyte in order to form iron phosphate. Then, Li counter metal is removed. Delithiated composite electrode was rinsed, and the custom cell is washed with 1:1 EC:DMC electrolyte inside the glovebox. Then, battery cell was reconstructed with K metal counter electrode and filled with 0.5 M KPF$_6$ in 1:1 EC:DMC electrolyte. The iron phosphate electrode is charged / discharged against K metal while monitoring in situ strains as shown in **Figure B8** below.
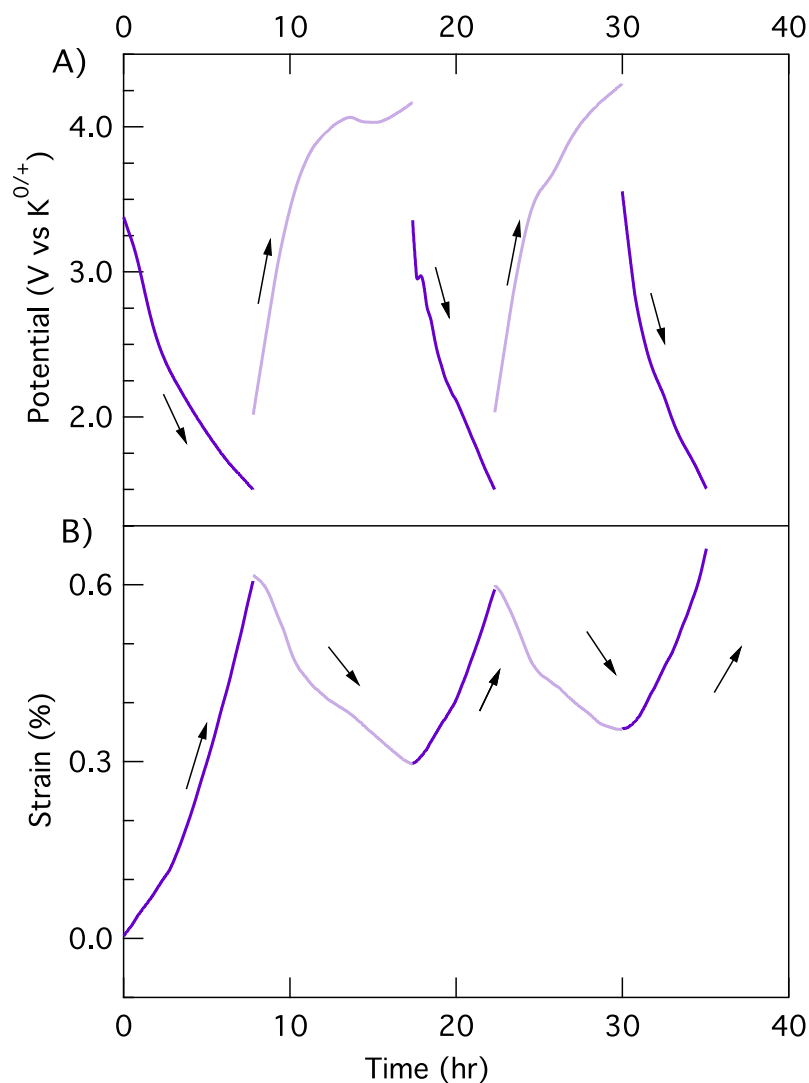
Figure B8. Voltage and strain evolution with time for the interrupted experiment against K counter electrode using 0.5 M KPF6 in 1:1 EC:DMC electrolyte during cycling.
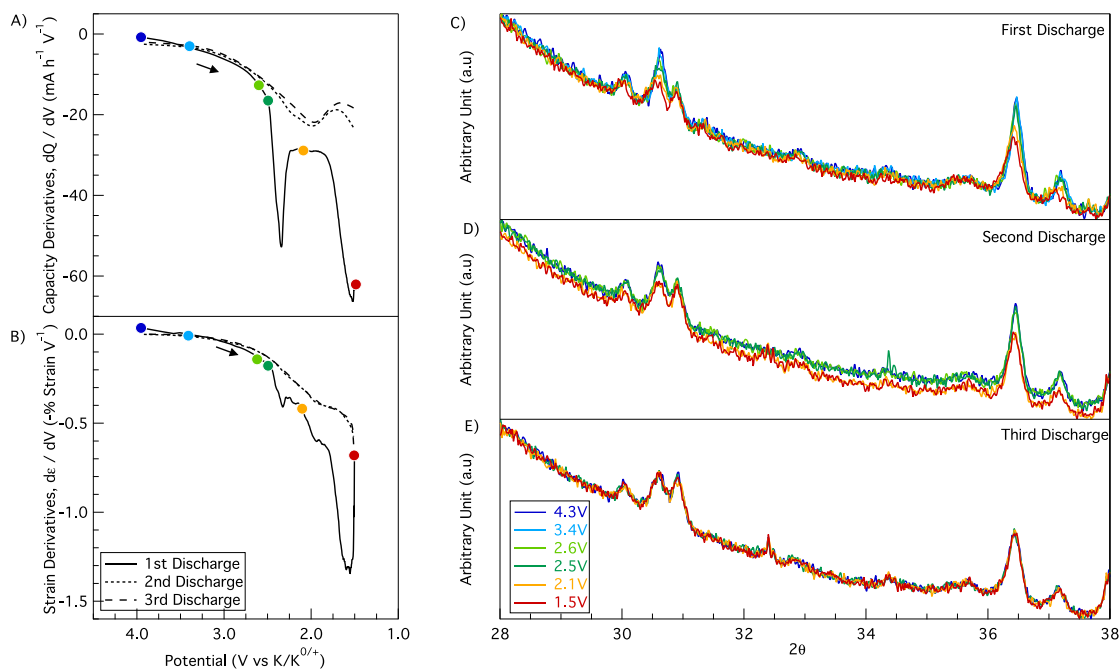
Figure B9. The figure is same as the **Figure 25** in the manuscript. Only, the XRD patterns are plotted on top of each o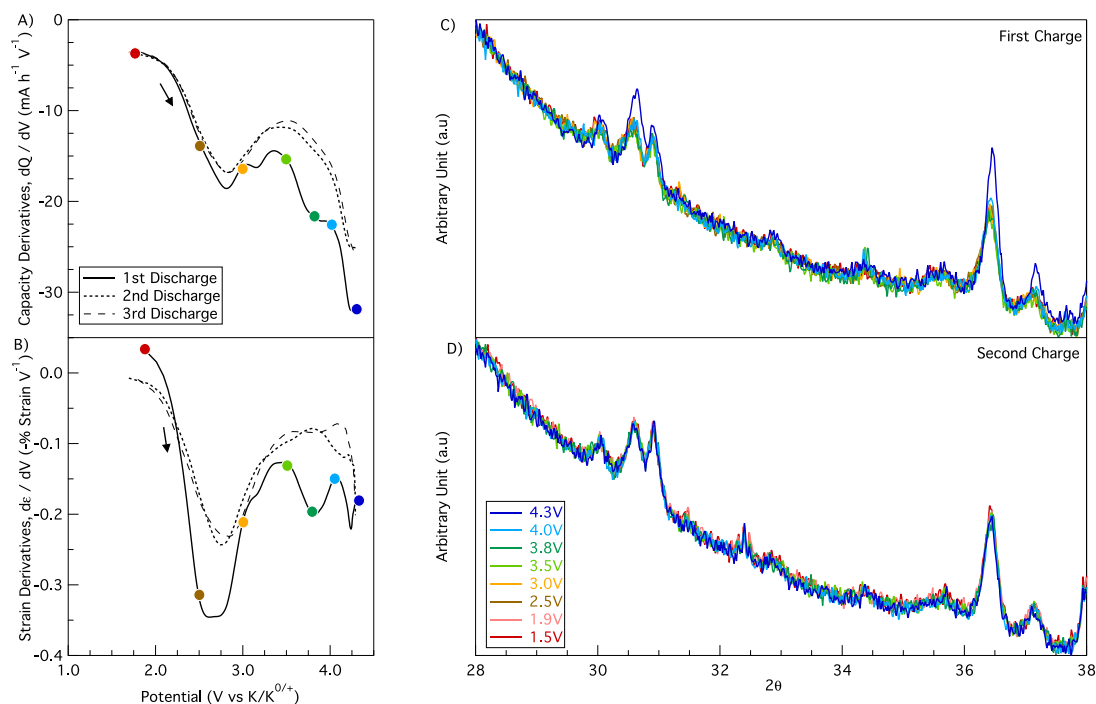ther in this figure. Structural, physical, and electrochemical response of the iron phosphate during first three discharge cycles A) capacity and B) strain derivatives with respect to voltage. (C-E) Corresponding XRD patterns at selected potentials colored as shown in the figure.
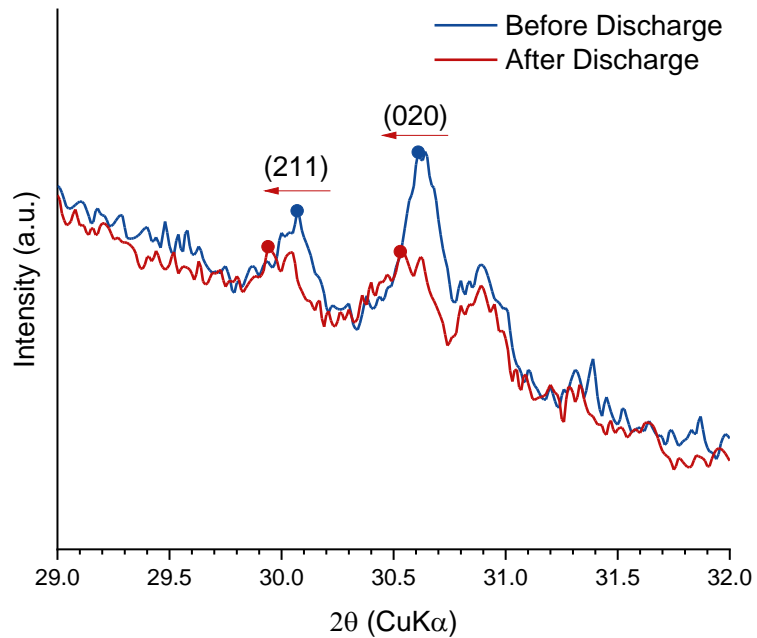
Figure B10. XRD spectra of electrode before and after the first discharge. Blue and red filled circles shown in the figure indicates the peak positions for the (211) and (020) planes before and after the potassium intercalation, respectively.

Figure B11. The figure is same as the **Figure 25.** Structural, physical, and electrochemical response of the iron phosphate during first three discharge cycles A) capacity and B) strain derivatives with respect to voltage. C-E) Corresponding XRD patterns at selected potentials colored and potential values are written for each pattern as shown in the figure.**Figure 26** in the manuscript. Only, the XRD patterns are plotted on top of each other in this figure. Structural, physical, and electrochemical response of the $FePO_4$ during charge cycles A) capacity and B) strain derivatives with respect to voltage. (C-D) Corresponding XRD patterns at selected potentials colored as shown in the figure.
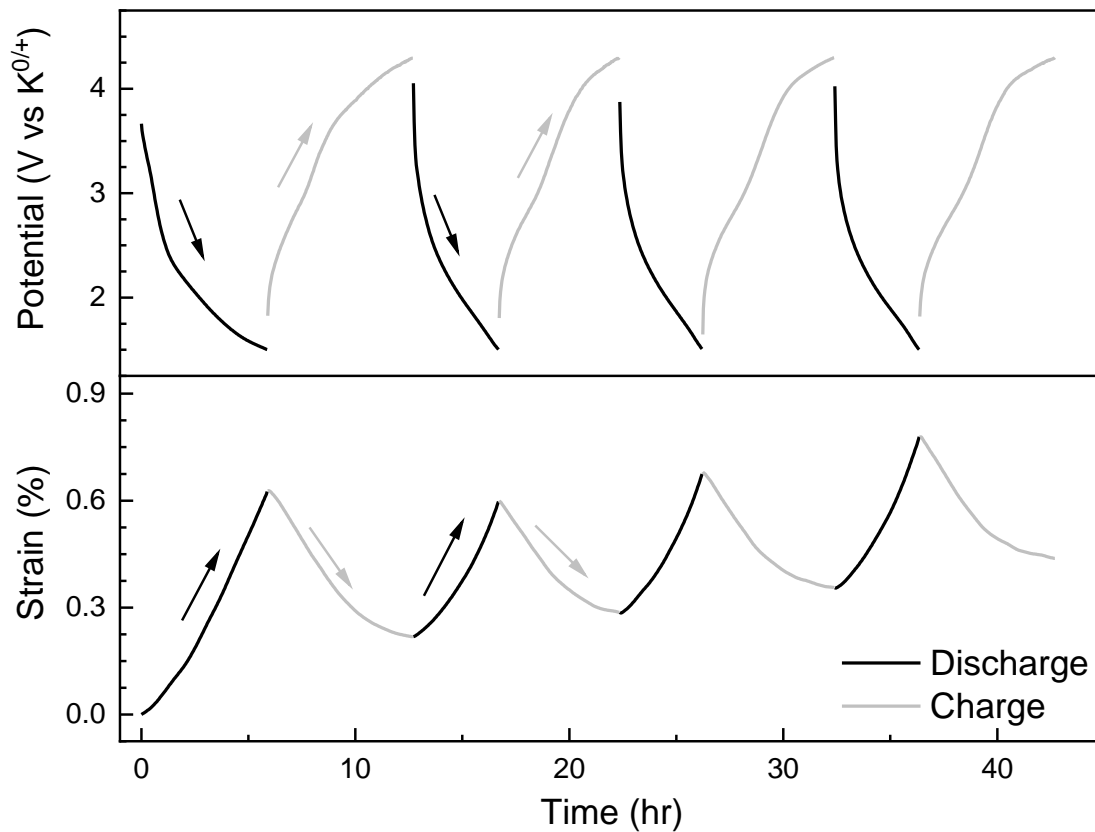
Figure B12. Voltage and strain evolution in iron phosphate electrode during potassium intercalation at C/25 rate in 0.5M KPF_6 in PC electrolyte.
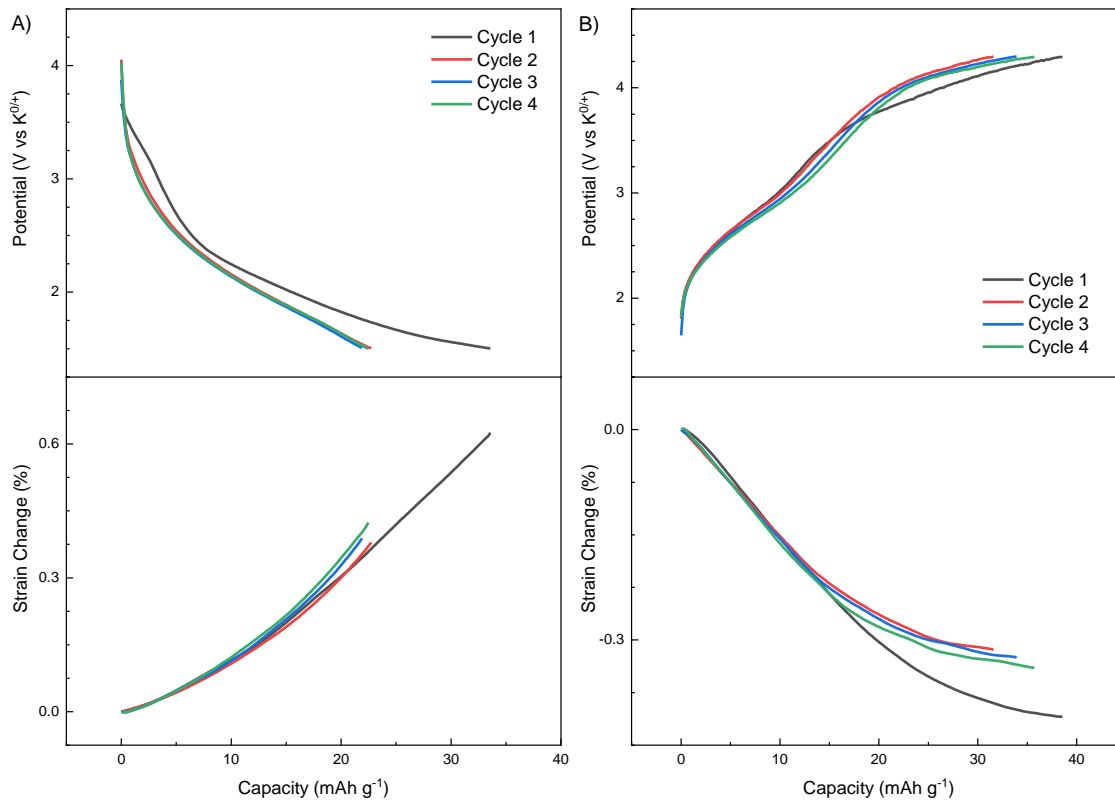
Figure B13. Change in strain versus (A) discharge and (B) charge capacity in iron phosphate during potassium intercalation at C/25 rate in 0.5M KPF$_6$ in PC electrolyte. Strain values are set to zero at the beginning of each charge and discharge cycles for better comparison.
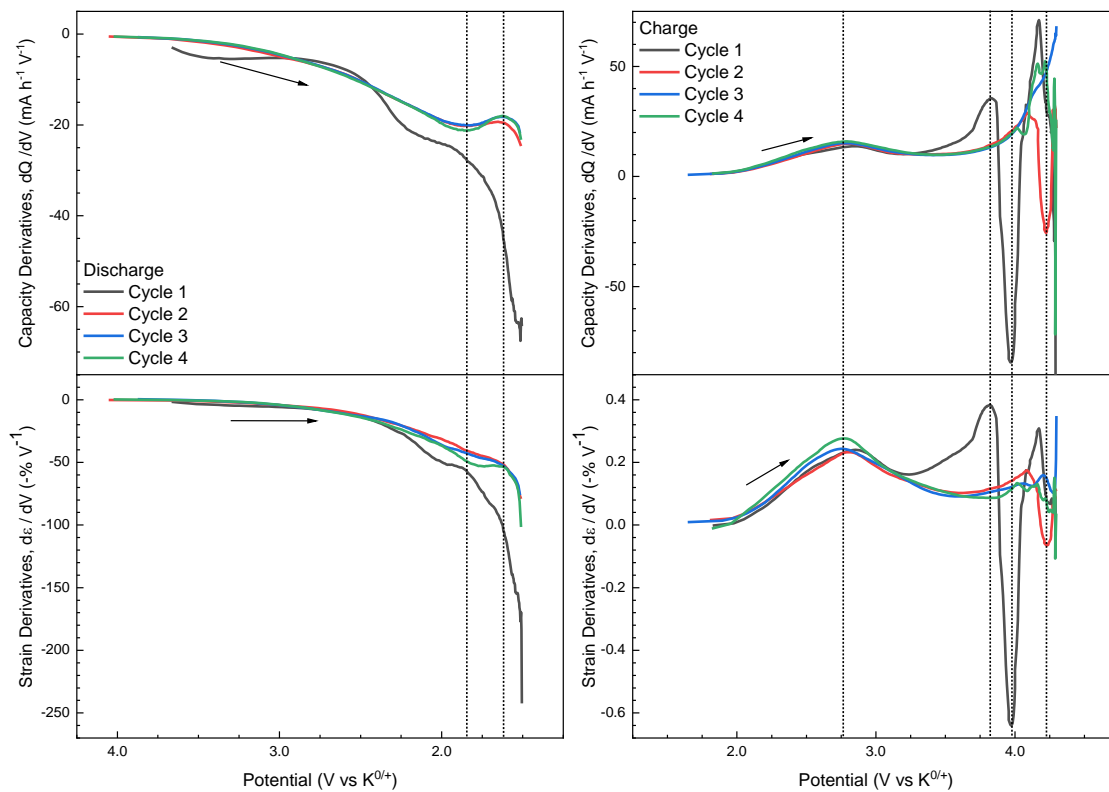
Figure B14. Capacity and strain derivatives in iron phosphate electrode during potassium intercalation for (A) discharge and (B) charge at C/25 rate in 0.5M KPF$_6$ in PC electrolyte.

SUPPLEMENTARY INFORMATION FOR THE IMPACT OF ALKALI-ION

INTERCALATION ON REDOX CHEMISTRY AND MECHANICAL DEFORMATIONS:

CASE STUDY ON INTERCALATION OF Li, Na, AND K IONS INTO FePO$_4$ CATHODE
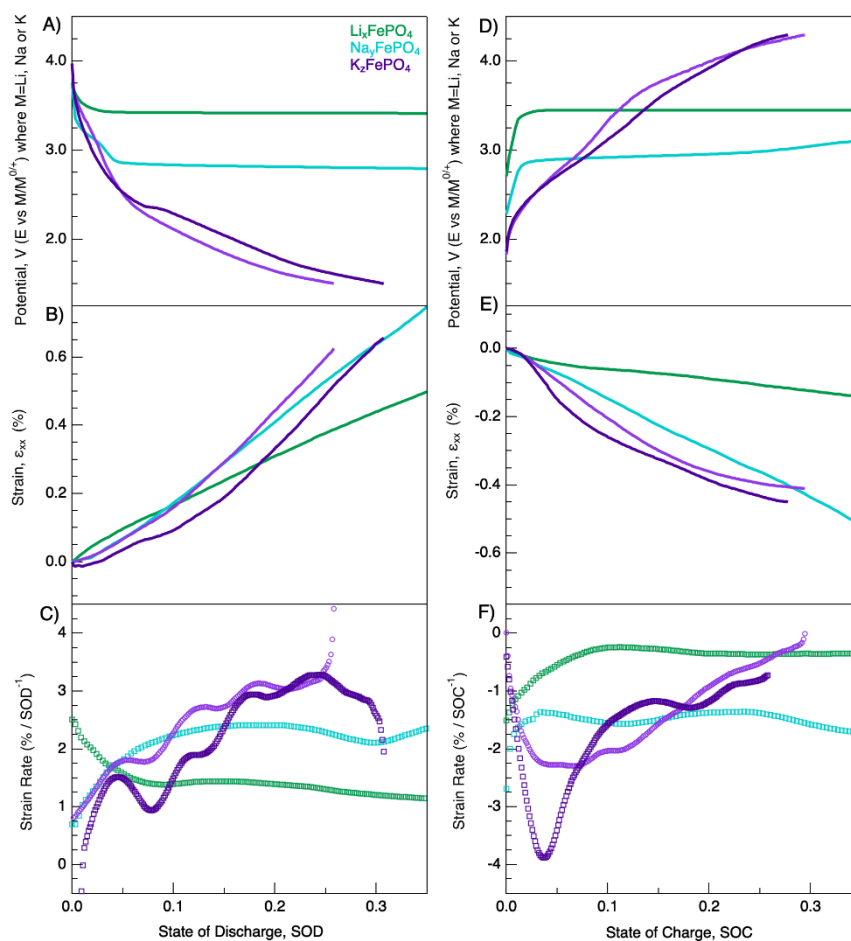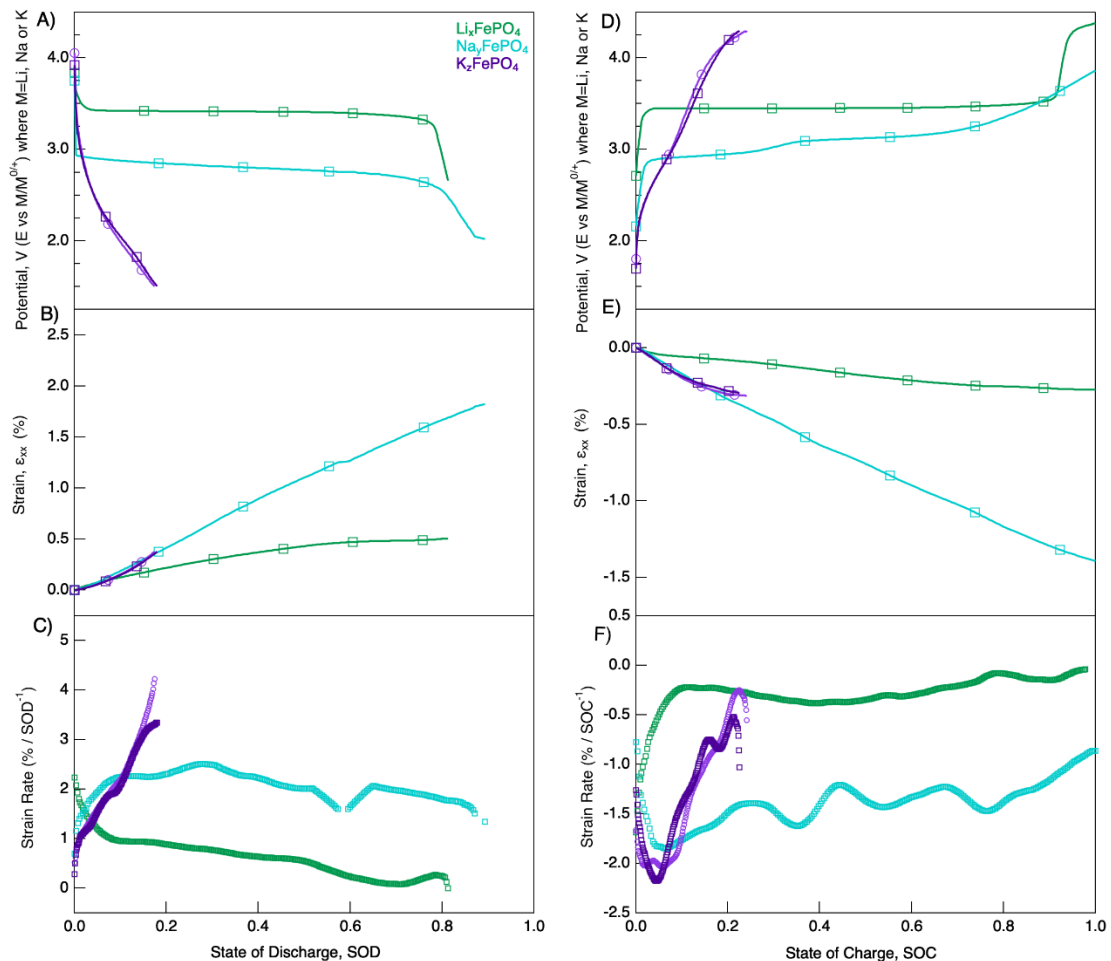

Figure C1. Potential evolution, strain generation and strain rates with respect to state of discharge (A,B, C) and charge (C, D, E) of Li (green), Na (blue) and K (purple) ions into FePO$_4$ electrode during the first cycle. The square and spherical symbol show when electrode is cycled either in EC:DMC or EC:PC solvents, respectively. The figure contains same data from **Figure 27**, only focuses on SOD / SOC until 0.35.
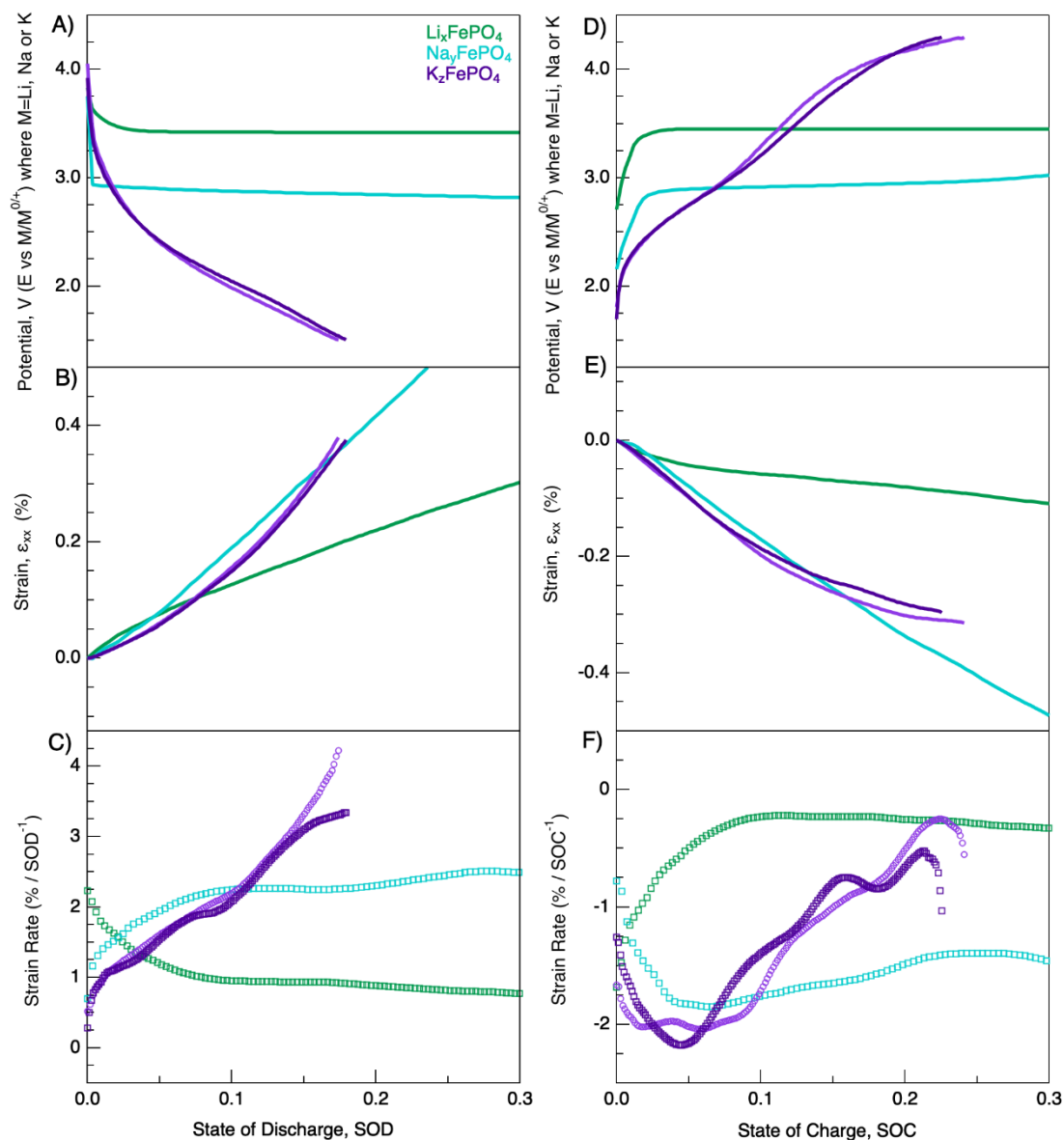
Figure C2. Potential evolution, strain generation and strain rates with respect to state of discharge (A,B, C) and charge (C, D, E) of Li (green), Na (blue) and K (purple) ions into FePO$_4$ electrode during the second cycle. The square and spherical symbol show when electrode is cycled either in EC:DMC or EC:PC solvents, respectively.

190

Figure C3. Potential evolution, strain generation and strain rates with respect to state of discharge (A,B, C) and charge (C, D, E) of Li (green), Na (blue) and K (purple) ions into $FePO_4$ electrode during the second cycle. The square and spherical symbol show when electrode is cycled either in EC:DMC or EC:PC solvents, respectively. The figure contains same data from **Figure C2**, only focuses on SOD / SOC until 0.3.
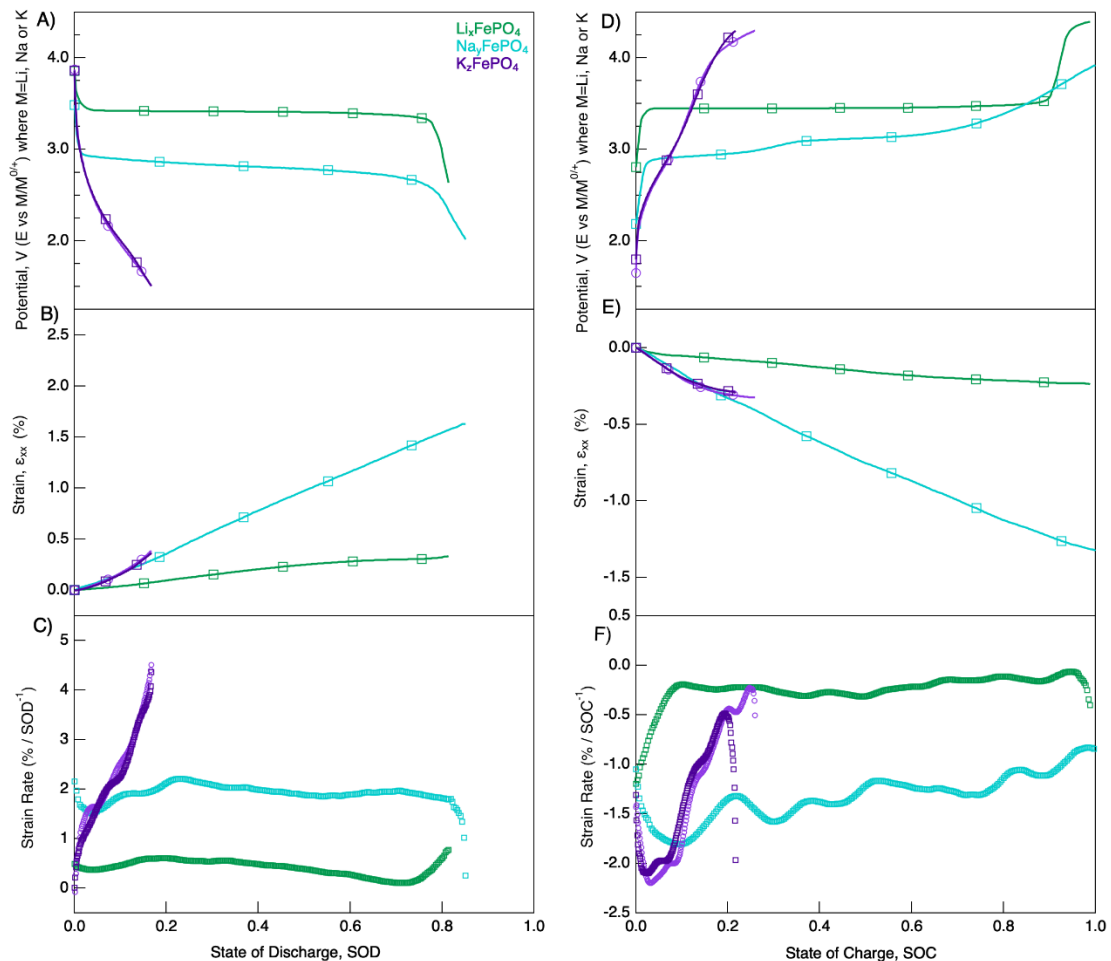
Figure C4. Potential evolution, strain generation and strain rates with respect to state of discharge (A,B, C) and charge (C, D, E) of Li (green), Na (blue) and K (purple) ions into FePO$_4$ electrode during the third cycle. The square and spherical symbol show when electrode is cycled either in EC:DMC or EC:PC solvents, respectively.
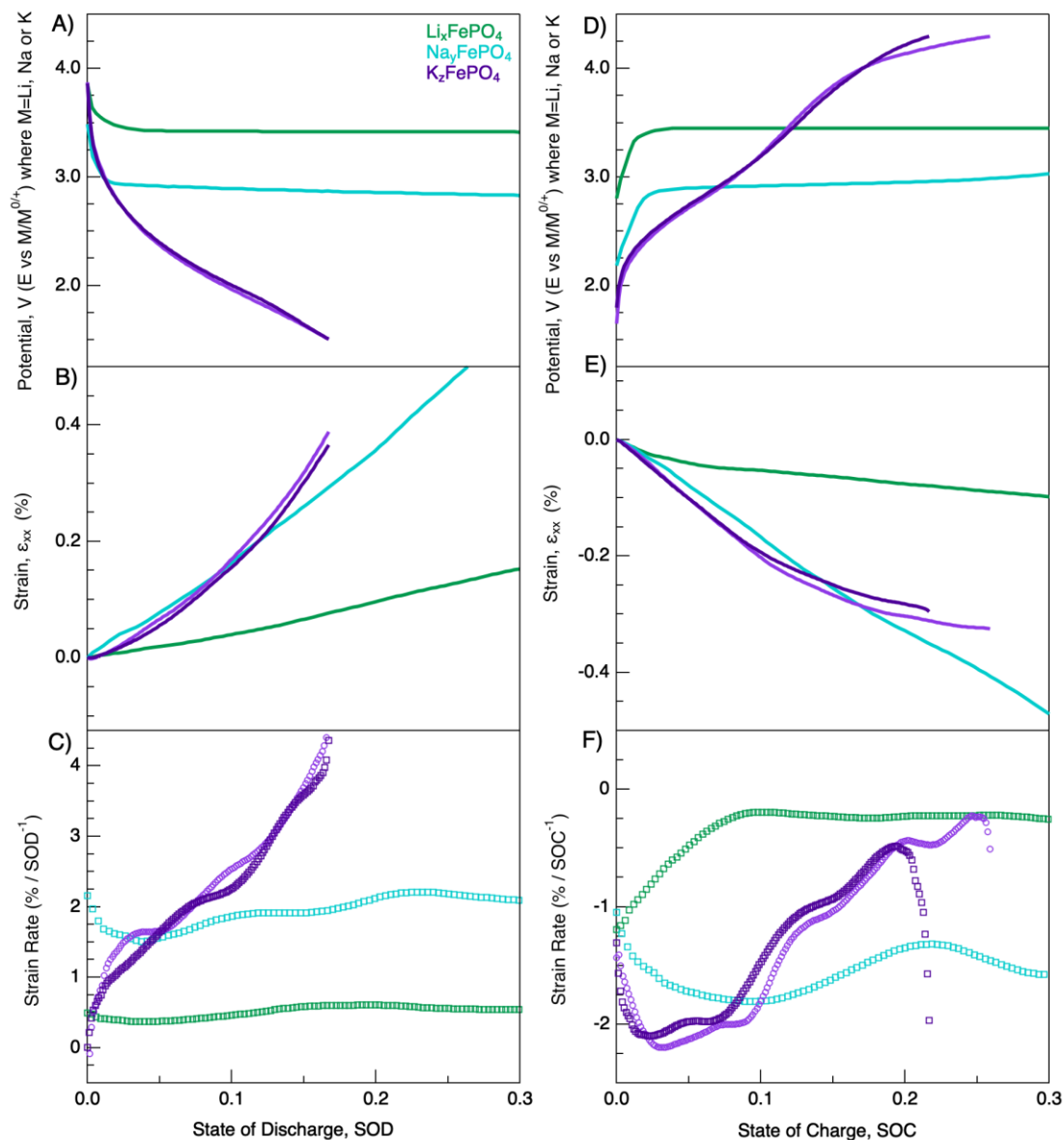
Figure C5. Potential evolution, strain generation and strain rates with respect to state of discharge (A,B, C) and charge (C, D, E) of Li (green), Na (blue) and K (purple) ions into FePO$_4$ electrode during the third cycle. The square and spherical symbol show when electrode is cycled either in EC:DMC or EC:PC solvents, respectively. The figure contains same data from **Figure C4**, only focuses on SOD / SOC until 0.3.
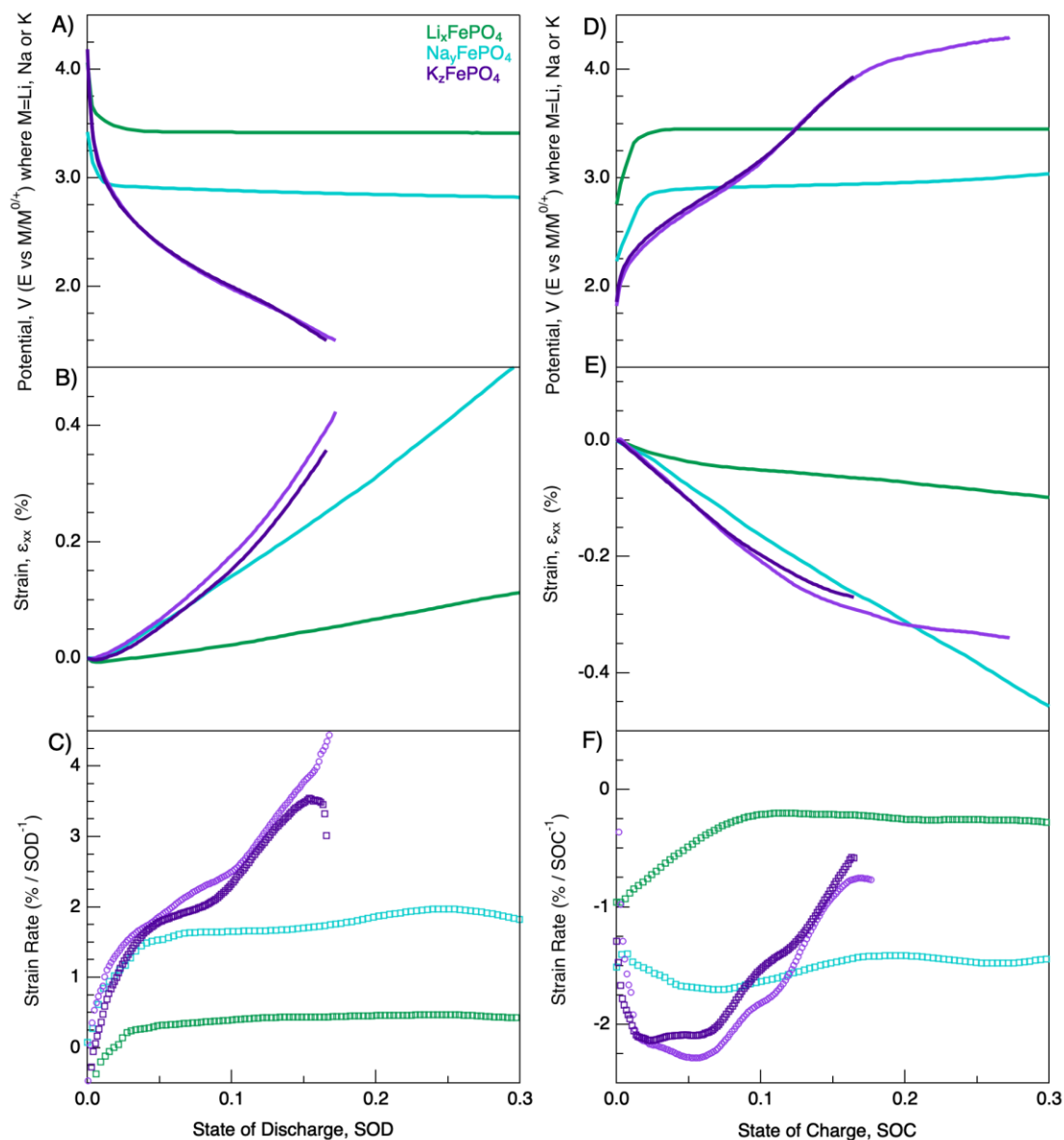
Figure C6. Potential evolution, strain generation and strain rates with respect to state of discharge (A,B, C) and charge (C, D, E) of Li (green), Na (blue) and K (purple) ions into FePO$_4$ electrode during the fourth cycle. The square and spherical symbol show when electrode is cycled either in EC:DMC or EC:PC solvents, respectively. The figure contains same data from **Figure 28**, only focuses on SOD / SOC until 0.3.
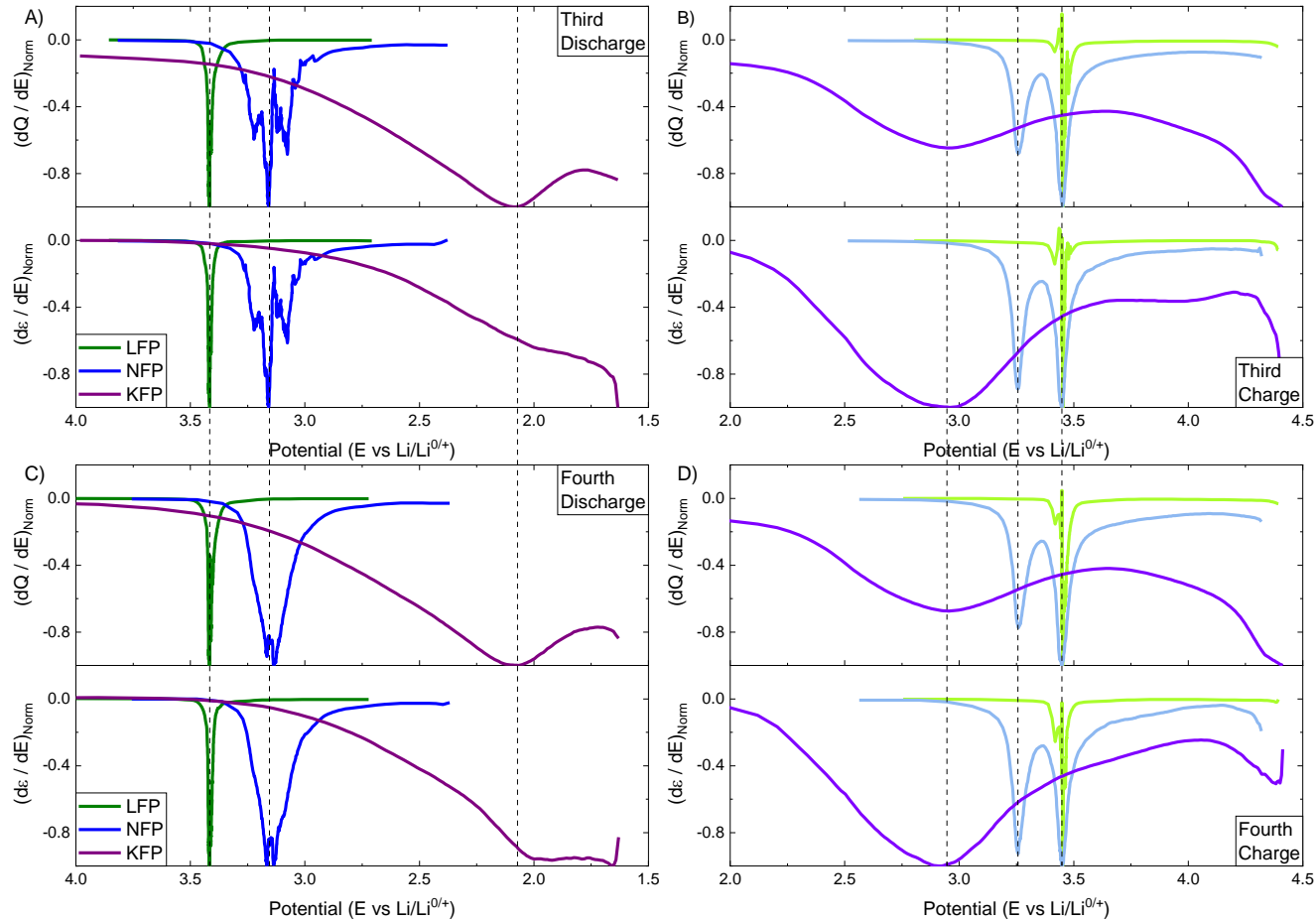
194

Figure C7. Normalized derivatives of capacity (dQ/dE) and strains (de/dE) with respect to potential for intercalation of Li (green), Na (blue) and K (purple) ions into FePO$_4$ during 3rd (A, B) and 4th (C, D) discharge and charge cycles. Derivatives are normalized by dividing the maximum nominal values in each charge and discharge cycles.

APPENDIX D

SUPPLEMENTARY INFORMATION FOR ELUCIDATING CYCLING RATE-DEPENDENT ELECTROCHEMICAL STRAINS IN SODIUM IRON PHOSPHATE CATHODES FOR Na-ION BATTERIES

Formation of Iron Phosphate Cathode via Electrochemical Displacement Method

Prior to each experiment, composite $LiFePO_4$ electrode galvanostatically delithiated at C/10 rate until the voltage reached 4.0 V against Na counter electrode. **Figure D1** (A,B) shows the potential and strain evolution during electrochemical displacement of Li from pristine $LiFePO_4$ electrode cycled in $NaClO_4$ in EC:DMC electrolyte against Na metal. The pristine LFP electrode showed very flat potential plateaus around 3.30 V (vs $Na/Na^{0/+}$) during electrochemical delithiation against Na counter electrodes. Delithiation capacity is calculated as 165 mA h g^{-1} when Li is extracted from pristine $LiFePO_4$ electrode and the capacity is similar to the theoretical capacity of the $LiFePO_4$ cathodes (170 mAh/g), which suggests that the lithium is successfully removed from the electrode structure. **Figure D1** (B) shows that during delithiation, electrode shrinks about 0.3%.

To further verify the extraction of Li from the pristine $LiFePO_4$ while forming $FePO_4$ electrode, we also performed ex situ XRD analysis. Swagelok coin cell system was used to prepare XRD samples for the verification of delithiation of pristine LFP electrodes. After the electrochemical displacement, carried out at C/10 rate to 4.0 V vs Na counter electrode, Swagelok coin cell was disassembled, and newly formed FP electrode removed from the cell. Electrode rinsed with 1 ml of 1:1 (v:v) EC:DMC to remove excess salt and dried for 24 h under ambient conditions. Samples

were characterized by X-ray diffraction (XRD, Bruker AXS D8 Discover diffractometer with General Area Detector Diffraction System, 40 kV, 35 mA) with Cu Kα radiation at scan rate of 1.0°/min with the 2θ range of 15–40°. **Figure D1** (C) shows the XRD pattern of the pristine LiFePO$_4$ and iron phosphate electrode formed by electrochemical displacement technique. The broad XRD peak around 34.5° was observed in the pristine composite lithium iron phosphate electrode. To verify its sources, we also perform XRD analysis on lithium iron phosphate powders, CMC binder, Super P carbon and Al foil individually. Two XRD peaks were observed from Al foil at 34.5° and 38.5°, which are associated with aluminum oxide (PDF #10-173) and aluminum (PDF #4-787) respectively. We found that the broad peak comes from the Al foil. XRD pattern of pristine electrode matches well with Triphylite LiFePO$_4$ (PDF #01-083-2092). After delithiation, peaks associated with LiFePO$_4$ disappear and new XRD spectra fits the Heterosite FePO$_4$ (PDF #00-034-0134) crystalline structure, showing the complete delithiation of LiFePO$_4$ to FePO$_4$. **Table D1** shows the calculated interplanar spacing before and after electrochemical displacement of LiFePO$_4$ composite electrode. These calculations show that electrochemical displacement of Li from LiFePO$_4$ reduces the interplanar spacing of the FePO$_4$. This observation agrees well with our strain measurement shown in **Figure D1**(B), which shows the shrinkage of composite electrode during electrochemical displacement of Li from LiFePO$_4$.
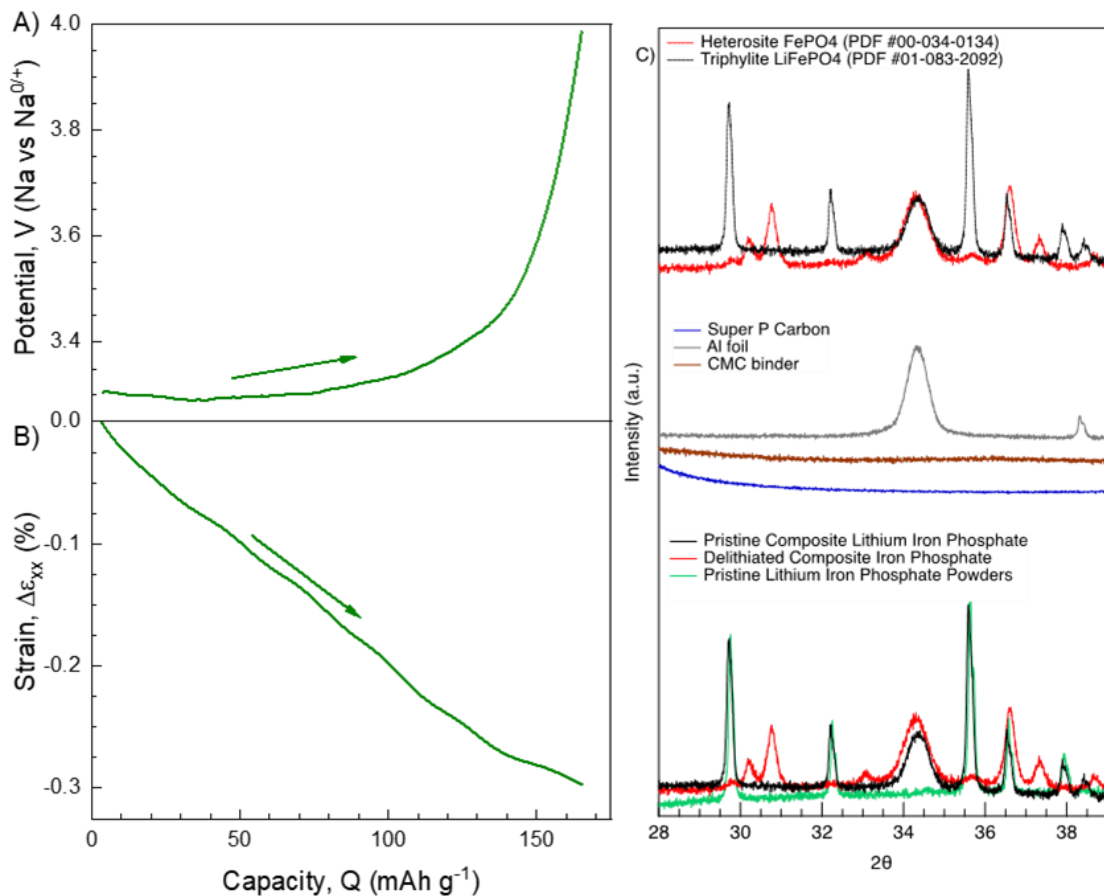
Figure D1. (A) Voltage and (B) strain evolution during electrochemical displacement of lithium from lithium iron phosphate LiFePO$_4$, to form iron phosphate, FePO$_4$, against Na counter electrode. Electrochemical displacement carried out until voltage reached 4.0 V vs Na/Na$^{0/+}$ in 1 M NaClO$_4$ with 1:1 (v:v) EC/DMC electrolyte at 0.1C rate. (C) XRD spectra of pristine LiFePO$_4$ composite electrode, delithiated composite iron phosphate after electrochemical delithiation, the pristine lithium iron phosphate powders, Super P carbon, Al foil and CMC binder. XRD spectra of Triphylite LiFePO$_4$ (PDF #01-083-2092) and Heterosite FePO$_4$ (PDF #00-034-0134) were also plotted in the **Figure D1**C.

Table D1. Interplanar spacing in LiFePO$_4$ and FePO$_4$ structure before and after electrochemical delithiation, respectively.

(hkl)		(200)	(211)	(311)	(121)
Before Electrochemical Delithiation (LiFePO$_4$)	**2θ/deg**	17.1526	29.7220	35.5892	36.5264
	d (Å)	5.1654	3.0034	2.5206	2.4580
After Electrochemical Delithiation (FePO$_4$)	**2θ/deg**	17.9401	30.1932	36.5776	37.3468
	d (Å)	4.9404	2.9576	2.4547	2.4059
Change	**Δd (Å)**	-0.2250	-0.0458	-0.0659	-0.0521
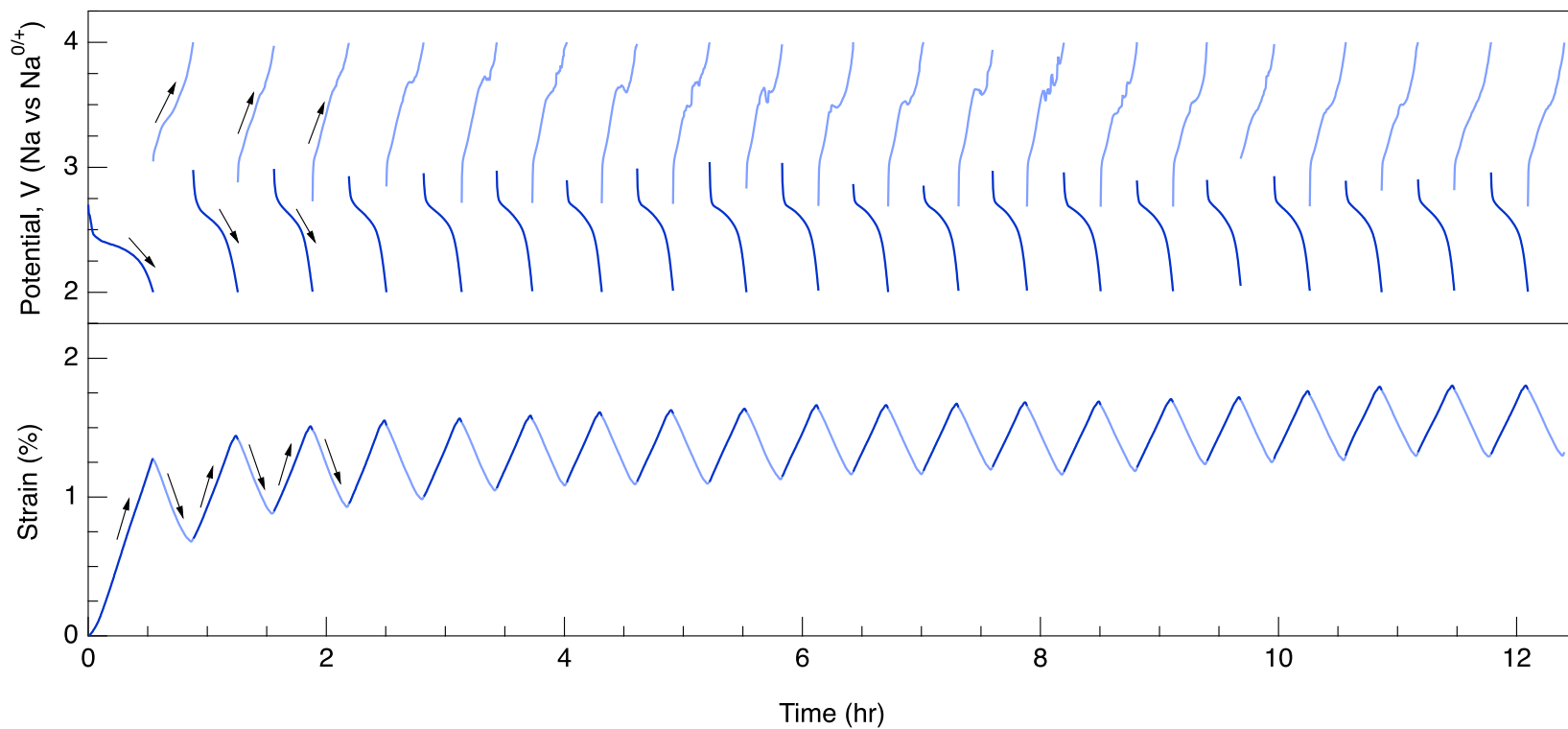
Figure D2. Voltage and strain evolution in iron phosphate composite electrode during sodium intercalation in 1 M NaClO$_4$ with 1:1 (v:v) EC/DMC electrolyte at 1C rate for 20 cycles.
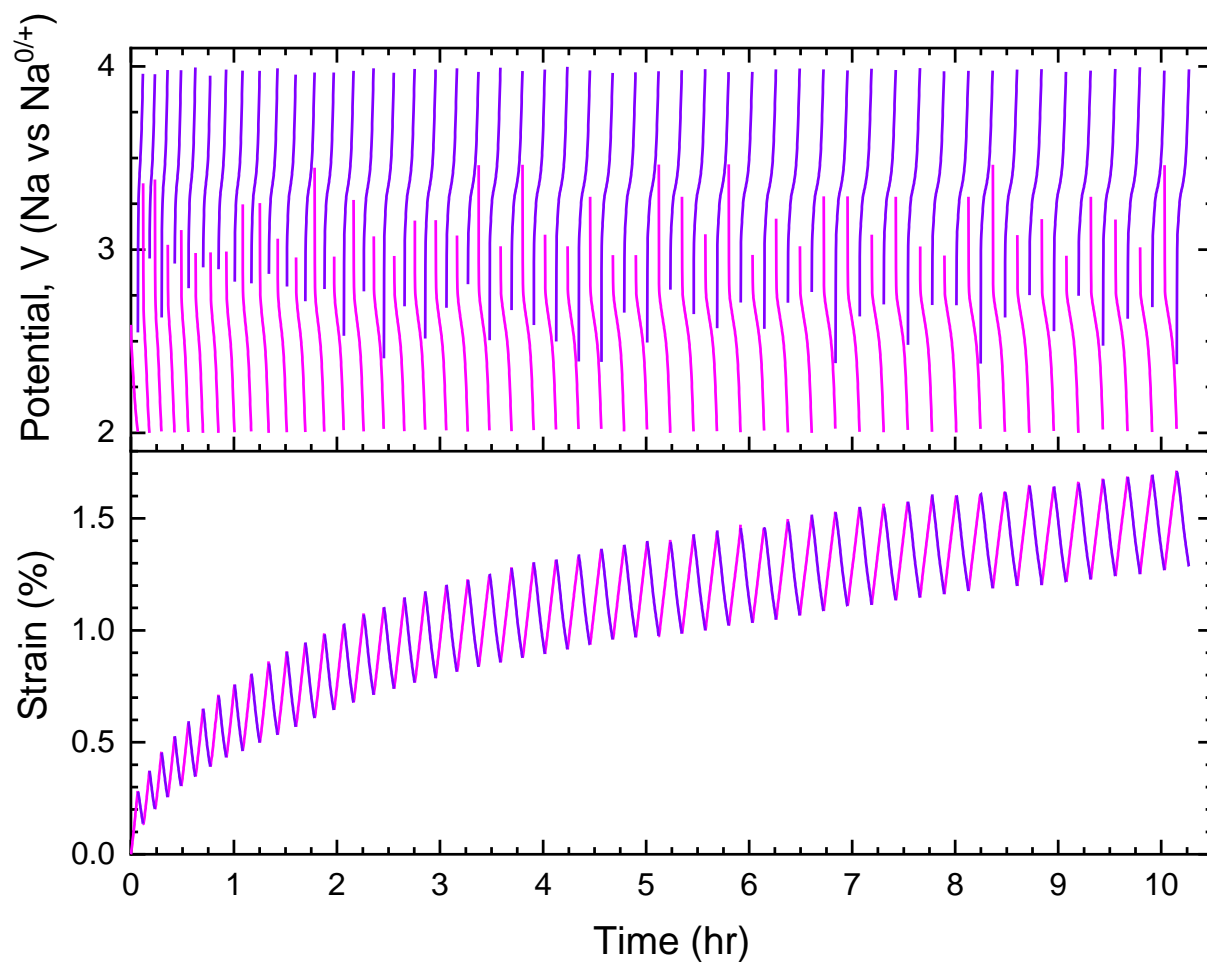
200

Figure D3. Voltage and strain evolution in iron phosphate composite electrode during sodium intercalation in 1 M NaClO$_4$ with 1:1 (v:v) EC/DMC electrolyte at 2C rate for 50 cycles.
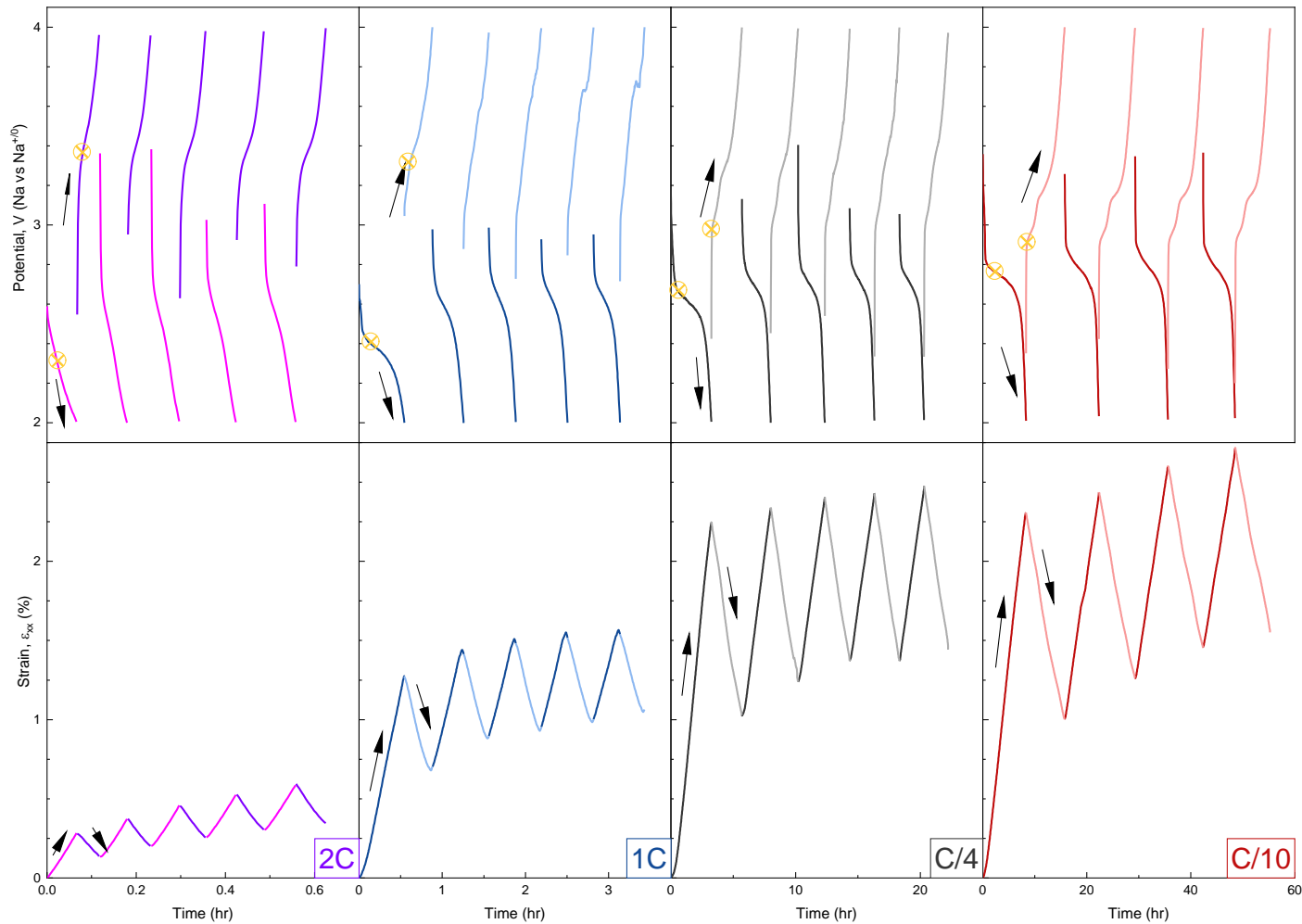
Figure D4. Voltage (top) and strain (bottom) evolution in iron phosphate composite electrode during sodium intercalation in 1 M NaClO$_4$ with 1:1 (v:v) EC/DMC electrolyte when cycled at (from left to right) 2C, 1C, C/4 and C/10 rates.
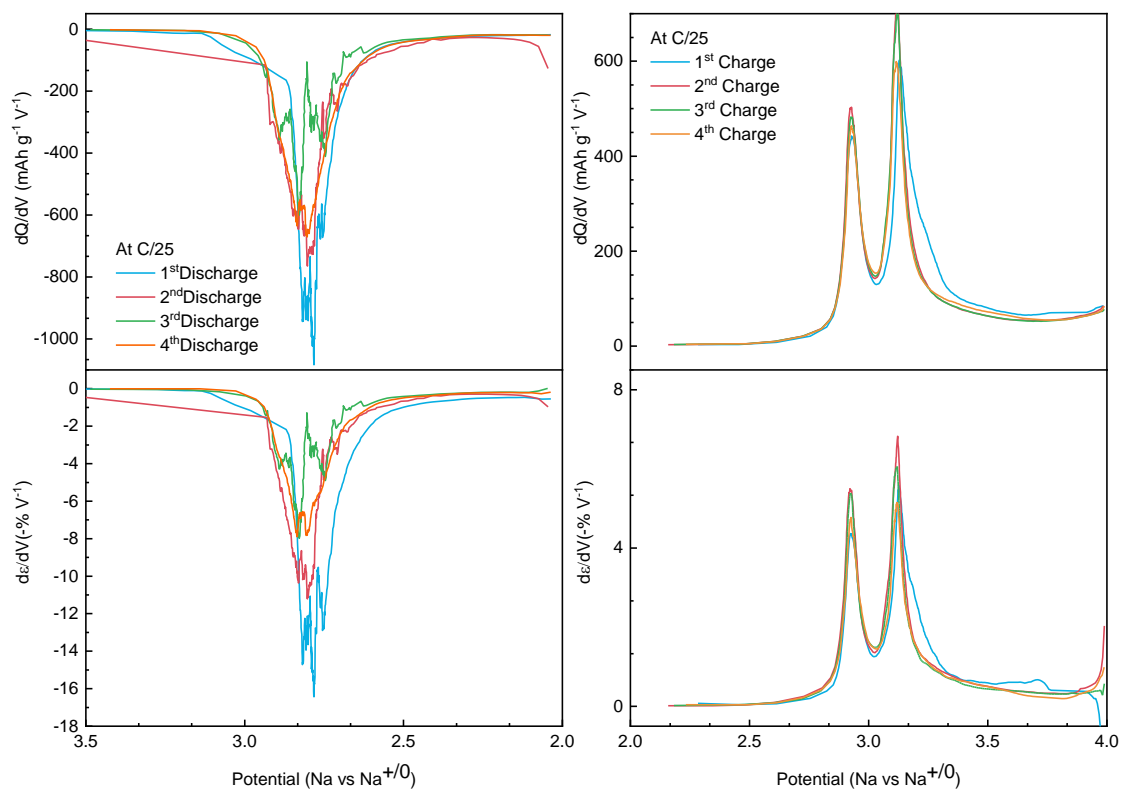
Figure D5. Capacity derivatives (A,B) and strain derivatives (C,D) in NaFePO$_4$ composite electrode cycled at different scan rates during sodiation (A,C) and desodiation (B,D) in 1 M NaClO$_4$ with 1:1 (v:v) EC/DMC electrolyte at C/25.
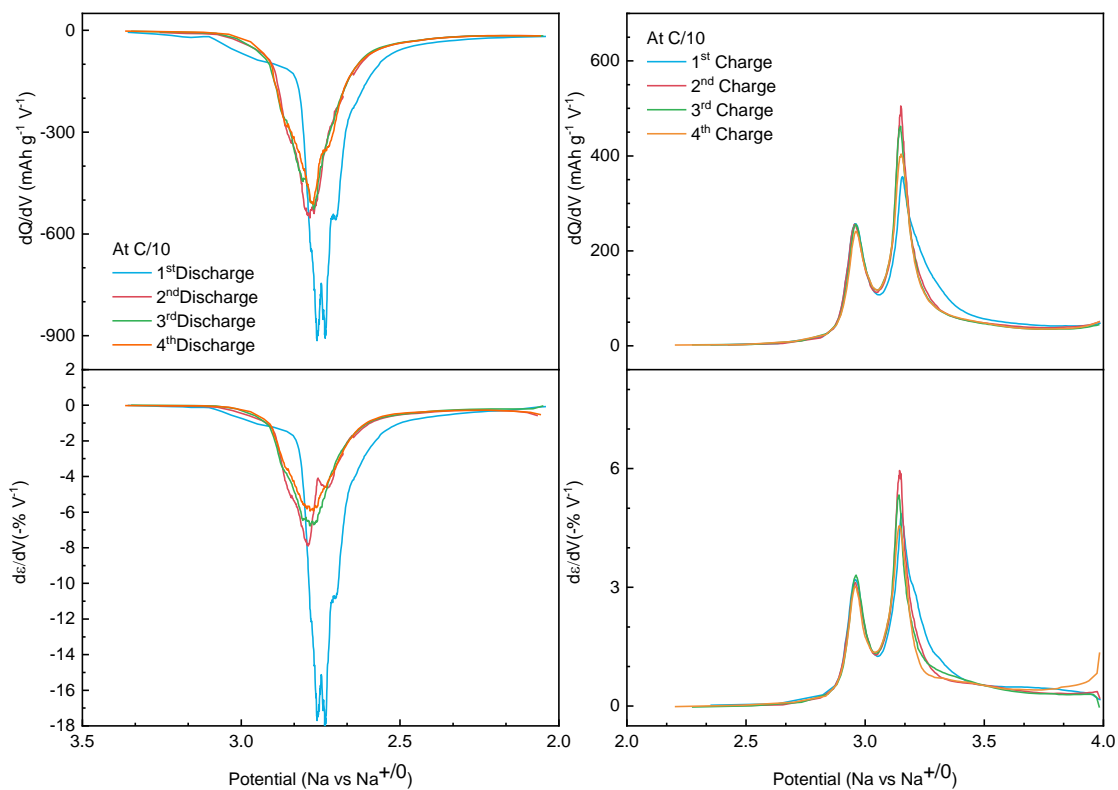
Figure D6. Capacity derivatives (A,B) and strain derivatives (C,D) in NaFePO$_4$ composite electrode cycled at different scan rates during sodiation (A,C) and desodiation (B,D) in 1 M NaClO$_4$ with 1:1 (v:v) EC/DMC electrolyte at C/10.
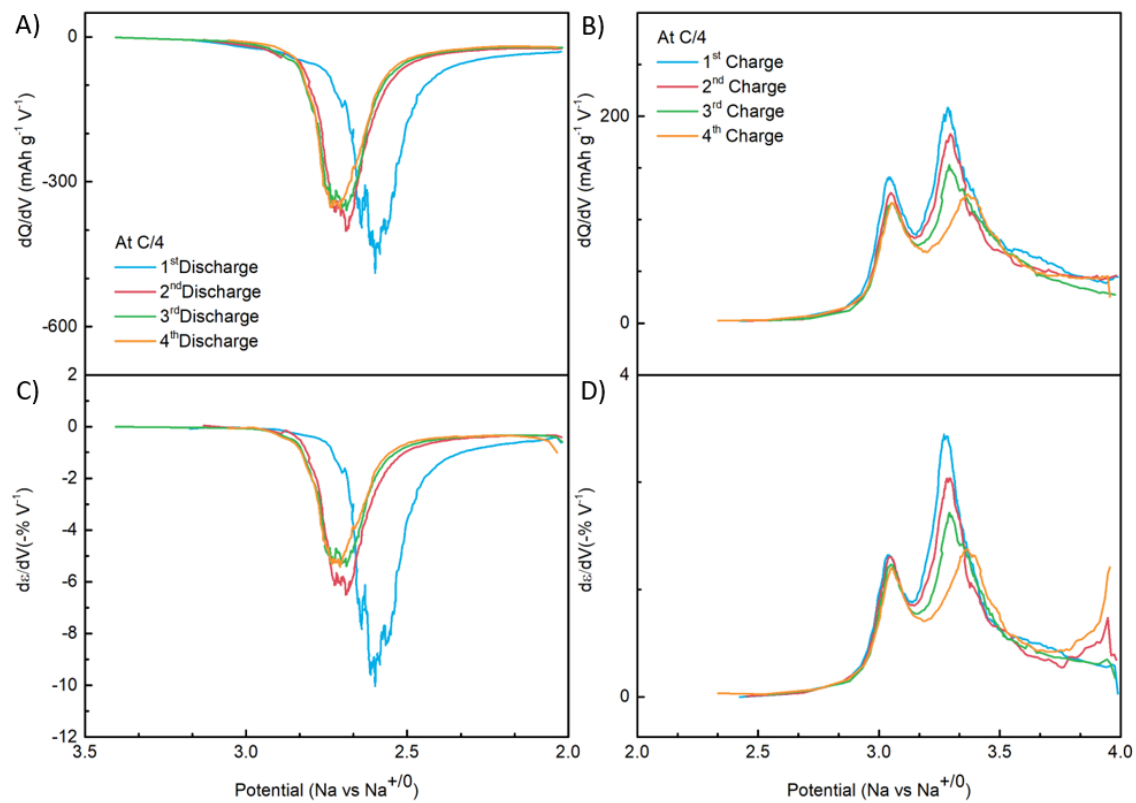
Figure D7. Capacity derivatives (A,B) and strain derivatives (C,D) in NaFePO$_4$ composite electrode cycled at different scan rates during sodiation (A,C) and desodiation (B,D) in 1 M NaClO$_4$ with 1:1 (v:v) EC/DMC electrolyte at C/4.
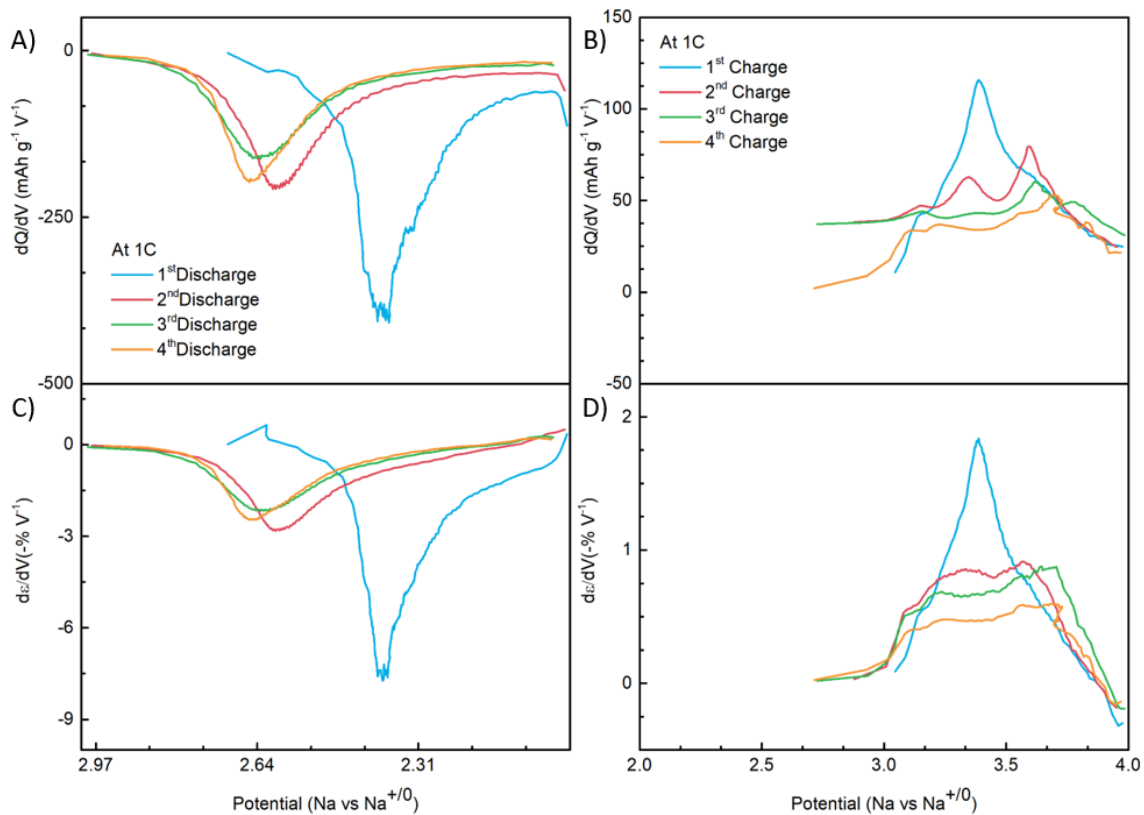
Figure D8. Capacity derivatives (A,B) and strain derivatives (C,D) in NaFePO$_4$ composite electrode cycled at different scan rates during sodiation (A,C) and desodiation (B,D) in 1 M NaClO$_4$ with 1:1 (v:v) EC/DMC electrolyte at 1C.

Figure D9. Capacity derivatives (A,B) and strain derivatives (C,D) in NaFePO$_4$ composite electrode cycled at different scan rates during sodiation (A,C) and desodiation (B,D) in 1 M NaClO$_4$ with 1:1 (v:v) EC/DMC electrolyte at 2C.
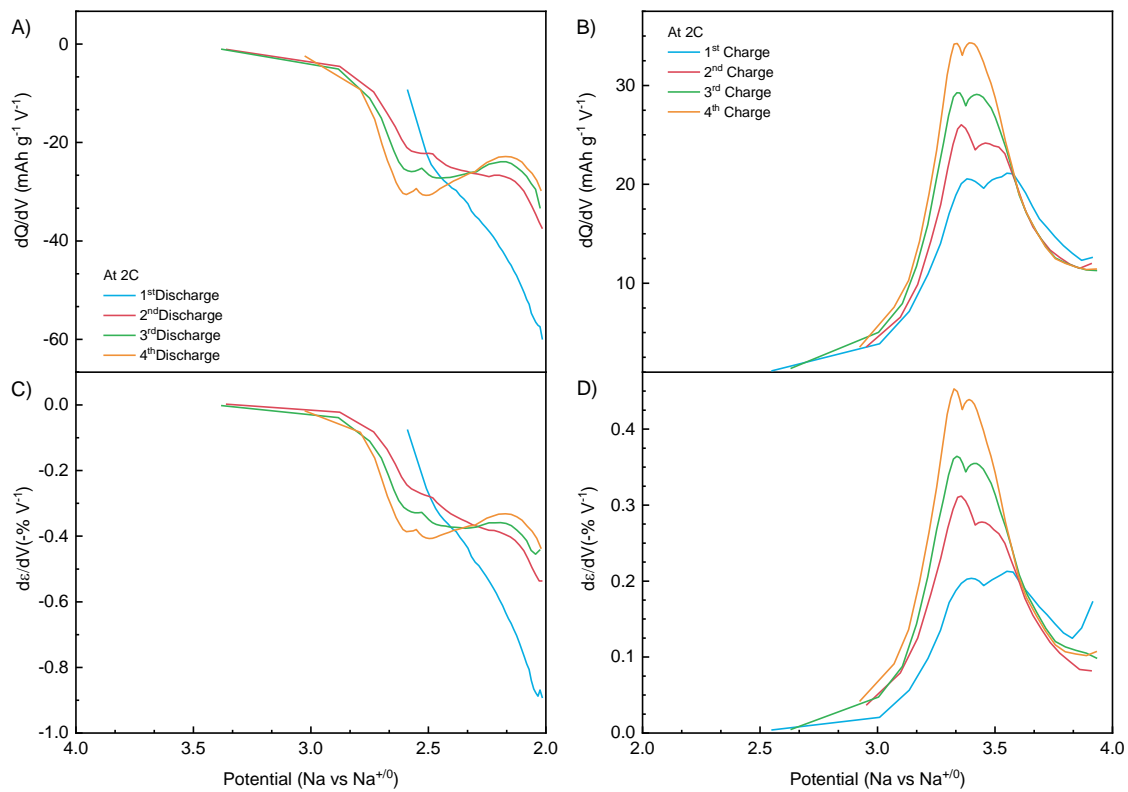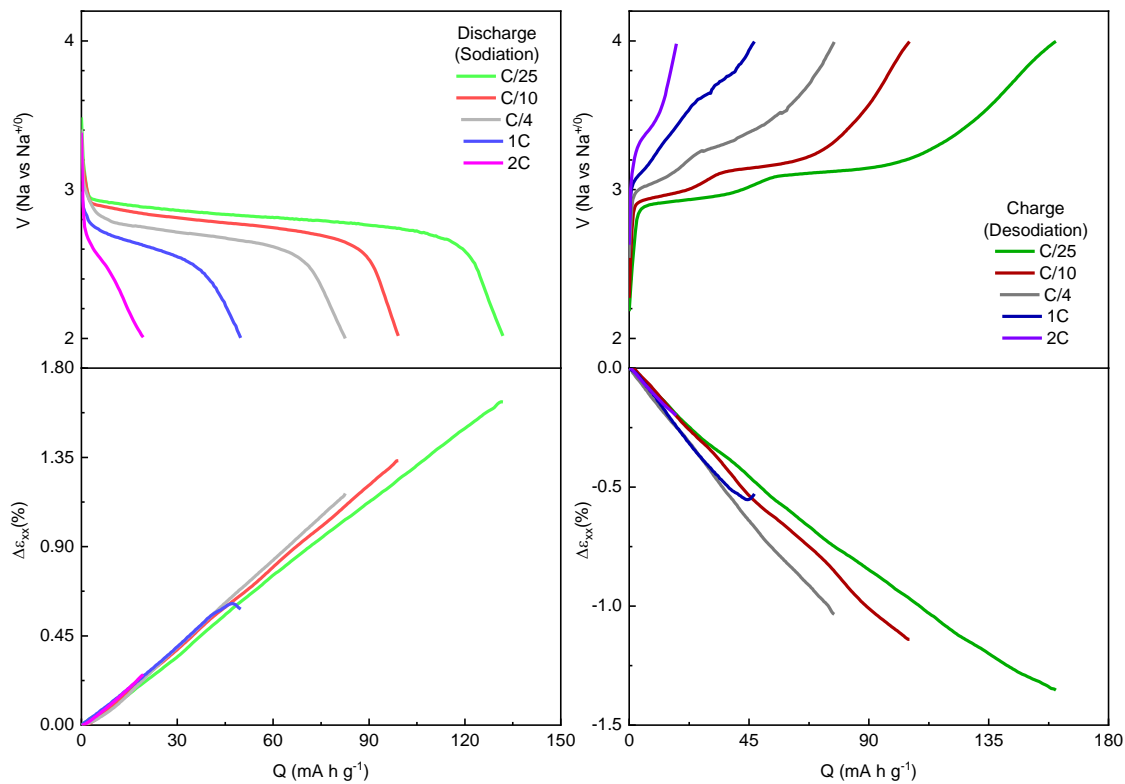
Figure D10. Voltage and strain evolution in iron phosphate composite electrode during sodium intercalation in 1 M NaClO$_4$ with 1:1 (v:v) EC/DMC electrolyte at different scan rates during 3rd cycle.

GITT Experiments

Experimental Details

Galvanostatic Intermittent Titration Technique (GITT) was conducted using an Arbin battery cycler. The NaFePO$_4$ cell were cycled between 2.0 and 4.4 V (vs. Na/Na+). All C-rates used in this study were based off of the theoretical capacity of NaFePO$_4$ (154 mA h g^{-1}). Prior to application of GITT, the electrochemical cells were first cycled galvanostatically 5 times at a current of 0.1 C. GITT was used to determine the equilibrium potentials and apparent diffusion coefficients as a function of composition. The thermodynamic equilibrium potentials were taken to be the open-circuit-voltage (OCV) at the end of the relaxation period.

Calculation Details

Chemical diffusion coefficients were calculated at the end of each step using the formula derived by Webbner et al[231]

$$D = \left(\frac{4}{\pi}\right)\left(\frac{V_M}{SFz_i}\right)^2 \left[\frac{I_0\left(\frac{dE}{d\delta}\right)}{\frac{dE}{d\sqrt{t}}}\right]^2 \tag{1}$$

where V_M is the molar volume of the electrode (44.11 cm^3 mol^{-1})[232], S is the electrochemically active surface area, F is Faraday's constant (96 485 C mol^{-1}), z_i is the charge number of species i, I_0 is the constant current applied during GITT, $\frac{dE}{d\delta}$ is the slope of the coulometric titration curve, and $\frac{dE}{d\sqrt{t}}$ is the slope of the linearized plot of the potential during the current pulse of duration t. The electrochemically active surface area was roughly estimated using the following equation[67]

$$S = \frac{1}{3}\left(\frac{6m_A}{d_p\rho_{FePO_4}}\right) \tag{2}$$

where m_A is the active material mass of the pristine NFP electrodes, d_p is the mean particle diameter ($\sim$250 nm), and ρ_{FePO4} is the mass density of $FePO_4$ (3.5 g cm^{-3}). The factor of 1/3 comes from the assumption that sodium extraction and insertion is analogous to lithium insertion and extraction along the [010] direction in LiFePO$_4$[233,234].If sufficiently small currents and pulse durations are applied so that the two derivatives in the earlier equation can be considered constant ($t \ll L^2/D$), then the following approximation may be used for determining diffusion coefficients[1]

$$D = \frac{4}{\pi\tau}\left(\frac{m_B V_M}{M_B S}\right)^2 \left(\frac{\Delta E_s}{\Delta E_t}\right)^2 \tag{3}$$

where τ is the current pulse duration, m_B is the electrode mass, M_B is the molecular weight of the electrode (150.82 g mol^{-1}), ΔE_s is the change in equilibrium voltages over a single galvanostatic titration, and ΔE_t is the total change in the cell voltage during the constant current pulse neglecting the iR drop. The apparent chemical diffusion coefficients of Na$^+$ in NFP at the end of each rest period was calculated using the above approximation. However, the Equation 1 was derived assuming ion diffusion in one-dimensional solid solution electrode materials[1] and is not valid at phase transition regions where the value of $\frac{dE}{d\delta}$ should be zero according to Gibbs phase rule[235]. Therefore, the values obtained in the phase transition region may not be reliable, but the values obtained in the solid solution regions are valid. The inability to satisfy this assumption is likely the reason for the deep minima observed in the phase transition region for the chemical diffusion coefficient.
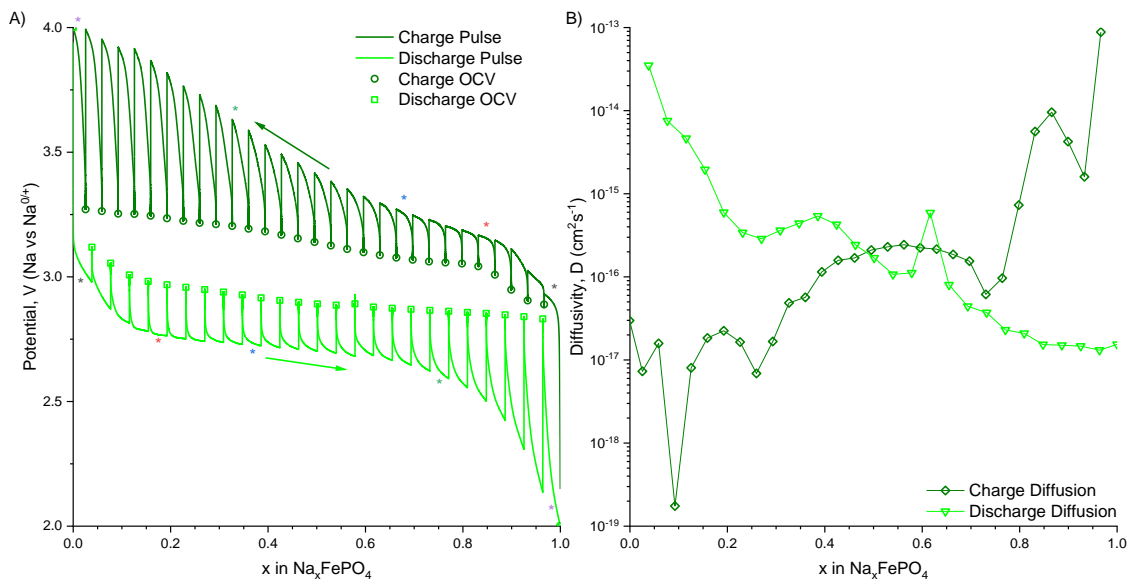
Figure D11. (A) Voltage evolution during GITT experiment for sodium insertion and extraction into Na$_x$FePO$_4$ electrode. GITT experiment was carried out with 1 h current pulse at C/40 rate and 10 h rest period in between current pulses in 1 M NaClO$_4$ with 1:1 (v:v) EC/DMC electrolyte. Colored asterisk (*) symbols show the position of voltage evolution during current pulses and resting periods used to produce **Figure D12** and **Figure D13**. (B) Apparent Na$^+$ diffusion coefficients in Na$_x$FePO4 electrode produced from GITT data.
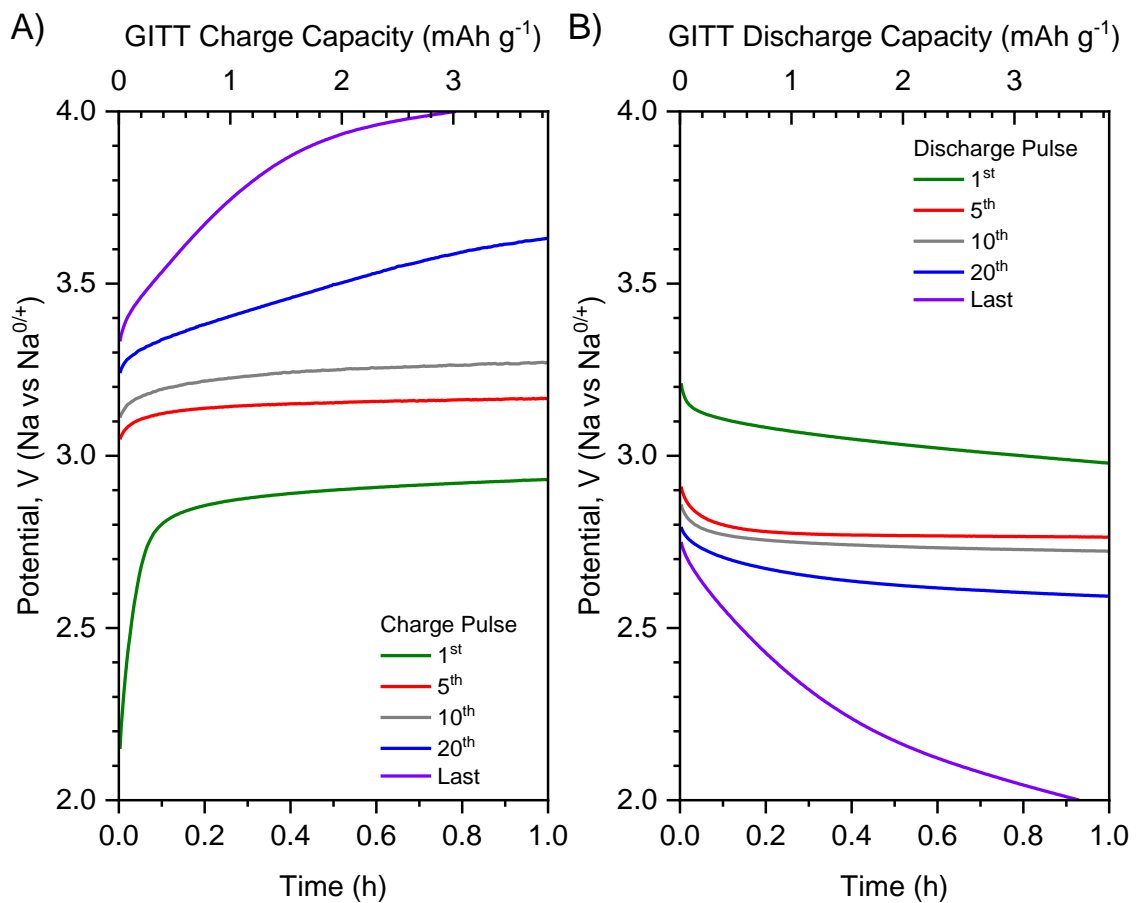
Figure D12. Evolution of voltage at different stages of GITT current pulses for (A) charge and (B) discharge stages. GITT experiment was carried out with 1 h current pulse at C/40 rate and 10 h rest period in between current pulses in 1 M NaClO$_4$ with 1:1 (v:v) EC/DMC electrolyte.
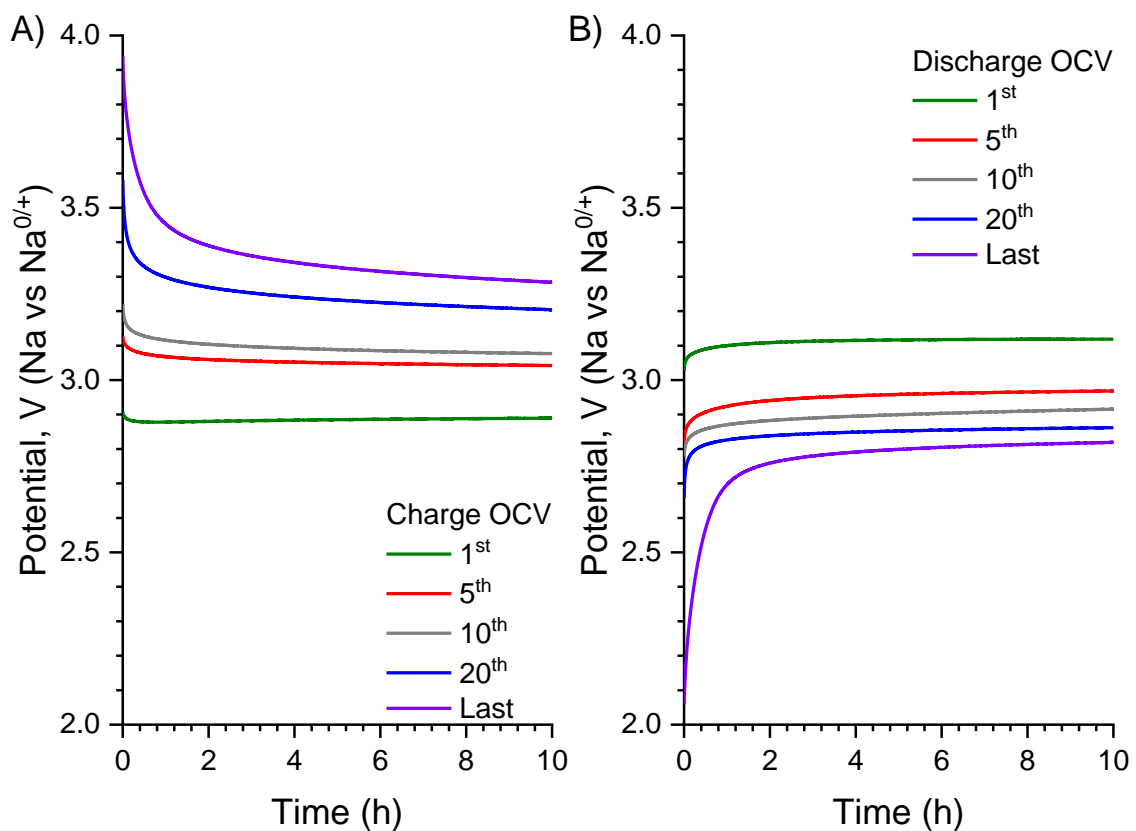
Figure D13. Evolution of voltage at different stages of GITT resting periods for (A) charge and (B) discharge stages. GITT experiment was carried out with 1 h current pulse at C/40 rate and 10 h rest period in between current pulses in 1 M NaClO$_4$ with 1:1 (v:v) EC/DMC electrolyte.

Predicting Strains in Composite Electrode

To investigate the strain on an unconstrained $NaFePO_4$ electrode during sodiation, the properties of the composite electrode are analyzed by assuming that the $NaFePO_4$ composite consists of a porous matrix of conductive carbon, Super P, and CMC binder[36].

Table D2. Material Properties of the Composite Electrode Matrix

Material Properties of the Composite Electrode Matrix				
Material	Fraction of Total Mass	Density (g/cm³)	Elastic Modulus (GPa)	Poisson's Ratio
NaFePO₄	0.8	3.53[236]	$84x10^9$	0.25[237]
CMC binder	0.1	1.6[238]	$1.2x10^9$	0.45[36]
Super P	0.1	1.9[239]	$32.47x10^9$	0.315[36]

The lower bound of the effective shear modulus containing both carbon black particles and CMC binder where K_m is the bulk modulus of the matrix of carbon black and CMC binder particles. The bulk modulus of the carbon black is K_{cb} and that of the CMC binder is K_{cmc}. G_m is the shear modulus of the matrix of carbon black and CMC binder particles. The shear modulus of the carbon black is G_{cb} and that of the CMC binder is G_{cmc}.

$$\frac{1}{K_m} = \frac{\phi_{m,cc}}{K_{cc}} + \frac{\phi_{m,cmc}}{K_{cmc}} \tag{4}$$

Lower bound of the bulk modulus containing both carbon black particles and CMC binder

$$\frac{1}{G_m} = \frac{\phi_{m,cc}}{G_{cc}} + \frac{\phi_{m,cmc}}{G_{cmc}} \tag{5}$$

Where

$$\phi_{m,cmc} = \frac{\phi_{cmc}}{\phi_{cmc}+\phi_{cc}} \tag{6}$$

$$\phi_{m,cb} = \frac{\phi_{cc}}{\phi_{cmc}+\phi_{cc}} \tag{7}$$

K_{pm} is the bulk modulus of a porous matrix of with solid components carbon black and CMC binder.

$$K_{pm} = \left(\frac{1}{3(1-2v_{pm})}\right)\left(\frac{K_m G_m}{3K_m+G_m}\right)\left(\frac{\rho_{pm}}{\rho_m}\right)^2 \tag{8}$$

Where the densities of the porous and solid matrices are

$$\rho_m = \phi_{m,cc}\rho_{cc} + \phi_{m,cmc}\rho_{cmc} \tag{9}$$

$$\rho_{pm} = \phi_{pm,cc}\rho_{cc} + \phi_{pm,cmc}\rho_{cmc} \tag{10}$$

The volume fractions of the conductive carbon and the CMC binder in the porous matrix is given by

$$\phi_{pm,cmc} = \frac{\phi_{cmc}}{\phi_{pm}} \tag{11}$$

$$\phi_{pm,cb} = \frac{\phi_{cc}}{\phi_{pm}} \tag{12}$$

The total volume fraction of the CMC, conductive carbon, and the porosity in the composite electrode is

$$\phi_{pm} = \phi_{cc} + \phi_{cmc} + \phi_p = 1 - \phi_{NFP} \tag{13}$$

The bulk modulus of the composite electrode[165] for NaFePO$_4$ particles, K_e is

$$K_{ce} = \frac{K_{pm}(1+\phi_{NFP}\xi_l\chi)}{1-\phi_{NFP}\Psi\chi} \tag{14}$$

Where

$$\chi = \frac{K_{NFP}-K_{pm}}{K_{NFP}-\xi_l K_{pm}} \tag{15}$$

$$\Psi = 1 + \frac{\phi_{NFP}\phi_{pm}(1-\gamma\phi_{pm})(K_{NFP}-K_{pm})\left(\frac{2(1-2v_{pm})}{(1+v_{pm})}-\frac{2(1-2v_{NFP})K_{NFP}}{(1+v_{NFP})K_{pm}}\right)}{K_{NFP}+\frac{2(1-2v_{NFP})K_{NFP}}{(1+v_{NFP})K_{pm}}(\phi_{NFP}K_{NFP}+\phi_{pm}K_{pm})} \tag{16}$$

$$\gamma = \frac{2\lambda^*-1}{\lambda^*} \tag{17}$$

The linear strain during sodiation of the composite electrode is

$$\varepsilon_{ce} = \epsilon_{NFP}\phi_{NFP} + \left(\frac{\varepsilon_{NFP}}{\frac{1}{K_{pm}}-\frac{1}{K_{NFP}}}\right)\left(\frac{1}{K_e} - \frac{1}{K_{average}}\right) \tag{18}$$

Where the average linear strain during sodiation is

$$\varepsilon_{average} = \varepsilon_{NFP}\phi_{NFP} + \phi_{pm}\varepsilon_{pm} \tag{19}$$

And the average bulk modulus of the composite electrode is

$$\frac{1}{K_{average}} = \frac{\phi_{NFP}}{K_{NFP}} + \frac{\phi_{pm}}{K_{pm}} \tag{20}$$

Table D3. Nomenclature for Equations used

Abbreviation	Definition
NFP	Sodium Iron Phosphate (NaFePO₄)
ce	Composite Electrode
cc	Conductive carbon
cmc	Carboxymethyl cellulose binder
pm	Porous matrix

Table D4. List of variables used and the descriptions

Variable	Definition
K_m	bulk modulus of the matrix of carbon black and CMC binder particles
K_{cc}	bulk modulus of the conductive carbon (Super P)
K_{cmc}	bulk modulus of the CMC binder
G_m	shear modulus of matrix of carbon black and CMC binder particles
G_{cc}	shear modulus of the conductive carbon
G_{cmc}	shear modulus of the CMC binder particles
$\Phi_{m,cc}$	Volume fraction in the conductive carbon/CMC matrix of the conductive carbon
$\Phi_{m,cc}$	Volume fraction in the conductive carbon/CMC matrix of the CMC
K_{pm}	bulk modulus of a porous matrix of with solid components conductive carbon and CMC binder
ν_{pm}	Poisson's ratio of the porous matrix, assumed to be 1/3[1]
ρ_{pm}	Density of the porous matrix consisting of conductive carbon, CMC binder, and porosity
ρ_m	Density of the solid matrix consisting of conductive carbon and CMC binder

Variable	Definition
ρ_{cc}	Density of the conductive carbon (Super P)
ρ_{cmc}	Density of the CMC binder
$\phi_{pm,cc}$	Volume fraction of the conductive carbon in the porous matrix of the conductive carbon and CMC
$\phi_{pm,cmc}$	Volume fraction of the CMC binder in the porous matrix of the conductive carbon and CMC binder
ϕ_{cmc}	Volume fraction of the CMC binder in the composite electrode
ϕ_{cmc}	Volume fraction of the CMC binder in the composite electrode
ϕ_{cmc}	Volume fraction of the CMC binder in the composite electrode
ϕ_{cc}	Volume fraction of the conductive carbon in the composite electrode
ϕ_{pm}	Volume fraction of the CMC, conductive carbon, and the porosity in the composite electrode
ϕ_p	Porosity within the composite electrode
ϕ_{NFP}	Volume fraction of the iron phosphate within the composite electrode
K_{ce}	Bulk modulus of the composite electrode
ν_{NFP}	Poisson's ratio of the $NaFePO_4$
K_{NFP}	Bulk modulus of particles in $NaFePO_4$
λ^*	Critical volume fraction for close packing of the particle filler, 2/3 [reference 7]
Ψ	Correction factor term
ϵ_{ce}	Linear strain of composite electrode
$\epsilon_{average}$	Average linear strain during sodiation
ϵ_{pm}	Linear strain of the porous matrix
ϵ_{NFP}	Linear strain of the $NaFePO_4$ during sodiation
$K_{average}$	Average bulk modulus of the composite electrode

Inputs for Transport-Mechanics Model

Density of $NaFePO_4$ (density)$c^{236} = 3.47 \times 10^5 \; \frac{g}{m^3}$

Constant Diffusivity $= 2 \times 10^{-15} \; cm^2/s$

Faraday's constant $= 26.801 \; \frac{Ah}{mol}$

Molecular Weight of $NaFePO_4$ host structure[240] $(MW) = 173.81 \; \frac{g}{mol}$

Maximum Concentration of Sodium $= \frac{density}{MW} = 2.61 \times 10^3 \; \frac{mol}{m^3}$

Theoretical Capacity of $NaFePO_4$ (alpha)[68] $= 0.154 \; \frac{Ah}{g}$

r_{max} (radius of sodium particle) $= 125 \times 10^{-9} \; m$

C-rates$=1/100,1/66,1/25,1/10,1/2,1$

APPENDIX E

SUPPLEMENTARY INFORMATION FOR RATE-DEPENDENT ELECTROCHEMICAL

STRAIN GENERATION IN COMPOSITE IRON PHOSPHATE CATHODES IN Li-ION

BATTERIES

Table E1. Discharge, charge, and irreversible strain evolution during electrochemical cycling at C/25 rate cycled with 1 M $LiClO_4$ in 1:1 EC:DMC electrolyte against Li counter electrode.

Cycle Number	Discharge Strain (%)	Charge Strain (%)	Irreversible Strain (%)
1	0.612	-0.345	0.267
2	0.448	-0.309	0.139
3	0.377	-0.293	0.084
4	0.344	-0.290	0.054
5	0.323	-0.288	0.035

Table E2. Discharge, charge, and irreversible strain evolution during electrochemical cycling at C/10 rate cycled with 1 M LiClO$_4$ in 1:1 EC:DMC electrolyte against Li counter electrode.

Cycle Number	Discharge Strain (%)	Charge Strain (%)	Irreversible Strain (%)
1	0.644	-0.368	0.276
2	0.467	-0.343	0.124
3	0.396	-0.325	0.071
4	0.369	-0.321	0.048
5	0.354	-0.322	0.032

Table E3. Discharge, charge, and irreversible strain evolution during electrochemical cycling at C/4 rate cycled with 1 M LiClO$_4$ in 1:1 EC:DMC electrolyte against Li counter electrode.

Cycle Number	Discharge Strain (%)	Charge Strain (%)	Irreversible Strain (%)
1	0.603	-0.402	0.200
2	0.467	-0.380	0.087
3	0.418	-0.362	0.056
4	0.392	-0.361	0.031
5	0.376	-0.347	0.029

Table E4. Discharge, charge, and irreversible strain evolution during electrochemical cycling at 1C rate cycled with 1 M LiClO$_4$ in 1:1 EC:DMC electrolyte against Li counter electrode.

Cycle Number	Discharge Strain (%)	Charge Strain (%)	Irreversible Strain (%)
1	0.452	-0.361	0.091
2	0.422	-0.389	0.033
3	0.424	-0.393	0.031
4	0.423	-0.395	0.028
5	0.413	-0.393	0.020
6	0.417	-0.404	0.013
7	0.413	-0.391	0.022
8	0.406	-0.394	0.013
9	0.403	-0.394	0.009
10	0.408	-0.398	0.010
11	0.398	-0.383	0.015
12	0.395	-0.382	0.012
13	0.393	-0.381	0.012
14	0.401	-0.386	0.015
15	0.394	-0.385	0.008
16	0.391	-0.377	0.014
17	0.383	-0.373	0.009
18	0.381	-0.376	0.006
19	0.385	-0.379	0.006
20	0.386	-0.380	0.006

Table E5. Discharge, charge and irreversible strain evolution during electrochemical cycling at 2.5C rate cycled with 1 M LiClO$_4$ in 1:1 EC:DMC electrolyte against Li counter electrode.

Cycle Number	Discharge Strain (%)	Charge Strain (%)	Irreversible Strain (%)
1	0.383	-0.305	0.078
2	0.355	-0.333	0.022
3	0.360	-0.343	0.017
4	0.362	-0.343	0.019
5	0.366	-0.353	0.013
6	0.372	-0.362	0.010
7	0.366	-0.354	0.012
8	0.359	-0.350	0.009
9	0.365	-0.351	0.014
10	0.372	-0.361	0.010
11	0.377	-0.360	0.017
12	0.364	-0.356	0.009
13	0.374	-0.362	0.011
14	0.368	-0.365	0.003
15	0.374	-0.373	0.001
16	0.377	-0.367	0.009
17	0.373	-0.364	0.010
18	0.374	-0.363	0.010
19	0.383	-0.376	0.008
20	0.379	-0.370	0.009
21	0.376	-0.365	0.011
22	0.378	-0.364	0.014
23	0.380	-0.373	0.007
24	0.366	-0.363	0.003
25	0.364	-0.357	0.006
26	0.373	-0.362	0.012
27	0.359	-0.351	0.008
28	0.371	-0.355	0.017
29	0.374	-0.358	0.016
30	0.357	-0.344	0.013
31	0.350	-0.342	0.008
32	0.358	-0.347	0.012
33	0.354	-0.344	0.010
34	0.357	-0.349	0.009
35	0.350	-0.342	0.008
36	0.350	-0.347	0.002
37	0.358	-0.343	0.015

Table E5. Continued

Cycle Number	Discharge Strain (%)	Charge Strain (%)	Irreversible Strain (%)
38	0.352	-0.340	0.012
39	0.352	-0.338	0.015
40	0.358	-0.346	0.012
41	0.348	-0.340	0.008
42	0.354	-0.348	0.006
43	0.352	-0.349	0.003
44	0.355	-0.345	0.010
45	0.347	-0.343	0.003
46	0.349	-0.333	0.017
47	0.341	-0.330	0.012
48	0.343	-0.335	0.008
49	0.343	-0.337	0.006
50	0.360	-0.357	0.003
51	0.349	-0.343	0.007
52	0.345	-0.342	0.003
53	0.338	-0.332	0.006
54	0.355	-0.342	0.013
55	0.353	-0.349	0.004
56	0.337	-0.322	0.014
57	0.350	-0.337	0.013
58	0.343	-0.337	0.006
59	0.349	-0.338	0.011
60	0.340	-0.324	0.016
61	0.347	-0.336	0.011
62	0.339	-0.336	0.003
63	0.345	-0.336	0.009
64	0.343	-0.336	0.007
65	0.339	-0.332	0.007
66	0.337	-0.326	0.011
67	0.343	-0.345	-0.001
68	0.346	-0.344	0.002
69	0.345	-0.332	0.014
70	0.329	-0.330	-0.001
71	0.341	-0.328	0.013
72	0.334	-0.338	-0.004
73	0.336	-0.327	0.009
74	0.341	-0.340	0.001
75	0.356	-0.335	0.020
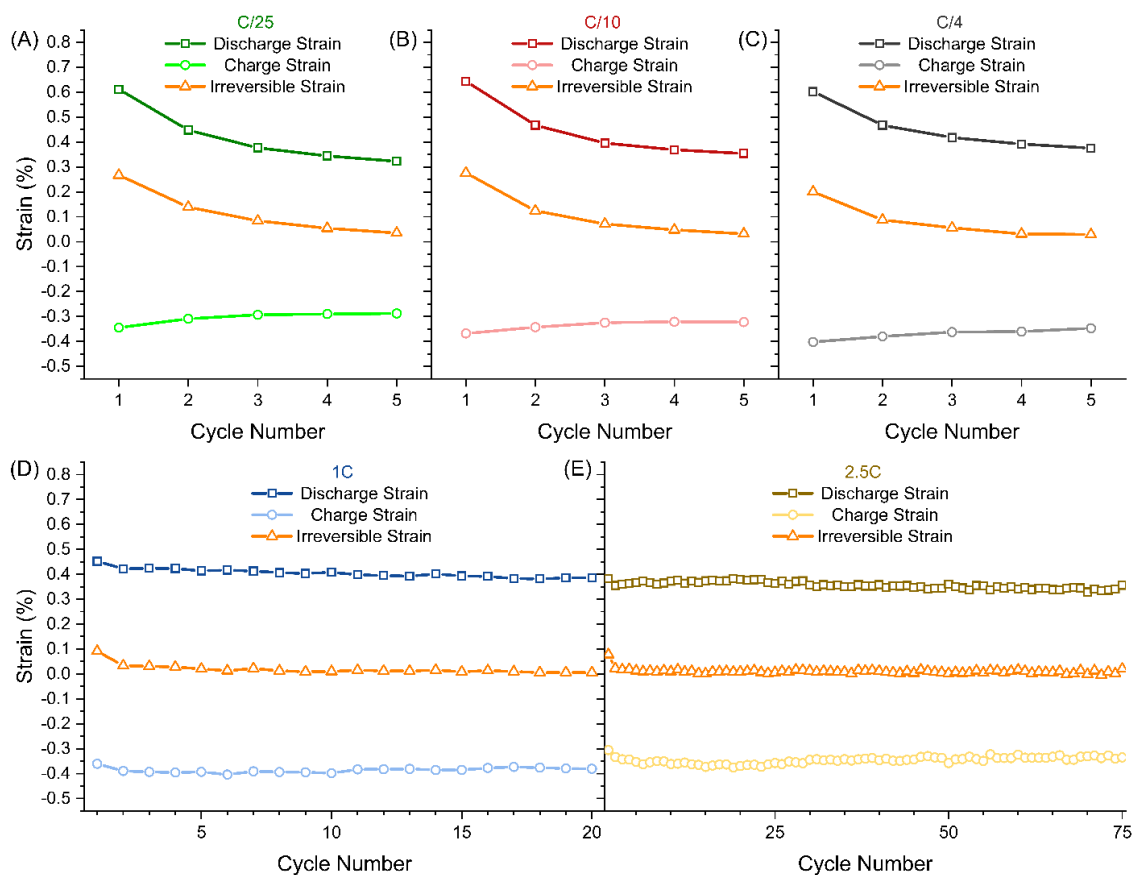
Figure E1. Discharge, charge, and irreversible strain evolution for FP composite electrode during cycling between 2.6-4.4 V against Li counter electrode at different scan rates with 1 M LiClO$_4$ in 1:1 EC:DMC electrolyte.
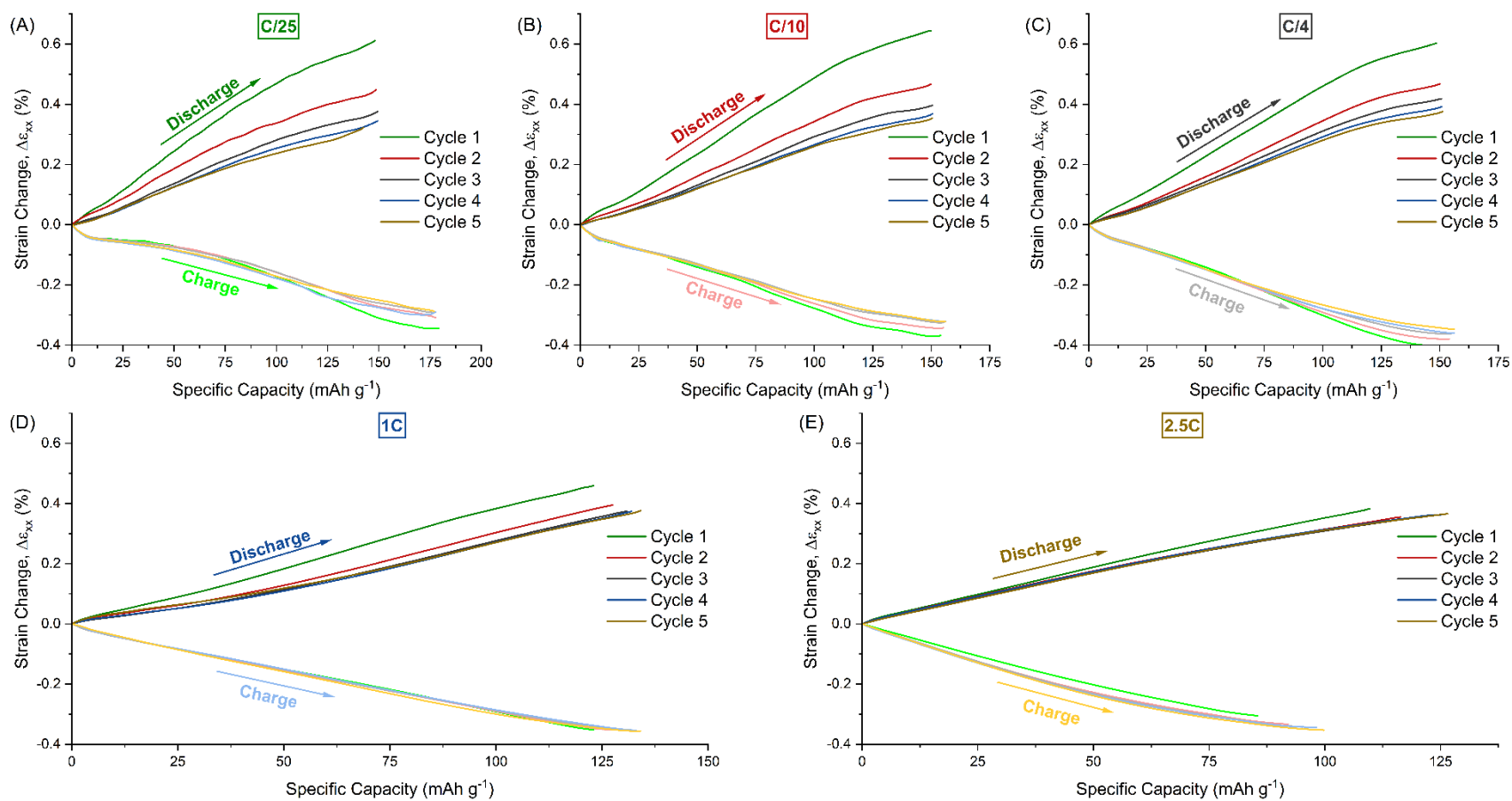
Figure E2. Strain evolution for FP electrode during charge and discharge cycles for (a) C/25, (b) C/10, (c) C/4, (d) 1C and € 2.5C rates. Strain evolution during discharge and charge cycles set to zero at the beginning of discharge and charge cycles, respectively.

226
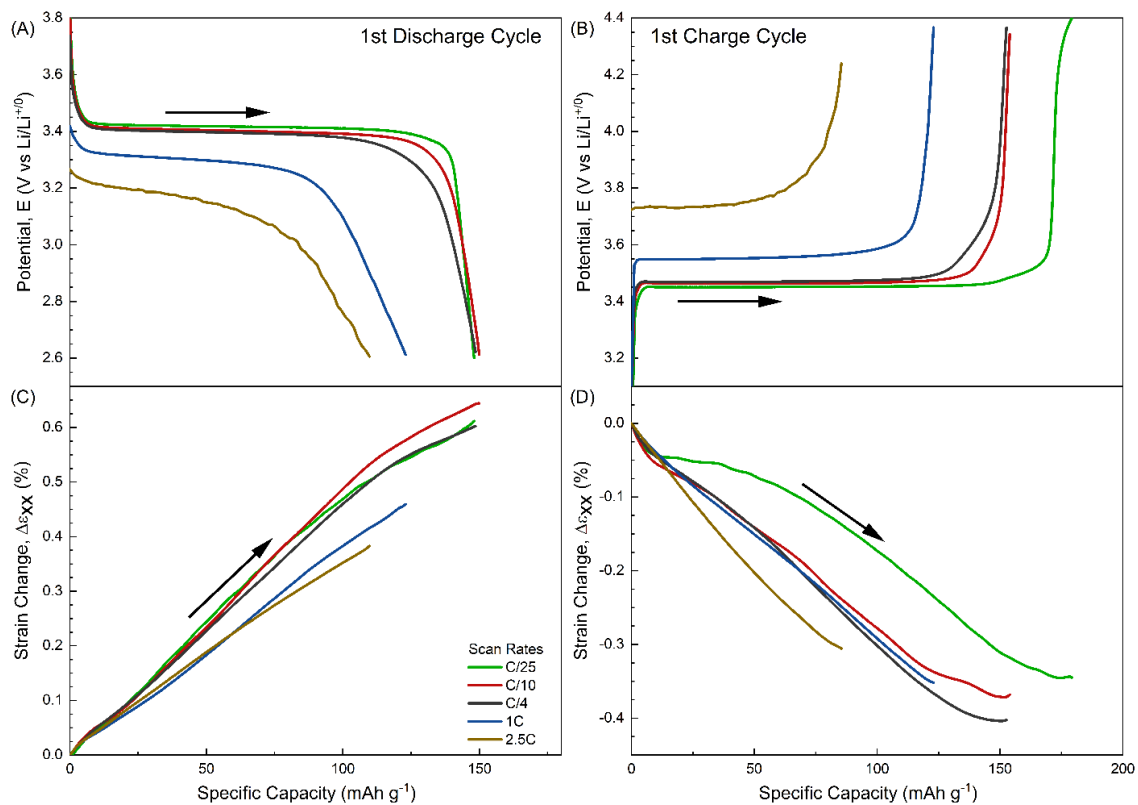
Figure E3. (a,b) Potential and (c,d) strain evolution of FP electrode cycled at different scan rates during the 1st cycle for (a,c) discharge and (b,d) charge cycles, respectively. Strain evolution during discharge and charge cycles set to zero at the beginning of discharge and charge cycles, respectively.
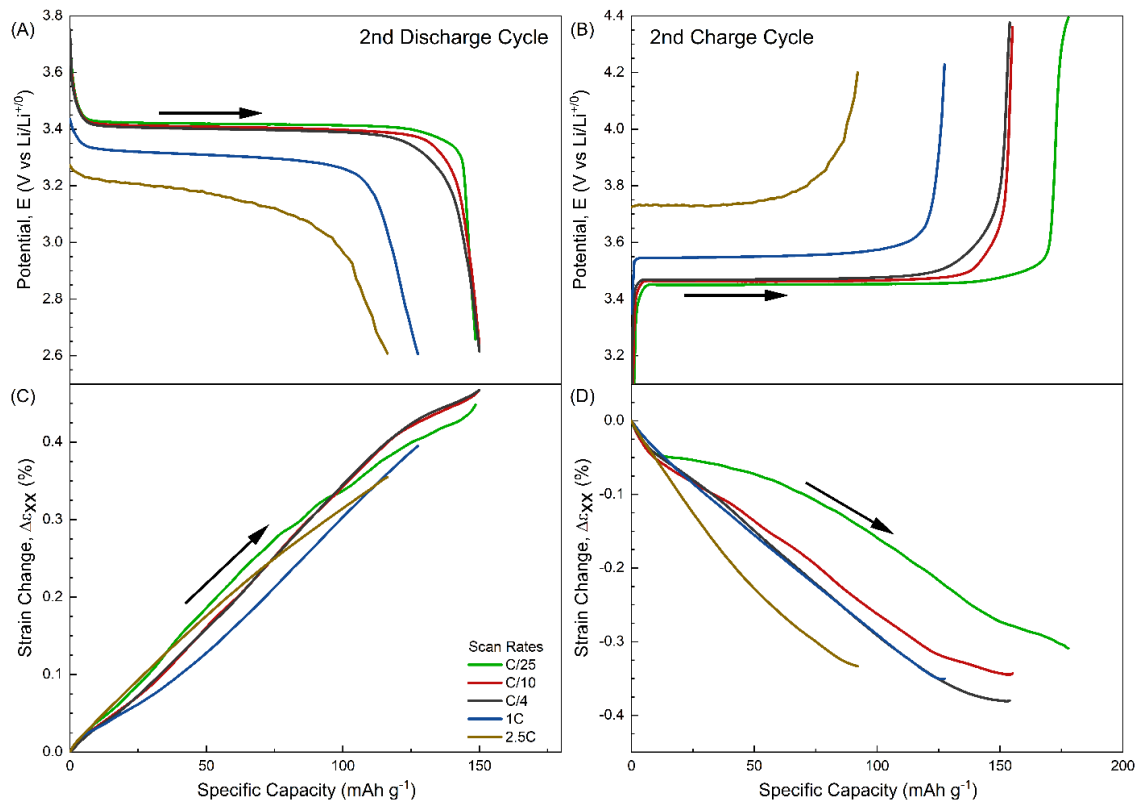
Figure E4. (a,b) Potential and (c,d) strain evolution of FP electrode cycled at different scan rates during the 2nd cycle for (a,c) discharge and (b,d) charge cycles, respectively. Strain evolution during discharge and charge cycles set to zero at the beginning of discharge and charge cycles, respectively.
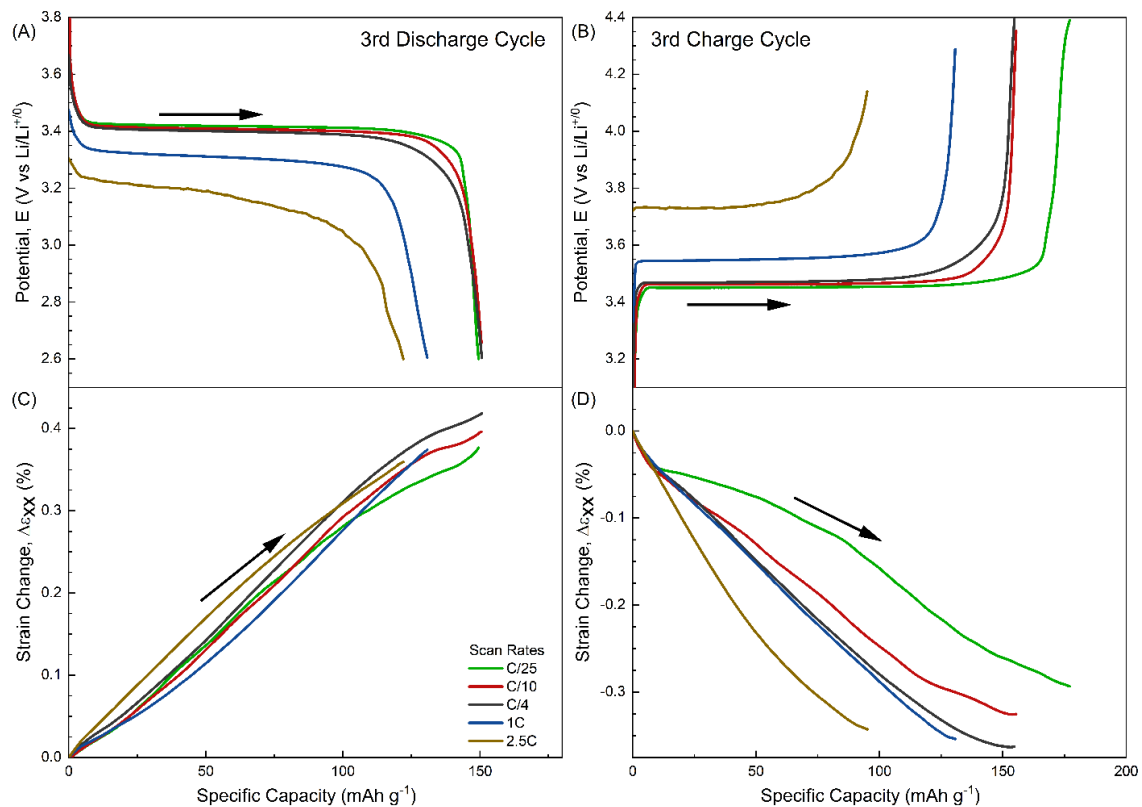
Figure E5. (a,b) Potential and (c,d) strain evolution of FP electrode cycled at different scan rates during the 3rd cycle for (a,c) discharge and (b,d) charge cycles, respectively. Strain evolution during discharge and charge cycles set to zero at the beginning of discharge and charge cycles, respectively
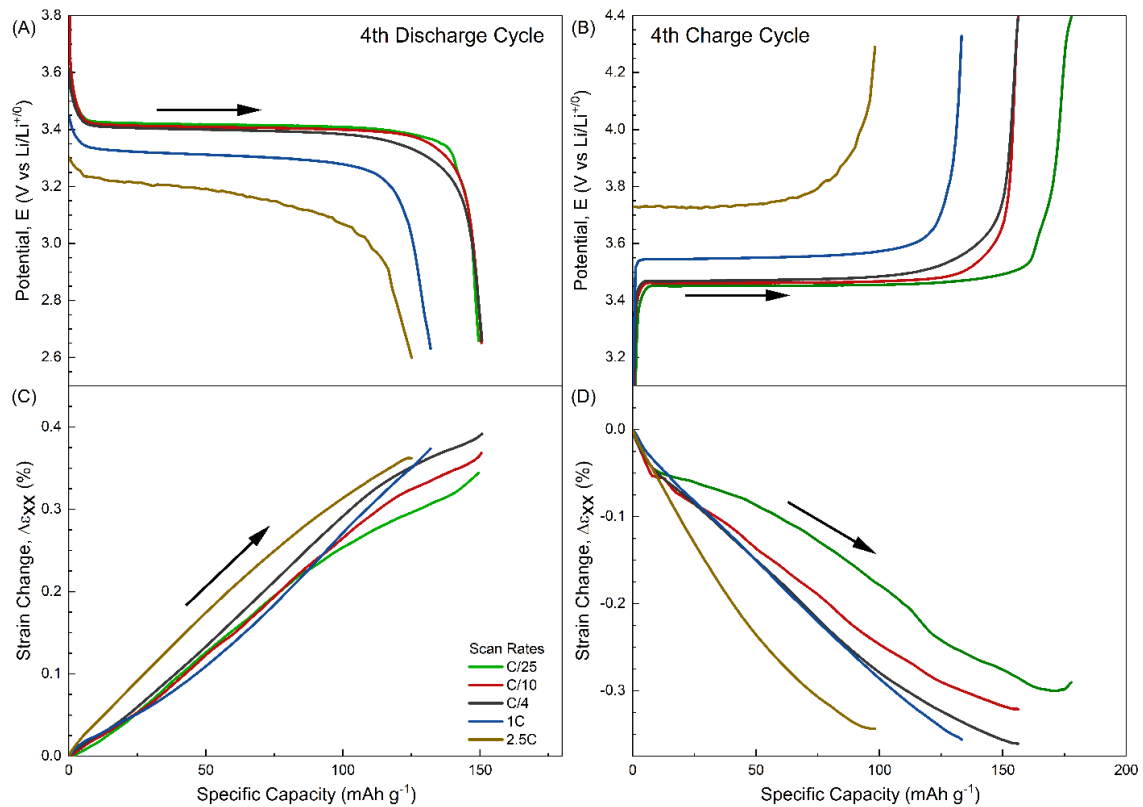
Figure E6. (a,b) Potential and (c,d) strain evolution of FP electrode cycled at different scan rates during the 4th cycle for (a,c) discharge and (b,d) charge cycles, respectively. Strain evolution during discharge and charge cycles set to zero at the beginning of discharge and charge cycles, respectively.
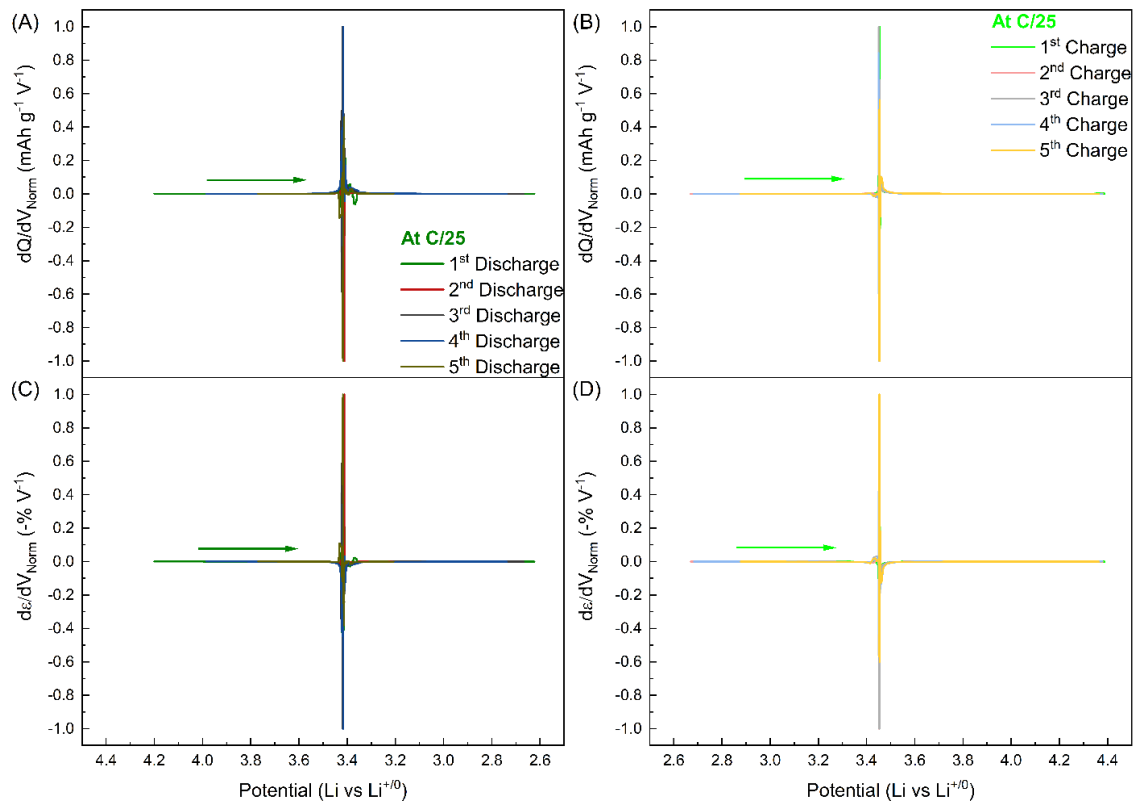
Figure E7. Normalized (a,b) capacity and (c,d) strain derivatives in FP composite electrodes during galvanostatic cycling at C/25 rate during (a,c) discharge and (b,d) discharge cycles with 1 M LiClO$_4$ in 1:1 EC:DMC.
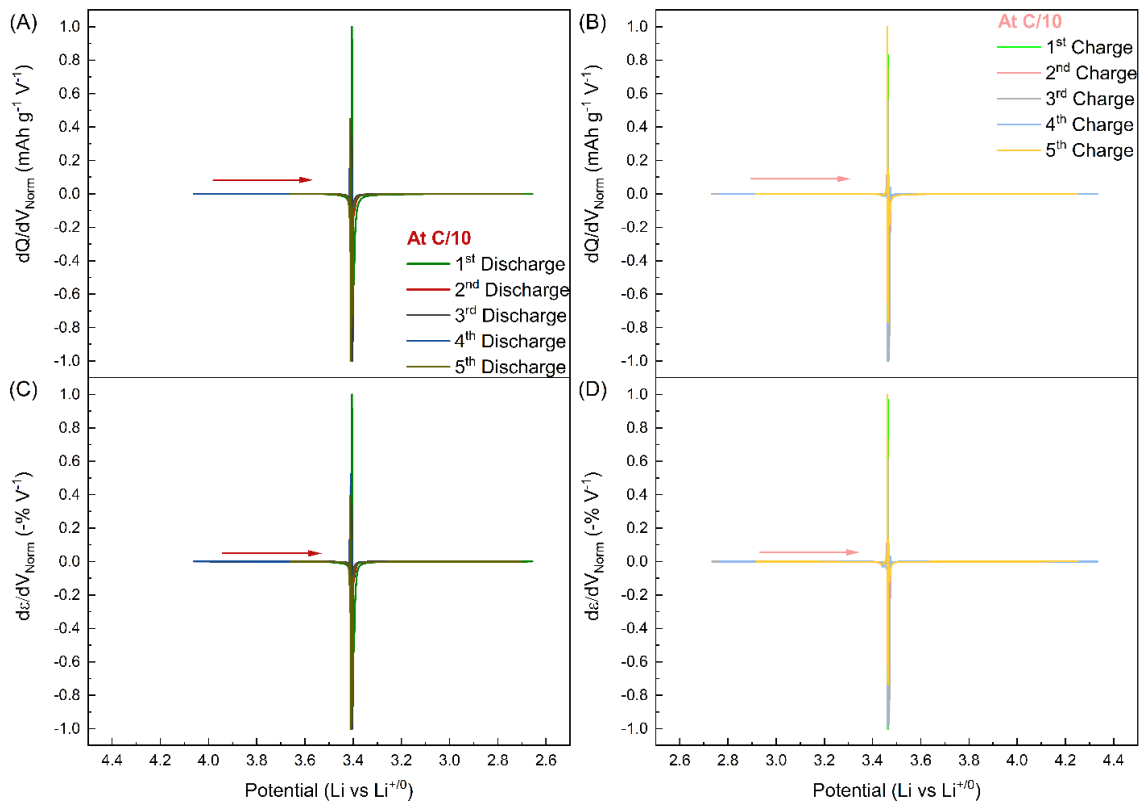
Figure E8. Normalized (a,b) capacity and (c,d) strain derivatives in FP composite electrodes during galvanostatic cycling at C/10 rate during (a,c) discharge and (b,d) discharge cycles with 1 M LiClO$_4$ in 1:1 EC:DMC.
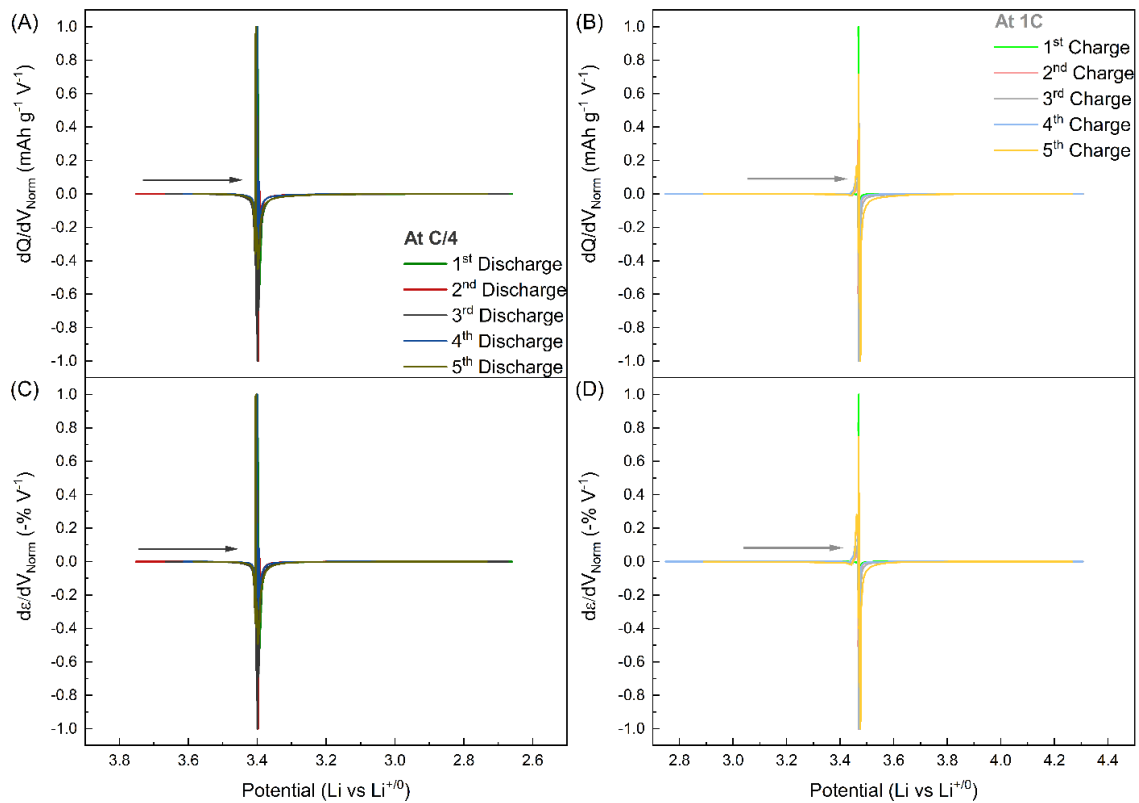
Figure E9. Normalized (a,b) capacity and (c,d) strain derivatives in FP composite electrodes during galvanostatic cycling at C/4 rate during (a,c) discharge and (b,d) discharge cycles with 1 M LiClO$_4$ in 1:1 EC:DMC.
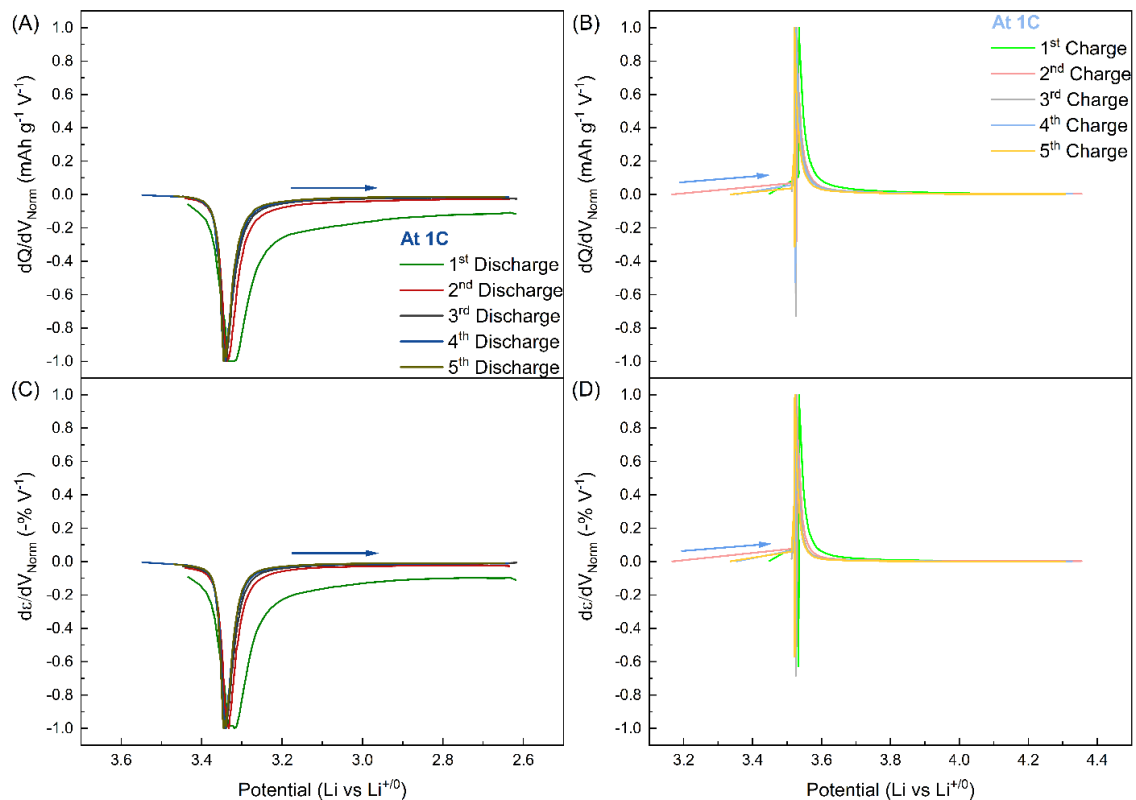
Figure E10. Normalized (a,b) capacity and (c,d) strain derivatives in FP composite electrodes during galvanostatic cycling at 1C rate during (a,c) discharge and (b,d) discharge cycles with 1 M LiClO$_4$ in 1:1 EC:DMC.
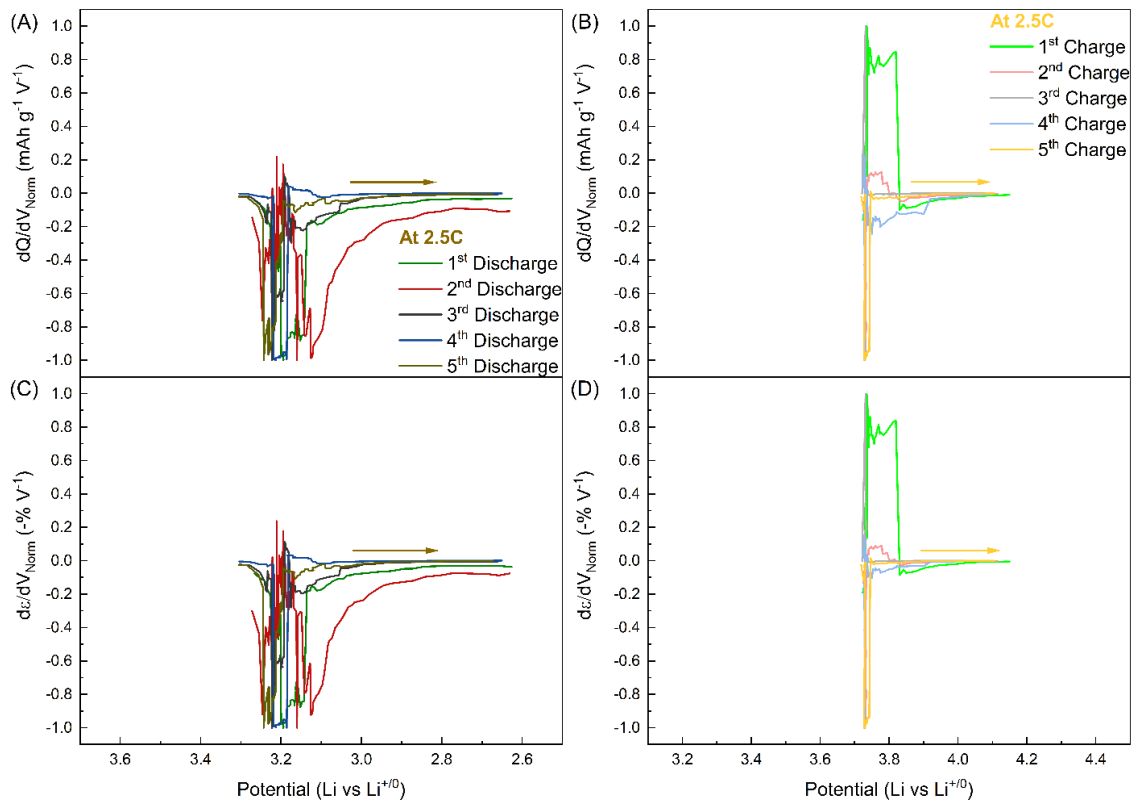
Figure E11. Normalized (a,b) capacity and (c,d) strain derivatives in FP composite electrodes during galvanostatic cycling at 2.5C rate during (a,c) discharge and (b,d) discharge cycles with 1 M LiClO$_4$ in 1:1 EC:DMC.
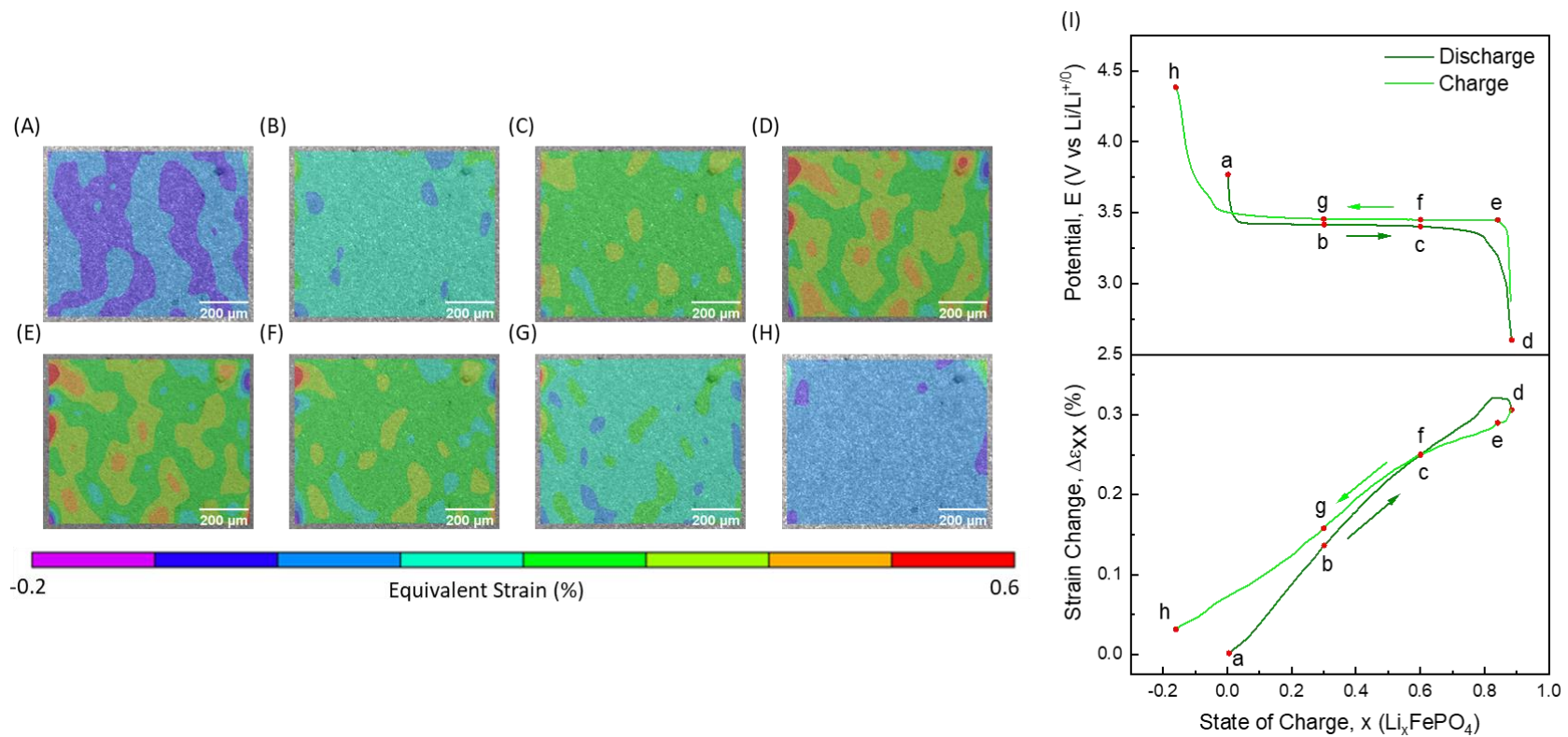
Figure E12. Counter plots of the equivalent strain in the composite LFP electrode at different states of charge and discharge when cycled at C/25 rate with 1 M $LiClO_4$ in 1:1 EC:DMC during the 5th cycle.
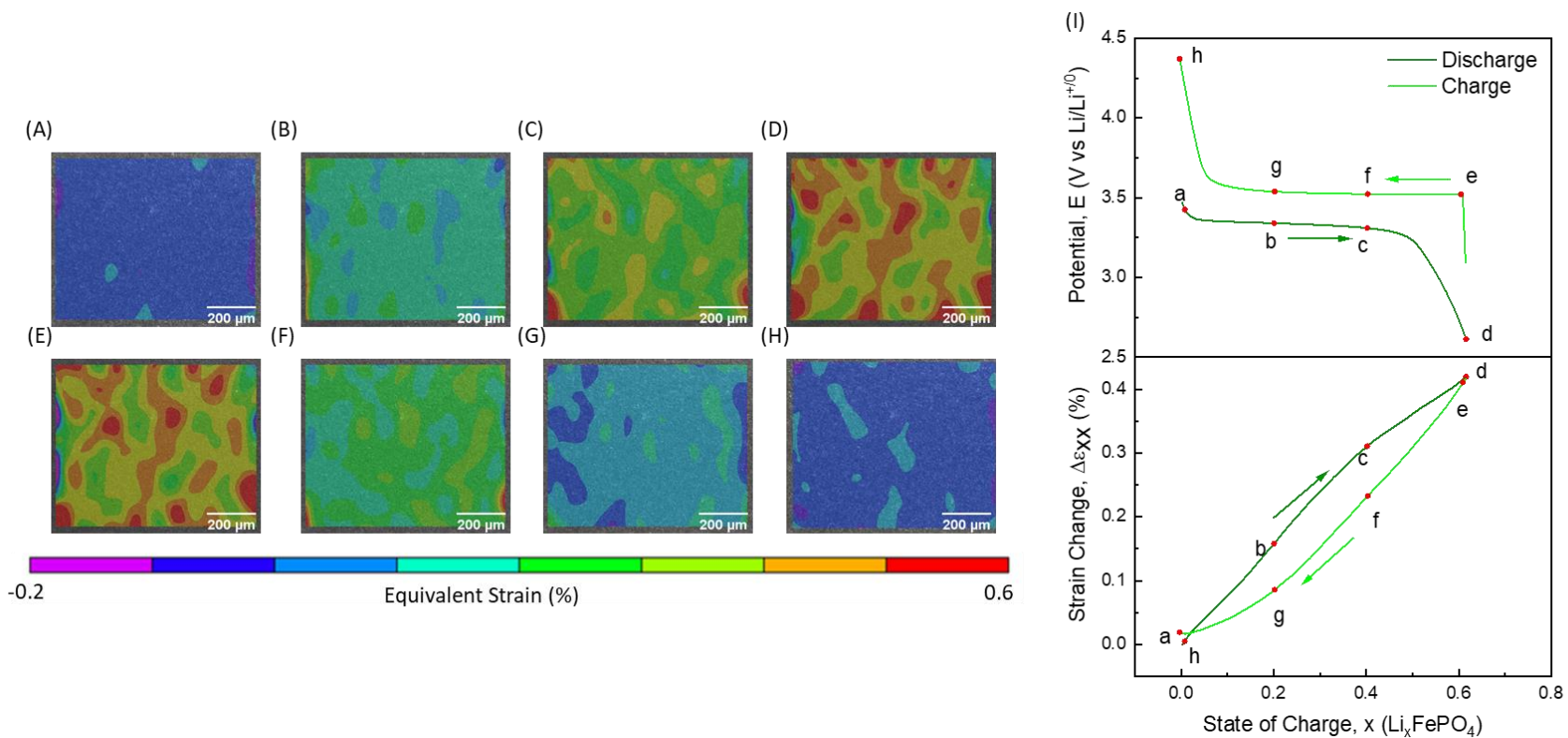
Figure E13. Counter plots of the equivalent strain in the composite LFP electrode at different states of charge and discharge when cycled at 1C rate with 1 M LiClO$_4$ in 1:1 EC:DMC during the 5th cycle.
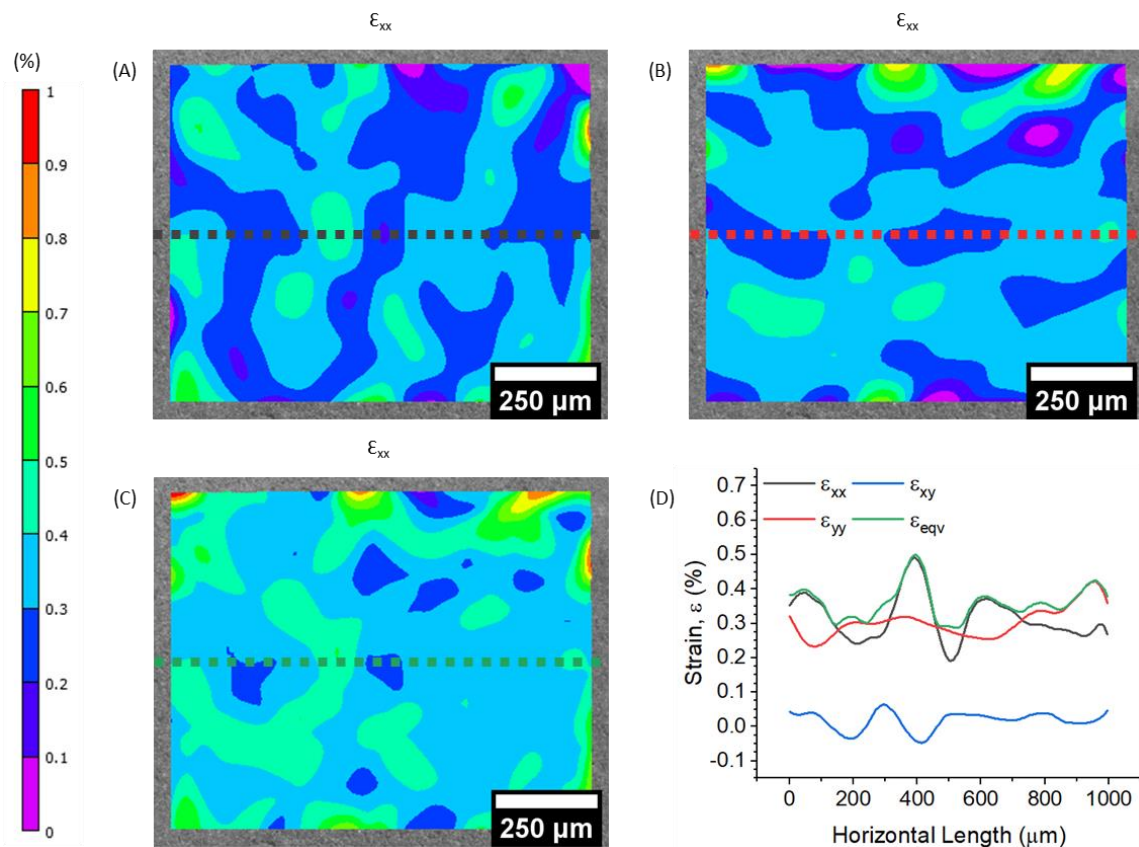
Figure E14. (a) Horizontal, (b) vertical, and (c) equivalent strain contour plots, and (d) line scans of strain components at the end of the fifth lithiation for the electrode cycled at C/25 rate with 1 M LiClO$_4$ in 1:1 EC:DMC. Line scans are taken from an arbitrary horizontal line within the region of interest.

SUPPLEMENTARY INFORMATION FOR THE COUPLING BETWEEN VOLTAGE

PROFILES AND MECHANICAL DEFORMATIONS IN LAGP SOLID ELECTROLYTE

DURING Li PLATING AND STRIPPING

Experimental

$Li_{1.5}$,$Al_{0.5}$$Ge_{1.5}$$P_3$$O_{12}$ powder (LAGP, Ampcera™, 300-500 nm particle size, MSE Supplies) was

used to prepare solid electrolyte without any further processing. The crystalline structure of the

pristine LAGP solid electrolyte powders (As received without any heat treatment) was

characterized by X-ray diffraction (XRD, Bruker D8 Advance XRD with Lynxeye Detector, 40

kV, 35 mA) with Cu Kα radiation with a step size of 0.016° and collection time of 5 seconds per

step (**Figure F1**A). XRD pattern of the solid electrolyte matches well with $LiGe_2P_3O_{12}$ (JCPDS 00-

041-0034)[241].

To prepare the electrolyte, 0.25 g of LAGP powder was loaded into the 1/2 inch die and cold-

pressed under 80 MPa for 5 min to form a pellet. The newly formed pellet was then sintered at

800ºC for 4 h. To obtain a flat surface for the DIC measurements, the solid electrolyte was cut in

half to obtain a semi-circle. The top, bottom, and flat side surfaces of the solid electrolyte were

polished with 1000 grit number sandpaper. The surface roughness of the solid electrolyte was

measured at about 300 nm by using NANOVEA Optical Profiler with Chromatic Confocal 740

µm. The flat side of the LAGP solid electrolyte was slightly immersed in the mixture of carbon

black:ethanol solution (1:50 in mass ratio) to create a speckle pattern. Then, the solid electrolyte was air-dried, and carbon black speckle patterns were produced on the flat side of the solid electrolyte LAGP solid electrolyte. A symmetrical Li | LAGP | Li cell was fabricated, and stainless-steel disks were used as a current collector and placed into a custom cell inside an argon-filled glove box. The lab-made custom battery cell and DIC allowed us to feasibly measure the strain development during the electrochemical processes in real time. Images were taken periodically every 60 seconds from the side view of the all-solid-state battery during battery cycling. DIC computes strains by tracking the changes in the speckle patterns in small neighborhoods called subsets during electromechanical deformation[36,242].
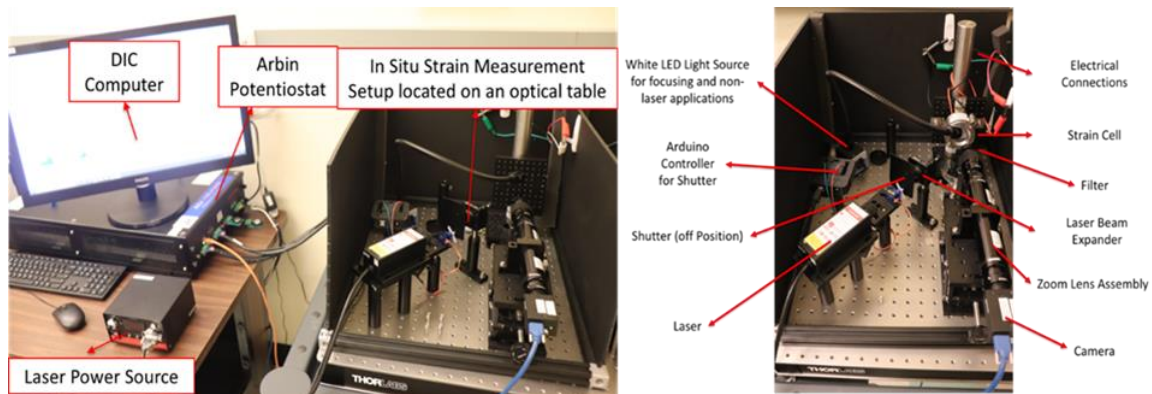
Figure F1. Experimental DIC setup to monitor strains in solid electrolytes.
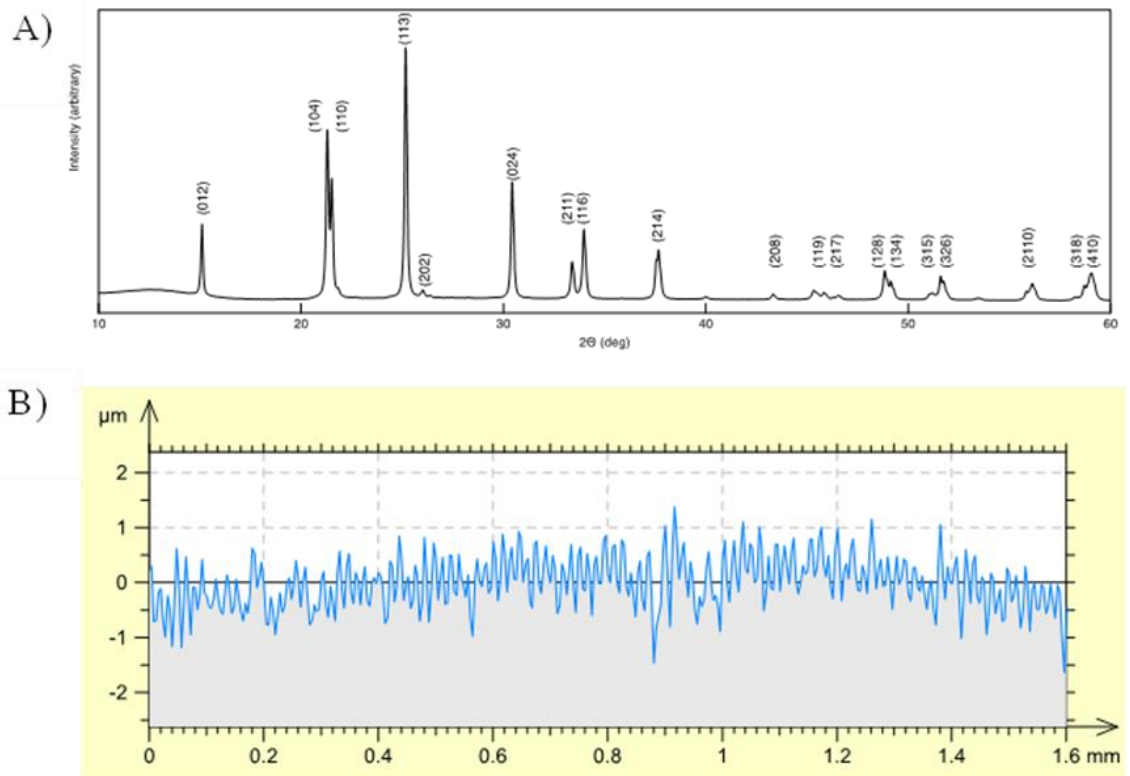
Figure F2. A) XRD analysis of pristine LAGP powders and B) Surface roughness profile of LAGP solid electrolyte pellet.
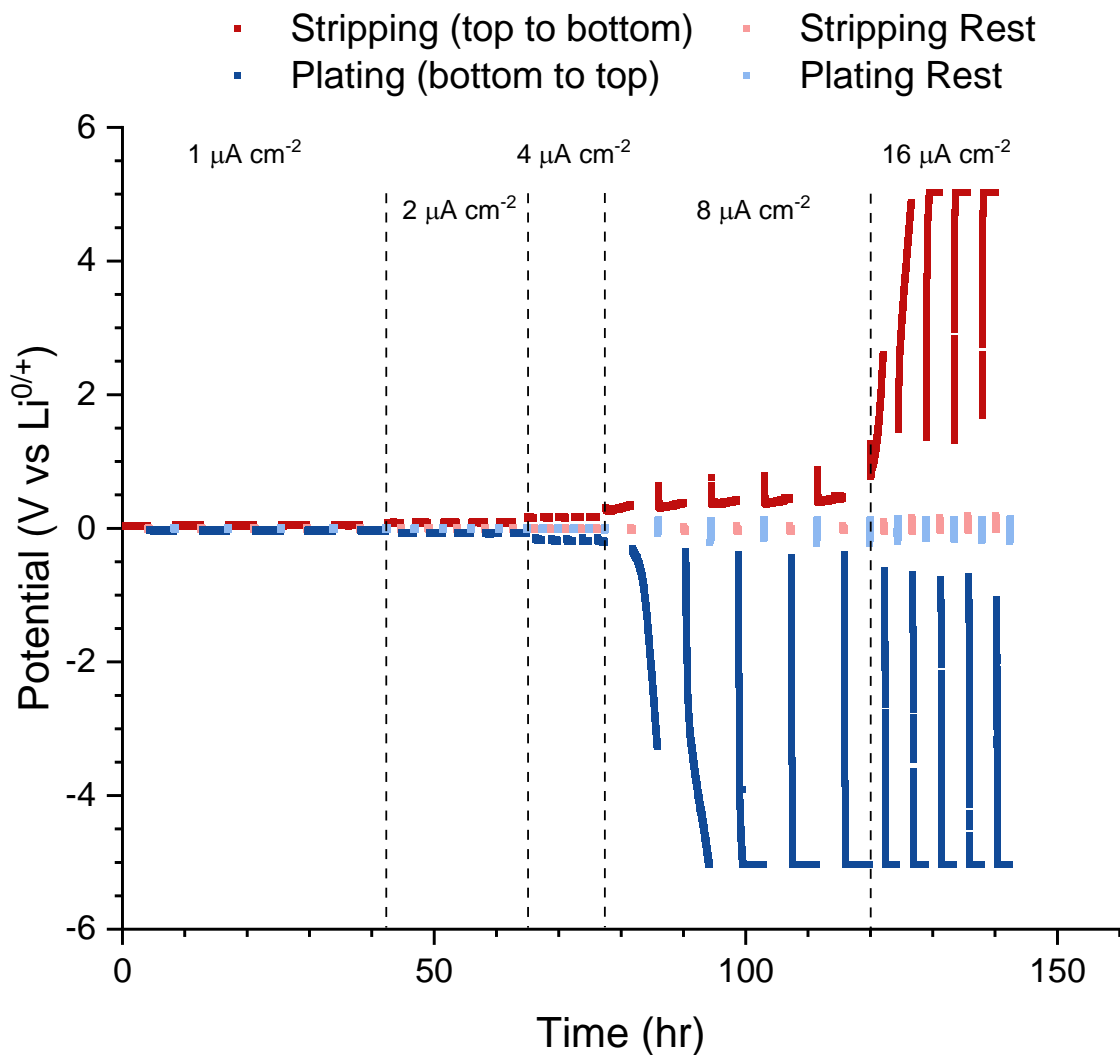
Figure F3. Galvanostatic voltage profiles in Li / LAGP / Li symmetrical cell cycled at 1, 2, 4, 8 and 16 μA/cm^2. Dark red and blue color show voltage evolution during stripping and plating, respectively. Light red and blue colors show potential during resting after stripping and plating cycles, respectively.
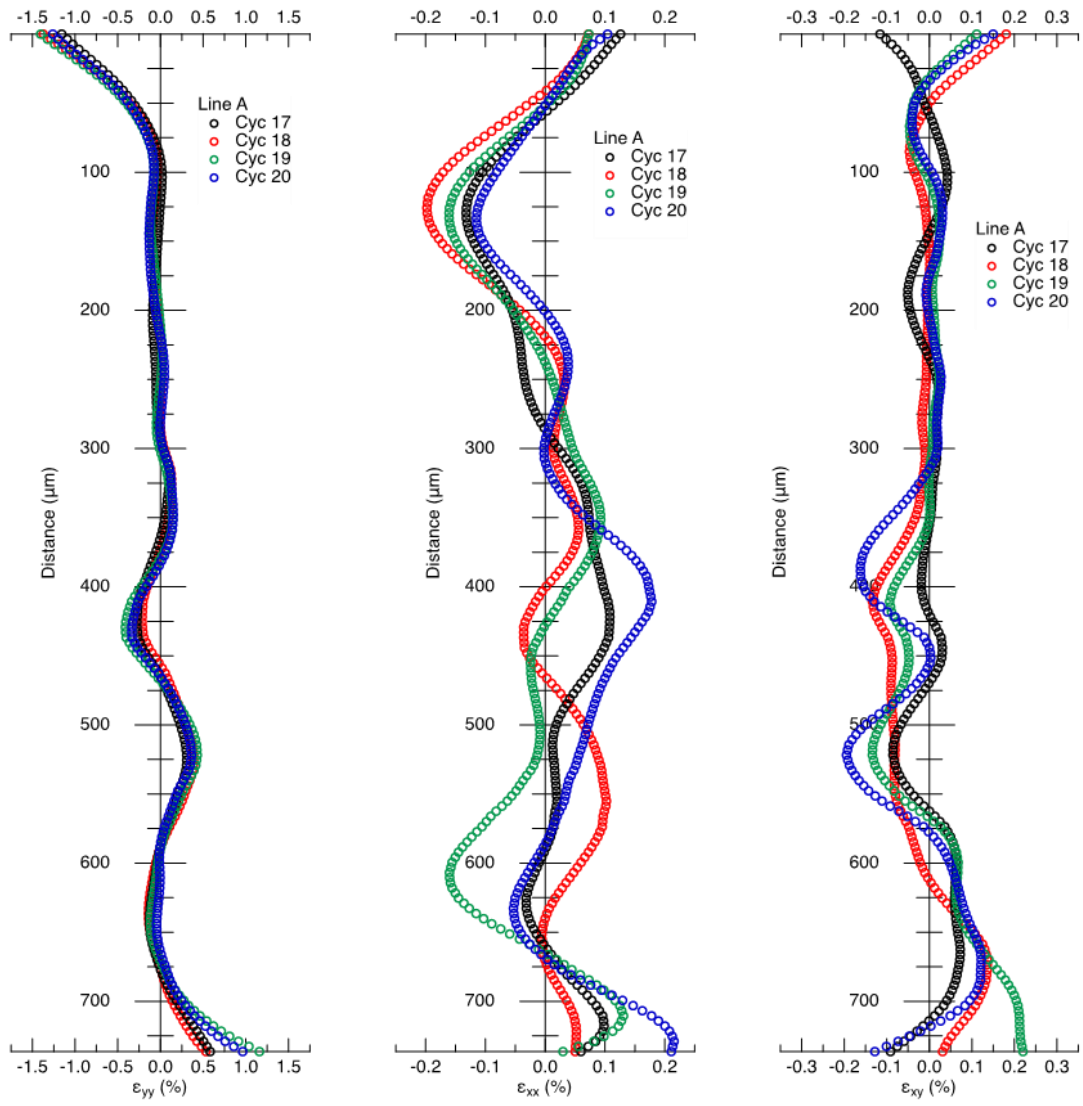
Figure F4. Strains along the vertical line A from **Figure 46**B.

243
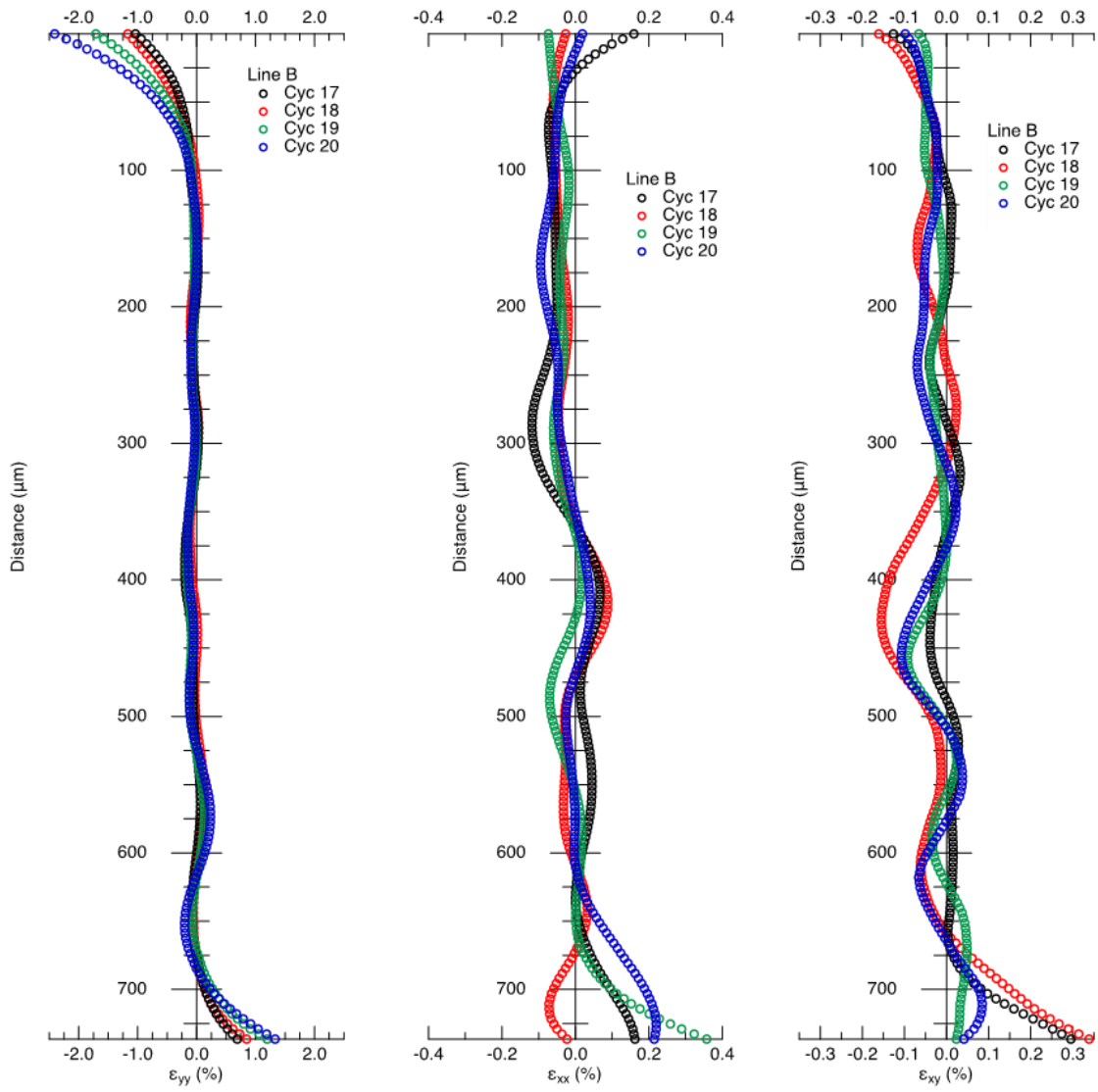
Figure F5. Strains along the vertical line A from **Figure 46**B.
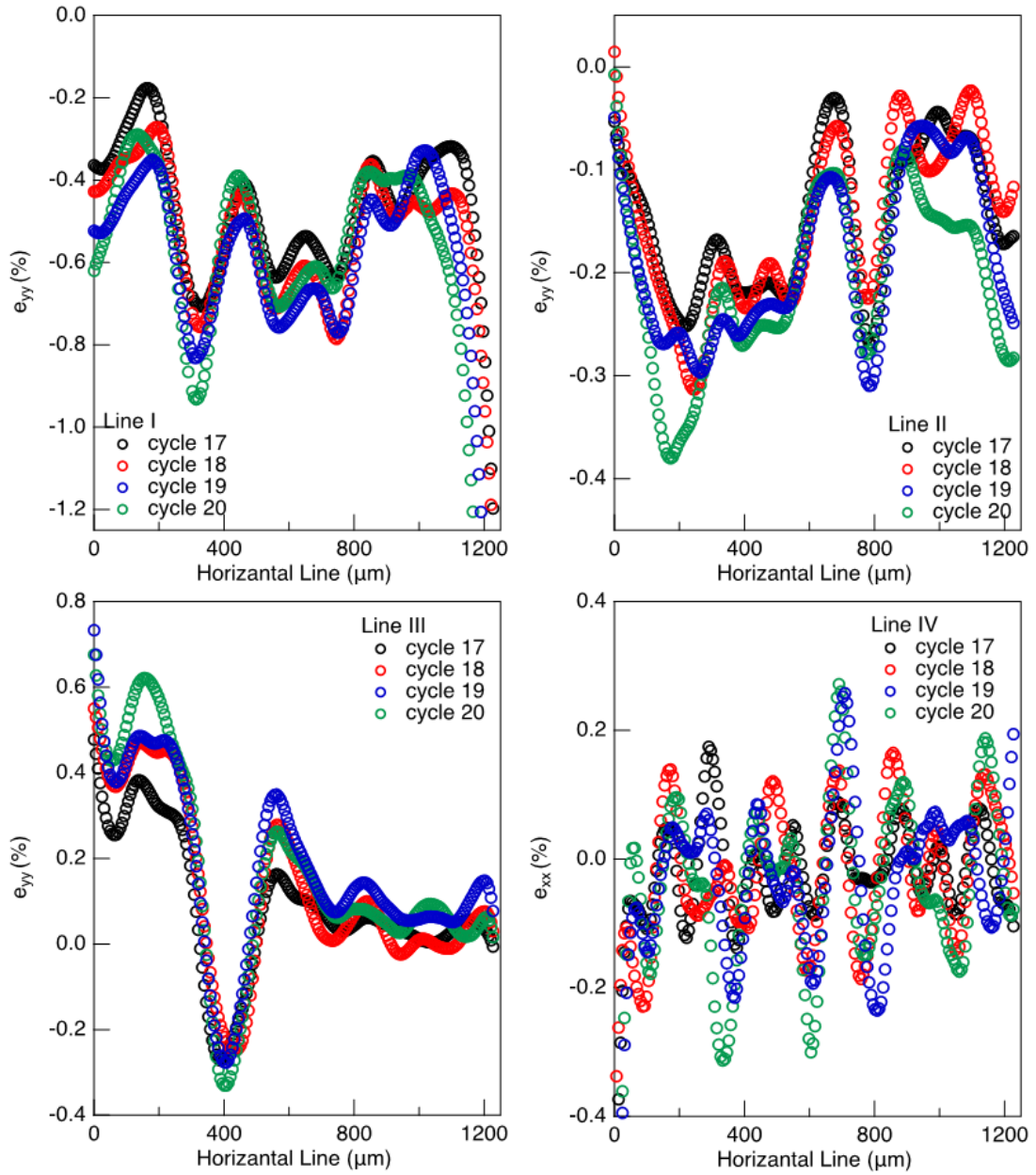
Figure F6. Normal strains, ε_{yy} along the horizontal lines I, II, III and IV from **Figure 46**B. Line I and II are 50 and 100 μm away from the upper Li metal / LAGP electrolyte respecively. Line III and IV are 50 and 25 μm away from the bottom Li metal / LAGP electrolyte, respectively.
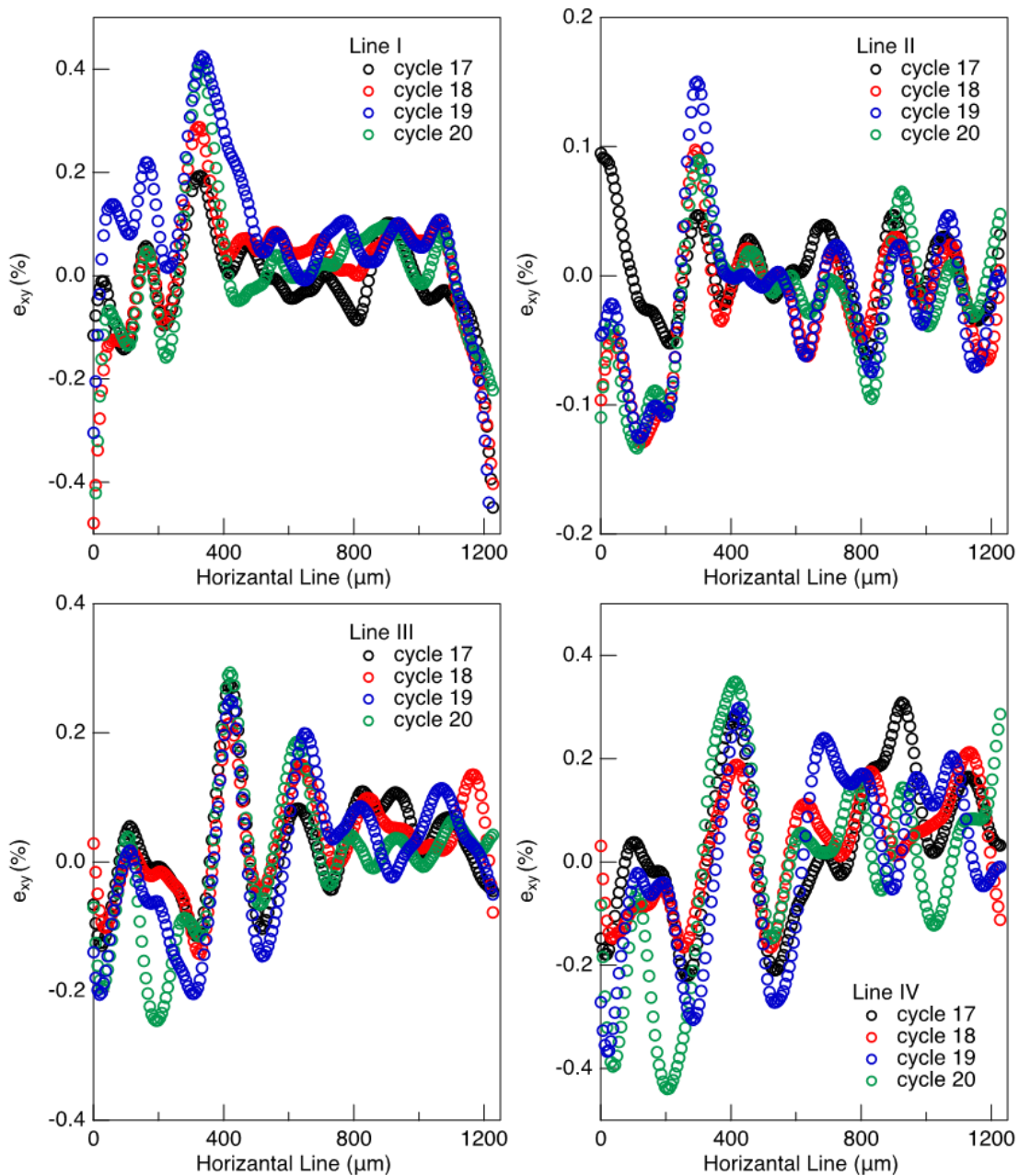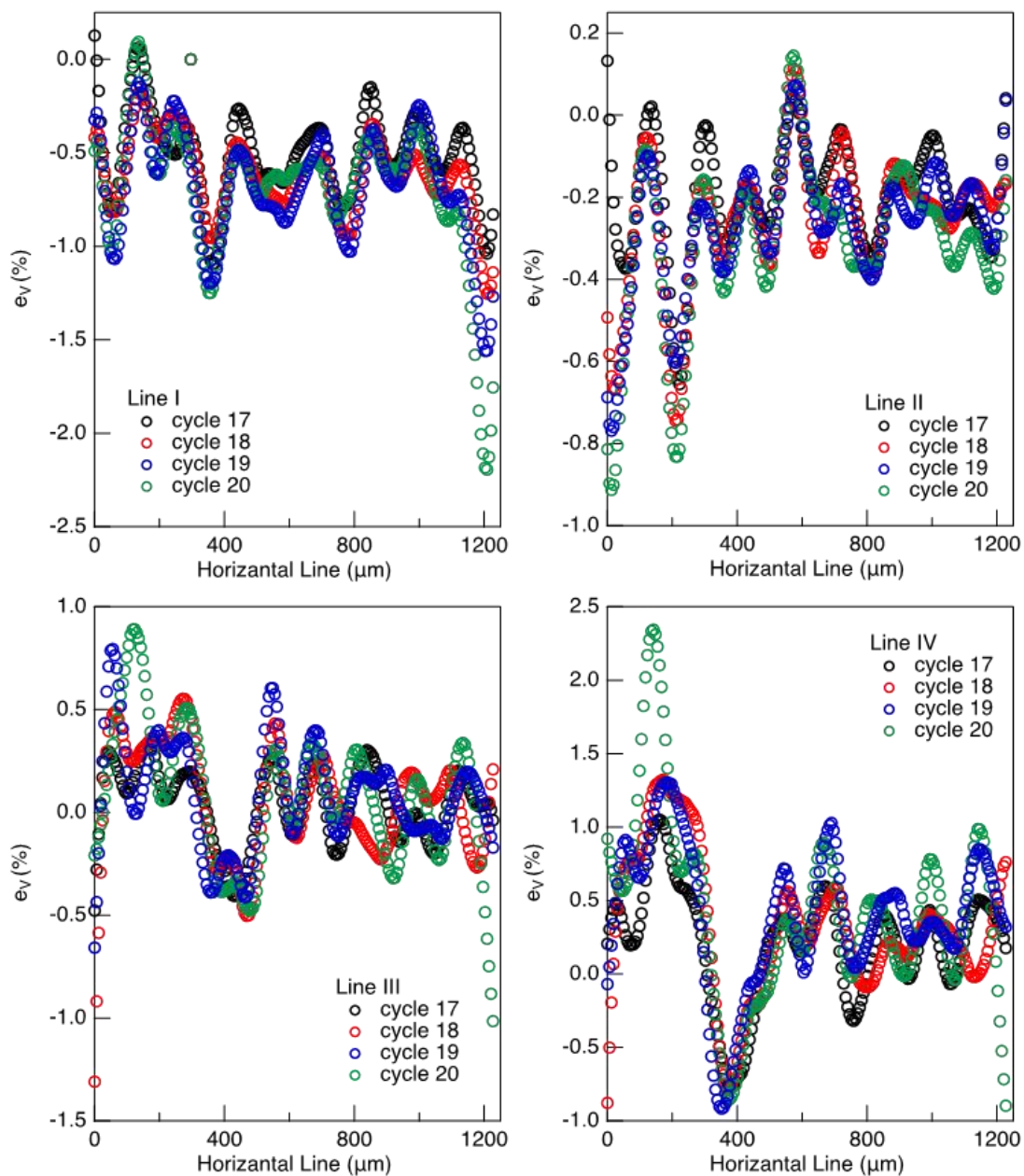
245
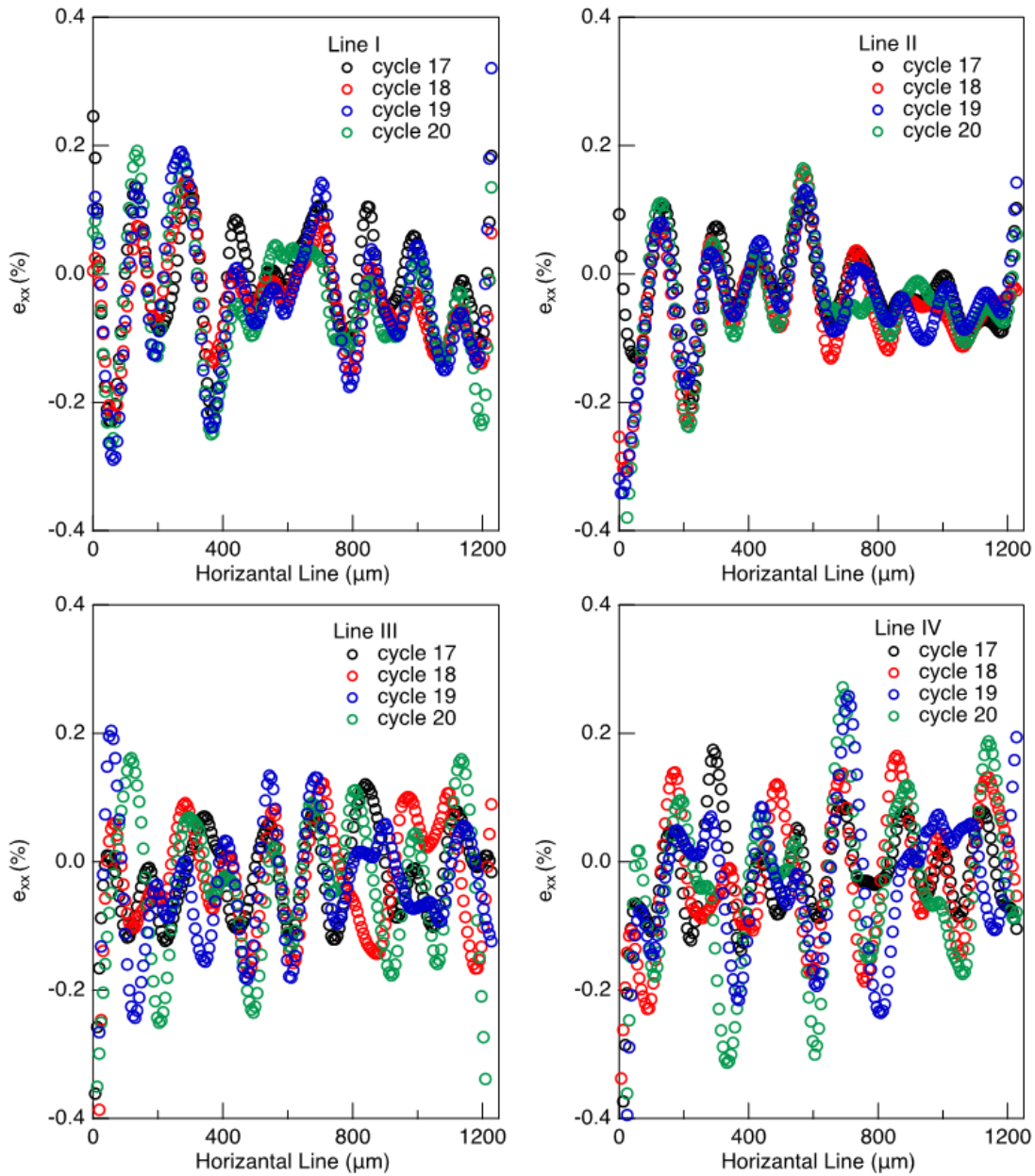
Figure F7. Normal strains, ε_{xx} along the horizontal lines I, II, III and IV from **Figure 46**B. Line I and II are 50 and 100 μm away from the upper Li metal / LAGP electrolyte respectively. Line III and IV are 50 and 25 μm away from the bottom Li metal / LAGP electrolyte, respectively.

Figure F8. Shear strains, ε_{xy} along the horizontal lines I, II, III and IV from **Figure 46**B. Line I and II are 50 and 100 μm away from the upper Li metal / LAGP electrolyte respectively. Line III and IV are 50 and 25 μm away from the bottom Li metal / LAGP electrolyte, respectively.
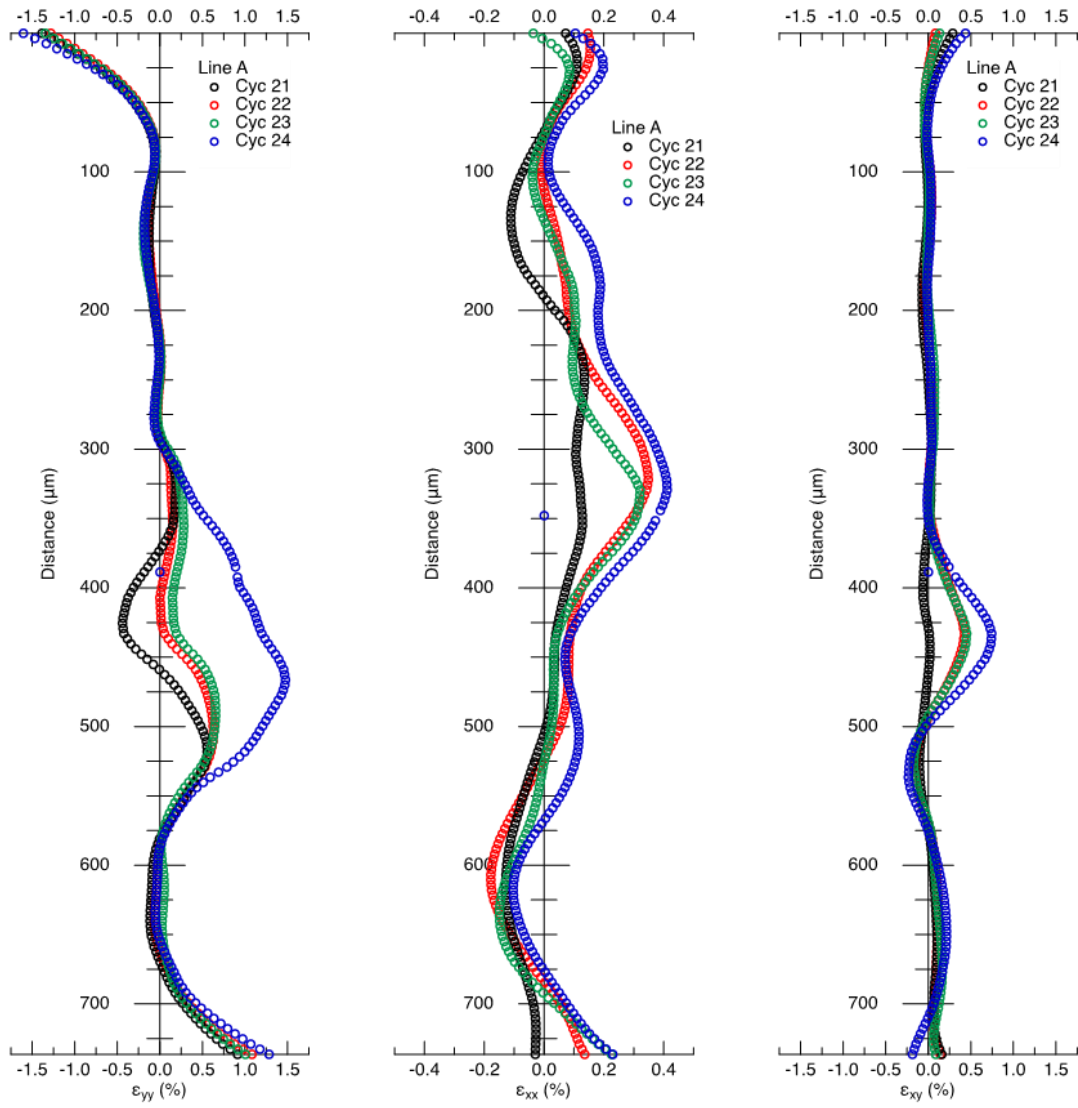
Figure F9. Volumetric strains, ε_V along the horizontal lines I, II, III and IV. Volumetric strains were calculated by using data in **Figure F6** and **Figure F7**. Line I and II are 50 and 100 μm away from the upper Li metal / LAGP electrolyte respectively. Line III and IV are 50 and 25 μm away from the bottom Li metal / LAGP electrolyte, respectively.

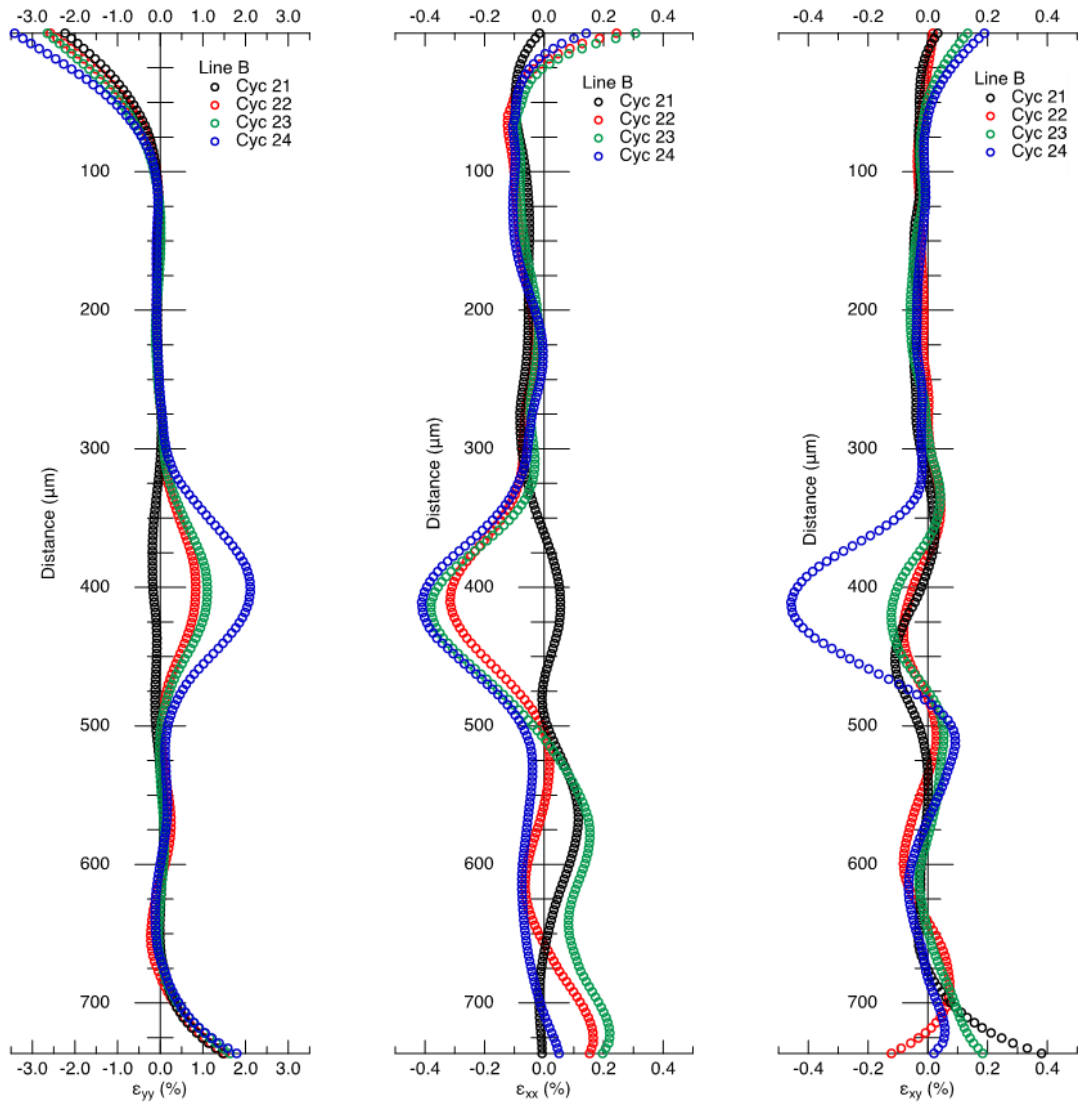**Figure F10.** Strains along the vertical line A from **Figure 47**C.

Figure F11. Strains along the vertical line B from **Figure 47**C.

SAMPLE PREPARATION FOR COMPOSITE ELECTRODES FOR IN-SITU STRESS
MEASUREMENTS

Brief Explanation

A custom electrochemical cell, previously described in a study done by Hannah et al[243,244], will be used to perform in situ curvature measurements for composite electrodes. To track the curvature evolution, laser beams produced by the Multi Beam Optical Sensor (MOSS) will be reflected off the substrate, which is coated by composite electrode, situated in the custom cell.

Slurry Preparation

Composite electrode slurry can be prepared following the procedure previously described for in situ strain measurements[98,115,245]. Briefly, binder of choice, carboxymethyl cellulose or poly(vinylidene fluoride) (PVDF), is mixed with ultra-pure water or N-Methyl-2-Pyrrolidinone (NMP), respectively, with Thinky centrifugal mixer. After the binder is dissolved in the solvent, active material and conductive carbon is added to the solution and further mixed to obtain the slurry.

Electrode Preparation

Two types of substrates can be used for the electrode preparation, gold coated borosilicate glass and silicon wafers. For the borosilicate substrate, gold coated side shown in **Figure G1**a should be coated with composite electrode for better electrical connection. For silicon wafer substrates, rough

side shown in **Figure G1**b is used for composite electrode coating. Back side of the substrates, shown in **Figure G2**, is used to reflect the laser beam.
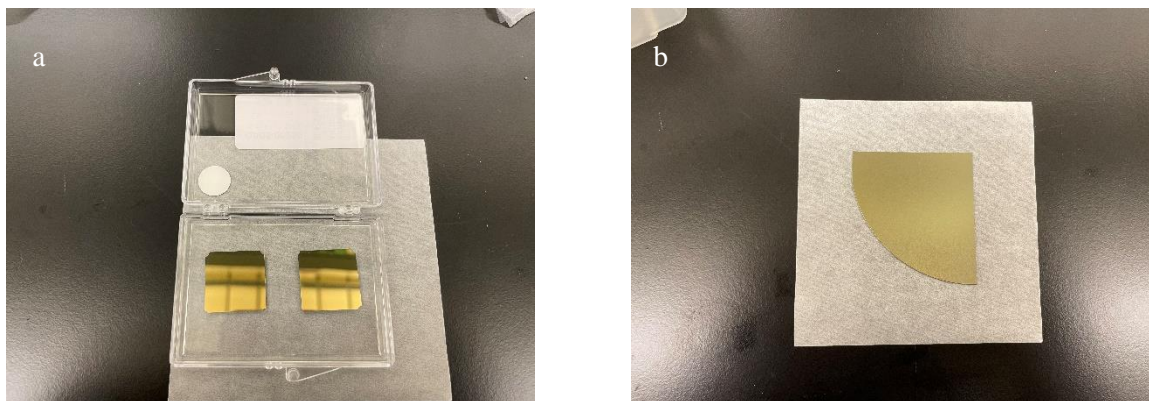

Figure G1. Composite electrode casting surfaces used for (a) Gold coated borosilicate glass and (b) silicon wafer substrates

The composite electrode slurry deposited on the substrate by using doctor blade casting method. Depending on the substrate and composite electrode slurry in question, doctor blade setting for the thickness of the casting can vary. For gold coated borosilicate glass (with a thickness of 200 µm) and silicon wafer (with a thickness of ~480 µm), doctor blade settings of 25 and 55 shown in **Figure G3** are suitable for initial trials, respectively.
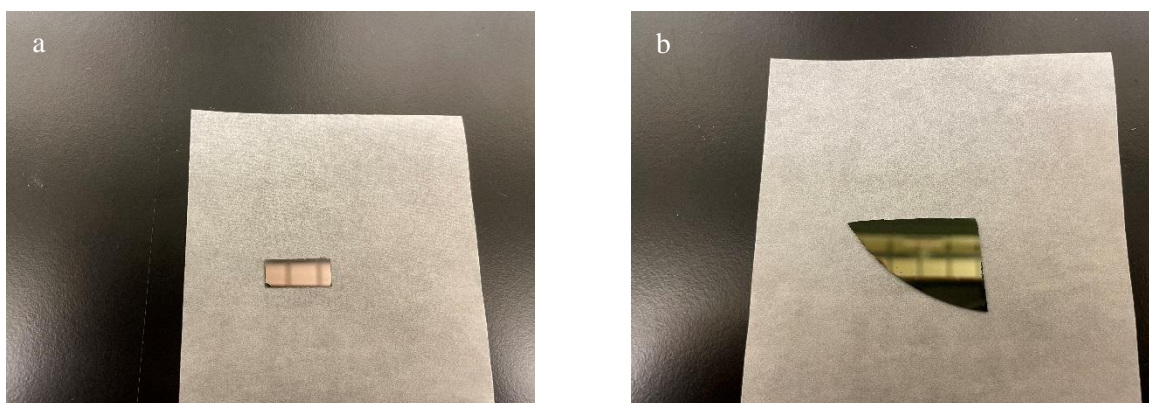

Figure G2. Laser reflection surfaces used in curvature measurement experiments for (a) Gold coated borosilicate glass and (b) silicon wafer substrates

To cast the electrodes, secure the substrate on a clean glass slide with one sided tape at two corners. Then, transfer the slurry from mixing canister to the surface of substrate carefully, without touching
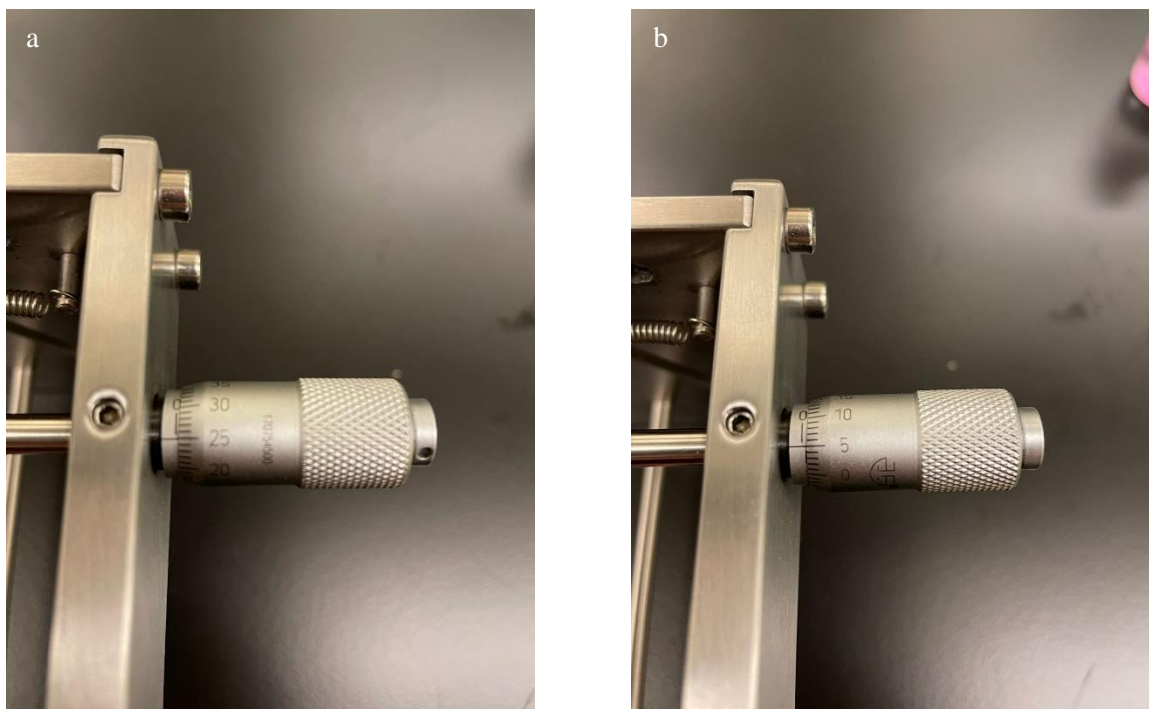
Figure G3. Reference doctor blade settings used for (a) gold coated borosilicate glass and (b) silicon wafer for composite electrode coating.

the surface with your transfer spatula. Continue with setting the doctor blade to appropriate thickness and slowly sliding it over the substrate to obtain a uniform slurry thickness. Finally, dry the composite electrode under the fume hood. If the desired uniformity of coating is not achieved, repeat this step to obtain a stress electrode shown in **Figure G4**.
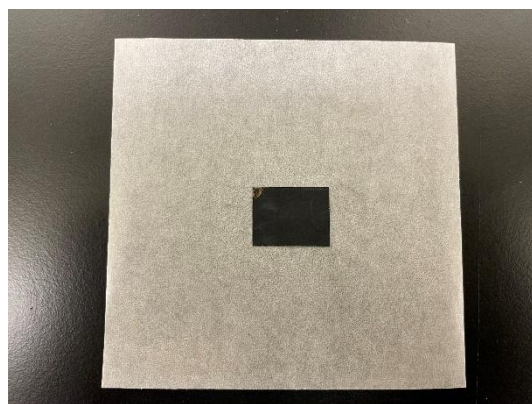

Figure G4. Slurry casted borosilicate glass for in situ curvature measurements

Cantilever Preparation for In-Situ Curvature Measurements

To measure the curvature occurring during the battery operations, prepared electrodes should be cut to 4 mm wide, at least 20 mm in length strips, called cantilevers. Both coated and uncoated surface of the substrate can be protected by sandwiching both sides between two weighing papers on a flat surface, making sure that the composite electrode coated face is facing up. Then, using a metal ruler as guide, shown in **Figure G5**a, score the substrate using the scriber, shown in **Figure G5**b, until it breaks. The cut piece can be mounted into the custom electrochemical cell for in situ curvature measurement like the Standard Operating Procedure described by Hannah et al[243] previously.
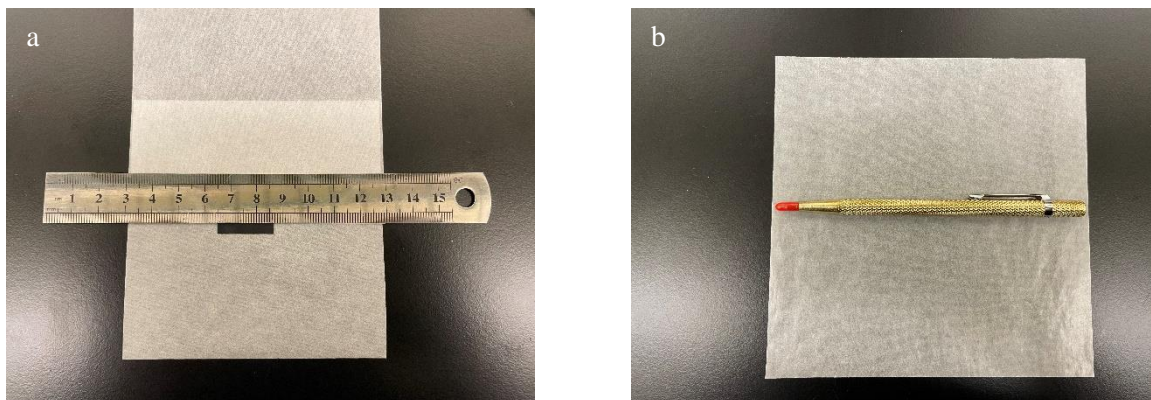

Figure G5. (a) Example of substrate cutting arrangement for composite electrode experiments. (b) Diamond tipped scriber used for glass cutting.

STANDARD OPERATING PROCEDURE FOR IN-SITU CURVATURE MEASUREMENT

DURING METAL ELECTRODEPOSITION

Brief Explanation

A custom electrochemical cell holder will be used to perform in situ curvature measurements metal electrodeposition on gold coated borosilicate cantilevers. A glass cuvette is used as reaction cell, while 3D printed electrochemical cell holder is situated on a 5-axis optical stage in front of MOSS system. Experiments are carried out to investigate the effect of electrodeposition rate on stress evolution.

Design of Experimental Cell

Figure H1 shows the exploded view of the experimental cell for the in-situ electrodeposition experiment. The main reaction cell is made from fused glass (Starma-GmbH, 96/G/40). Main body and the cover are designed in-house and 3d printed using polylactic acid (PLA) filament. Cantilevers used as electrodeposition media is secured to the top cover with sample holders made from SS 316 (Grainger) and Viton O-rings are used to prevent sample holder from moving during electrodeposition. A platinum wire (99.997% metal basis, Alfa Aesar) and saturated calomel electrode (Gamry Instruments) are used as working and reference electrodes, respectively.
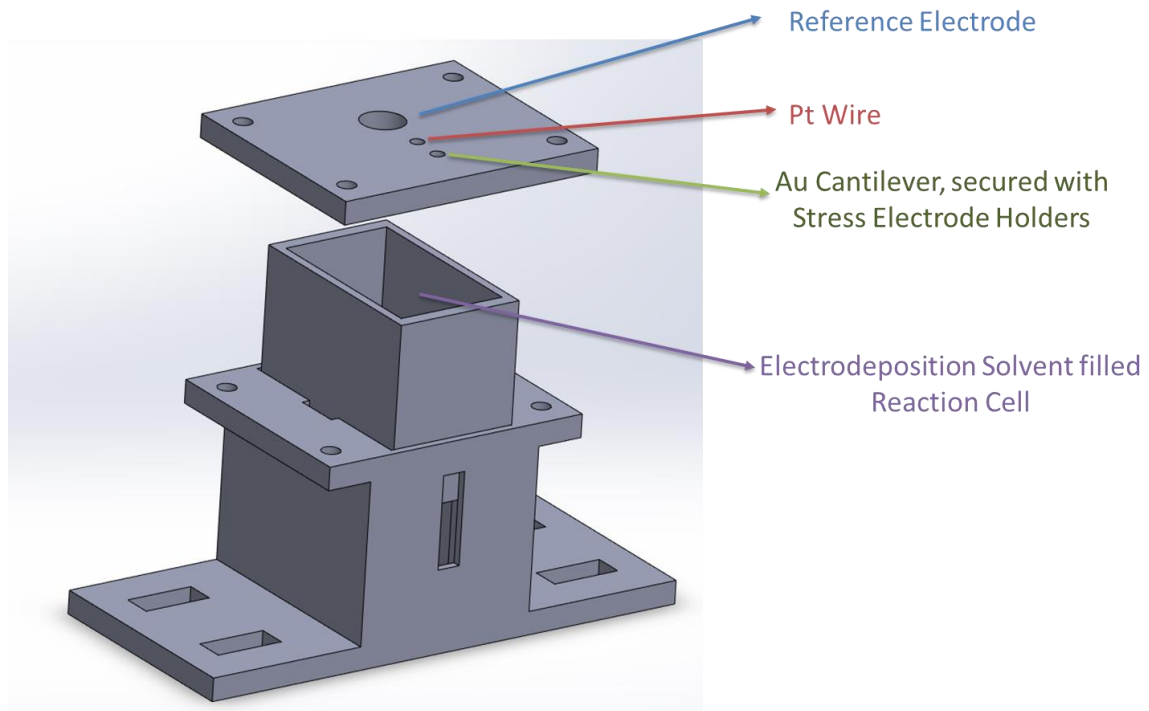
Figure H1. Exploded view of custom three electrode electrodeposition cell

Conversion of Sample Stage for Electrodeposition Experiments

1- Remove the mounting post used for battery measurements, shown in **Figure H2**, by removing four ¼" screws using 3/16" hex key.

2- Remove the tilt plate, shown in **Figure H3**a, by removing six hidden ¼" setscrews using 1/8" hex key, as shown in **Figure H3**b.

3- Remove the x-translator, shown in **Figure H4**, by removing four ¼" screws using 3/16" hex key. Note that one side of the translator will be hidden under the breadboard, so after removing one side of the translator, shift the plate all the way to other side to remove the remaining two screws.

4- Be careful with the placement of x-y translator used in the electrodeposition experiment. Note the location of bottom left screw in the figure sss and insert the remaining three ¼" screws using 3/16" hex key.

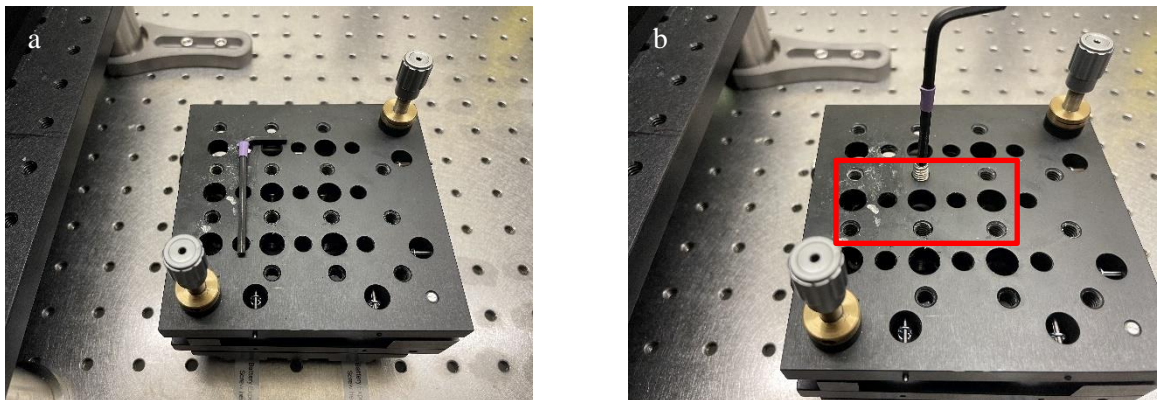**Figure H2**. Removal of mounting post for battery measurements

Figure H3. (a) Removal of tilt plate and using 1/8" hex key and (b) location of hidden setscrews

5- In order to increase the footprint of 8-32 screws used in the assembly of laboratory jack, use two different size washers, shown in **Figure H6**a. First, insert the small washer (**Figure H6**b), then place the bigger washer to the 8-32 screw, as shown in **Figure H6**c.
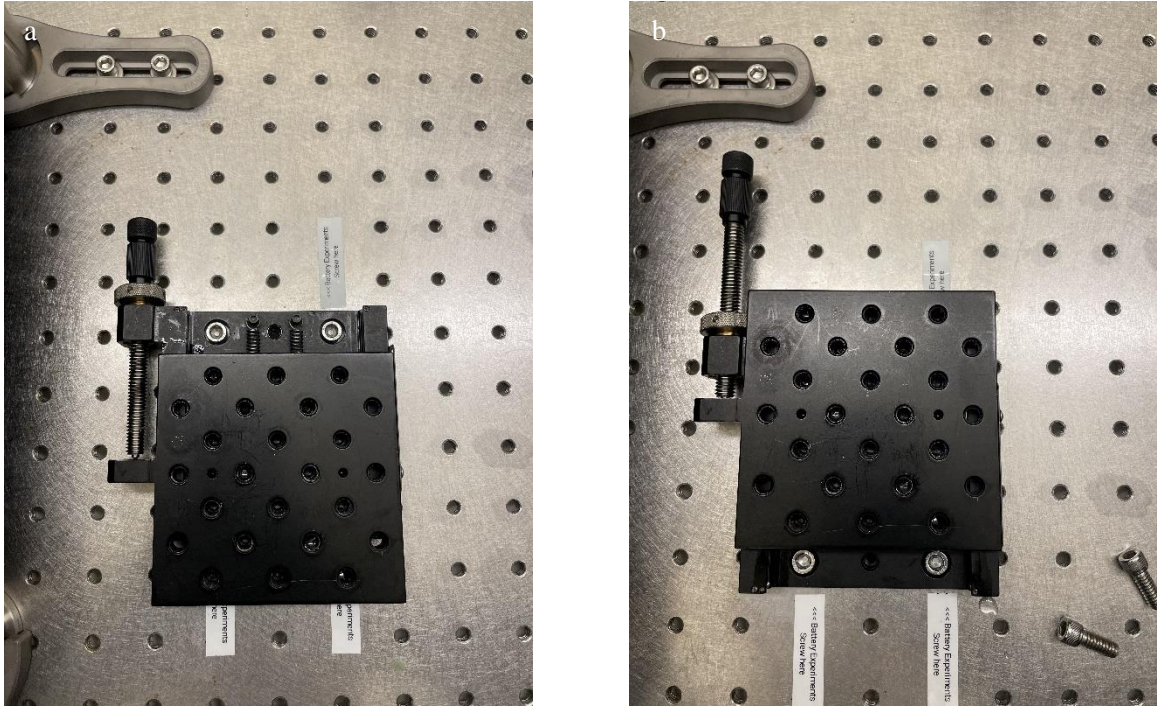
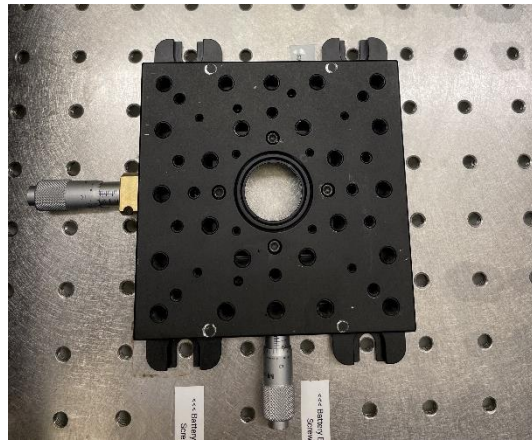**Figure H4.** Removal of x-axis translator for (a) right and (b) left side screws

Figure H5. Placement of x-y translator for electrodeposition setup

Figure H6. (a) 8-32 screw and two sizes of washers for lift stage assembly while (b) first small and then (c) big washer inserted to the screw.

6- Place the laboratory jack-tilt plate assembly on the x-y translator as shown in **Figure H7**a, and secure it using the previously prepared four 8-32 screws using 9/64" hex key. Final form of the electrodeposition sample stage can be seen in **Figure H7**b.
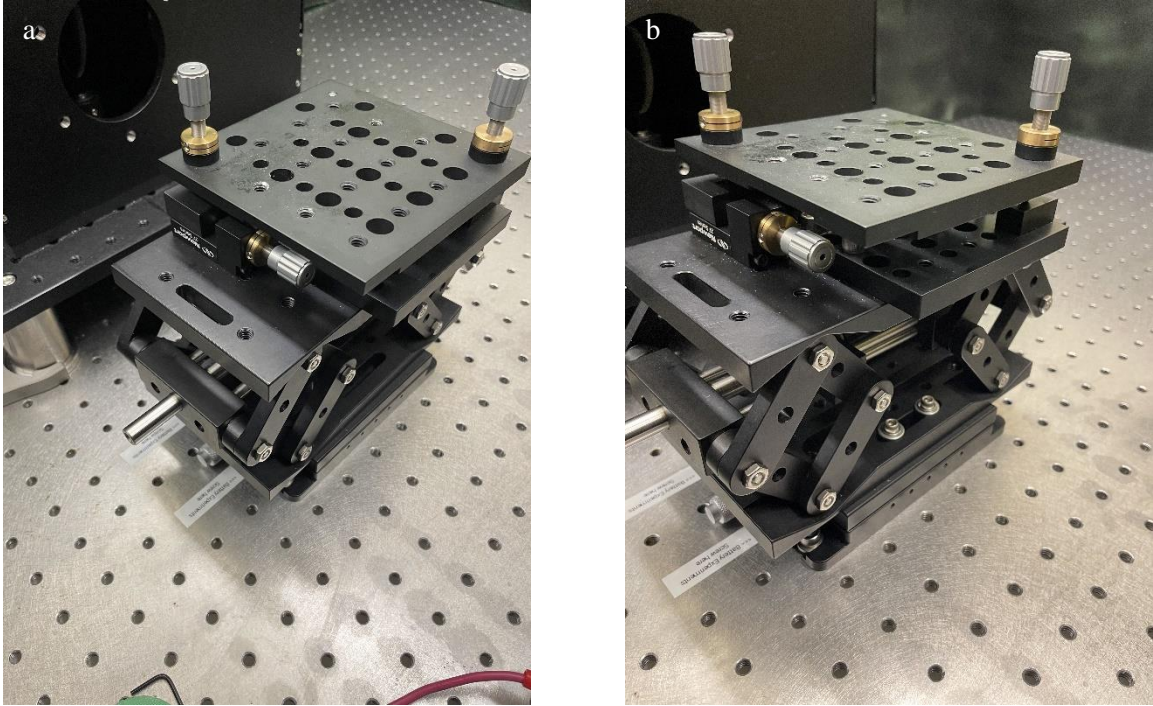

Figure H7. (a) Placement of laboratory jack-tilt plate assembly and (b) final electrodeposition sample stage assembly.

Preparation of Electrodeposition Experiment

To increase the consistency between experiments in terms of stress evolution, precut gold coated borosilicate cantilevers with a dimension of 4 mm x 22 mm x 200 µm (width x length x thickness) are used for electrodeposition experiments, stored in a wafer storage box, shown in **Figure H8**a. To remove the cantilever from the sticky surface, slowly work your way around the cantilever with a safety blade until the safety blade is completely under the cantilever. Then, using a tweezer, secure the cantilever in the sample holder where reflective surface is facing the laser beam and attach the electrical connection as shown in **Figure H8**b.
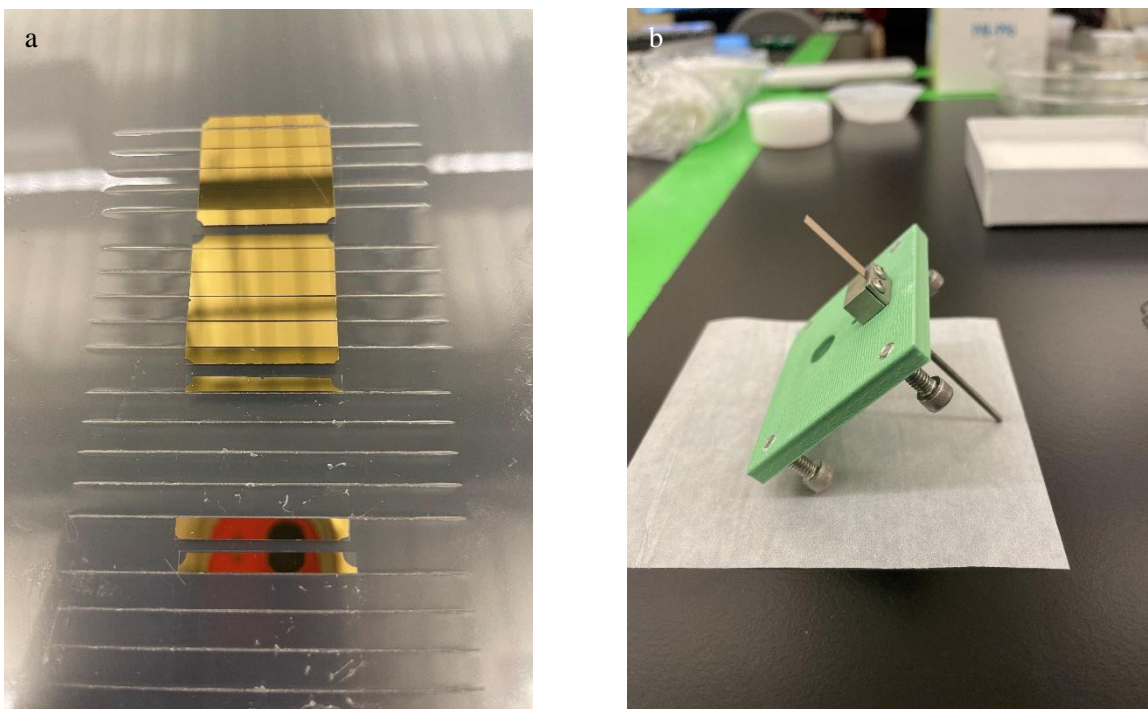
Figure H8. (a) Precut gold coated borosilicate cantilevers. (b) Fully assembled working electrode for electrodeposition experiment.

After the working electrode is secured to the top cover, fill the reaction cell with the electrodeposition solution 3 mm below its upper limit and place the reaction cell into the main body. To secure the top cover to main body, screw the four 8-32 screws using 9/64" hex key. Put the whole electrodeposition experiment holder assembly on the sample stage and place counter and saturated calomel reference electrode as shown in **Figure H9**.

To record the potential of counter electrode during the experiment, potentiostat cables should be connected to their respective electrodes as described below (**Figure H10**.

- Black and green alligator clips with matching cable colors: Connect to counter electrode.
- Red and white alligator clips with matching cable colors: Connect to working electrode.
- Green alligator clip with black cable: Connect to counter electrode.
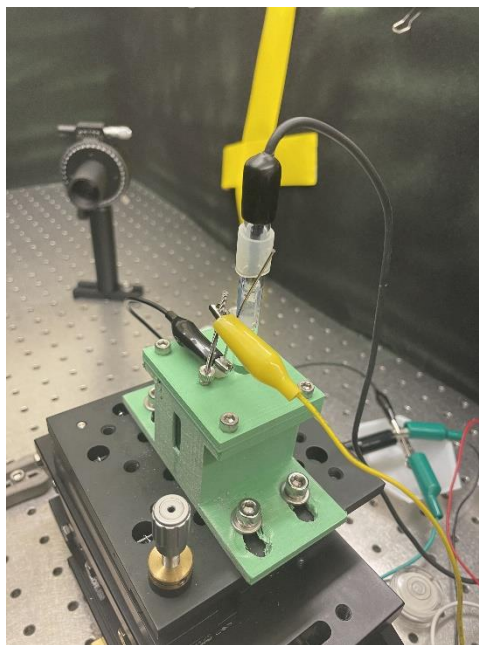- White alligator clip with red cable: Connect to reference electrode.

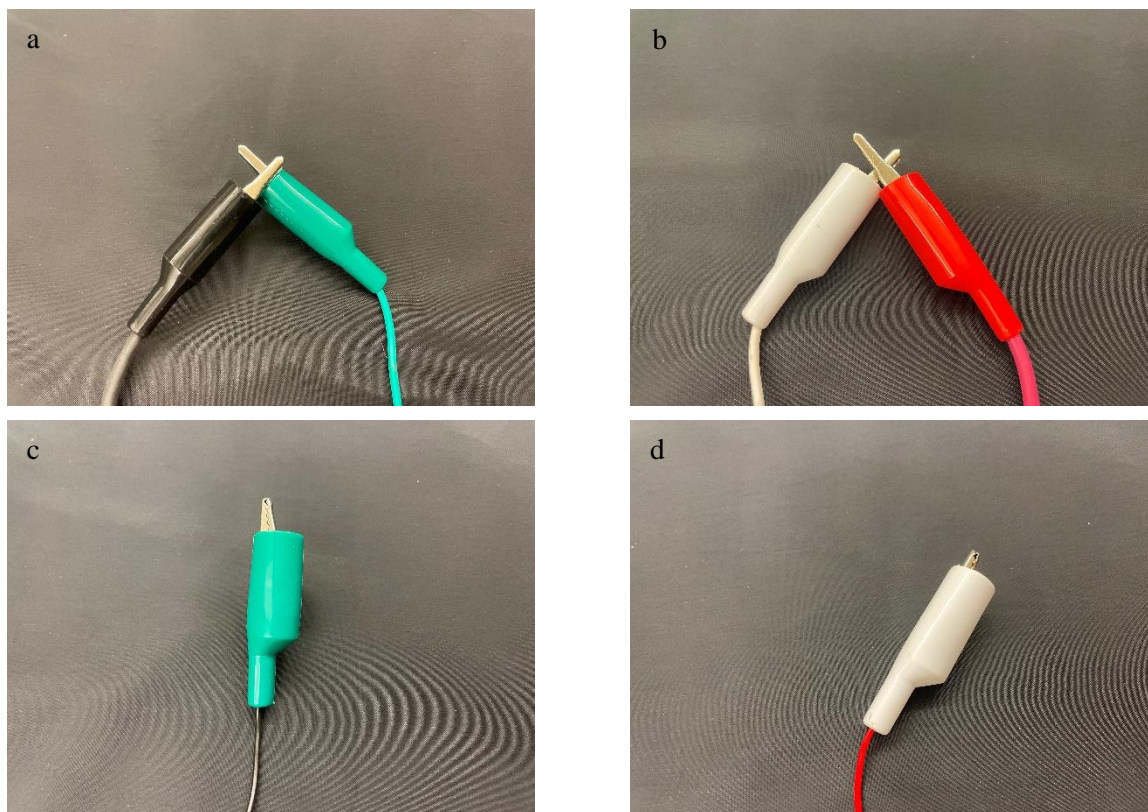**Figure H9.** Fully assembled electrodeposition cell

Figure H10. Potentiostat connections for (a) counter electrode, (b) working electrode, (c) counter electrode (reference connection) and (d) reference electrode (reference connection).

VITA

Bertan Ozdogru

Candidate for the Degree of

Doctor of Philosophy

Dissertation: CHEMO-MECHANICS OF IRON PHOSPHATE CATHODE IN ALKALI
                 METAL-ION BATTERIES

Major Field: Chemical Engineering

Biographical:

    Education:

    Completed the requirements for the Doctor of Philosophy in Chemical Engineering at
    Oklahoma State University, Stillwater, Oklahoma in December, 2022.

    Completed the requirements for the Master of Science in Chemical Engineering at
    Izmir Institute of Technology, Izmir, Turkey in 2018.

    Completed the requirements for the Bachelor of Science in Chemical Engineering at
    Izmir Institute of Technology, Izmir, Turkey in 2015.

    Experience:

    August 2018-Present   Graduate Research Assistant at
                                          Oklahoma State University

    September 2015-February 2018   Graduate Research Assistant at
                                          Izmir Institute of Technology

    Professional Memberships:

    The Electrochemical Society